



**NON-COUPLED AND MUTUALLY COUPLED SWITCHED  
RELUCTANCE MACHINES FOR AN E-BIKE TRACTION  
APPLICATION: POLE CONFIGURATIONS, DESIGN, AND  
COMPARISON**



**NON-COUPLED AND MUTUALLY COUPLED SWITCHED  
RELUCTANCE MACHINES FOR AN E-BIKE TRACTION  
APPLICATION: POLE CONFIGURATIONS, DESIGN, AND  
COMPARISON**

**BY BROCK HOWEY, B.TECH**

A thesis submitted to the McMaster School of Graduate Studies in partial  
fulfilment of the requirements for the Doctor of Philosophy degree in Mechanical  
Engineering.

Doctor of Philosophy in Mechanical Engineering (2018)

McMaster University, Hamilton, Ontario.

**TITLE:** Non-Coupled and Mutually Coupled Switched Reluctance  
Machines for an E-Bike Traction Application: Pole  
Configurations, Design, and Comparison

**AUTHOR:** Brock Howey, B.Tech (McMaster University)

**SUPERVISOR:** Dr. Ali Emadi

**PAGES:** 302

# Lay Abstract

This thesis studies the design process and analysis of two different motor types, for an electric bicycle application. They are designed to replace a commercially available permanent magnet synchronous motor (PMSM). This type of motor is typically expensive due to the rare-earth magnet material it requires. The two motors discussed in this thesis are switched reluctance motors (SRMs), which do not require magnet material, and thus have the potential to save cost (in addition to other benefits). One of the SRMs has magnetic fields that are independently controlled (CSRMs), and one has fields that are controlled together to produce torque (MCSRMs). The magnetics, control, thermal, and structural aspects of the CSRMs and MCSRMs are studied in detail. Novel geometry considerations (i.e. novel pole configurations) which impact the magnetics of each machine are compared to find the best-performing configuration for each machine type.



# Abstract

This thesis discusses the design of both a conventional non-coupled switched reluctance motor (CSRSM) and a mutually-coupled SRM (MCSRSM) for an exterior rotor e-bike application. Several novel pole configurations were analyzed for each machine type, and the performance of the final CSRSM and MCSRSM designs were compared for this application.

A commercially available e-bike permanent magnet synchronous motor (PMSM) was purchased, reverse engineered, and validated to define the geometry constraints and performance targets for the designs. Since switched reluctance motors do not use rare-earth permanent magnets, they are often seen as a potential low-cost alternative to permanent magnet machines. The goal of this research is to explain the relative advantages of CSRSMs and MCSRSMs when compared to PMSM machines for a direct-drive e-bike application. The final CSRSM and MCSRSM designs are analyzed in detail; electromagnetic, controls, thermal, and structural considerations are all studied. A prototype of the final CSRSM design was manufactured and validated experimentally, using a dynamometer setup.

The finalized CSRSM design is shown to be competitive with the PMSM machine when considering torque output, and is superior in terms of peak efficiency, and high speed torque performance. However, the CSRSM noise output and torque ripple were not compared to the PMSM, and a less-common

asymmetric-bridge converter is required for the CSRМ, which may hinder the ability for the machine to be implemented into existing e-bike packages.

The high speed torque performance of the MCSRМ is shown to be inferior to both the CSRМ and PMSM, as is the torque quality and efficiency. The MCSRМ is shown to be highly resistant to saturation which gives it the potential for high torque output at low speed (if thermal limits are not breached), though low saturation levels also contribute to low machine power factor. The MCSRМ may be better suited to lower speed, high torque applications, for this reason.

# Acknowledgements

I would like to take the opportunity to thank my supervisor Dr. Ali Emadi for the opportunity to be part of the team at the Canada Excellence Research Chair in Hybrid Powertrain program at the McMaster Automotive Resource Center. He has fostered a fantastic, highly driven research environment that was a pleasure to be a part of.

I would also like to thank Dr. Berker Bilgin, for his mentoring and guidance. I count myself extremely lucky to have had such an effective mentor. Dr. Bilgin's enthusiasm and passion were a continuous positive influence on my experience. His patience, understanding, and faith he places in others helped push me to continually improve myself, and for this I am truly grateful.

To my close friends Chelsey Boudreau, Kim Beatty, Dan Beatty, Elizabeth Rowan, and Hannah Pickering: You have all given me a huge amount of support and encouragement, when I truly needed it. You gave me light when all I could see was black - without your help, I wouldn't be here today. I will never forget and will always be grateful. I love you all.

I also wish to thank my close friends Alex Shmyryov and Ryan Babich for their continued encouragement, advice, and perspective. You guys rock.

Finally, I would like to thank my parents for their continued patience and understanding, and for teaching me that anything is possible if you put your mind to it.

# Contents

<b>Lay Abstract</b>	<b>iii</b>
<b>Abstract</b>	<b>iv</b>
<b>Acknowledgements</b>	<b>vi</b>
<b>Contents</b>	<b>vii</b>
<b>List of Figures</b>	<b>xv</b>
<b>List of Tables</b>	<b>xxix</b>
<b>List of Abbreviations and Symbols</b>	<b>xxxii</b>
<b>Declaration of Academic Achievement</b>	<b>xxxvii</b>
<b>Chapter 1 Introduction</b>	<b>1</b>
1.1 Background.....	1
1.2 Contributions .....	2
1.3 Thesis Outline.....	4
<b>Chapter 2 Fundamentals of Non-Coupled and Mutually Coupled Switched Reluctance Motors</b>	<b>7</b>
2.1 Introduction .....	7
2.2 Non-Coupled Switched Reluctance Motors (SRMs).....	10
2.2.1 Structure.....	10
2.2.2 Torque Production and Electromagnetics.....	17
2.2.3 Mutual Inductance Effects .....	26
2.2.4 Control Considerations .....	27
2.3 Mutually Coupled Switched Reluctance Motors (MCSRMs).....	38

2.3.1	Structure.....	38
2.3.2	Torque Production and Electromagnetics.....	40
2.3.3	Control Considerations .....	49
2.4	Loss Mechanisms .....	57
2.4.1	Core Loss .....	57
2.4.2	Copper Loss .....	60
2.5	Summary.....	63
<b>Chapter 3 Modelling of Non-Coupled and Mutually Coupled Switched Reluctance Motors</b>		<b>64</b>
3.1	Introduction .....	64
3.2	CSRMs.....	67
3.2.1	FEA Characterization .....	67
3.2.2	CSRМ Dynamic Model .....	69
3.3	MCSRMs.....	72
3.3.1	FEA Characterization .....	72
3.3.2	MCSRМ Dynamic Model.....	78
3.4	Additional Modelling .....	80
3.4.1	Electrical Angle Calculation.....	80
3.4.2	Current Reference Modelling .....	81
3.5	Summary.....	82
<b>Chapter 4 E-Bikes and Their Propulsion</b>		<b>83</b>
4.1	Introduction .....	83
4.2	Electric Bicycle Market.....	84
4.3	Classification of Electric Bicycles.....	86

4.3.1	Types of Power Assist .....	88
4.3.2	Motor Configurations .....	88
4.4	Motors in Electric Bicycles .....	93
4.4.1	Geared Motors .....	93
4.4.2	Direct-Drive Motors .....	95
4.5	Summary.....	98
<b>Chapter 5 Target Definition: Commercial Surface-Mounted Permanent Magnet E-Bike Motors</b>		<b>99</b>
5.1	Introduction .....	99
5.2	OEM Specifications.....	99
5.3	Electromagnetic FEA Modelling.....	101
5.4	Dynamometer Testing .....	104
5.4.1	Dynamometer Specifications .....	104
5.4.2	Testing Procedure (Condensed).....	105
5.4.3	Calibration and Sources of Error .....	106
5.4.4	Results.....	109
5.5	Finalized Design Targets.....	113
5.5.1	Torque-Speed Requirements.....	113
5.5.2	Input Current and Voltage Requirements .....	114
5.5.3	Packaging Requirements.....	115
5.5.4	Assumptions.....	118
5.6	Summary.....	119
<b>Chapter 6 Design of a Non-Coupled Switched Reluctance E-Bike Motor</b>		<b>120</b>
6.1	Introduction .....	120
6.2	Electromagnetics Design .....	120

6.2.1	Motor Design Process .....	120
6.2.2	Stator Pole-Arc Angle.....	125
6.2.3	Rotor Pole-Arc Angle .....	128
6.2.4	Stator Pole Height.....	130
6.2.5	Rotor Pole Height .....	131
6.2.6	Yoke Thickness.....	133
6.2.7	Coil Design .....	136
6.2.8	Pole Tapering.....	143
6.2.9	Pole Tip Fillets.....	145
6.2.10	Pole Base Fillets.....	147
6.2.11	Stack Length .....	149
6.2.12	Airgap .....	150
6.2.13	Selection of Pole Configuration.....	152
6.2.14	Coil Retention – Wedges vs. Shoes .....	161
6.3	Current Control.....	164
6.3.1	Genetic Algorithm Firing Angle Optimization.....	164
6.4	Loss and Efficiency Analysis .....	168
6.4.1	Torque-Speed – Efficiency Maps .....	169
6.5	Thermal Analysis.....	173
6.5.1	Torque-Speed – Transient Thermal Maps .....	175
6.5.2	Drive Cycle Response.....	178
6.6	FEA Validation.....	182
6.6.1	2D Switched Voltage FEA Validation – Critical Points.....	182
6.7	Structural Analysis .....	186
6.8	Summary.....	187

<b>Chapter 7 Experimental Verification: Non-Coupled 12/16 Switched Reluctance Motor</b>	<b>188</b>
7.1 Introduction .....	188
7.2 Additional Design Considerations.....	188
7.2.1 Main Bearing Selection .....	190
7.2.2 Bearing Preload.....	192
7.2.3 Rotor Assembly .....	194
7.2.4 Stator Assembly.....	196
7.2.5 Additional Components .....	199
7.3 Manufacturing Tolerances.....	202
7.3.1 Bearing Fits.....	202
7.3.2 Bolt and Dowel Fits .....	207
7.3.3 Resolver Press Fit .....	208
7.3.4 Radial Tolerances .....	209
7.3.5 Axial Tolerances .....	212
7.4 Testing .....	216
7.4.1 Stacking Factor .....	216
7.4.2 Axial Stack Alignment.....	217
7.4.3 Internal Clearances .....	218
7.4.4 Winding Testing .....	219
7.4.5 Rotating Assembly Balancing .....	221
7.5 Validation .....	224
7.5.1 Dynamometer Setup .....	224
7.5.2 Current Transducer Calibration .....	226
7.5.3 Resolver Calibration .....	227
7.5.4 Static Flux-Linkage Validation.....	229
7.5.5 Dynamic Torque-Speed Validation .....	235



7.6 Summary.....	240
<b>Chapter 8 Design of a Mutually Coupled Switched Reluctance E-Bike Motor</b>	<b>241</b>
8.1 Introduction .....	241
8.2 Electromagnetics Design.....	242
8.2.1 Motor Design Process.....	242
8.2.2 Stator Pole-Arc Angle.....	248
8.2.3 Rotor Pole-Arc Angle .....	250
8.2.4 Stator Pole Height.....	251
8.2.5 Rotor Pole Height .....	252
8.2.6 Yoke Thickness.....	254
8.2.7 Coil Design .....	257
8.2.8 Pole Tapering.....	261
8.2.9 Pole Tip Fillets.....	263
8.2.10 Pole Base Fillets.....	265
8.2.11 Stack Length .....	267
8.2.12 Airgap .....	268
8.2.13 Selection of Pole Configuration.....	269
8.2.14 Coil Retention – Wedges vs. Shoes .....	273
8.3 Current Control.....	275
8.3.1 $\phi_{dq}$ Sweep.....	275
8.4 Loss and Efficiency Analysis .....	278
8.4.1 Torque-Speed – Efficiency Maps .....	279
8.5 Thermal Analysis.....	283
8.5.1 Torque-Speed – Transient Thermal Maps .....	285
8.5.2 Drive Cycle Response.....	288

8.6 FEA Validation.....	290
8.6.1 2D Switched Voltage FEA Validation – Critical Points.....	290
8.7 Summary.....	294
<b>Chapter 9 Conclusions</b>	<b>296</b>
9.1 Conclusions .....	296
9.2 Future Work.....	298
<b>References</b>	<b>302</b>
<b>Appendix</b>	<b>307</b>
9.3 A. Phase Transformations ( $abc \rightarrow dq$ ) .....	307
9.3.1 Phase Transformations.....	307
9.4 B. CSRSM Structural Analysis.....	309
9.4.1 Assumptions and Loading Conditions .....	309
9.4.2 Shaft Analysis .....	318
9.4.3 Front Endcap.....	325
9.4.4 Rear Endcap.....	335
9.4.5 Winding Wedge Engagement .....	342
9.5 C. MCSRSM Analyses (No Rotor Yoke).....	346
9.6 D. CSRSM Expanded Voltage/Torque Equations.....	348
9.6.1 $abc$ -Reference Frame .....	348
9.7 E. MCSRSM Expanded Voltage Equation .....	352
9.7.1 $\alpha\beta$ -Reference Frame.....	352
9.8 F. Tolerance Calculations .....	354
9.8.1 Resolver Press Fit .....	356
9.8.2 Radial Tolerances .....	358

9.8.3 Axial Tolerances .....	358
9.9 G. Torque Equation Validation .....	363

# List of Figures

Fig. 2.1 SRM / MCSRМ configurations (coils not shown): (a) radial flux SRM; (b) axial flux SRM.....	7
Fig. 2.2 Geometry: (a) 12/16 CSRМ; (b) 15/10 MCSRМ.....	8
Fig. 2.3 Reference phase current waveforms (phase 1): (a) CSRМ; (b) MCSRМ.....	8
Fig. 2.4 Flux lines (unaligned position): (a) CSRМ; (b) MCSRМ.....	9
Fig. 2.5 Flux lines (aligned position): (a) CSRМ; (b) MCSRМ.....	9
Fig. 2.6 SRM at different positions: (a) completely unaligned, (b) beginning of alignment, (c) fully aligned, (d) fully aligned still, (e) end of alignment, (f) completely unaligned.....	13
Fig. 2.7 Idealized inductance vs. rotor position.....	14
Fig. 2.8 Idealized inductance vs. rotor position – phase excitation overlap.....	15
Fig. 2.9 Flux-linkage vs. phase current (linear operation).....	18
Fig. 2.10 Flux-linkage vs. phase current (non-linear saturated operation).....	19
Fig. 2.11 $\psi/i$ work cycle.....	20
Fig. 2.12 Simplified circuit representation of a phase winding.....	21
Fig. 2.13 Phase current waveforms (3-phase CSRМ – dynamic model): (a) low speed; (b) high speed.....	28
Fig. 2.14 Phase torque vs. total torque output (3-phase CSRМ – dynamic model): (a) low speed; (b) high speed.....	29
Fig. 2.15 Phase voltage (3-phase CSRМ – dynamic model): (a) low speed; (b) high speed.....	29
Fig. 2.16 Phase flux-linkage (3-phase CSRМ – dynamic model): (a) low speed; (b) high speed.....	30
Fig. 2.17 $\psi/i$ curves (3-phase CSRМ, phase A – dynamic model): (a) low speed; (b) high speed.....	30

Fig. 2.18 3-Phase asymmetric-bridge converter (switch freewheeling diodes removed).....	31
Fig. 2.19 Mode 1: forward current (asymmetric-bridge converter).....	31
Fig. 2.20 Mode 2: freewheeling current (asymmetric-bridge converter).....	32
Fig. 2.21 Mode 3: reverse current (asymmetric-bridge converter).....	32
Fig. 2.22 Control system: phase current control.....	33
Fig. 2.23 Phase current regulation using hysteresis controller - low speed ( $v_{Net} \gg 0$ ).....	35
Fig. 2.24 Phase current regulation using hysteresis controller - high speed ( $v_{Net} \approx 0$ ).....	36
Fig. 2.25 Torque-speed map - critical behavior (CSRSM).....	36
Fig. 2.26 Control system: speed control + current control.....	37
Fig. 2.27 Flux-linkage vs. phase current (phase 1, linear operation).....	41
Fig. 2.28 Flux-linkage vs. phase current (phase 1, non-linear saturated operation).....	43
Fig. 2.29 $\psi/i$ work cycle (phase 1): (a) square-wave excitation; (b) sinusoidal excitation.....	44
Fig. 2.30 Phase current waveforms (3-phase MCSRM – dynamic model): (a) low speed; (b) high speed.....	50
Fig. 2.31 Phase torque vs. total torque output (3-phase MCSRM – dynamic model): (a) low speed; (b) high speed.....	50
Fig. 2.32 Phase voltage (3-phase MCSRM – dynamic model): (a) low speed; (b) high speed.....	51
Fig. 2.33 Phase flux-linkage (3-phase MCSRM – dynamic model): (a) low speed; (b) high speed.....	51
Fig. 2.34 $\psi/i$ curves (3-phase MCSRM, phase A – dynamic model): (a) low speed; (b) high speed.....	52
Fig. 2.35 3-Phase full-bridge converter (switch freewheeling diodes removed).....	52

Fig. 2.36 Mode 1: forward current (full-bridge converter).....	53
Fig. 2.37 Mode 2: freewheeling current (full-bridge converter).....	54
Fig. 2.38 Mode 3: reverse current (full-bridge converter).....	54
Fig. 2.39 Phase current regulation using hysteresis controller - low speed ( $v_{Net} \gg 0$ ) .....	55
Fig. 2.40 Phase current regulation using hysteresis controller - high speed ( $v_{Net} \approx 0$ ) .....	56
Fig. 2.41 Torque-speed map - critical behavior (MCSRМ).....	56
Fig. 2.42 Magnetic hysteresis: (a) hard magnetic loop; (b) soft magnetic loop.....	58
Fig. 3.1 Full dynamic modelling procedure.....	66
Fig. 3.2 CSRМ FEA characterization process .....	67
Fig. 3.3 LUTs: (a) phase current; (b) phase torque.....	69
Fig. 3.4 CSRМ mathematical model algebraic loop.....	71
Fig. 3.5 CSRМ model implemented in control loop.....	71
Fig. 3.6 MCSRМ FEA characterization process .....	72
Fig. 3.7 LUTs (sliced @ 60° elec.): (a) d-axis current; (b) q-axis current.....	77
Fig. 3.8 Torque LUT (sliced @ 60° elec.) .....	78
Fig. 3.9 MCSRМ mathematical model algebraic loop .....	79
Fig. 3.10 MCSRМ model implemented in control loop .....	80
Fig. 4.1 Projected annual global e-bike sales [11].....	85
Fig. 4.2 Projected e-bike market share of bicycle market for different regions [12] .....	86
Fig. 4.3 Conventional bicycle layout, with gears, brakes, and freewheel (simplified, top view).....	89
Fig. 4.4 Typical mid-drive e-bike layout, without regen capability (simplified, top view).....	89
Fig. 4.5 Shimano STEPS mid-drive setup - disassembled.....	90

Fig. 4.6 Typical hub motor e-bike layout, without regen capability (simplified, top view): (a) front hub; (b) rear hub.....	91
Fig. 4.7 E-bike layouts, with regen capability (simplified, top view): (a) front hub; (b) mid-drive; (c) rear hub.....	92
Fig. 4.8 “Spoke-type” IPM motor from Shimano STEPS mid-drive .....	94
Fig. 4.9 Direct-drive SPM e-bike motor - Crystalyte HS3548 .....	96
Fig. 4.10 Permanent magnet material in SPM rotor - Crystalyte HS3548 .....	96
Fig. 5.1 Grin Technologies motor simulator (setup for HS3548) [18] .....	101
Fig. 5.2 Crystalyte HS3548 PMSM stator (2 phases removed).....	102
Fig. 5.3 Simplified 2D JMAG FEA model of the Crystalyte HS3548 motor .....	103
Fig. 5.4 PMSM dynamometer testing setup.....	104
Fig. 5.5 PMSM dynamometer testing setup - detail view.....	105
Fig. 5.6 Factory-installed thermistor location.....	108
Fig. 5.7 Temperature calculated from internal thermistor .....	108
Fig. 5.8 PMSM torque-speed map (with OEM [18], FEA, and experimental curves) .....	110
Fig. 5.9 PMSM inverter DC input current (with OEM [18] and experimental curves) .....	110
Fig. 5.10 PMSM RMS phase current (with OEM [18] and experimental curves) .....	111
Fig. 5.11 PMSM mechanical output power (with OEM [18] and experimental curves) .....	111
Fig. 5.12 Finalized torque-speed outline design targets [18].....	113
Fig. 5.13 PMSM torque ripple map .....	114
Fig. 5.14 Disassembled Crystalyte HS3548 PMSM.....	116
Fig. 6.1 CSRSM electromagnetic design process .....	122
Fig. 6.2 CSRSM geometry parameter definition .....	124

Fig. 6.3	Effect of varying $\beta_R$ and $\beta_S$ (final 12/16 design, 75 A constant current): (a) $T$ effects; (b) $V_{Ph}$ effects; (c) peak and RMS comparison; (d) normalized voltage and loss performance rating ....	126
Fig. 6.4	Static torque waveforms for $\beta_R > \beta_S$ vs. $\beta_R = \beta_S$ (12/8 example) .....	129
Fig. 6.5	Dynamic torque waveforms @ 1 RPM for $\beta_R > \beta_S$ (12/8 example)....	130
Fig. 6.6	Dynamic torque waveforms @ 1 RPM for $\beta_R = \beta_S$ (12/8 example)....	130
Fig. 6.7	Effect of varying $h_S$ (final 12/16 design, 75 A constant current): (a) $T$ effects; (b) $V_{Ph}$ effects; (c) peak and RMS comparison; (d) normalized voltage and loss performance rating .....	131
Fig. 6.8	Effect of varying $h_R$ (final 12/16 design, 75 A constant current): (a) $T$ effects; (b) $V_{Ph}$ effects; (c) peak and RMS comparison; (d) normalized voltage and loss performance rating .....	132
Fig. 6.9	Effect of varying $b_S$ (final 12/16 design, 75 A constant current): (a) $T$ effects; (b) $V_{Ph}$ effects; (c) peak and RMS comparison; (d) normalized voltage and loss performance rating .....	134
Fig. 6.10	Effect of varying $b_R$ (final 12/16 design, 75 A constant current): (a) $T$ effects; (b) $V_{Ph}$ effects; (c) peak and RMS comparison; (d) normalized voltage and loss performance rating .....	135
Fig. 6.11	Static-current phase torque vs. position (12/8 example) .....	139
Fig. 6.12	Static-current airgap flux density vs. position (12/8 example).....	139
Fig. 6.13	Static-current stator pole flux density vs. position (12/8 example).....	140
Fig. 6.14	Static-current induced phase voltage vs. position (12/8 example) ....	140
Fig. 6.15	Effect of varying $N_{Turns}$ (final 12/16 design, 75 A constant current): (a) $T$ effects; (b) $V_{Ph}$ effects; (c) peak and RMS comparison; (d) normalized voltage and loss performance rating ....	141
Fig. 6.16	Effect of varying $\alpha_R$ (final 12/16 design, 75 A constant current): (a) $T$ effects; (b) $V_{Ph}$ effects; (c) peak and RMS comparison; (d) normalized voltage and loss performance rating .....	144



Fig. 6.17	Effect of varying $\alpha_S$ (final 12/16 design, 75 A constant current): (a) $T$ effects; (b) $V_{Ph}$ effects; (c) peak and RMS comparison; (d) normalized voltage and loss performance rating .....	145
Fig. 6.18	Effect of varying $\zeta_R$ (final 12/16 design, 75 A constant current): (a) $T$ effects; (b) $V_{Ph}$ effects; (c) peak and RMS comparison; (d) normalized voltage and loss performance rating .....	146
Fig. 6.19	Effect of varying $\zeta_S$ (final 12/16 design, 75 A constant current): (a) $T$ effects; (b) $V_{Ph}$ effects; (c) peak and RMS comparison; (d) normalized voltage and loss performance rating .....	147
Fig. 6.20	Effect of varying $\gamma_R$ (final 12/16 design, 75 A constant current): (a) $T$ effects; (b) $V_{Ph}$ effects; (c) peak and RMS comparison; (d) normalized voltage and loss performance rating .....	148
Fig. 6.21	Effect of varying $\gamma_S$ (final 12/16 design, 75 A constant current): (a) $T$ effects; (b) $V_{Ph}$ effects; (c) peak and RMS comparison; (d) normalized voltage and loss performance rating .....	149
Fig. 6.22	Effect of varying $l_{Stack}$ (final 12/16 design, 75 A constant current): (a) $T$ effects; (b) $V_{Ph}$ effects; (c) peak and RMS comparison; (d) normalized voltage and loss performance rating ....	150
Fig. 6.23	Effect of varying $l_{Airgap}$ (final 12/16 design, 75 A constant current): (a) $T$ effects; (b) $V_{Ph}$ effects (c) peak and RMS comparison; (d) normalized voltage and loss performance rating ....	151
Fig. 6.24	Final exterior rotor design cross-sections (without tapering/filletts): (a) 12/8; (b) 12/16; (c) 12/20; (d) 12/28 .....	153
Fig. 6.25	Torque waveform comparison below base speed (max current) .....	154
Fig. 6.26	$\psi/i$ comparison – capability limits (solid) & 400 RPM (dotted) .....	154
Fig. 6.27	Copper loss maps: (a) 12/8; (b) 12/16; (c) 12/20; (d) 12/28.....	156
Fig. 6.28	Iron loss maps: (a) 12/8; (b) 12/16; (c) 12/20; (d) 12/28.....	157
Fig. 6.29	RMS current maps: (a) 12/8; (b) 12/16; (c) 12/20; (d) 12/28.....	159
Fig. 6.30	Efficiency maps: (a) 12/8; (b) 12/16; (c) 12/20; (d) 12/28 .....	160

Fig. 6.31	Coil retention method comparison (final 12/16 design).....	163
Fig. 6.32	Optimized firing tables for finalized 12/16 design: (a) turn-on; (b) turn-off.....	168
Fig. 6.33	Analyzed torque-speed points (final 12/16 design).....	169
Fig. 6.34	Torque-speed maps (final 12/16 design) - with: (a) mean dynamic model vs. FEA error contours; (b) peak dynamic model vs. FEA error contours; (c) Net RMS torque ripple contours .....	170
Fig. 6.35	Torque-speed maps (final 12/16 design) - with: (a) rotor iron loss contours; (b) stator iron loss contours; (c) total iron loss contours .....	171
Fig. 6.36	Torque-speed maps (final 12/16 design) - with: (a) RMS phase current contours; (b) copper loss contours .....	172
Fig. 6.37	Torque-speed maps (final 12/16 design) – with: (a) total loss contours; (b) motor efficiency contours .....	173
Fig. 6.38	Radial geometry representation in MotorCAD (final 12/16 design).....	174
Fig. 6.39	Axial geometry representation in MotorCAD - rotated (final 12/16 design).....	174
Fig. 6.40	Rotor transient thermal performance maps after 5 minutes (final 12/16 design): (a) pole; (b) yoke.....	175
Fig. 6.41	Stator transient thermal performance maps after 5 minutes (final 12/16 design): (a) pole; (b) yoke.....	176
Fig. 6.42	Winding transient thermal performance map after 5 minutes (final 12/16 design): (a) peak; (b) average.....	176
Fig. 6.43	Time to 120°C peak winding temperature (final 12/16 design) .....	177
Fig. 6.44	Speed-time e-bike drive cycle .....	179
Fig. 6.45	Torque-time e-bike drive cycle.....	180
Fig. 6.46	Drive-cycle transient thermal response (final 12/16 design).....	181

Fig. 6.47 Switched voltage waveforms @ 10 RPM, 75 A reference (final 12/16 design).....	182
Fig. 6.48 2D switched voltage FEA validation @ 10 RPM, 75 A reference (final 12/16 design): (a) torque; (b) phase current; (c) phase flux-linkage .....	183
Fig. 6.49 Switched voltage waveforms @ 400 RPM, 75A reference (final 12/16 design).....	184
Fig. 6.50 2D switched voltage FEA validation @ 400 RPM, 75 A reference (final 12/16 design): (a) torque; (b) phase current; (c) phase flux-linkage .....	185
Fig. 7.1 Assembly component detail (12/16 CSRSM prototype) .....	189
Fig. 7.2 Manufactured prototype 12/16 CSRSM .....	189
Fig. 7.3 Main bearings – cross-section highlighted in cyan (12/16 CSRSM prototype).....	191
Fig. 7.4 Rotor assembly detail (12/16 CSRSM prototype) .....	194
Fig. 7.5 Manufactured rotor assembly (end cover A removed for inspection).....	195
Fig. 7.6 Stator assembly detail (12/16 CSRSM prototype).....	196
Fig. 7.7 Manufactured stator assembly: (a) insulation; (b) side A; (c) side B. ....	197
Fig. 7.8 Prototype thermocouple positions (3 per phase) .....	198
Fig. 7.9 Resolver, gearing, and mounting detail – shaft cross-section highlighted in cyan (12/16 CSRSM prototype).....	199
Fig. 7.10 Additional components: (a) resolver-rotor/pulley assembly; (b) resolver-stator assembly.....	200
Fig. 7.11 Full assembly, with resolver and gearing system attached (12/16 CSRSM prototype).....	201
Fig. 7.12 Dowel and bolt positional accuracy tolerance concept .....	208
Fig. 7.13 Radial tolerances (12/16 CSRSM prototype) .....	209

Fig. 7.14 Stator heating using induction heater (12/16 prototype) .....	210
Fig. 7.15 Shaft cooling before insertion (12/16 prototype) .....	210
Fig. 7.16 Shaft insertion procedure.....	211
Fig. 7.17 Axial pre-load spring operating principle (12/16 CSR prototype) .....	213
Fig. 7.18 Axial tolerance stack-up (12/16 CSR prototype).....	215
Fig. 7.19 Prototype stator stack (83 laminations for stator– 78 for rotor) .....	217
Fig. 7.20 Axial stack alignment (12/16 prototype).....	217
Fig. 7.21 Plastigauge testing of internal clearances (side “A” shown – side “B” circled) .....	218
Fig. 7.22 Prototype motor - balancing setup.....	221
Fig. 7.23 Prototype motor - balancing test report .....	223
Fig. 7.24 DSP - converter block diagram as used in dynamometer setup .....	225
Fig. 7.25 Full dynamometer testing setup.....	226
Fig. 7.26 Position error vs. stroke # .....	227
Fig. 7.27 Phase resistance measurement.....	231
Fig. 7.28 Flux-linkage testing - with indexer visible.....	231
Fig. 7.29 Capturing phase current and voltage waveforms using oscilloscope .....	232
Fig. 7.30 Flux-linkage validation $\psi-\theta$ (12/16 CSR prototype).....	233
Fig. 7.31 Flux-linkage validation $\psi-i$ (12/16 CSR prototype).....	233
Fig. 7.32 Dynamometer Torque Loss vs. Speed .....	238
Fig. 8.1 MCSRM electromagnetic design process.....	244
Fig. 8.2 MCSRM geometry parameter definition.....	247
Fig. 8.3 Effect of varying $\beta_S$ (final 15/10 design, 3-phase AC, $I_{Amp} = 75$ A, $\phi_{dq} = 45^\circ$ ): (a) $T$ effects; (b) $V_{Ph}$ effects; (c) peak and RMS comparison; (d) normalized voltage and loss performance rating ....	249

- Fig. 8.4 Effect of varying  $\beta_R$  (final 15/10 design, 3-phase AC,  $I_{Amp} = 75$  A,  $\phi_{dq} = 45^\circ$ ): (a)  $T$  effects; (b)  $V_{Ph}$  effects; (c) peak and RMS comparison; (d) normalized voltage and loss performance rating .... 251
- Fig. 8.5 Effect of varying  $h_S$  (final 15/10 design, 3-phase AC,  $I_{Amp} = 75$  A,  $\phi_{dq} = 45^\circ$ ): (a)  $T$  effects; (b)  $V_{Ph}$  effects; (c) peak and RMS comparison; (d) normalized voltage and loss performance rating .... 252
- Fig. 8.6 Effect of varying  $h_R$  (final 15/10 design, 3-phase AC,  $I_{Amp} = 75$  A,  $\phi_{dq} = 45^\circ$ ): (a)  $T$  effects; (b)  $V_{Ph}$  effects; (c) peak and RMS comparison; (d) normalized voltage and loss performance rating .... 253
- Fig. 8.7 Effect of varying  $b_S$  (final 15/10 design, 3-phase AC,  $I_{Amp} = 75$  A,  $\phi_{dq} = 45^\circ$ ): (a)  $T$  effects; (b)  $V_{Ph}$  effects; (c) peak and RMS comparison; (d) normalized voltage and loss performance rating .... 255
- Fig. 8.8 Effect of varying  $b_R$  (final 15/10 design, 3-phase AC,  $I_{Amp} = 75$  A,  $\phi_{dq} = 45^\circ$ ): (a)  $T$  effects; (b)  $V_{Ph}$  effects; (c) peak and RMS comparison; (d) normalized voltage and loss performance rating .... 256
- Fig. 8.9 Effect of varying  $N_{Turns}$  (final 15/10 design, 3-phase AC,  $I_{Amp} = 75$  A,  $\phi_{dq} = 45^\circ$ ): (a)  $T$  effects; (b)  $V_{Ph}$  effects; (c) peak and RMS comparison; (d) normalized voltage and loss performance rating .... 260
- Fig. 8.10 Effect of varying  $\alpha_R$  (final 15/10 design, 3-phase AC,  $I_{Amp} = 75$  A,  $\phi_{dq} = 45^\circ$ ): (a)  $T$  effects; (b)  $V_{Ph}$  effects; (c) peak and RMS comparison; (d) normalized voltage and loss performance rating .... 261
- Fig. 8.11 Effect of varying  $\alpha_S$  (final 15/10 design, 3-phase AC,  $I_{Amp} = 75$  A,  $\phi_{dq} = 45^\circ$ ): (a)  $T$  effects; (b)  $V_{Ph}$  effects; (c) peak and RMS comparison; (d) normalized voltage and loss performance rating .... 262
- Fig. 8.12 Effect of varying  $\zeta_R$  (final 15/10 design, 3-phase AC,  $I_{Amp} = 75$  A,  $\phi_{dq} = 45^\circ$ ): (a)  $T$  effects; (b)  $V_{Ph}$  effects; (c) peak and RMS comparison; (d) normalized voltage and loss performance rating .... 263

Fig. 8.13	Effect of varying $\zeta_S$ (final 15/10 design, 3-phase AC, $I_{Amp} = 75$ A, $\phi_{dq} = 45^\circ$ ): (a) $T$ effects; (b) $V_{Ph}$ effects; (c) peak and RMS comparison; (d) normalized voltage and loss performance rating ....	264
Fig. 8.14	Effect of varying $\gamma_R$ (final 15/10 design, 3-phase AC, $I_{Amp} = 75$ A, $\phi_{dq} = 45^\circ$ ): (a) $T$ effects; (b) $V_{Ph}$ effects; (c) peak and RMS comparison; (d) normalized voltage and loss performance rating ....	265
Fig. 8.15	Effect of varying $\gamma_S$ (final 15/10 design, 3-phase AC, $I_{Amp} = 75$ A, $\phi_{dq} = 45^\circ$ ): (a) $T$ effects; (b) $V_{Ph}$ effects; (c) peak and RMS comparison; (d) normalized voltage and loss performance rating ....	266
Fig. 8.16	Effect of varying $l_{Stack}$ (final 15/10 design, 3-phase AC, $I_{Amp} =$ $75$ A, $\phi_{dq} = 45^\circ$ ): (a) $T$ effects; (b) $V_{Ph}$ effects; (c) peak and RMS comparison; (d) normalized voltage and loss performance rating ....	267
Fig. 8.17	Effect of varying $l_{Airgap}$ (final 15/10 design, 3-phase AC, $I_{Amp} =$ $75$ A, $\phi_{dq} = 45^\circ$ ): (a) $T$ effects; (b) $V_{Ph}$ effects; (c) peak and RMS comparison; (d) normalized voltage and loss performance rating ....	268
Fig. 8.18	Coil retention method comparison (final 15/10 design).....	274
Fig. 8.19	$\phi_{dq}$ selection algorithm.....	276
Fig. 8.20	$\phi_{dq}$ map for finalized 15/10 design .....	278
Fig. 8.21	Torque-speed maps (final 15/10 design) - with: (a) mean dynamic model vs. FEA error contours; (b) peak dynamic model vs. FEA error contours; (c) Net RMS torque ripple contours .....	280
Fig. 8.22	Torque-speed maps (final 15/10 design) - with: (a) rotor iron loss contours; (b) stator iron loss contours; (c) total iron loss contours .....	281
Fig. 8.23	Torque-speed maps (final 15/10 design) - with: (a) RMS phase current contours; (b) copper loss contours .....	282
Fig. 8.24	Torque-speed maps (final 15/10 design) - with: (a) total loss contours; (b) motor efficiency contours .....	283

Fig. 8.25 Radial geometry representation in MotorCAD (final 15/10 design) .....	284
Fig. 8.26 Axial geometry representation in MotorCAD - rotated (final 15/10 design) .....	284
Fig. 8.27 Rotor transient thermal performance maps after 5 minutes (final 15/10 design): (a) pole; (b) yoke .....	285
Fig. 8.28 Stator transient thermal performance maps after 5 minutes (final 15/10 design): (a) pole; (b) yoke .....	286
Fig. 8.29 Winding transient thermal performance map after 5 minutes (final 15/10 design) .....	286
Fig. 8.30 Time to 240°C peak winding temperature (final 15/10 design) .....	287
Fig. 8.31 Speed-time e-bike drive cycle .....	288
Fig. 8.32 Torque-time e-bike drive cycle.....	289
Fig. 8.33 Drive-cycle transient thermal response (final 15/10 design).....	289
Fig. 8.34 Switched voltage waveforms @ 10 RPM, 75A reference (final 15/10 design).....	290
Fig. 8.35 2D switched voltage FEA validation @ 10 RPM, 75A reference (final 15/10 design): (a) torque; (b) phase current; (c) phase flux-linkage .....	291
Fig. 8.36 Switched voltage waveforms @ 400 RPM, 75A reference (final 15/10 design).....	292
Fig. 8.37 2D switched voltage FEA validation @ 400 RPM, 75A reference (final 15/10 design): (a) torque; (b) phase current; (c) phase flux-linkage .....	293
Fig. X.1 Torque condition – shaft surfaces.....	312
Fig. X.2 Torque condition - front endcap surfaces (rear endcap similar).....	312
Fig. X.3 Bump loading - shaft surfaces .....	313
Fig. X.4 Bump loading - front endcap surfaces (rear endcap similar).....	314

Fig. X.5 Corner loading - shaft surfaces .....	315
Fig. X.6 Corner loading - front endcap surfaces (rear endcap similar) .....	316
Fig. X.7 Lumped mass + inertia loads - shaft .....	319
Fig. X.8 Different fixture locations used for shaft analysis .....	319
Fig. X.9 Von-Mises stress - shaft (case 2) .....	320
Fig. X.10 Von-Mises stress - shaft (case 3) .....	320
Fig. X.11 Von-Mises stress - shaft (case 4) .....	321
Fig. X.12 Von-Mises stress - shaft (case 5) .....	321
Fig. X.13 Deformation - shaft (case 2) .....	322
Fig. X.14 Deformation - shaft (case 3) .....	322
Fig. X.15 Deformation - shaft (case 4) .....	323
Fig. X.16 Deformation - shaft (case 5) .....	323
Fig. X.17 Lumped mass + inertia loads - front endcap .....	326
Fig. X.18 Different fixture locations used for front endcap analysis .....	326
Fig. X.19 Von-Mises stress - front endcap (case 1) .....	327
Fig. X.20 Von-Mises stress - front endcap (case 2) .....	328
Fig. X.21 Von-Mises stress - front endcap (case 3) .....	328
Fig. X.22 Von-Mises stress - front endcap (case 4) .....	329
Fig. X.23 Von-Mises stress - front endcap (case 5) .....	329
Fig. X.24 Von-Mises stress - front endcap (case 6) .....	330
Fig. X.25 Deformation - front endcap (case 1) .....	330
Fig. X.26 Deformation - front endcap (case 2) .....	331
Fig. X.27 Deformation - front endcap (case 3) .....	331
Fig. X.28 Deformation - front endcap (case 4) .....	332
Fig. X.29 Deformation - front endcap (case 5) .....	332
Fig. X.30 Deformation - front endcap (case 6) .....	333
Fig. X.31 Lumped mass + inertia loads - rear endcap .....	336
Fig. X.32 Different fixture locations used for rear endcap analysis .....	336
Fig. X.33 Von-Mises stress - rear endcap (case 1) .....	337



Fig. X.34 Von-Mises stress - rear endcap (case 2) .....	338
Fig. X.35 Von-Mises stress - rear endcap (case 3) .....	338
Fig. X.36 Von-Mises stress - rear endcap (case 4) .....	339
Fig. X.37 Deformation - rear endcap (case 1) .....	339
Fig. X.38 Deformation - rear endcap (case 2) .....	340
Fig. X.39 Deformation - rear endcap (case 3) .....	340
Fig. X.40 Deformation - rear endcap (case 4) .....	341
Fig. X.41 Deformation – slot wedge @ 120°C.....	344
Fig. X.42 Von-Mises stress - slot wedge @ 120°C .....	345
Fig. X.43 15/5 MCSRM flux path comparison: (a) with yoke; (b) without yoke .....	346
Fig. X.44 Co-energy vs. field-energy torque vs. FEA (12/16 CSRM) .....	363
Fig. X.45 Phase $\psi/i$ plots (12/16 CSRM).....	364

# List of Tables

TABLE 3.1 CSRM FEA simulation matrix example ( $N_{Current} = 2, N_{Angles} =$ 2) .....	68
TABLE 3.2 MCSRM FEA simulation matrix ( $N_{Current} = 2, N_{Angles} = 2$ ).....	74
TABLE 3.3 MCSRM $dq$ FEA simulation matrix ( $N_{Current} = 2, N_{Angles} = 2$ ).....	75
TABLE 3.4 MCSRM $dq$ FEA simulation matrix - using $i_q$ symmetry ( $N_{Current} = 2, N_{Angles} = 2$ ).....	76
TABLE 5.1 Crystalyte HS3548 motor - distributor specifications [15].....	100
TABLE 5.2 Grin Technologies C7225-NC-25A inverter - OEM specifications [16]–[17] .....	100
TABLE 5.3 Measured HS3548 machine dimensions .....	115
TABLE 5.4 Finalized geometry constraints for SRM and MCSRM designs.....	117
TABLE 5.5 Additional constraints for SRM and MCSRM designs.....	118
TABLE 6.1 CSRM initial geometric parameter sweep ranges.....	123
TABLE 6.2 Wire size impact on phase resistance (for final 12/16 geometry) .....	137
TABLE 6.3 Coil retention comparison cases (final 12/16 design).....	161
TABLE 6.4 Optimizer and model parameters .....	166
TABLE 6.5 Drive cycle parameters.....	178
TABLE 7.1 Main bearing specifications .....	192
TABLE 7.2 Bearing preload guidelines.....	193
TABLE 7.3 Recommended shaft fits for cylindrical-bore radial ball bearings (adapted from Table 7.2 in [22]) – final selection highlighted. ....	203
TABLE 7.4 Recommended housing fits for radial ball bearings (adapted from Table 7.2 in [22]) – final selection highlighted. ....	204

TABLE 7.5 Bearing load conditions for tolerance selection .....	206
TABLE 7.6 Minimum internal clearance between endcaps and windings.....	218
TABLE 7.7 Measured line-line inductance variation with position .....	219
TABLE 7.8 Measured phase resistance at room temperature.....	220
TABLE 8.1 MCSRМ initial geometric parameter sweep ranges .....	246
TABLE 8.2 Wire size impact on phase resistance (for final 15/10 geometry) .....	258
TABLE 8.3 Pole configuration performance comparison (best $T_{Ave}$ results): 400 RPM, 3-phase AC @ $I_{Amp} = 75$ A, $\phi_{dq} = 45^\circ$ .....	270
TABLE 8.4 Pole configuration performance comparison (best $T_{Ave}/V_{RMS}$ results): 400 RPM, 3-phase AC @ $I_{Amp} = 75$ A, $\phi_{dq} = 45^\circ$ .....	271
TABLE 8.5 Pole configuration performance comparison (best $T_{Ave}/P_{Cu}$ results): 400 RPM, 3-phase AC @ $I_{Amp} = 75$ A, $\phi_{dq} = 45^\circ$ .....	272
TABLE 8.6 Coil retention comparison cases (final 15/10 design).....	273
TABLE 8.7 Sweep model parameters .....	277
TABLE 9.1 Performance comparison – PMSM vs. 12/16 CSRМ vs. 15/10 MCSRМ.....	297
TABLE X.1 Structural analysis assumptions .....	310
TABLE X.2 Material properties for structural FEA.....	311
TABLE X.3 Lumped mass and inertia properties of component assemblies .....	317
TABLE X.4 Loading cases for shaft structural analysis.....	318
TABLE X.5 Minimum fatigue life for each loading case - shaft .....	324
TABLE X.6 Loading cases for front endcap structural analysis .....	325
TABLE X.7 Fixture degrees of freedom - front endcap.....	327
TABLE X.8 Minimum fatigue life for each loading case - front endcap .....	333
TABLE X.9 Loading cases for rear endcap structural analysis.....	335
TABLE X.10 Fixture degrees of freedom - rear endcap .....	337

TABLE X.11	Minimum fatigue life for each loading case - rear endcap.....	341
TABLE X.12	Slot wedge analysis – simulation parameters.....	343
TABLE X.13	Slot wedge analysis - material parameters .....	343
TABLE X.14	Pole configuration performance comparison (no rotor yoke): 400 RPM, 3-phase AC @ $I_{Amp} = 75$ A, $\phi_{dq} = 45^\circ$ .....	347

# List of Abbreviations and Symbols

Symbols	
$N_{Ph}$	# phases
$N_S$	# stator poles
$N_R$	# rotor poles
$N_{Current}$	# current points
$N_{Angles}$	# angle points
$N_{Sims}$	# simulations
$N_{Cycles}$	# electrical cycles
$N_{Steps}$	# simulation steps
$N_{AWG}$	American Wire Gauge size
$N_{Turns}$	# coil turns
$N_{Strands}$	# coil strands
$N_{Lam}$	# laminations in stack
$p$	# pole pairs per phase
$p_R$	rotor pole pairs
$p_S$	stator pole pairs
$L$	instantaneous inductance [ $H$ ]
$L_{Ph}$	phase inductance [ $H$ ]
$L_{dq}$	$dq$ mutual inductance vector [ $H$ ]
$L_a$	inductance-phase A [ $H$ ]
$\psi$	instantaneous flux linkage [ $Wb.T$ ]
$\psi_{Ph}$	phase flux linkage [ $Wb.T$ ]
$\psi_{dq}$	$dq$ mutual flux linkage vector [ $Wb.T$ ]
$\psi_{PhLUT}$	flux linkage LUT [ $Wb.T$ ]
$\psi_{m_a}$	peak flux linkage-phase A [ $Wb.T$ ]
$\psi_a$	flux linkage-phase A [ $Wb.T$ ]
$W_C$	co-energy [ $J$ ]
$W_{C_a}$	co-energy-phase A [ $J$ ]
$W_F$	stored (field) energy [ $J$ ]
$W_{F_a}$	stored (field) energy-phase A [ $J$ ]
$R$	resistance [ $\Omega$ ]
$R_{Ph}$	phase resistance [ $\Omega$ ]
$i$	instantaneous current [ $A$ ]
$i_{Ph}$	phase current [ $A$ ]
$i_{m_a}$	peak phase current-phase A [ $A$ ]

$i_{dq}$	$dq$ phase current vector [A]
$i_a$	phase current-phase A [A]
$i_{Peak}$	peak current [A]
$i_{RMS}$	RMS current [A]
$i_{Ref}$	reference phase current [A]
$i_{LB}$	hysteresis reference current upper bound [A]
$i_{UB}$	hysteresis reference current lower bound [A]
$I_{Amp}$	phase current amplitude [A]
$I_{Rated}$	rated motor phase current amplitude [A]
$v$	instantaneous voltage [V]
$v_{Ph}$	phase voltage [V]
$v_{Peak}$	peak voltage [V]
$v_{RMS}$	RMS voltage [V]
$v_{EMF}$	induced voltage (EMF) [V]
$v_{Drop}$	resistive voltage drop [V]
$v_{DC}$	DC-link voltage [V]
$v_{Net}$	net voltage applied to phase [V]
$v_{abc}$	phase voltage [V]
$t$	time [s]
$T_s$	discrete-time sampling period [s]
$\theta_{Mech}$	mechanical rotor position [ $^{\circ}mech.$ ]
$\theta_{Elec}$	electrical angle [ $^{\circ}elec.$ ]
$\theta_{ON}$	CSRM current turn-on angle [ $^{\circ}elec.$ ]
$\theta_{OFF}$	CSRM current turn-off angle [ $^{\circ}elec.$ ]
$\phi_{dq}$	MCSRM $dq$ -excitation angle [ $^{\circ}elec.$ ]
$\omega$	angular velocity [ $^{\circ}/s$ ]
$\omega_{RPM}$	rotor mechanical rotation speed [RPM]
$T$	torque [Nm]
$T_{Ave}$	average torque [Nm]
$T_{PhLUT}$	phase torque LUT [Nm]
$T_{Motor}$	motor torque [Nm]
$T_{Ref}$	reference torque [Nm]
$T_{Ripple}$	net RMS torque ripple [Nm]
$P$	power [W]
$P_{In}$	input electrical power [W]
$P_{Loss}$	power loss [W]
$P_{Cu}$	copper resistive power loss [W]
$P_{Stored}$	stored magnetic power [W]
$P_{Out}$	mechanical power output [W]
$F$	force [N]
$F_{Bump}$	radial bump load force [N]

$F_{Corner}$	axial cornering load force [ $N$ ]
$F_{Load}$	load force [ $N$ ]
$F_{Preload}$	bearing preload force [ $N$ ]
$\alpha_g$	acceleration due to gravity [ $m/s^2$ ]
$l_{Stack}$	lamination stack length [ $N$ ]
$l_{Airgap}$	airgap [ $N$ ]
$l_{Fe_1}$	thickness of one lamination (steel only) [ $mm$ ]
$l_{Stack}$	thickness of stack (steel + insulation) [ $mm$ ]
$m_{Fe_1}$	mass of one lamination (steel only) [ $mm$ ]
$m_{Stack}$	mass of stack (steel + insulation) [ $mm$ ]
$m$	mass [ $kg$ ]
$k$	discrete-time step #
$J_x$	moment of inertia around x-axis [ $kg/m^2$ ]
$J_y$	moment of inertia around y-axis [ $kg/m^2$ ]
$J_z$	moment of inertia around z-axis [ $kg/m^2$ ]
$f_{Current}$	current sampling frequency [ $kHz$ ]
$f_{Switch}$	switching frequency limit [ $kHz$ ]
$d$	diameter [ $mm$ ]
$\Delta d_{Min}$	minimum clearance/interference [ $mm$ ]
$\Delta d_{Max}$	maximum clearance/interference [ $mm$ ]
$\beta_S$	stator pole-arc angle [ $^\circ$ ]
$\beta_{S_{LB}}$	stator pole-arc angle lower bound [ $^\circ$ ]
$\beta_{S_{UB}}$	stator pole-arc angle upper bound [ $^\circ$ ]
$\beta_R$	rotor pole-arc angle [ $^\circ$ ]
$\beta_{R_{LB}}$	rotor pole-arc angle lower bound [ $^\circ$ ]
$\beta_{R_{UB}}$	rotor pole-arc angle upper bound [ $^\circ$ ]
$h_R$	rotor pole height [ $mm$ ]
$h_{R_{LB}}$	rotor pole height lower bound [ $mm$ ]
$h_{R_{UB}}$	rotor pole height upper bound [ $mm$ ]
$h_S$	stator pole height [ $mm$ ]
$b_R$	rotor yoke thickness [ $mm$ ]
$b_S$	stator yoke thickness [ $mm$ ]
$\alpha_R$	rotor pole taper angle [ $^\circ$ ]
$\alpha_S$	stator pole taper angle [ $^\circ$ ]
$\zeta_R$	rotor pole tip fillet radius [ $mm$ ]
$\zeta_S$	stator pole tip fillet radius [ $mm$ ]
$\gamma_R$	rotor pole base fillet radius [ $mm$ ]
$\gamma_S$	stator pole base fillet radius [ $mm$ ]
$k_{Ph}$	phase excitation order
$S$	# of strokes per mechanical rotation

$j$	imaginary number
$U_{per}$	permissible residual unbalance [ $g \cdot mm$ ]
$\varepsilon$	unbalance magnitude constant [ $mm/s$ ]
$x_{j,k}$	variable $x$ at row $j$ and column $k$
$\Gamma$	mechanical angle for one electrical cycle [ $^\circ$ ]
$\sigma$	mechanical stress [ $MPa$ ]
<b>Acronyms</b>	
SRM	Switched Reluctance Motor
CSRSM	Conventional (non-coupled) SRM
MCSRSM	Mutually Coupled SRM
PM	Permanent Magnet
PMSM	PM Synchronous Motor
IPMSM	Interior PMSM
SPMSM	Surface PMSM
IPM	Interior Permanent Magnet
SPM	Surface Permanent Magnet
PAS	Pedal Assist System
DC	Direct Current
AC	Alternating Current
OE	Original Equipment
OEM	Original Equipment Manufacturer
RMS	Root Mean Square
EMF	Electro-Motive Force (induced voltage)
MMF	Magneto-Motive Force
FEA	Finite Element Analysis
DQ	Direct-Quadrature
SF	Safety Factor
NVH	Noise, Vibration, and Harshness
LB	Lower Bound
UB	Upper Bound
IGBT	Insulated-Gate Bipolar Transistor
MOSFET	Metal Oxide Semiconductor Field-Effect Transistor
<b>Units</b>	
$H$	Henrys
$Hz$	Hertz
$kHz$	Kilohertz
$Wb$	Webers
$T$	Turns
$J$	Joules
$W$	Watts



<i>A</i>	Amperes
<i>V</i>	Volts
$\Omega$	Ohms
<i>N</i>	Newtons
<i>Nm</i>	Newton Meters
<i>Pa</i>	Pascals
<i>MPa</i>	Megapascals
<i>s</i>	Seconds
<i>min</i>	Minutes
<i>rad</i>	Radians
$^{\circ}$	Degrees
$^{\circ}elec.$	Electrical Degrees
$^{\circ}mech.$	Mechanical Degrees
<i>m</i>	Meters
<i>mm</i>	Millimeters
<i>kg</i>	Kilograms
<i>g</i>	Grams

# Declaration of Academic Achievement

All of the text, figures, and ideas presented in this manuscript were created by Brock Howey, unless explicitly stated otherwise. Any ideas that were not original or were based on academic literature have been properly referenced, to the best knowledge of the author. The only exception to this is where such information is considered basic common knowledge in the field.

Dr. Berker Bilgin and Dr. Ali Emadi have provided guidance during the research process and review of this manuscript, with the original odd pole-phase index MCSRМ research topic being proposed by Dr. Bilgin. However, all research contributions and experimental work were conducted solely by Brock Howey.

The dynamic models, Matlab tools, and FEA scripts used for the analyses in this report were contributed to heavily by Brock Howey, but were a group research collaboration, with results and validations published in academic journal/conference papers [1]–[4].

The design process for the CSRМ and MCSRМ have been detailed in [5] and [6], respectively. However, the content has been significantly expanded for this thesis, and all content presented was originally created by Brock Howey.

This page was left intentionally blank.

# Chapter 1

## Introduction

### Background

Electric and hybrid vehicles are becoming more widely adopted as fuel prices increase and environmental concerns motivate consumers. Electric bicycles (e-bikes) are a relatively new type of inexpensive electric vehicle that is being adopted for similar reasons. Most electric/hybrid vehicles today use Interior Permanent Magnet Synchronous Motors (IPMSM) as the drive motor. E-bikes using a planetary gearbox can use IPM machines, but direct-drive e-bikes typically use Surface Permanent Magnet Synchronous Motors (SPMSM). Both IPMSMs and SPMSMs typically use rare earth magnets that are subject to significant price volatility [1]. Switched Reluctance Motors (SRMs) have the potential to reach similar performance and efficiency numbers as permanent magnet machines, without the magnets [1]. Finding a motor topology that avoids the use of permanent magnets is important, because cost is of critical importance to electric and hybrid vehicle success; as such vehicles already cost a premium compared to conventional Internal Combustion Engine (ICE) vehicles. When considering e-bikes, cost is an even more critical factor, as they are often marketed as a low-cost urban transportation option.

SRMs have a large constant-power region which is essential, especially for pure electric vehicles, as it can eliminate the need for forward gears [2] and further

reducing the vehicle cost. In addition, SRMs have a simple mechanical design compared to other motor designs, and as such they are robust in nature. The downsides to SRMs are the typically high noise/vibration, high torque ripple, and the requirement for an unconventional asymmetric-bridge converter.

An alternative to the conventional SRM (CSRSM) is the mutually coupled SRM (MCSRSM). This machine type has much of the same potential and characteristics as the CSRSM, but trades the extended constant-power region for the ability to use a conventional full-bridge inverter, more conventional control strategies, and the potential for higher low-speed torque output.

## Contributions

In this research, both a CSRSM and a MCSRSM are designed for an external-rotor, direct-drive e-bike application.

In academic literature, the differences between different SRM pole configurations are not well studied. This is compounded by the fact that it is difficult to compare motor characteristics for different pole configurations unless the motors are designed for the exact same application. In this thesis, four motors are designed for an e-bike application, with 12/8, 12/16, 12/20, and 12/28 pole configurations, respectively. The results are compared in detail, to provide a justification for the choice of pole configuration for this application. Three of these pole configurations are also novel, where the number of rotor poles exceeds the number of stator poles.

A prototype of the finalized 12/16 CSRМ design is manufactured and validated experimentally. All manufacturing considerations have been justified in detail, including specific considerations to reduce noise and vibration in the final design. The manufacturing process and testing procedures have also been documented in this thesis, along with the final experimental verification results.

There is also limited academic literature pertaining to concentrated-wound MCSRMs. As with the CSRМ, the differences between different MCSRМ pole configurations are not well studied. In this thesis, the performance of numerous pole configurations is compared, and the choice of pole configuration for this application is justified. The 12/8, 12/16, 12/20, 12/28, 15/5, 15/10, 15/20, 15/25, 21/7, 21/14, 21/28, 24/8, and 24/16 pole configurations are compared, of which several are novel. All pole configurations using an odd number of poles are also considered to be novel.

In addition to these contributions, this thesis also focuses on a relatively low speed, external rotor motor application. A low motor speed application is a challenging target for SRMs, and thus the motor designs had to be highly refined to meet the design targets. The motor design process used to meet the strict design targets is considered to be another contribution.

Finally, the external rotor configuration of CSRMs and MCSRMs has not been exhaustively studied in literature, and the unique electromagnetic, structural, and thermal considerations for this configuration are all contributions in this thesis.

## Thesis Outline

This manuscript is divided into eight chapters, following this introduction. A brief description of the chapter contents is provided here.

In **Chapter 2**, the theoretical fundamentals of CSRМ and MCSRМ operation are discussed, including the general machine voltage and torque equations. Basic control concepts, loss mechanisms, and different electromagnetic effects on machine performance are also discussed.

In **Chapter 3**, the modelling fundamentals of CSRМ and MCSRМ are studied. This chapter discusses electromagnetic FEA machine characterization, and how this can be used to create lookup tables that describe the non-linear machine behavior. The chapter then explains how the machine characterization can be used in conjunction with dynamic modelling to reduce simulation time, without sacrificing accuracy. The different dynamic models for the CSRМ and MCSRМ topologies are discussed in detail. Simulation sampling considerations are also discussed briefly in this chapter.

**Chapter 4** presents details about e-bikes and the motors that propel them. A background on the e-bike market is presented, along with relevant Canadian legislation and the classification of e-bikes. Finally, different e-bike configurations are outlined, along with the unique traction motor requirements for e-bikes.

**Chapter 5** takes the unique e-bike motor requirements discussed in Chapter 4, and expands on them. A commercial e-bike motor is purchased and analyzed in

detail to create geometry and performance requirements for the SRM designs in subsequent chapters.

**Chapter 6** focuses on the detailed electromagnetic design of a conventional non-coupled SRM, given the target requirements outlined in Chapter 5. Each geometry parameter is analyzed in detail and the final selections are justified. The efficiency maps of designs using four different pole configurations are compared in detail. The multi-objective GA control optimization strategy used for current control is discussed. A MotorCAD thermal analysis is used to validate the thermal design, and an ANSYS static structural FEA analysis is presented to validate the structural design.

**Chapter 7** presents the finalized 12/16 CSRSM manufacturing considerations, manufacturing process, testing, and design validation results. All design decisions for the final prototype design have been extensively detailed. The design validation process is discussed, and the final results have been analyzed.

**Chapter 8** is very similar to Chapter 6, but focuses on the design of a MCSRM. Each geometry parameter is analyzed in detail and the final selections are justified. The results for several different pole configurations are compared. Different methods of determining the best AC current excitation angle have been discussed. A MotorCAD thermal analysis is used to validate the thermal design. This chapter has the same general format as Chapter 6, and the differences between the MCSRM and CSRSM are discussed in each section.



**Chapter 9** summarizes the final conclusions of this thesis. Areas of potential future research are outlined.

# Chapter 2

## Fundamentals of Non-Coupled and Mutually Coupled Switched Reluctance Motors

### Introduction

CSRSM and MCSRSM operation is based on the concept of magnetic reluctance; that is, the tendency for magnetic flux to take the path of least magnetic resistance.

Both the CSRSM and MCSRSM can use either axial or radial flux designs, as shown in Fig. 2.1; each with their own specific packaging benefits. This dissertation will primarily focus on radial flux machines, as these are most common for vehicle applications.

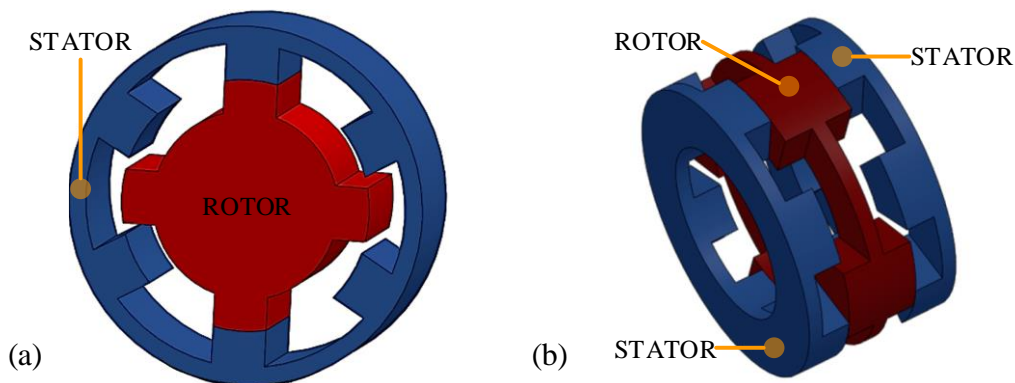


Fig. 2.1 SRM / MCSRSM configurations (coils not shown): (a) radial flux SRM; (b) axial flux SRM

Reluctance machines like the CSRSM and MCSRSM have a “salient” structure; meaning that the poles visibly protrude from the yokes and the airgap is

non-uniform (there is angular space between poles). The overall structure is nearly identical for both machines, with the only differences being the coil winding directions, and the current waveforms that feed the machine, as shown in Fig. 2.2 and Fig. 2.3 respectively.

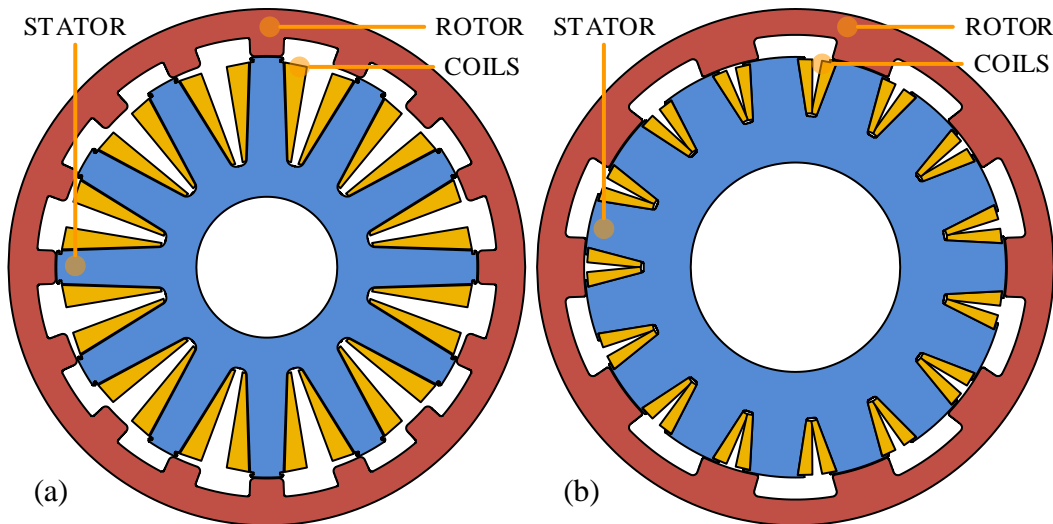


Fig. 2.2 Geometry: (a) 12/16 CSR; (b) 15/10 MCSRM

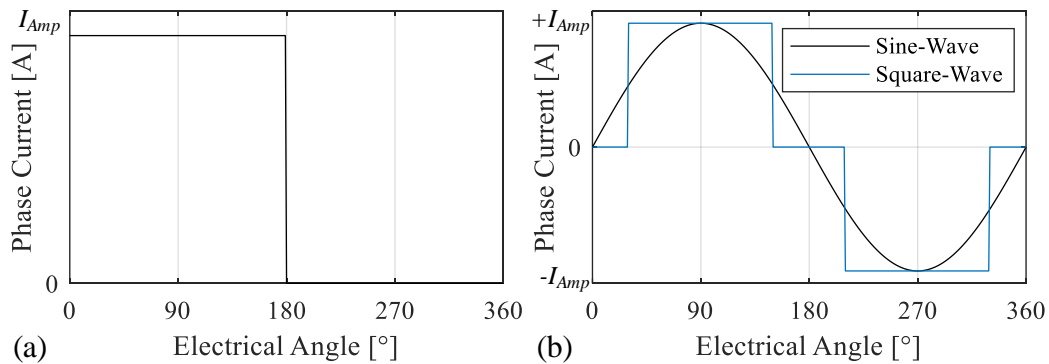


Fig. 2.3 Reference phase current waveforms (phase 1): (a) CSR; (b) MCSRM

Using the different coil directions and phase current waveforms, the flux takes a different path in each machine. With CSRs, there is minimal mutual coupling between phases, whereas the MCSRM utilizes mutual coupling for torque

production. The flux lines for the unaligned and aligned positions are compared in Fig. 2.4 and Fig. 2.5, respectively. The significance of these figures will be detailed further in this chapter.

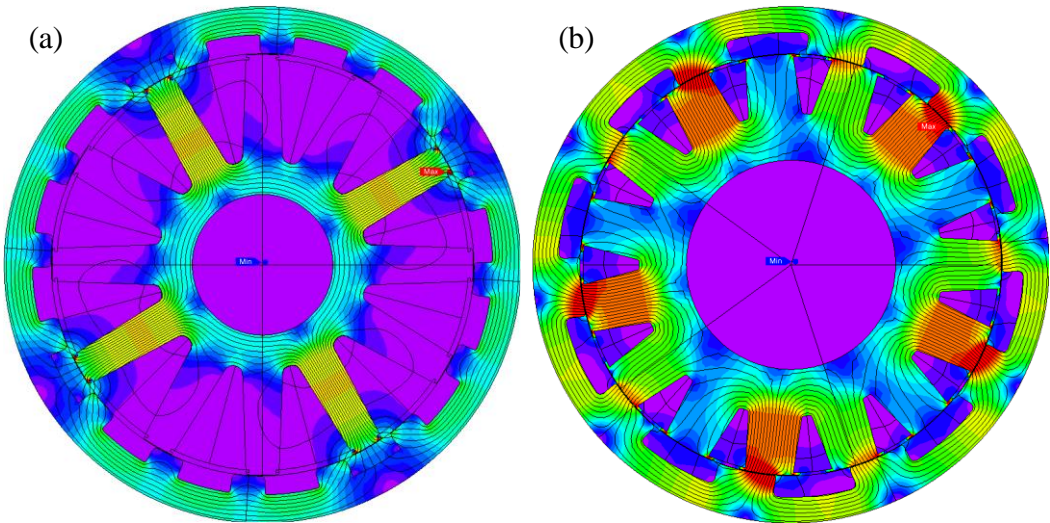


Fig. 2.4 Flux lines (unaligned position): (a) CSR; (b) MCSRM

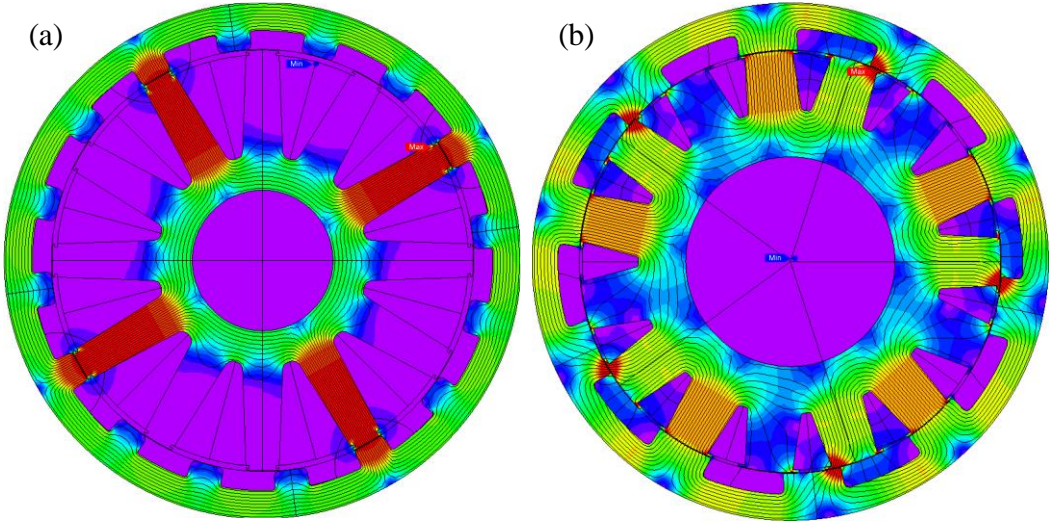


Fig. 2.5 Flux lines (aligned position): (a) CSR; (b) MCSRM

## Non-Coupled Switched Reluctance Motors (SRMs)

### Structure

#### *Operational Principles*

In essence, a non-coupled SRM works by exciting the stator electromagnetic coils on and off in a sequence of “pulses”. When a given phase is excited, the rotor (a ferromagnetic object) will try to align within the resulting magnetic field, due to the “reluctance torque” pulse created. As the phases are energized in a rotating fashion, the rotor will rotate with the field, producing continuous torque. Though there may be some overlap between phase excitations, they are typically energized separately, in sequence, and mutual coupling between phases is assumed to be negligible.

#### *Pole Configuration Constraints*

A switched reluctance motor can operate using any number of phases, and different pole number arrangements. Single phase machines are not particularly useful for traction applications and thus will not be discussed in this thesis. Typically, three or four phase machines are used for traction applications. The addition of a phase adds cost to the converter, as an additional phase-leg circuit must be added. However, it can be beneficial to have more phases, as this gives more control over the system.

The addition of poles has the potential benefit of reducing torque ripple, however this can add cost and can reduce the time between phase excitations potentially making control more challenging (this will be discussed later in this

chapter) [3]. The number of poles on the rotor and stator must be different to ensure that the machine can start in any position. The CSRSM must have an even number of stator poles to ensure balanced flux distribution. The pole relationship between rotor and stator poles is [7]:

$$N_R = \frac{N_S}{N_{Ph}} p \kappa$$

The  $\kappa$  term checks for a locked rotor condition, and will return 0 if there is a locked rotor (invalid configuration), or 1 for valid configurations [7]:

$$\kappa = \prod_{i=1}^{i=N_f} \text{ceil} \left( \frac{\text{mod}(p, f(i))}{f(i)} \right)$$

where:

$\kappa = \text{valid configuration check (1 = valid, 0 = invalid)}$

$p = \text{positive integer}$

$N_{Ph} = \# \text{ phases}$

$N_S = \# \text{ stator poles}$

$N_R = \# \text{ rotor poles}$

$N_f = \# \text{ prime factors}$

$f = \text{prime factor array of } N_{Ph}$

For example, if  $N_{Ph} = 3$ ,  $p = 4$ , and  $N_S = 12$ , then  $f = [3]$ , and:

$$\begin{aligned} N_R &= \frac{12}{3} 4 \prod_{i=1}^{i=1} \text{ceil} \left( \frac{\text{mod}(4,3)}{3} \right) \\ &= 16 \end{aligned}$$

This would be designated as a “12/16” SRM, as shown in Fig. 2.2 (a).

### *Pole Angle Constraints*

The selection of pole angles is rather complicated; in order to understand, one must understand torque production in SRMs, which is explained in the next section. In essence, the motor only produces torque when the inductance is changing with time. Since the phase inductance is dependent on flux-linkage, and the flux-linkage depends on rotor position, the pole arc design is inter-related with this. Considering a 12/16 example, the important rotor positions are summarized in Fig. 2.6.

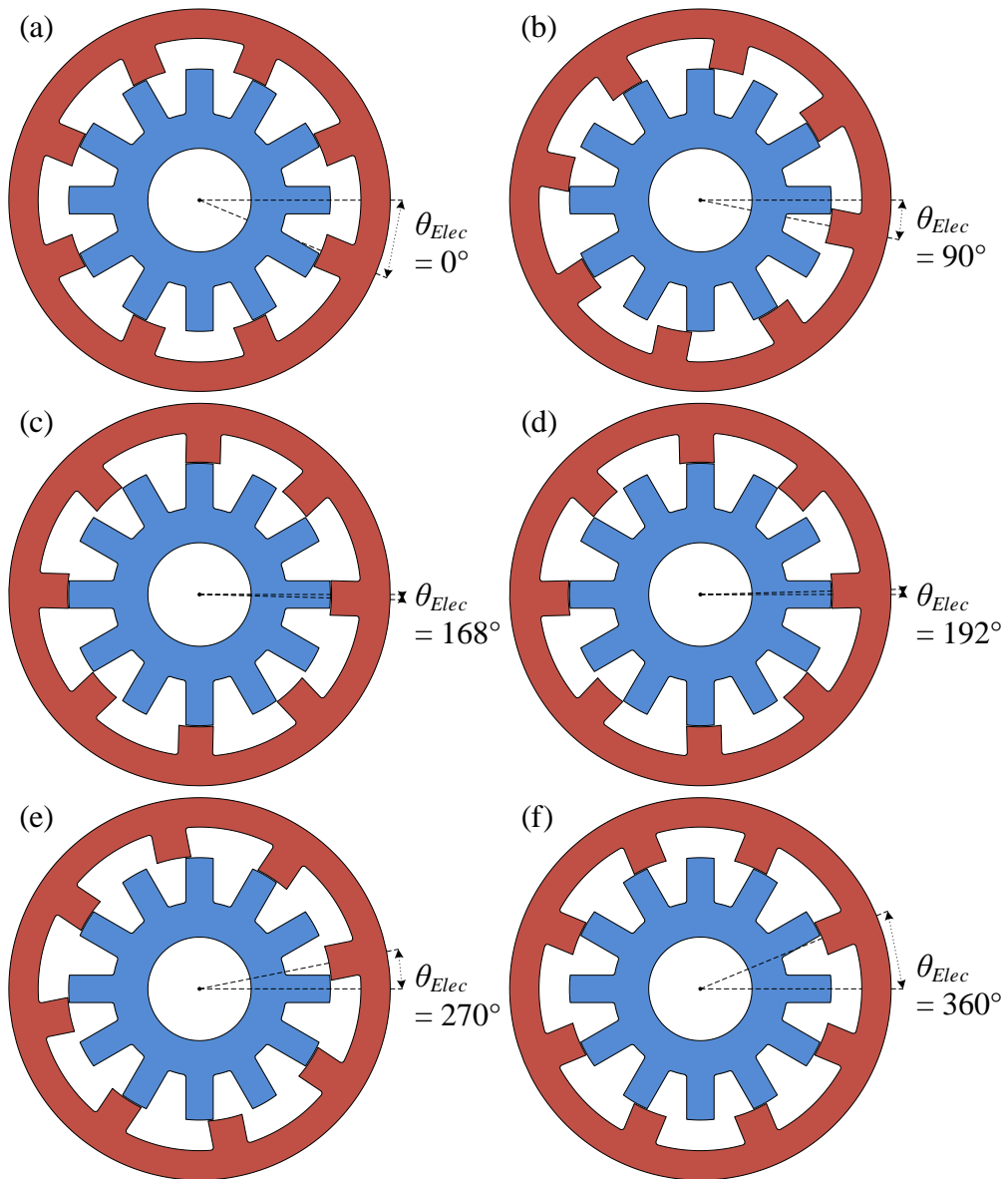


Fig. 2.6 SRM at different positions: (a) completely unaligned, (b) beginning of alignment, (c) fully aligned, (d) fully aligned still, (e) end of alignment, (f) completely unaligned

Each of the positions in Fig. 2.6 can be noted in Fig. 2.7, which illustrates the idealized inductance waveforms as a function of position.



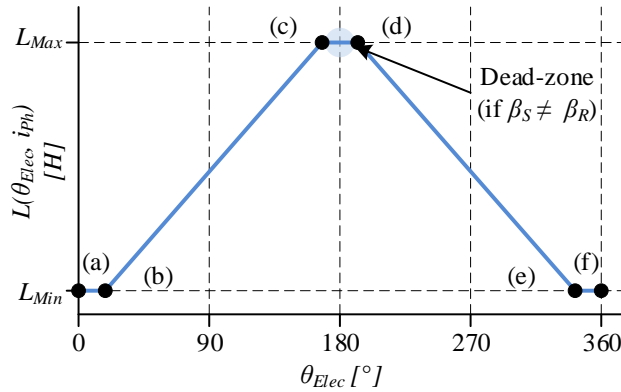


Fig. 2.7 Idealized inductance vs. rotor position

Observing the idealized inductance waveforms helps explain the required pole angles for an SRM. It is important to note that the rules presented here are guidelines; and may not apply in special scenarios. Generally, the first guideline is [3]:

$$\beta_S < \beta_R$$

where:

$$\beta_S = \text{stator pole - arc angle } [^\circ]$$

$$\beta_R = \text{rotor pole - arc angle } [^\circ]$$

The reasoning for  $\beta_S$  being less than  $\beta_R$  is because this allows for more coil space on the stator, as coils are not needed on the rotor [4]. In addition, if the rotor pole is much wider than the stator pole, a torque dead-zone can be created, as the inductance is constant (position ‘(c)’ to ‘(d)’ in Fig. 2.7). This is not always an issue however, as discussed in **Chapter 6**. In practice, it may be beneficial to have  $\beta_R > \beta_S$  in certain cases, to reduce rotor pole saturation, so the guideline does not always apply. The second guideline is:

$$\beta_S > \alpha_E$$

$$N_{Strokes} = N_{Ph} N_R$$

$$\alpha_E = \frac{360^\circ}{N_{Strokes}}$$

where:

$$\alpha_E = \text{mechanical angle between phase excitations } [^\circ]$$

$$N_{Strokes} = \# \text{ strokes per mechanical rotation}$$

In order to produce torque at any rotor angle, this must be true (given idealized conditions). Since torque is actually produced by multiple phases, subsequent phases must be set to trigger when the current phase finishes its torque pulse, otherwise there will be a gap in the torque production. In Fig. 2.8, from position ‘1a’ to ‘1b’ the forward phase produces positive torque, then it is turned off, and the next phase will produce torque between ‘2a’ and ‘2b’.

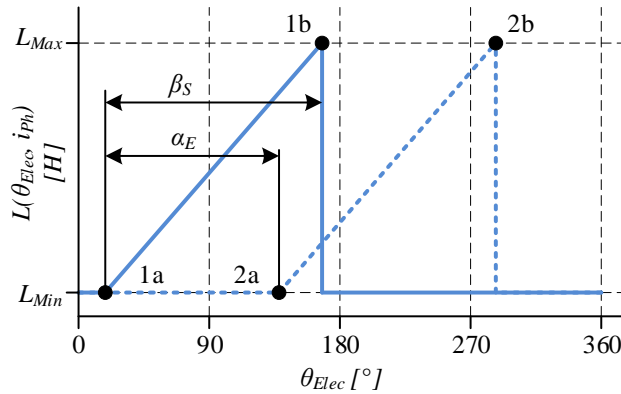


Fig. 2.8 Idealized inductance vs. rotor position – phase excitation overlap

As illustrated in Fig. 2.8, if  $\beta_S > \alpha_E$ , then the phase torque waveforms will overlap and gaps in torque can be avoided. The timing of phase excitation is discussed in the **Control Considerations** section. The final guideline is [3]:

$$(\beta_S + \beta_R) < \Gamma$$

$$\Gamma = \frac{360^\circ}{N_R}$$

where:

$$\Gamma = \text{mechanical angle for one electrical cycle [}^\circ\text{]}$$

This is important to ensure that there is no overlap between stator teeth and the corresponding rotor tooth. This is undesirable as it gives another flux path other than the intended flux path, reducing the saliency in the machine and thus reducing torque [4]. The reduction in saliency is reflected by an increase in unaligned inductance, which can also make it harder to force current into the windings [4].

### ***Other Considerations***

Both the rotor and stator are made of laminations (generally slices of silicon steel that are sandwiched and insulated between each other). This is because of the need to reduce eddy currents (loss mechanisms will be discussed later in this chapter).

The machine stator yoke diameter is generally constrained by packaging, while the rotor diameter will scale with the stator size. The shaft diameter is typically dependent on the loading it will receive, and thus is also fixed.

Knowing these preliminary facts, one can create the basic structure of a SRM, however the optimization of these parameters has to be approached using an iterative design approach to determine the best balance of parameters for given packaging, output, and control requirements.

## Torque Production and Electromagnetics

The torque produced in an SRM is due to reluctance torque, as the system rotates in an effort to reduce the reluctance of the magnetic circuit. Conventional machine equations typically focus on torque generation by mutual interaction of fields, and thus are not useful for SRMs. Instead, the torque of the motor can be characterized as a function of flux-linkage and current. Flux-linkage refers to how much flux is ‘linked’ or flowing through the magnetic circuit, and it is a function of rotor position. Current is controlled by the controller, and is varied in an on-off fashion (pulsed). The inductance of the machine is related to flux-linkage and current:

$$L = \frac{d\psi}{di}$$

where:

$$L = \text{phase inductance [H]}$$

$$\psi = \text{phase flux linkage [Wb} \cdot \text{turns]}$$

$$i = \text{phase current [A]}$$

This can be visualized through a  $\psi/i$  diagram (the inductance is the slope), as shown in Fig. 2.9. The diagram can be looked at as having the same characteristic as a B-H curve for a material (in this case the stator tooth material because this is where the machine saturates). This diagram is related to the B-H curve, as flux-linkage is similar to  $B$ , where current is similar to  $H$ . For a linear case:

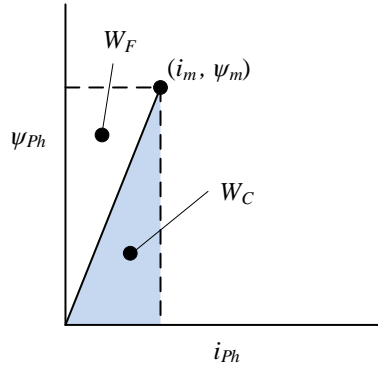


Fig. 2.9 Flux-linkage vs. phase current (linear operation)

The field energy  $W_{F_a}$  is the energy stored in the magnetic field of phase A, whereas the co-energy  $W_{C_a}$  of phase A directly relates to phase torque production. In this simplified linear case, the stored and co-energy are equivalent:

$$\begin{aligned}
 W_{C_a} &= \text{AREA UNDER GRAPH} \\
 &= \frac{1}{2} \psi_{m_a} i_{m_a} \\
 &= \frac{1}{2} L_a i_{m_a}^2 \\
 &= W_{F_a}
 \end{aligned}$$

where:

$$W_{F_a} = \text{field or stored energy} - \text{phase A [J]}$$

$$W_{C_a} = \text{co} - \text{energy} - \text{phase A [J]}$$

$$\psi_{m_a} = \text{peak flux linkage} - \text{phase A [Wb.t]}$$

$$i_{m_a} = \text{peak phase current} - \text{phase A [A]}$$

$$L_a = \text{inductance} - \text{phase A [H]}$$

This is undesirable when the goal is to produce torque, as half of the input energy does not contribute to torque production. Thus, for SRMs to produce reasonable torque output for a given input power, they must operate in the non-linear region of the B-H curve [5], as shown in Fig. 2.10.

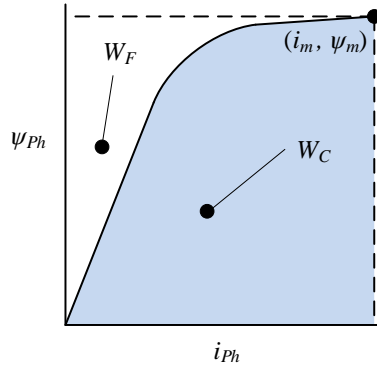


Fig. 2.10 Flux-linkage vs. phase current (non-linear saturated operation)

In the non-linear case, the co-energy is larger than the stored energy; meaning more of the input energy contributes to torque production (power factor effectively improves):

$$W_{C_a} = \int_0^{i_{m_a}} \psi_a \cdot di_a$$

$$W_{F_a} = \int_0^{\psi_{m_a}} i_a \cdot d\psi_a$$

$$W_{C_a} > W_{F_a}$$

where:

$$\psi_a = \text{flux linkage} - \text{phase A [Wb.t]}$$

$$i_a = \text{phase current} - \text{phase A [A]}$$

When a full electrical cycle is considered, the  $\psi/i$  diagram can be expanded, as shown in Fig. 2.11. Note that point ‘B’ has a different flux linkage than point ‘A’. This is due to flux linking in the unaligned position, which reduces  $W_C$ , and thus torque. The more salient the machine is, the lower the unaligned flux linkage will be.

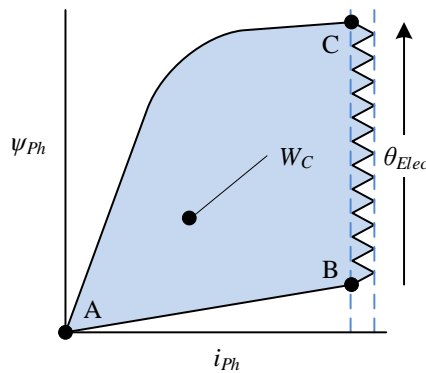


Fig. 2.11  $\psi/i$  work cycle

### ***Motoring Cycle***

#### *A to B*

At the start of the cycle, when the rotor is at the unaligned position, the coil is switched on and current rises over a short period of time. This creates a stronger field, indicated by the increased flux-linkage at point ‘B’.

#### *B to C*

Once the coil is turned on, the tooth continues rotating until nearly fully aligned, at point ‘C’. The reluctance in the aligned position is low, so the flux-linkage is at its maximum at this point. During this period, the current is kept constant by chopping, and this is visible in Fig. 2.11.

*C to A*

After the rotor reaches the turn-off angle, it is typically near the aligned position. The phase current is shut off, and the flux-linkage eventually drops back to zero once the field has been completely eliminated. Since it is near the aligned position as this happens, the reluctance is lower than the energizing stage, and thus the flux-linkage is higher for the same current.

### ***Generating Cycle***

The power generation cycle is the reverse of the torque production cycle. Unlike conventional electric machines, the SRM must keep coils energized during regenerative mode; otherwise there will be no flux flowing and no EMF. This means that there is some additional copper loss and voltage drop experienced during the regenerative mode of operation. Since this thesis focuses on motoring operation, the generating mode of operation will not be examined further. More information about the generating mode of operation is available in [8] and [9].

### ***Phase Voltage***

In order to understand the equations in the next section, a simplified model of the coil phase circuit is illustrated in Fig. 2.12.

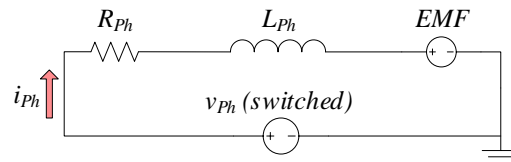


**Fig. 2.12 Simplified circuit representation of a phase winding**



Please note that for the following equations, the inductance ( $L$ ) and flux linkage ( $\psi$ ) are functions of rotor position ( $\theta$ ) and current ( $i$ ). In this section “ $L(\theta, i)$ ” and “ $\psi(\theta, i)$ ” have been replaced with “ $L$ ” and “ $\psi$ ” respectively, for ease of reading. All vector and matrix terms are presented in **bold**. The voltage equation can be deduced from the simplified circuit. This is explained well in [5], and this explanation will be expanded on below. The phase voltage equation is [10]:

$$\mathbf{v}_{Ph} = R_{Ph}\mathbf{i}_{Ph} + \frac{d\boldsymbol{\psi}_{Ph}}{dt}$$

*(Equation 2.1)*

Since  $\psi = Li$ :

$$\begin{aligned}\mathbf{v}_{Ph} &= R_{Ph}\mathbf{i}_{Ph} + \frac{d\mathbf{L}_{Ph}\mathbf{i}_{Ph}}{dt} \\ &= R_{Ph}\mathbf{i}_{Ph} + \mathbf{L}_{Ph}\frac{d\mathbf{i}_{Ph}}{dt} + \omega\frac{d\mathbf{L}_{Ph}}{d\theta}\mathbf{i}_{Ph}\end{aligned}$$

where:

$R_{Ph}$  = phase resistance [ $\Omega$ ]

$t$  = time [s]

$\mathbf{v} = \mathbf{v}_{Ph}$  = instantaneous voltage input [V]

$\mathbf{i} = \mathbf{i}_{Ph}$  = instantaneous current input [A]

$\omega$  = rotor mechanical rotation speed  $\left[\frac{\text{rad}}{\text{s}}\right]$

$\theta$  = rotor mechanical angle [rad]

$\boldsymbol{\psi} = \boldsymbol{\psi}_{Ph}$  = flux linkage [Wb.t]

$\mathbf{L} = \mathbf{L}_{Ph}$  = inductance [H]

In order to make the next section easier to read, subscripts have been removed from the equations where possible. Unaligned inductance is assumed to be negligible under maximum phase current, to simplify the calculations. The machine equations presented here do not make any steady state assumptions ( $\frac{di}{dt} \neq 0$ ), and thus the equations have not been fully simplified (this is not necessary and makes the formulas less general).

### *Deriving the Torque Equation*

The power input into the machine is:

$$\begin{array}{l|l}
 \mathbf{P}_{In} = \mathbf{v}\mathbf{i} & \text{or, in terms of } \psi: \\
 = R_{Ph}\mathbf{i}^2 + \mathbf{L}\mathbf{i}\frac{d\mathbf{i}}{dt} + \mathbf{i}^2\frac{d\mathbf{L}}{dt} & = R_{Ph}\mathbf{i}^2 + \mathbf{i}\frac{d\psi}{dt}
 \end{array}$$

The machine loss, considering only copper loss, is:

$$\begin{aligned}
 \mathbf{P}_{Loss} &= P_{Cu} \\
 &= R_{Ph}\mathbf{i}^2
 \end{aligned}$$

The change in field energy with time is:

$$\mathbf{P}_{Stored} = \frac{d\mathbf{W}_F}{dt}$$

and the mechanical power output of the machine is:

$  \begin{aligned}  P_{Out} &= P_{In} - P_{Loss} - P_{Stored} \\  &= R_{p\bar{n}} i^2 + Li \frac{di}{dt} + i^2 \frac{dL}{dt} - R_{p\bar{n}} i^2 \\  &\quad - \frac{dW_F}{dt} \\  &= Li \frac{di}{dt} + i^2 \frac{dL}{dt} - \frac{dW_F}{dt}  \end{aligned}  $	<p>or, in terms of <math>\psi</math>:</p> $  \begin{aligned}  &= R_{p\bar{n}} i^2 + i \frac{d\psi}{dt} - R_{p\bar{n}} i^2 \\  &\quad - \frac{dW_F}{dt} \\  &= i \frac{d\psi}{dt} - \frac{dW_F}{dt}  \end{aligned}  $
--	--

The torque output can then be calculated from the mechanical power output:

$  \begin{aligned}  P_{Out} &= T\omega \\  T &= \frac{P_{Out}}{\omega} \\  &= Li \frac{di}{\omega dt} + i^2 \frac{dL}{\omega dt} - \frac{dW_F}{\omega dt} \\  &= Li \frac{di}{d\theta} + i^2 \frac{dL}{d\theta} - \frac{dW_F}{d\theta} \\  &\quad \text{(Equation 2.2a)}  \end{aligned}  $	<p>or, in terms of <math>\psi</math>:</p> $  \begin{aligned}  &= i \frac{d\psi}{\omega dt} - \frac{dW_F}{\omega dt} \\  &= i \frac{d\psi}{d\theta} - \frac{dW_F}{d\theta} \\  &\quad \text{(Equation 2.2b)}  \end{aligned}  $
--	---

*Linear Case (not saturated)*

Considering the linear case, the change in stored energy would simply be:

$  \begin{aligned}  \frac{dW_F}{d\theta} &= \frac{d}{d\theta} \left( \frac{1}{2} Li^2 \right) \\  &= Li \frac{di}{d\theta} + \frac{1}{2} i^2 \frac{dL}{d\theta}  \end{aligned}  $	<p>or, in terms of <math>\psi</math>:</p> $  \begin{aligned}  &= \frac{d}{d\theta} \left( \frac{1}{2} \psi i \right) \\  &= \frac{1}{2} \psi \frac{di}{d\theta} + \frac{1}{2} i \frac{d\psi}{d\theta}  \end{aligned}  $
---	---

So, using *Equation 2.2*:

$  \begin{aligned}  T &= Li \frac{di}{d\theta} + i^2 \frac{dL}{d\theta} - \frac{dW_F}{d\theta} \\  &= Li \frac{di}{d\theta} + i^2 \frac{dL}{d\theta} - Li \frac{di}{d\theta} - \frac{1}{2} i^2 \frac{dL}{d\theta} \\  &= \frac{1}{2} i^2 \frac{dL}{d\theta}  \end{aligned}  $	<p style="text-align: center;">or, in terms of <math>\psi</math>:</p> $  \begin{aligned}  &= i \frac{d\psi}{d\theta} - \frac{dW_F}{d\theta} \\  &= i \frac{d\psi}{d\theta} - \frac{1}{2} \psi \frac{di}{d\theta} - \frac{1}{2} i \frac{d\psi}{d\theta} \\  &= \frac{1}{2} i \frac{d\psi}{d\theta} - \frac{1}{2} \psi \frac{di}{d\theta}  \end{aligned}  $
---	---

*Non-Linear Case (highly saturated)*

The non-linear case makes things more complicated and the problem has to be solved numerically. The change in stored energy becomes:

$$\frac{dW_F}{d\theta} = \frac{d}{d\theta} \left( \int i d\psi \right)$$

So, using *Equation 2.2*:

$  \begin{aligned}  T &= Li \frac{di}{d\theta} + i^2 \frac{dL}{d\theta} - \frac{dW_F}{d\theta} \\  &= Li \frac{di}{d\theta} + i^2 \frac{dL}{d\theta} - \frac{d}{d\theta} \left( \int i d\psi \right)  \end{aligned}  $	<p style="text-align: center;">or, in terms of <math>\psi</math>:</p> $  \begin{aligned}  &= i \frac{d\psi}{d\theta} - \frac{dW_F}{d\theta} \\  &= i \frac{d\psi}{d\theta} - \frac{d}{d\theta} \left( \int i d\psi \right)  \end{aligned}  $
--	--

where:

$T$  = torque [Nm]

$W_C$  = co – energy [J]

$P_{In}$  = input electrical power [W]

$P_{Loss}$  = power loss [W]

$P_{Stored}$  = stored magnetic power [W]

$P_{Out}$  = mechanical power output [W]

When the **bold** terms are replaced with their respective matrix representations, the voltage and total torque can be calculated at any rotor position. This is detailed in *Appendix D*.

In this section, the phase voltage equation, voltage drop, and field energy ( $W_F$ ) are used to calculate the net machine power and thus, the torque. This net power is the co-energy power, and thus the torque can also be directly calculated by using the co-energy ( $W_C$ ):

$$\begin{aligned} T &= \frac{dW_C}{d\theta} \\ &= \frac{d}{d\theta} \left( \int \psi di \right) \end{aligned}$$

(Equation 2.3)

Calculation using the field energy method (Equation 2.2) and the co-energy method (Equation 2.3) are shown to be equivalent in *Appendix G*.

## Mutual Inductance Effects

In SRMs, the reluctance torque is produced by the self-inductance of the stator coils. In most machines, the interaction of the stator and rotor mutual inductances produces the torque [5]. However, since there are no coils on the rotor for a reluctance machine, only self-inductance is considered.

Since the stator pole pairs are energized individually, the flux links through the energized stator poles, through the rotor, and back around the yoke of the machine to complete the magnetic circuit. Since there should be little or no flux travelling through the other poles in the machine, there is very little capability for

the flux to link with these coils and create mutual inductance. A very small amount of flux may leak however, and this will reduce the self-inductance of the machine and thus the torque output slightly.

## Control Considerations

### *Electrical Angles*

The unaligned position (or the  $0^\circ$  electrical position) for a given CSRMM phase is defined as the position where the stator pole for a given phase is directly centered between two adjacent rotor poles, as shown previously in Fig. 2.4.

The magnetic circuit is energized once for every rotor pole, meaning that the electrical cycle repeats after each rotor pole has passed. Thus, it is possible to convert from mechanical angle to electrical angle using the following relationship (assuming that  $0^\circ_{\text{mech.}}$  is aligned with  $0^\circ_{\text{elec.}}$  by convention):

$$\theta_{Elec} = N_R \theta_{Mech}$$

However, it is important to know the electrical angles for all phases. In order to calculate this, it is important to know the electrical angle offset between phases:

$$\begin{aligned} \boldsymbol{\theta}_{Elec_0} &= \begin{bmatrix} \theta_{Elec_{1_0}} \\ \dots \\ \theta_{Elec_{N_{Ph_0}}} \end{bmatrix} \\ &= \left( \frac{360^\circ}{N_{Ph}} \right) \mathbf{k}_{Ph} \end{aligned}$$

The electrical angle offset for each phase depends on the phase excitation order  $k_{Ph}$ , which in-turn depends on the pole-configuration, and rotation direction:

$$\mathbf{k}_{Ph} = \begin{bmatrix} k_{Ph_1} \\ \dots \\ k_{Ph_{N_{Ph}}} \end{bmatrix}$$

$$0 \leq \mathbf{k}_{Ph} < N_{Ph}$$

The full electrical angle equation can then be presented:

$$\begin{aligned} \boldsymbol{\theta}_{Elec} &= \begin{bmatrix} \theta_{Elec_1} \\ \dots \\ \theta_{Elec_{N_{Ph}}} \end{bmatrix} \\ &= \text{mod} \left( N_R \theta_{Mech} + \left( \frac{360^\circ}{N_{Ph}} \right) \mathbf{k}_{Ph}, 360^\circ \right) \end{aligned}$$

### Continuous Torque Production

In order to create continuous torque, the phases are excited in the order given by  $k_{Ph}$ , as shown in Fig. 2.13. The phase torque is summed to obtain the total machine output torque, as shown in Fig. 2.14.

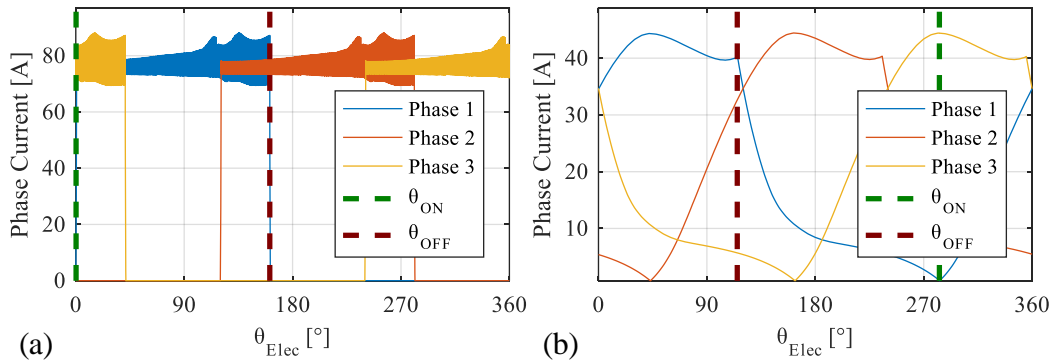
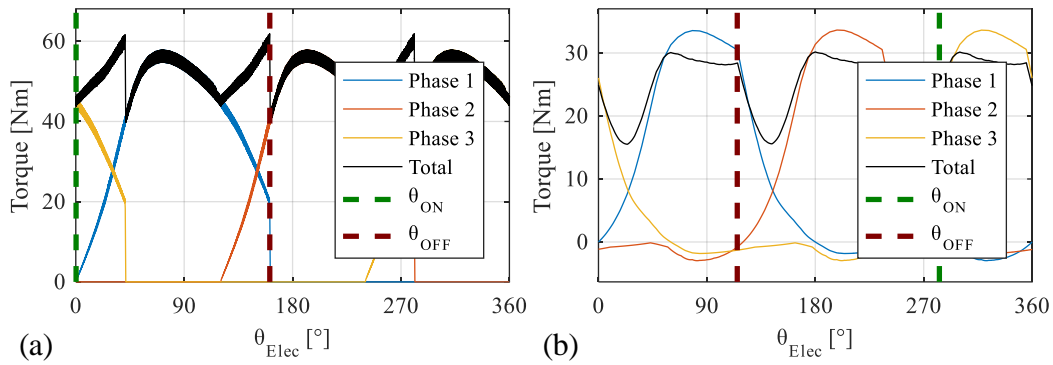
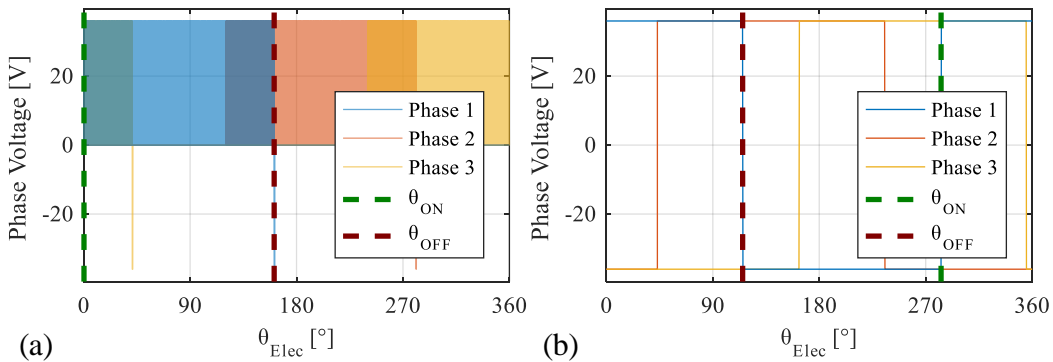


Fig. 2.13 Phase current waveforms (3-phase CSRSM – dynamic model): (a) low speed; (b) high speed



**Fig. 2.14** Phase torque vs. total torque output (3-phase CSRМ – dynamic model): (a) low speed; (b) high speed

Observing Fig. 2.13, it is clear that the phase firing angles advance as the motor speed increases, due to increased induced voltage. This is reflected by the reduced switching in the phase voltage waveforms (see Fig. 2.15); meaning that the converter cannot not regulate current. This behavior is explained in detail in the *Current Controller* section.



**Fig. 2.15** Phase voltage (3-phase CSRМ – dynamic model): (a) low speed; (b) high speed

The phase flux-linkage curves are compared in Fig. 2.16.



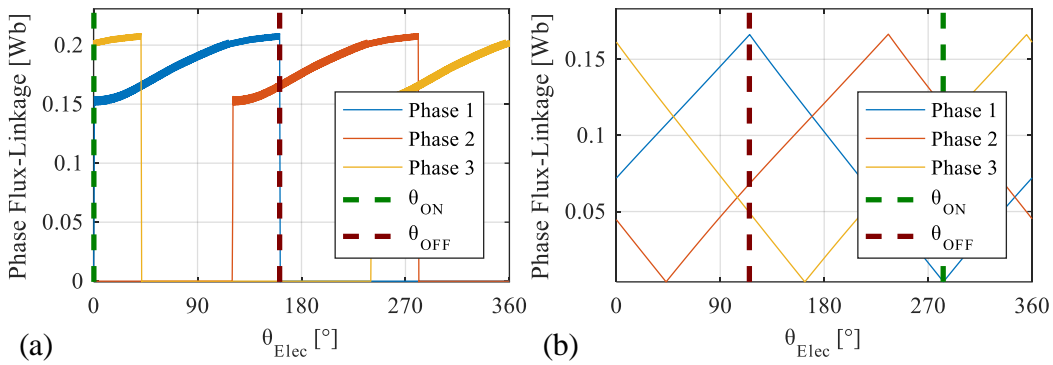


Fig. 2.16 Phase flux-linkage (3-phase CSRSM – dynamic model): (a) low speed; (b) high speed

Finally, the  $\psi/i$  curves are compared in Fig. 2.17. Due to the increasing induced voltage at high speed, it is not possible to obtain as high of a phase current, and the co-energy area decreases. This reduces the torque output at high speed.

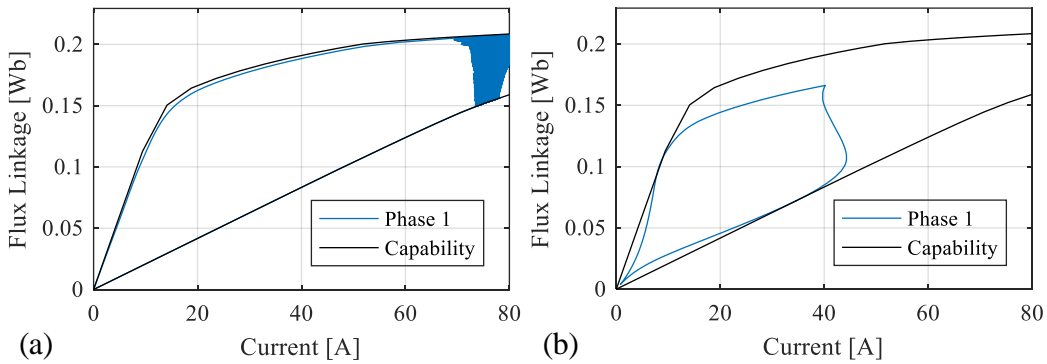


Fig. 2.17  $\psi/i$  curves (3-phase CSRSM, phase A – dynamic model): (a) low speed; (b) high speed

### Converter

In order to separately control the current in each phase, an asymmetric-bridge converter is required, as illustrated in Fig. 2.18. Typically, each switch (either a MOSFET or IGBT) will have a diode in parallel to provide a freewheeling path for current to dissipate in the switch, but these diodes have been removed for clarity in this image.

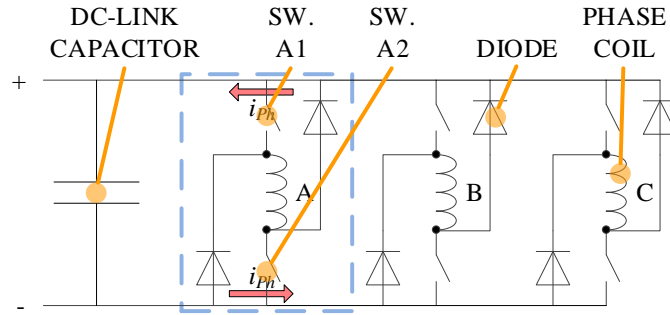


Fig. 2.18 3-Phase asymmetric-bridge converter (switch freewheeling diodes removed)

The phases in an asymmetric-bridge converter are completely isolated (there is no neutral). In addition, only positive current can be controlled, since AC current is not needed for conventional SRMs. There are three fundamental operation modes for this converter, as shown in Fig. 2.19-Fig. 2.21.

### 1) Forward Current (magnetization)

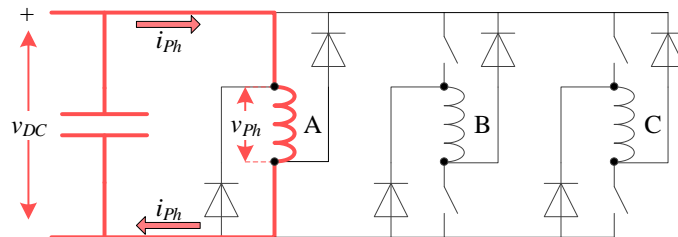


Fig. 2.19 Mode 1: forward current (asymmetric-bridge converter)

In order to supply forward current to phase ‘A’, switch ‘A1’ and switch ‘A2’ are closed. This applies positive DC-link voltage to the phase to start building current.

## 2) Freewheeling (current regulation)

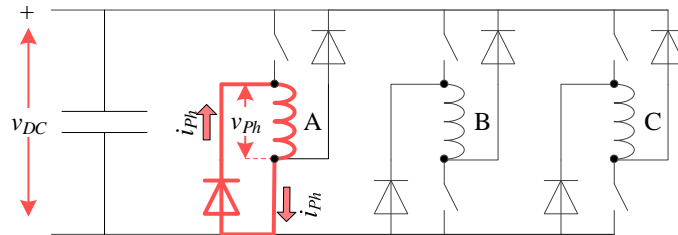


Fig. 2.20 Mode 2: freewheeling current (asymmetric-bridge converter)

In freewheeling mode, the goal is to slowly reduce phase current. This is achieved by shorting the phase against itself by closing switch ‘A2’. The current remaining in the phase coils will then circulate through the short and slowly dissipate through resistive power loss.

## 3) Reverse Current (demagnetization)

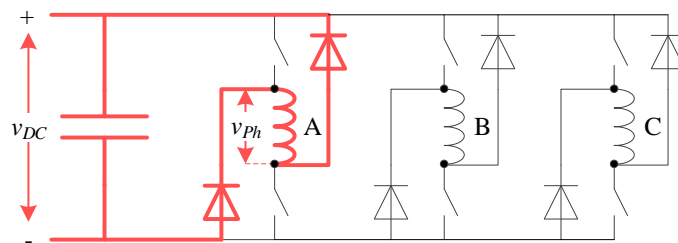


Fig. 2.21 Mode 3: reverse current (asymmetric-bridge converter)

In order to quickly remove current from the phase coils, the supply to the phase needs to be reversed, to provide a path for current back to the DC-link. When switch ‘A1’ and switch ‘A2’ are turned off, the diodes provide this path, and the energy in the phase returns to the DC-link. This reduces the current in the phase

coils much more quickly than freewheeling due to the negative voltage applied to the phase.

### ***Current Controller***

The phase current control system is illustrated in Fig. 2.22.

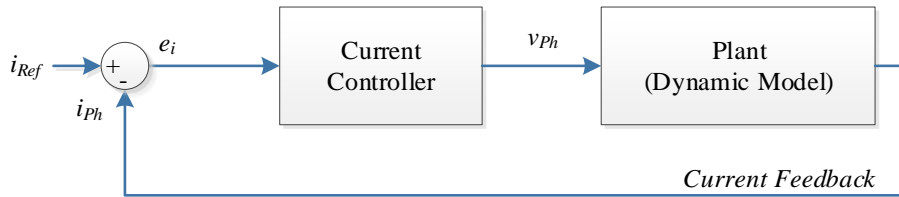


**Fig. 2.22 Control system: phase current control**

Different controller types can be implemented, as is the case with any control system. However, since the converter has discrete input states (on, freewheeling, and off), the current control is discontinuous in nature. Therefore, a “hysteresis controller” is naturally well suited for this application. Hysteresis controllers constrain current to remain within a set “hysteresis” range of the target current, by utilizing the different converter states. The hysteresis band is illustrated in Fig. 2.23 and Fig. 2.24.

Hysteresis controllers can either use “soft chopping” or “hard chopping”. Soft chopping is typically preferred over hard chopping because it can provide more precise current regulation (depending on motor inductance and switching frequency).

With soft chopping, if  $(\theta_{ON} \leq \theta_{Elec} < \theta_{OFF})$ :

$$v_{Ph} = \begin{cases} +v_{DC} & | & i_{Ph} < i_{LB} \\ -R_{Ph}i_{Ph} & | & i_{Ph} > i_{UB} \\ v_{Ph} & | & i_{LB} \leq i_{Ph} \leq i_{UB} \end{cases}$$

With soft chopping, converter ‘mode 1’ is used when the phase current is below the hysteresis band, ‘mode 2’ is used when it is above the band, and the mode is unchanged when inside the band.

With hard chopping, if  $(\theta_{ON} \leq \theta_{Elec} < \theta_{OFF})$ :

$$v_{Ph} = \begin{cases} +v_{DC} & | & i_{Ph} < i_{LB} \\ -v_{DC} & | & i_{Ph} > i_{UB} \\ v_{Ph} & | & i_{LB} \leq i_{Ph} \leq i_{UB} \end{cases}$$

With hard chopping, converter ‘mode 1’ is used when the phase current is below the hysteresis band, ‘mode 3’ is used when it is above the band, and the mode is unchanged when inside the band.

Otherwise, if  $(\theta_{Elec} < \theta_{ON})$  or  $(\theta_{Elec} > \theta_{OFF})$ :

$$v_{Ph} = \begin{cases} -v_{DC} & i_{Ph} > 0 \\ 0 & otherwise \end{cases}$$

Finally, when the motor is outside the firing angles, ‘mode 3’ is applied to return the stored phase energy back to the DC-link, and then the phase is turned off. The current regulation accuracy depends on motor EMF, phase voltage drop, DC-link voltage, and maximum switching frequency. The net voltage applied to a phase, under any condition, is based on the phase voltage equation:

$$v_{Ph} = v_{Drop} + v_{EMF}$$

$$v_{Net} = v_{DC} - v_{Ph}$$

If  $v_{Net}$  is large, it will be possible to inject current into the windings quickly. However, this can make regulating current difficult once it has reached its target value, as the current will often overshoot the target. When the phase is turned off, it may also undershoot the target. This effectively means that the switching frequency must increase to improve the current regulation, as shown in Fig. 2.23.

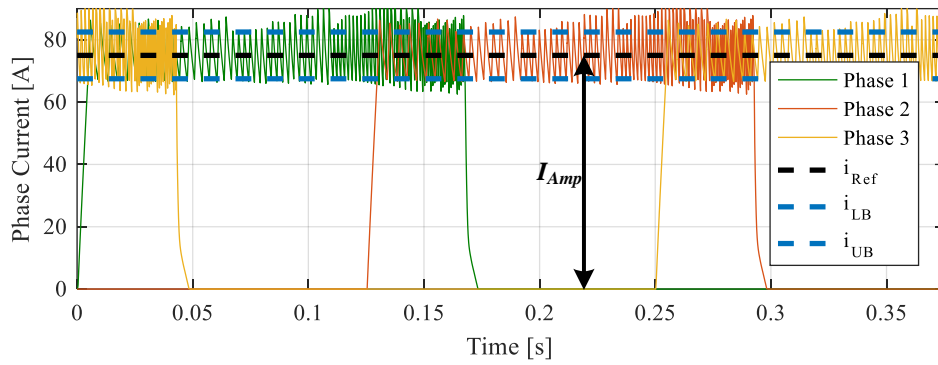


Fig. 2.23 Phase current regulation using hysteresis controller - low speed ( $v_{Net} \gg 0$ )

A switching frequency limit of  $f_{Switch}$  is required to prevent damage to the converter switching devices. This limit may be imposed by the maximum converter logic processor clock frequency, or as a fraction of this clock frequency. However, typically  $f_{Switch}$  is enforced by the current sensor sampling frequency ( $f_{Current}$ ).

If  $v_{Net}$  is small (i.e.  $v_{DC}$  is small, or the motor is running at high speed and  $v_{Ph}$  is high), then it will take longer to inject current into the windings. This effectively reduces the switching frequency and the phase current overshoot. When  $v_{Net}$  becomes very small, it will not be possible to inject current quickly enough to reach the current target during the conduction period, as shown in Fig. 2.24.

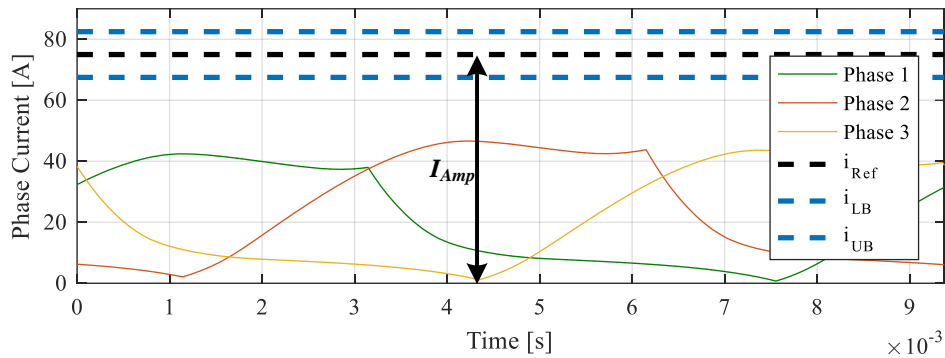


Fig. 2.24 Phase current regulation using hysteresis controller - high speed ( $v_{Net} \approx 0$ )

The firing angles can be advanced to start injecting current sooner to give it time to reach the target value. This is called “single pulse” operation, since the current waveforms have a single peak (no hysteresis regulation), as illustrated previously in Fig. 2.13 (b). This is why torque drops in the constant power region of the torque-speed curve (see Fig. 2.25)

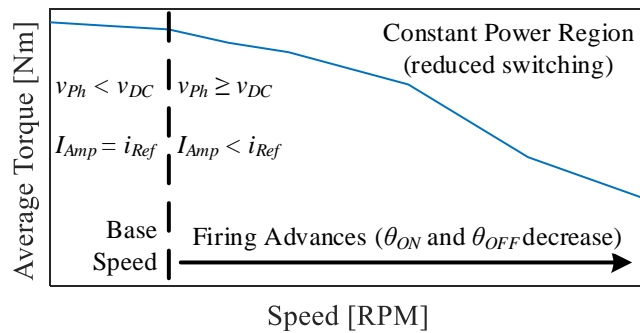
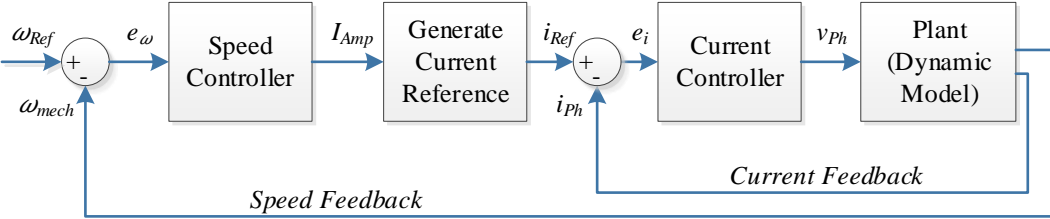


Fig. 2.25 Torque-speed map - critical behavior (CSR)

**Speed Controller**

Speed control can be added to the control system by wrapping the current control loop (Fig. 2.22) inside a speed control loop, as shown in Fig. 2.26.



**Fig. 2.26 Control system: speed control + current control**



## Mutually Coupled Switched Reluctance Motors (MCSRMs)

### Structure

#### *Operational Principles*

The MCSRMs use sinusoidal alternating current (AC) waveforms instead of current pulses. This allows for the use of a conventional 3-phase AC full-bridge inverter, which is used for most other machine types. In order to use a standard full-bridge inverter, more than one phase must be excited at a given time, as each phase has a common neutral with the other phases. Thus, in order for the machine to operate, there must be mutual coupling between phases. The fundamental principle of torque generation is the same as a non-coupled SRM, though mutual inductance effects provide an additional source of torque.

#### *Pole Configuration Constraints*

The motor pole configurations that give balanced magnetic pull and symmetrically distributed flux paths can be determined using the same equation that was used for the CSRMs [7]. The only difference is that the number of stator poles does not have to be even for the MCSRMs, as flux can be allowed to link between different phases (mutual coupling):

$$N_R = \frac{N_S}{N_{Ph}} p \kappa$$

The  $\kappa$  term checks for a locked rotor condition, and will return 0 if there is a locked rotor (invalid configuration), or 1 for valid configurations [7]:

$$\kappa = \prod_{i=1}^{i=N_f} \text{ceil} \left( \frac{\text{mod}(p, f(i))}{f(i)} \right)$$

where:

$\kappa = \text{valid configuration check (1 = valid, 0 = invalid)}$

$p = \text{positive integer}$

$N_{Ph} = \# \text{ phases}$

$N_S = \# \text{ stator poles}$

$N_R = \# \text{ rotor poles}$

$N_f = \# \text{ prime factors}$

$f = \text{prime factor array of } N_{Ph}$

For example, if  $N_{Ph} = 3$ ,  $p = 2$ , and  $N_S = 15$ , then  $f = [3, 5]$ , and:

$$\begin{aligned} N_R &= \frac{15}{3} 2 \prod_{i=1}^{i=2} \text{ceil} \left( \frac{\text{mod}(2, f(i))}{f(i)} \right) \\ &= 10 \left[ \text{ceil} \left( \frac{\text{mod}(2,3)}{3} \right) \cdot \text{ceil} \left( \frac{\text{mod}(2,5)}{5} \right) \right] \\ &= 10 \end{aligned}$$

This would be designated as a “15/10” SRM, as shown in Fig. 2.2 (b).

### ***Pole Angle Constraints***

The pole angle constraints for MCSRMs are not as clearly defined as for a CSRm. Since more than one phase is excited at a given time, one phase will be partially aligned when the other is unaligned. Since MCSRMs rely on the same principle of reluctance torque however, it is important to ensure that an unaligned

position exists for each stator pole (like the CSRМ). The MCSRМ electrical cycles are twice the length of CSRМ electrical cycles, but positive torque is produced in each half of the electrical cycle, so the equation is effectively identical:

$$2(\beta_S + \beta_R) < \Gamma$$

$$\Gamma = \frac{2(360^\circ)}{N_R}$$

where:

$$\Gamma = \text{mechanical angle for one electrical cycle } [^\circ]$$

### Torque Production and Electromagnetics

MCSRMs are typically modelled using  $dq$  theory – which simplifies the expression of mutual coupling between phases (this is detailed in **Chapter 3**). Transforming a 3-phase system into the  $dq$ -reference frame is detailed in **Appendix A**. The mutual inductance of the machine can then be represented as a function of the mutual flux-linkage and phase current:

$$L_{dq} = \frac{d\psi_{dq}}{di_{dq}}$$

where:

$$L_{dq} = \text{mutual inductance } [H]$$

$$\psi_{dq} = \text{mutual flux linkage } [Wb \cdot \text{turns}]$$

$$i_{dq} = dq \text{ phase current vector } [A]$$

Though 3-phase representations are rarely used for MCSRМ analysis, as they become highly complex, the fundamentals will first be outlined in this

reference frame to highlight the differences with the CSRМ. Then the formulae will be represented using the more practical  $\alpha\beta$  and/or  $dq$ -reference frames.

The energy conversion process in a MCSRМ can be illustrated using a  $\psi/i$  diagram; though there are some differences compared to the CSRМ. Since each term is produced by mutual excitation, the  $dq$  results are transformed back to the  $abc$  reference frame, and only phase A is plotted for the  $\psi/i$  diagram in Fig. 2.27. Since AC current waveforms are used to excite the MCSRМ, the  $\psi/i$  diagram has both a positive magnetization loop and a negative one. The following figures assume square wave AC waveforms are used, as these results can be compared to the CSRМ diagrams more intuitively.

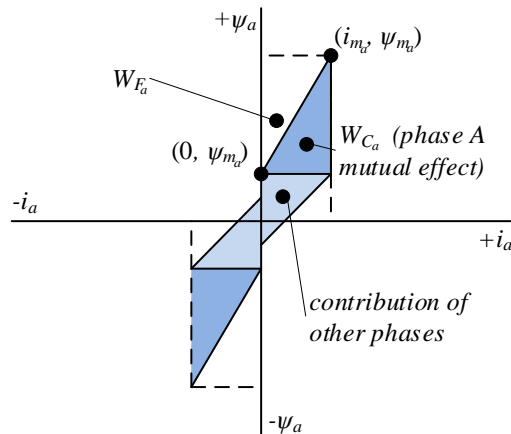


Fig. 2.27 Flux-linkage vs. phase current (phase 1, linear operation)

The field energy  $W_{F_a}$  is the energy stored in the magnetic field of phase A, whereas the co-energy  $W_{C_a}$  of phase A contributes to torque generation. In this simplified linear case, the stored and co-energy are equivalent:

$$W_{C_a} = \text{AREA UNDER GRAPH}$$

$$\begin{aligned} &= \frac{1}{2} \psi_{m_a} i_{m_a} \\ &= \frac{1}{2} L_a i_{m_a}^2 \\ &= W_{F_a} \end{aligned}$$

where:

$$W_{F_a} = \text{field or stored energy – phase A [J]}$$

$$W_{C_a} = \text{co – energy – phase A [J]}$$

$$\psi_{m_a} = \text{peak flux linkage – phase A [Wb.t]}$$

$$i_{m_a} = \text{peak phase current – phase A [A]}$$

$$L_a = \text{inductance – phase A [H]}$$

When considering the co-energy of the MCSRM, only the positive magnetization loop is considered, as this is the maximum energy per electrical cycle contributing to torque. The negative magnetization loop also contributes to torque, but later in the electrical cycle; not at the same time. Due to this, the energy from both loops cannot be summed. Effectively, there are two positive torque pulses per electrical cycle for the MCSRM, instead of one for the CSRМ.

The linear co-energy which contributes to torque is still only half the input energy, just like the CSRМ. In order to improve the power factor, and thus torque output, the motor can be saturated, as illustrated in Fig. 2.28.

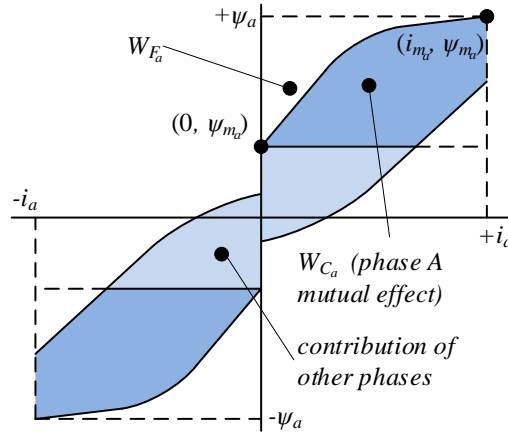


Fig. 2.28 Flux-linkage vs. phase current (phase 1, non-linear saturated operation)

In the non-linear case, the co-energy is larger than the stored energy; meaning more of the input energy contributes to torque production (power factor improves):

$$W_{C_a} = \int_{i_{m_0}}^{i_{m_a}} \psi_a \cdot di_a$$

$$W_{F_a} = \int_{\psi_{m_0}}^{\psi_{m_a}} i_a \cdot d\psi_a$$

$$W_{C_a} > W_{F_a}$$

where:

$$\psi_a = \text{flux linkage} - \text{phase A [Wb.t]}$$

$$i_a = \text{phase current} - \text{phase A [A]}$$

$$\psi_{m_0} = \text{flux linkage when } (i_a = 0) - \text{phase A [Wb.t]}$$

When a full electrical cycle is considered, the  $\psi/i$  diagram can be expanded, as shown in Fig. 2.29. A fixed-amplitude AC square wave can be used to excite the machine; however fixed-amplitude AC sinusoidal excitation can also be used. Both

have been illustrated in Fig. 2.29, to help explain the shape of the  $\psi/i$  diagrams. The square-wave excitation produces a  $\psi/i$  diagram that looks similar to that of the CSRSM (Fig. 2.11), but has both a positive and negative component since it is an AC waveform. Each half of the sinusoidal excitation waveform is parabolic, in contrast to the square-wave excitation waveform; altering the shape of the  $\psi/i$  diagram.

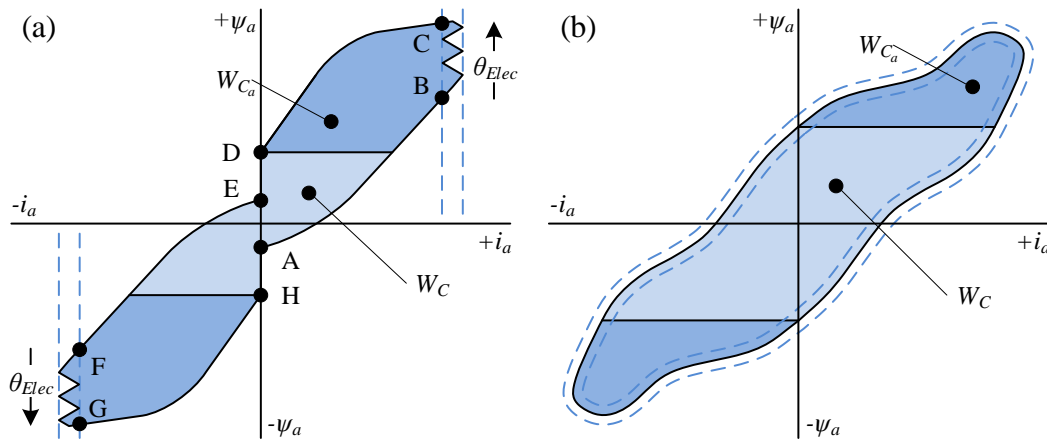


Fig. 2.29  $\psi/i$  work cycle (phase 1): (a) square-wave excitation; (b) sinusoidal excitation

### Motoring Cycle

#### Loop A-B-C-D-E

The A-B-C-D-E loop represents the positive half of the AC current waveform ( $0^\circ$  to  $180^\circ$  electrical). Starting at point ‘A’, positive current is injected into phase ‘A’, until it hits the phase current reference at ‘B’. The rotor position does not change between these points for the square-wave case. Due to the current in the other phases, the flux-linkage at point ‘A’ is not zero.

At point ‘B’, the current control regulates current while the rotor rotates to the turn-off point at ‘C’ (square wave).

Once the phase has been turned off at point ‘C’, the current starts to drop in the coil, reducing the flux-linkage until the current in the phase is completely dissipated, at ‘D’.

The phase current remains at zero until the negative turn-on angle at point ‘E’. The flux-linkage is non-zero between ‘D’ and ‘E’ due to excitation in the other phases.

If the excitation is sinusoidal, this process is more challenging to explain. The current only reaches zero for an instant with sinusoidal excitation and current regulation (chopping) occurs during the entire cycle.

#### *Loop E-F-G-H-A*

The work loop is the same for E-F-G-H-A as it is for A-B-C-D-E, with the only exception being that the current direction is reversed. This loop represents the negative half of the AC current waveform (180° to 360° electrical).

#### ***Generating Cycle***

The generating cycle for the MCSRМ is the reverse of the motoring cycle. As with the CSRМ, the MCSRМ must first provide energy to magnetize the coils, before energy can be captured and returned to the source.



### *Phase Voltage*

Please note that for the following equations, the inductance ( $L$ ) and flux linkage ( $\psi$ ) are functions of rotor position ( $\theta$ ) and current ( $i$ ). In this section “ $L(\theta, i)$ ” and “ $\psi(\theta, i)$ ” have been replaced with “ $L$ ” and “ $\psi$ ” respectively, for ease of reading. All vector and matrix terms are presented in **bold**. Recall the phase voltage equation (*Equation 2.1*) for the CSRMs:

$$\mathbf{v}_{Ph} = R_{Ph}\mathbf{i}_{Ph} + \frac{d\boldsymbol{\psi}_{Ph}}{dt}$$

The same voltage equation applies for the MCSRM (and all electric machines, for that matter). The only difference is that the matrix terms are not diagonal anymore, as they include mutual coupling effects. Since the MCSRM has mutually coupled phases, it makes sense to represent the equations in the  $\alpha\beta$ -reference frame or  $dq$ -reference frame, as this significantly simplifies the matrix calculations. Transforming to the  $\alpha\beta$ -reference frame allows for the system to be represented as a two-phase system; simplifying the matrix calculations. In the  $dq$ -reference frame, the two-phase system becomes pseudo-stationary. When considering the dynamic voltage waveforms, it makes sense to use the position-dependent  $\alpha\beta$ -reference frame:

$$\mathbf{v}_{\alpha\beta} = R_{Ph}\mathbf{i}_{\alpha\beta} + \frac{d\boldsymbol{\psi}_{\alpha\beta}}{dt}$$

(*Equation 2.4*)

where:

$$R_{Ph} = \text{phase resistance } [\Omega]$$

$$t = \text{time [s]}$$

$$\mathbf{v}_{\alpha\beta} = \alpha\beta \text{ instantaneous voltage input [V]}$$

$$\mathbf{i}_{\alpha\beta} = \alpha\beta \text{ instantaneous current input [A]}$$

$$\omega = \text{rotor mechanical rotation speed } \left[ \frac{\text{rad}}{\text{s}} \right]$$

$$\theta = \text{rotor mechanical angle [rad]}$$

$$\boldsymbol{\psi}_{\alpha\beta} = \alpha\beta \text{ flux – linkage [Wb.t]}$$

When the **bold** terms are replaced with their respective matrix representations, the voltage can be calculated at any rotor position. This is detailed in *Appendix E*, for the  $\alpha\beta$ -reference frame.

### *Deriving the Torque Equation*

The MCSRM torque equation can be expressed in different ways, but the most common representation of the torque equation is the general machine torque equation ( $T_{Mutual}$ ). This term is presented in the  $dq$ -reference frame and is the same equation typically used to represent reluctance torque in IPMSM machines. However, to accurately represent the dynamic torque of the machine, it is important to account for non-linear effects and the simplifications made in the  $T_{Mutual}$  equation, using an additional term,  $T_{Nonlinear}$ . In this representation,  $T_{Nonlinear}$  is determined through an FEA-calculated look-up table (LUT), as discussed in [3]. The dynamic torque can then be calculated:

$$T = T_{Mutual} + T_{Nonlinear}$$

$$\begin{aligned}
 &= \left(\frac{3}{2}\right) \left(\frac{N_R}{2}\right) (L_d - L_q) i_d i_q + T_{Nonlinear} \\
 &= \left(\frac{3}{2}\right) \left(\frac{N_R}{2}\right) \left(\frac{\psi_d}{i_d} - \frac{\psi_q}{i_q}\right) i_d i_q + T_{Nonlinear} \\
 &= \left(\frac{3}{2}\right) \left(\frac{N_R}{2}\right) \left(\frac{\psi_d}{i_d} i_d i_q - \frac{\psi_q}{i_q} i_d i_q\right) + T_{Nonlinear} \\
 &= \left(\frac{3}{2}\right) \left(\frac{N_R}{2}\right) (\psi_d i_q - \psi_q i_d) + T_{Nonlinear}
 \end{aligned}$$

**(Equation 2.5)**

If  $\psi_{dq}$  and  $i_{dq}$  are complex (i.e. d-axis = real, q-axis = imaginary), then the torque can also be represented as:

$$T = \left(\frac{3}{2}\right) \left(\frac{N_R}{2}\right) \text{imag}(\text{conj}(\boldsymbol{\psi}_{dq}) \mathbf{i}_{dq}) + T_{Nonlinear}$$

where:

$$\begin{aligned}
 \psi_d, \psi_q &= d \text{ and } q - \text{axis flux - linkage [Wb.t]} \\
 &= f(\theta, \mathbf{i}_{dq})
 \end{aligned}$$

$$\begin{aligned}
 T_{Nonlinear} &= f(\theta, \mathbf{i}_{dq}) \\
 &= T_{LUT}(\theta, \mathbf{i}_{dq}) - T_{Mutual}(\theta, \mathbf{i}_{dq})
 \end{aligned}$$

$$L_d, L_q = d \text{ and } q - \text{axis inductance [H]}$$

$$i_d, i_q = d \text{ and } q - \text{axis current [A]}$$

$$\text{conj}(\ ) = \text{complex conjugate}$$

$$\text{imag}(\ ) = \text{imaginary component}$$

## Control Considerations

### *Electrical Angles*

The  $0^\circ$  electrical position for the MCSRМ is defined as the position where the rotor poles are fully aligned with the stator poles of the phase in question, as shown in previously in Fig. 2.4.

Due to the winding strategy used in the MCSRМ, and the sinusoidal current excitation, the magnetic field changes direction every half electrical cycle. The circuit must be magnetized once for each rotor pole alignment, meaning that the electrical cycle repeats after the rotor has rotated by two rotor poles. Thus, it is possible to convert from mechanical angle to electrical angle using the following relationship (assuming that  $0^\circ_{\text{mech.}}$  is aligned with  $0^\circ_{\text{elec.}}$ , by convention.):

$$\theta_{Elec} = \frac{\theta_{Mech}}{2N_R}$$

The full electrical angle equation is otherwise identical to that of the CSRМ:

$$\begin{aligned}\boldsymbol{\theta}_{Elec} &= \begin{bmatrix} \theta_{Elec_1} \\ \dots \\ \theta_{Elec_{N_{Ph}}} \end{bmatrix} \\ &= \text{mod} \left( \frac{\theta_{Mech}}{2N_R} + \left( \frac{2\pi}{N_{Ph}} \right) \mathbf{k}_{Ph}, 2\pi \right)\end{aligned}$$

### *Continuous Torque Production*

In order to create continuous torque, the phases are excited in the order given by  $k_{Ph}$ , as shown in Fig. 2.30. The phase torque is summed to obtain the total machine output torque, as shown in Fig. 2.31.

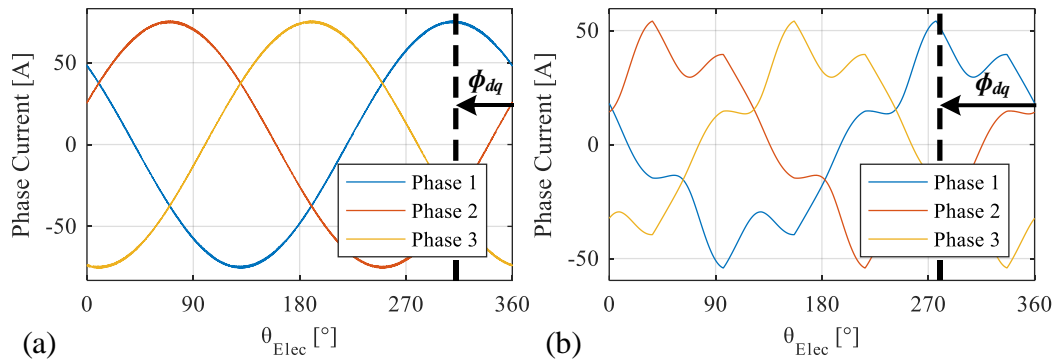


Fig. 2.30 Phase current waveforms (3-phase MCSRM – dynamic model): (a) low speed; (b) high speed

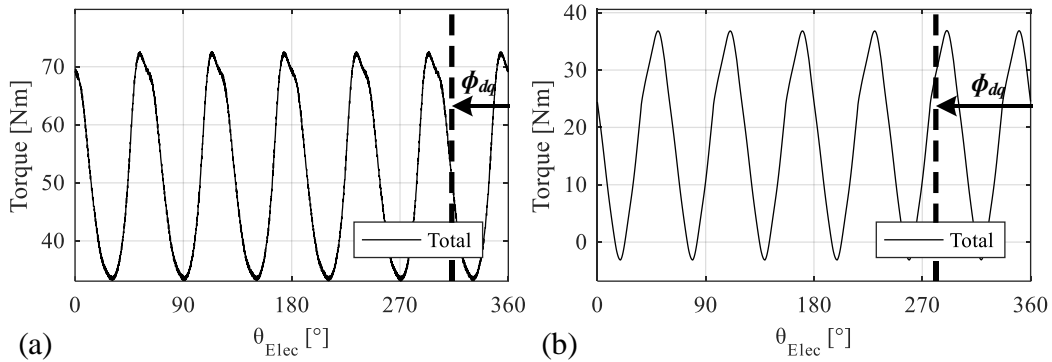


Fig. 2.31 Phase torque vs. total torque output (3-phase MCSRM – dynamic model): (a) low speed; (b) high speed

Observing Fig. 2.30, it is clear that the current waveform phase-shift (or  $dq$ -excitation angle) advances as the motor speed increases, due to increased induced voltage. This is reflected by the reduced switching in the phase voltage waveforms (see Fig. 2.32); meaning that the converter cannot regulate current. This behavior is explained in detail in the *Current Controller* section.

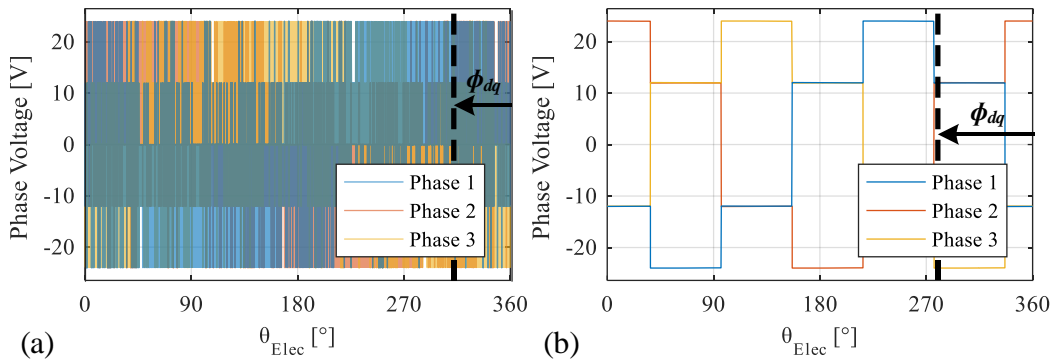


Fig. 2.32 Phase voltage (3-phase MCSRM – dynamic model): (a) low speed; (b) high speed

The phase flux-linkage curves are compared in Fig. 2.33.

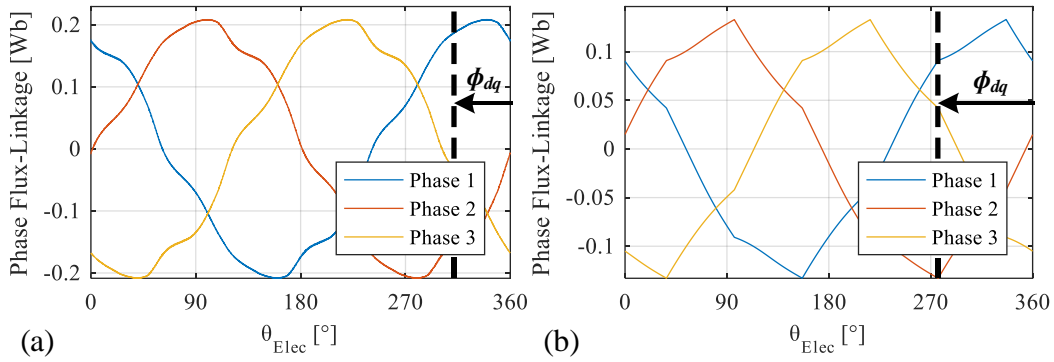


Fig. 2.33 Phase flux-linkage (3-phase MCSRM – dynamic model): (a) low speed; (b) high speed

Finally, the  $\psi/i$  curves are compared in Fig. 2.34. Due to the increased induced voltage at high speed, it is not possible to obtain as high of a phase current, and the co-energy area decreases. This reduces the torque output at high speed, just like the CSRMs.

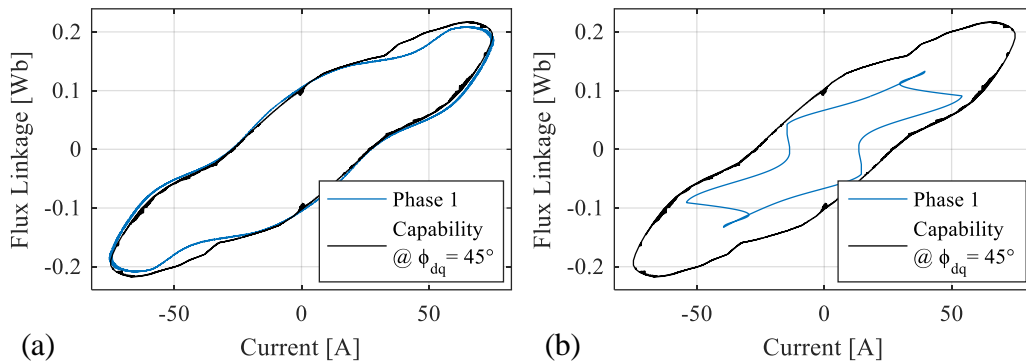


Fig. 2.34  $\psi/i$  curves (3-phase MCSRM, phase A – dynamic model): (a) low speed; (b) high speed

### Converter

Since the MCSRM takes advantage of mutual coupling, it is not necessary to have independent current control for each phase. Each negative phase lead can therefore be connected in ‘Y-configuration’ and a more conventional full-bridge inverter can be used, as illustrated in Fig. 2.35. Typically, each switch (either a MOSFET or IGBT) will have a diode in parallel to provide a freewheeling path for current to dissipate in the switch, but these diodes have been removed for clarity in this image.

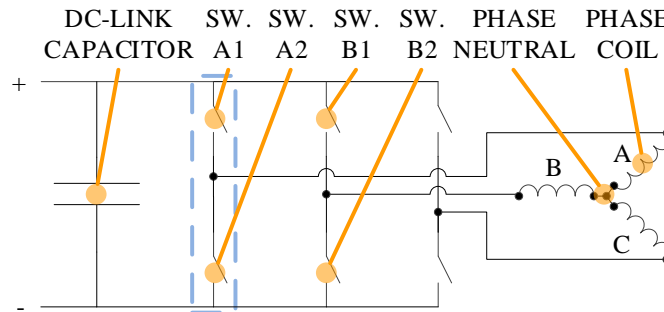


Fig. 2.35 3-Phase full-bridge converter (switch freewheeling diodes removed)

This type of inverter can regulate both positive and negative current, but each phase must have the same current waveform shape, with  $120^\circ$  electrical shift between phases, due to the Y-connected phases. There are three fundamental operation modes for this converter, just like the CSRМ, as shown in Fig. 2.36-Fig. 2.38.

### 1) Forward Current (current on)

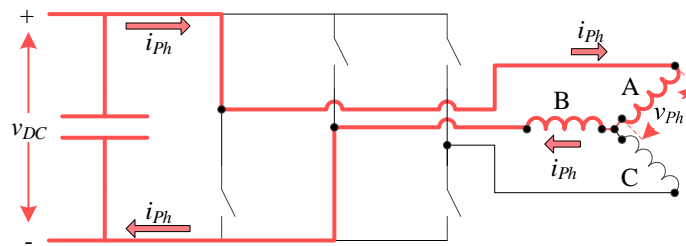


Fig. 2.36 Mode 1: forward current (full-bridge converter)

In order to supply forward current to phase ‘A’ switch ‘A1’ and switch ‘B2’ are closed. This applies the DC-link voltage across both phase ‘A’ and phase ‘B’ in series to start building current. Note that the Y-connected neutral causes a negative voltage to be applied to phase ‘B’, so the current waveform will be negative while phase ‘A’ is being injected with positive current.

If negative current is desired in phase ‘A’ (and positive current in phase ‘B’), the same concept applies, but switches ‘B1’ and ‘A2’ would be closed instead of ‘A1’ and ‘B2’.



## 2) Freewheeling (current regulation)

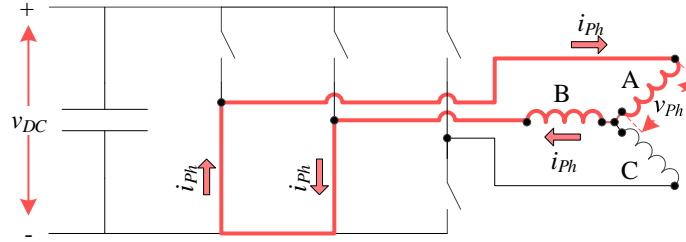


Fig. 2.37 Mode 2: freewheeling current (full-bridge converter)

Like the CSRМ, the goal of freewheeling is to reduce the amplitude of current in the phase slowly (be it positive, or negative current), using resistive power loss to bleed the excess current. With a full-bridge inverter, this can be accomplished by closing switches ‘A2’ and ‘B2’ for positive phase ‘A’ current. Switches ‘A1’ and ‘B1’ can be closed instead to achieve the same effect in the opposite direction.

## 3) Reverse Current (current off)

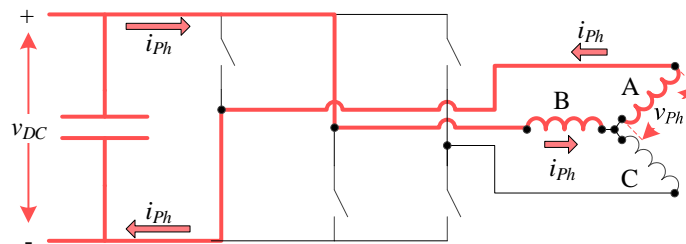


Fig. 2.38 Mode 3: reverse current (full-bridge converter)

If negative current is desired in phase ‘A’ (and positive current in phase ‘B’), the same concept applies as for forward current operation, but switches ‘B1’ and ‘A2’ would be closed instead of ‘A1’ and ‘B2’.

It is important to note that only regulation of one phase has been discussed here. In actual operation, three phases are excited at a given time rather than just two.

### ***Current Controller***

The phase current control system is the same as the CSRSM, as shown in Fig. 2.22. There are several different controller types that can be used to regulate current for a MCSRSM, but only hysteresis control will be outlined here. It follows the same principles as the CSRSM hysteresis controller, with the only difference being that the hysteresis band is AC sinusoidal or square-wave, as shown in Fig. 2.39 and Fig. 2.40.

The net phase voltage applied to the coils affects the switching frequency for the same reasons as the CSRSM. These effects are illustrated in Fig. 2.39 and Fig. 2.40 for low speed and high speed respectively.

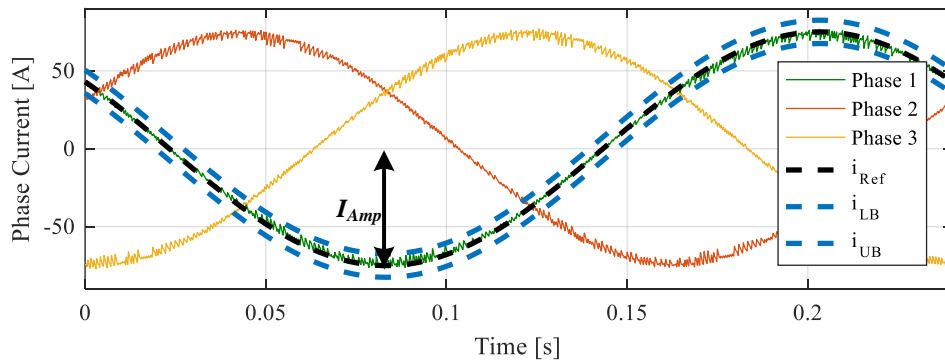


**Fig. 2.39** Phase current regulation using hysteresis controller - low speed ( $v_{Net} \gg 0$ )

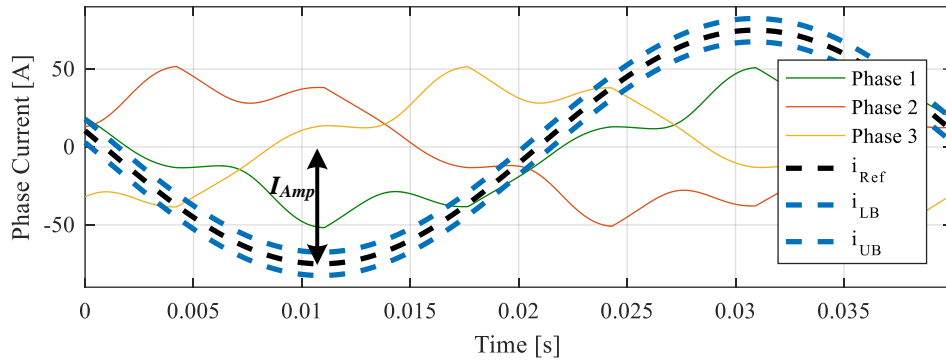


Fig. 2.40 Phase current regulation using hysteresis controller - high speed ( $v_{Net} \approx 0$ )

When  $v_{Net}$  becomes very small, it will not be possible to inject current quickly enough to reach the current target during the conduction period. The  $dq$ -excitation angle can be advanced to start injecting current sooner to give it time to reach the target value, just like the firing angles are advanced for the CSRSM. This is why torque drops in the constant power region of the torque-speed curve (see Fig. 2.41)

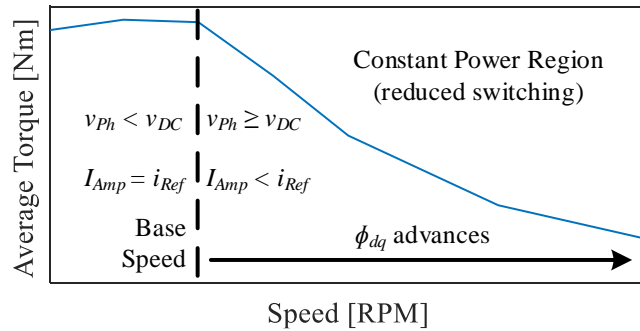


Fig. 2.41 Torque-speed map - critical behavior (MCSRMs)

### Speed Controller

A speed controller can be implemented in the same manner as for the CSRSM (illustrated in Fig. 2.26).

## Loss Mechanisms

There are different loss mechanisms in electric machines that can significantly influence their design. Both CSRMs and MCSRMs only use stator excitation, and thus do not have rotor copper losses that an induction or wound rotor machine would. However, iron losses can be significant in these machines due to the high saturation levels and high excitation frequencies experienced at high speed. This section will discuss the different loss mechanisms in these machines.

### Core Loss

#### *Hysteresis*

Hysteresis loss is caused by a material's resistance to magnetic domain switching [6]. When magnetizing a material in a magnetic field, the domains align; when demagnetizing, they are left unaligned. It takes some amount of energy to move the magnetic domains, which is converted into heat. If magnetization frequencies are increased, as is the case with high speed operation, this problem is intensified. The same is true when flux densities are increased, as more domains are affected.

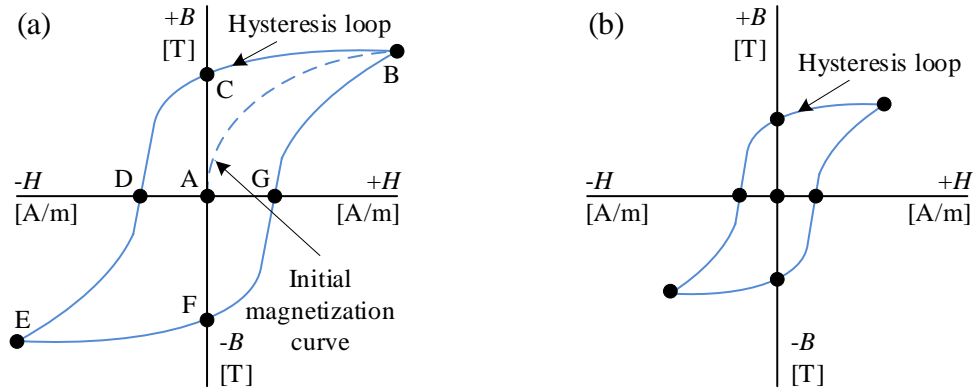


Fig. 2.42 Magnetic hysteresis: (a) hard magnetic loop; (b) soft magnetic loop

Fig. 2.42 details the hysteresis loops for hard and soft magnetic materials respectively. The hysteresis loop has additional implications for ‘hard’ magnetic materials in PM machines, though this is outside the scope of this thesis. When dealing with CSRMs/MCSRMs, the hysteresis loop refers to the laminations of the machine – typically silicon or cobalt steel. Therefore, only the running loop of B-C-D-E-F-G-B is considered. At ‘B’, the material is magnetically saturated. Upon removal of the field ( $H$ ), the flux density ( $B$ ) will decrease to the value at ‘C’, called the residual magnetism. A negative field (coercive force) must be applied to completely demagnetize material (point ‘D’). Then the same process continues in the negative magnetization direction. Up to point ‘E’, the field is increased in the negative direction, saturating the material. At point ‘F’ there is no field, but the material is magnetized in the negative direction, and at point ‘G’ the material is once again completely demagnetized. With a soft magnetic material, little coercive force is needed to magnetize or demagnetize the material.

Hysteresis losses can be managed by utilizing lamination materials with and a smaller hysteresis loop area. Typically, soft magnetic materials are utilized as they have a very small hysteresis loop.

It is useful to quantify power loss per unit volume when referring to hysteresis loss, as this loss will be dependent on the location in the magnetic circuit. The hysteresis power loss ( $P_{Hyst}$ ) can then be quantified in relation to the B-H curve of the material [6]:

$$\frac{P_{Hyst}}{V_{Fe}} = \int H \cdot dB$$

where:

$$V_{Fe} = \text{volume of iron [m}^3\text{]}$$

$$H = \text{magnetic field intensity } \left[ \frac{A}{m} \right]$$

$$B = \text{magnetic flux density [T]}$$

### ***Eddy Current Loss***

Whenever the flux-linkage changes in a magnetic circuit, an EMF will be induced that opposes the magnetic field change. This is tied with how an inductor operates (quickly changing current is resisted). This current is induced in the iron circuit – creating eddies of current that waste power through resistive loss in the iron, termed eddy current loss ( $P_{Eddy}$ ).

$$e = - \frac{d\psi}{dt}$$

$$P_{Eddy} = \frac{e^2}{R_{Fe}}$$

where:

$$e = \text{back EMF [V]}$$

$$t = \text{time [s]}$$

$$\psi = \text{flux linkage [Wb.t]}$$

$$R_{Fe} = \text{resistance of magnetic circuit material } [\Omega]$$

In order to reduce the eddy current loss, different materials can be used which have isolated particles (i.e. powdered iron), or different alloying elements can be used to modify the iron resistance. However, the most common approach is to use laminated steel. Using this method, the magnetic circuit is formed out of stacked “laminations” which are very thin slices of steel electrically insulated from each other. This effectively reduces the area in which an eddy can form, and thus the eddy current “loops” are smaller, reducing the loss associated with them. In other terms, the resistance in this direction increases, and thus the losses decrease.

### Copper Loss

Copper loss is caused by the resistance of copper windings producing heat as current is passed through them. Since CSRMs and MCSRMs have to create their own field (they do not have permanent magnets), the resistive power loss ( $P_{Cu}$ ) can be significant.

$$P_{Cu} = N_{Ph}(i_{Ph}^2 R_{Ph})$$

where:

$$i_{ph} = \text{phase current [A]}$$

$$N_{ph} = \# \text{ phases}$$

$$R_{ph} = \text{phase resistance } [\Omega]$$

A high number of coil turns may be desired to produce a stronger magnetic field for a given current, and thus more torque. However, since only a finite amount of copper can be physically contained in the coil slots, wire diameter may be made smaller to accommodate more turns, or the number of parallel wire strands may be reduced; increasing losses. It is important that these losses are controlled however, as they affect the efficiency and the thermal capabilities of the machine. The insulation around the winding conductors has a maximum temperature rating that can be breached if loss is not controlled here.

Another issue with copper loss occurs during high frequency operation. Skin effect causes the current in a conductor to concentrate on the outside perimeter rather than evenly through the conductor. This may or may not be an issue depending on the size of the wire used; as the skin depth may be large enough that there is no effect. Skin effect still needs to be considered and checked for however; otherwise extra copper could be added to the machine with no benefit; causing increased costs and weight. The approximate skin depth and effective resistance are summarized as follows [6]:

$$\delta = \frac{1}{\sqrt{\pi f \mu \sigma}}$$

$$R_{AC} = R_{DC} \left[ 1 + \frac{(r_0/\delta)^4}{48 + 0.8(r_0/\delta)^4} \right]$$



where:

$\delta = \text{skin depth [m]}$

$f = \text{electrical frequency [Hz]}$

$\mu = \text{magnetic permeability } \left[ \frac{H}{m} \right]$

$\sigma = \text{electrical conductivity} = \frac{1}{\rho} \left[ \frac{S}{m} \right]$

$\rho = \text{resistivity } \left[ \frac{\Omega}{m} \right]$

$r_0 = \text{conductor radius [m]}$

$R_{DC} = \text{DC resistance of wire } [\Omega]$

$R_{AC} = \text{AC equivalent resistance } [\Omega] \text{ at } f \text{ frequency}$

## Summary

In this chapter, the fundamentals of both CSRMs and MCSRMs have been discussed in detail. First, the structure of the CSRМ was discussed, along with basic operating principles, pole configuration constraints, and pole angle constraints. The energy conversion process is detailed, along with the benefits of saturation. Using the phase voltage equation, the torque equation is derived for both the linear and non-linear cases. The control considerations, including current and speed control, converter topology, firing angles, and calculation of electrical angles, are all outlined.

Next, the MCSRM structure and operating principles are discussed. The energy conversion process is discussed for the mutually coupled case, along with the derivation of the linear and non-linear torque equations. The converter topology,  $dq$ -excitation angle, and electrical angle calculation are all discussed in detail.

Finally, loss mechanisms for both machines are discussed. Core losses are explained (both hysteresis loss and eddy current loss), along with DC and AC copper loss effects.

# Chapter 3

## Modelling of Non-Coupled and Mutually Coupled Switched Reluctance Motors

### Introduction

CSRMs and MCSRMs both have highly non-linear behavior that can make analyzing these machines challenging. As discussed in *Chapter 2*, it is not possible to use analytical expressions directly for either machine, since the flux-linkage varies with current and position. Electromagnetic Finite Element Analysis (FEA) can be used to accurately model the performance of these machines. This is suitable for static (current source) simulations, as the FEA simulations are relatively quick. However, it is typically desirable to simulate the dynamic behavior inside a current control loop to simulate motor performance at different current/speed points and different control conditions, as illustrated in Fig. 2.22.

However, if FEA is going to be used for dynamic analyses that account for flux weakening behavior, complex switched-voltage-source simulations must be used and often the converter circuit must be modelled in FEA as well. Since dynamic analyses include all switching dynamics, the FEA time step must be small enough to account for the fundamental switching frequency at the desired speed. Thus, the number of simulation steps can be high, requiring a prohibitive amount of computation time. For example, at 1 RPM, the number of simulation steps

( $N_{Steps}$ ) required to represent one electrical cycle of a 12/16 CSRM for a 10 kHz switching frequency ( $f_{Switch}$ ) is:

$$\omega_{Elec} = \omega_{RPM} \left( \frac{1 \text{ min}}{60 \text{ s}} \right) N_R = \frac{1(16)}{60} = 0.27 \frac{\text{cycles}}{\text{s}}$$

$$T_{Sim} = \frac{N_{Cycles}}{\omega_{Elec}} = \frac{1}{0.27} = 3.75 \text{ s}$$

$$T_s = \frac{1}{f_{Switch}} = \frac{1}{10000} = 0.0001 \text{ s}$$

$$N_{Steps} = \frac{T_{Sim}}{T_s} = \frac{3.75}{0.0001} = 37\,500 \text{ steps}$$

Thus, over 37 thousand FEA simulation steps would be required, requiring a large amount of simulation time for just a single operating point. Since many operating points need to be simulated (different current amplitudes, speeds, and firing angles, etc.), it is clear that this method quickly becomes computationally prohibitive.

This chapter presents the fundamentals of dynamic modelling as it applies to CSRMs and MCSRMs. With the modelling approaches in this chapter, FEA is only used to create look-up tables (LUTs) that describe the non-linear machine behavior. Once the LUTs have been obtained, FEA is no-longer required. The LUTs are then used in combination with the analytical equations to accurately model the dynamic behavior of the machine.

Running the dynamic model will require the same number of simulation steps as a dynamic FEA simulation, but since an analytical model is used, this process is significantly more computationally efficient. The machine can also be

simulated under a multitude of different input conditions (current amplitudes, speeds, etc.) without re-running FEA and requiring further computation time.

This chapter only discusses the fundamentals of CSRM and MCSRM dynamic modelling, due to length constraints. Interested readers are directed to [7] for a more detailed explanation of dynamic modelling. An overview of the modelling procedure is illustrated in Fig. 3.1.

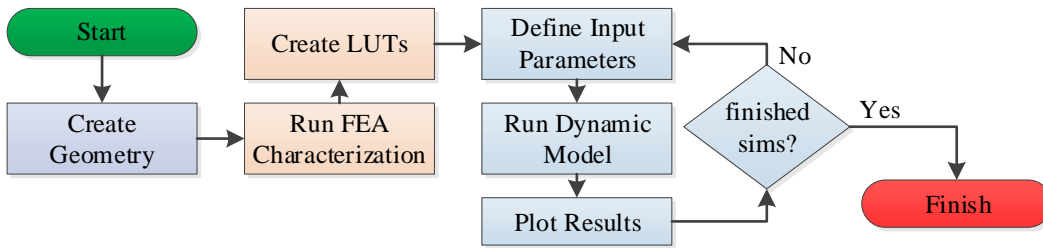


Fig. 3.1 Full dynamic modelling procedure

## CSRMs

When considering CSRMs, mutual coupling is assumed to be negligible. This is due to the isolated phases and the way the flux links in the magnetic circuit. When mutual coupling is neglected, it significantly simplifies the FEA characterization, as only the behavior of one phase needs to be evaluated.

### FEA Characterization

An FEA machine characterization is used to create the non-linear LUTs required by the dynamic model. The FEA characterization process is highlighted in Fig. 3.2.

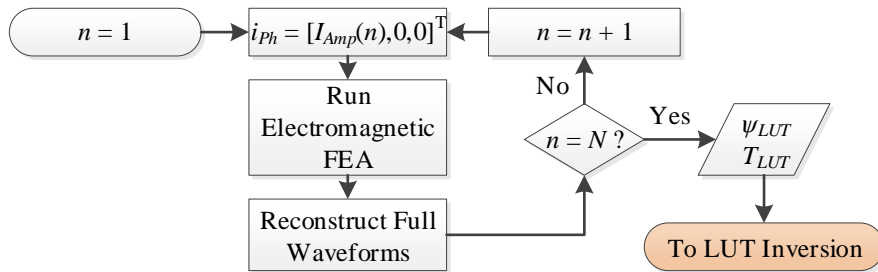


Fig. 3.2 CSRM FEA characterization process

### Defining the 2D LUT Ranges

The critical non-linear parameters that require LUTs are the phase flux-linkage and torque. Both of these parameters vary with rotor position ( $\theta_{Elec}$ ) and phase current ( $i_{Ph}$ ), meaning that 2D LUTs need to be generated for each parameter. The FEA simulation matrix for a 3-phase CSRM with  $\theta_{Elec} = [0, 180]$  and  $i_{Ph} = [0, 20]$  is shown in TABLE 3.1. In this case, the number of current levels ( $N_{Current}$ ) is 2, and the number of positions ( $N_{Angles}$ ) is also 2.

FEA Sim. #	FEA Step #	$\theta_{Elec1}$	$i_{Ph1}$	$\psi_{PhLUT}$	$T_{PhLUT}$
1	1	0	0	$sim_{1,1}$	
	2	180		$sim_{1,2}$	
2	1	0	20	$sim_{2,1}$	
	2	180		$sim_{2,2}$	

**TABLE 3.1 CSRM FEA simulation matrix example**  
( $N_{Current} = 2, N_{Angles} = 2$ )

The example shown here only illustrates the simulations required for 2x2-size LUTs. In practice, a full characterization with roughly 20 current levels and 60 discrete positions provides a good quality characterization. This would result in a 60x20 LUT size. The total number of simulation steps is thus:

$$N_{Sims} = N_{Current} = 20$$

$$\begin{aligned} N_{Steps} &= N_{Sims} N_{Angles} \\ &= 1200 \end{aligned}$$

Since CSRMs have symmetric flux-linkage and phase torque waveforms about the aligned position, only half the electrical cycle needs to be simulated. This cuts the number of simulation steps in half (600 steps). The waveforms can then be mirrored programmatically to create the full 60x20-size LUTs, as shown in Fig. 3.3.

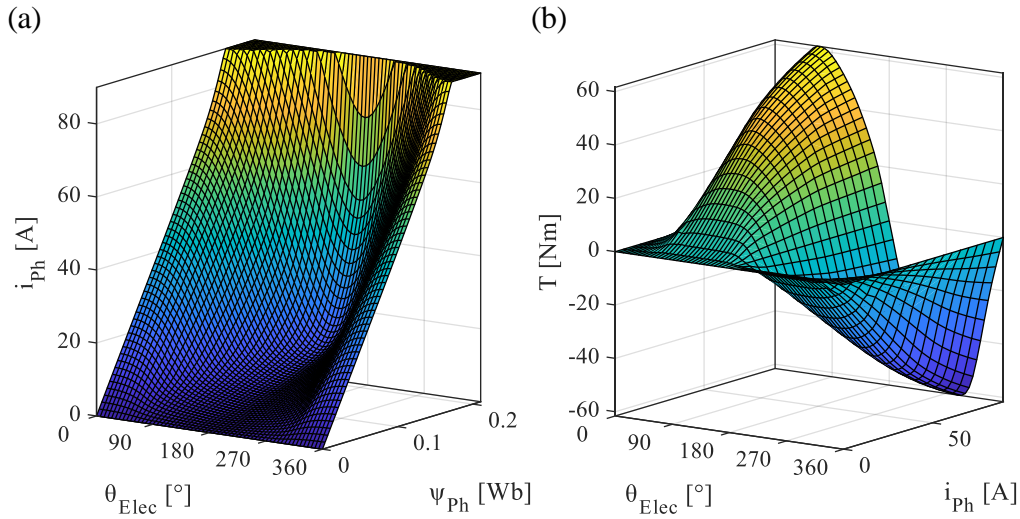


Fig. 3.3 LUTs: (a) phase current; (b) phase torque

## CSRM Dynamic Model

### Equivalent Circuit

The mathematical model is used to represent the relationship between phase voltage and phase current. This relationship is described by the phase voltage equation, as discussed in *Chapter 2*:

$$\mathbf{v}_{Ph} = R_{Ph}\mathbf{i}_{Ph} + \frac{d\boldsymbol{\psi}_{Ph}}{dt}$$

It is possible to rearrange this equation into two forms:

$$\text{Derivative Form: } \mathbf{i}_{Ph} = \frac{1}{R_{Ph}} \left( \mathbf{v}_{Ph} - \frac{d\boldsymbol{\psi}_{Ph}}{dt} \right)$$

$$\text{Integral Form: } \boldsymbol{\psi}_{Ph} = \int (\mathbf{v}_{Ph} - R_{Ph}\mathbf{i}_{Ph})dt$$

The derivative form can use the  $\boldsymbol{\psi}_{Ph}$  LUT in Fig. 3.3(a) directly, whereas the integral form requires that the LUT be inverted ( $\boldsymbol{\psi}_{Ph} \rightarrow \mathbf{i}_{Ph}$ ). The inversion adds some complexity, but improves the robustness of the model, as derivative use is



avoided. Since derivatives amplify noise in a dynamic system, the integral form is preferred.

### ***LUT Inversion***

The LUTs in Fig. 3.3(a) have been inverted, to be effectively used in the mathematical CSRMs model. The goal of this inversion is to complete the transformation:

$$\boldsymbol{\psi}_{Ph_{LUT}}(\boldsymbol{\theta}_{Elec}, \mathbf{i}_{Ph}) \rightarrow \mathbf{i}_{Ph_{LUT}}(\boldsymbol{\theta}_{Elec}, \boldsymbol{\psi}_{Ph})$$

This process is typically conducted programmatically, and is explored in detail in [7].

### ***Full Model***

After inverting the flux-linkage LUT, it is possible to implement the integral form of the phase voltage equation into the dynamic model. Either a continuous or discrete time implementation can be used for dynamic modelling. In the real system, the current controller is implemented on a digital microcontroller that controls the converter switches. Other parts of the system also have discrete sampling rates (i.e. current sensors), and thus the use of discrete-time modelling is intuitive. When considering the discrete time case, the integral form of the equivalent circuit becomes:

$$\boldsymbol{\psi}_{Ph}(k) = \boldsymbol{\psi}_{Ph}(k - 1) + [\mathbf{v}_{Ph}(k) - R_{Ph}\mathbf{i}_{Ph_{LUT}}(k)]T_s$$

where:

$$k = \text{discrete} - \text{time step \#}$$

$$T_s = \text{discrete – time sampling period [s]}$$

This equation can be implemented in an algebraic loop, using the inverted LUT  $i_{Ph_{LUT}}$ , as illustrated in Fig. 3.4.

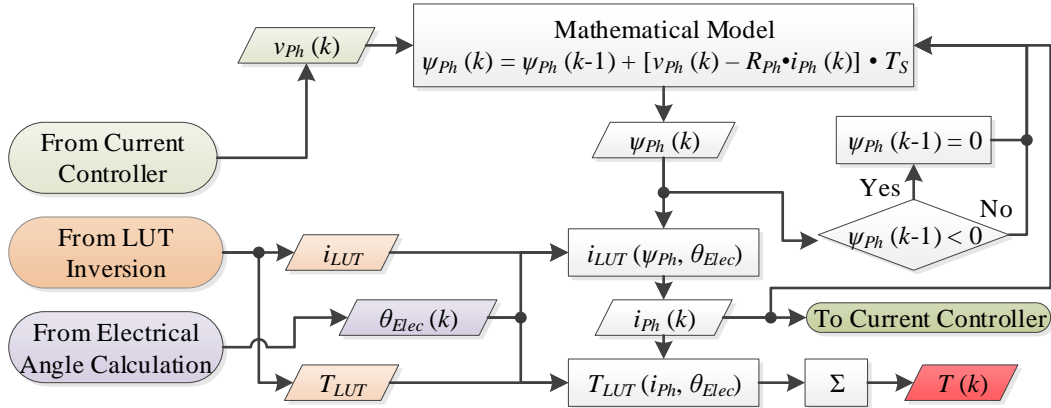


Fig. 3.4 CSRMM mathematical model algebraic loop

When the full current control system (Fig. 2.22) is considered, the dynamic model acts as the plant. This full system can be modelled as shown in Fig. 3.5.

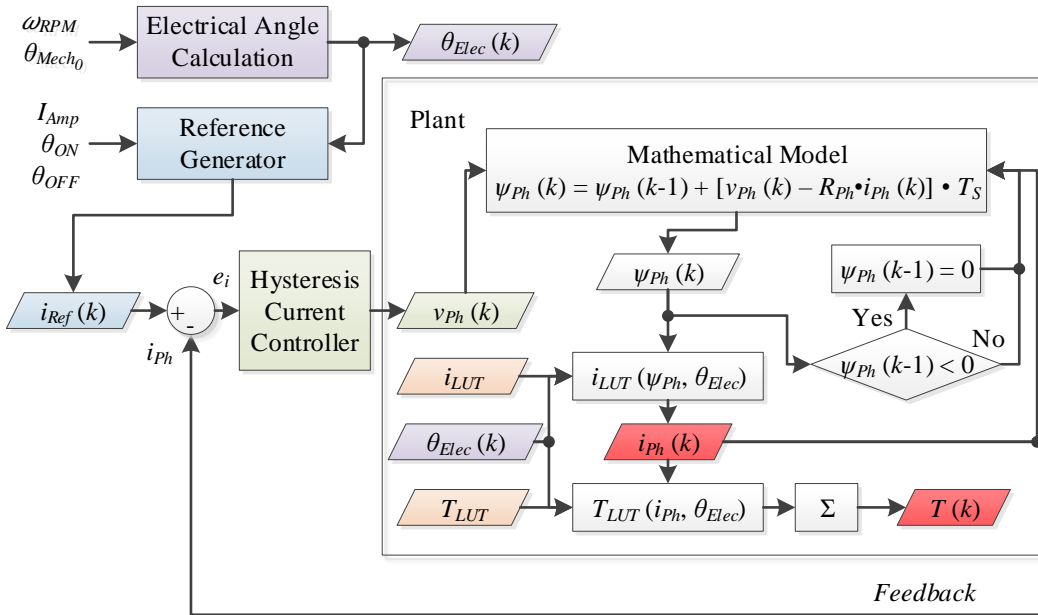


Fig. 3.5 CSRMM model implemented in control loop

## MCSRMs

With MCSRMs, the behavior of one phase is significantly impacted by the other phases. Thus, multiple phases must be excited simultaneously during the characterization to account for all mutual effects. This makes FEA characterization far more complex, with more excitation cases that need to be analyzed. The MCSRm is primarily modelled in the  $dq$ -reference frame. Phase transformations to and from the  $dq$ -reference frame are detailed in *Appendix A*.

### FEA Characterization

The critical non-linear parameters that require LUTs are the phase flux-linkage and torque output, just like the CSRm. The FEA characterization process is highlighted in Fig. 3.6.

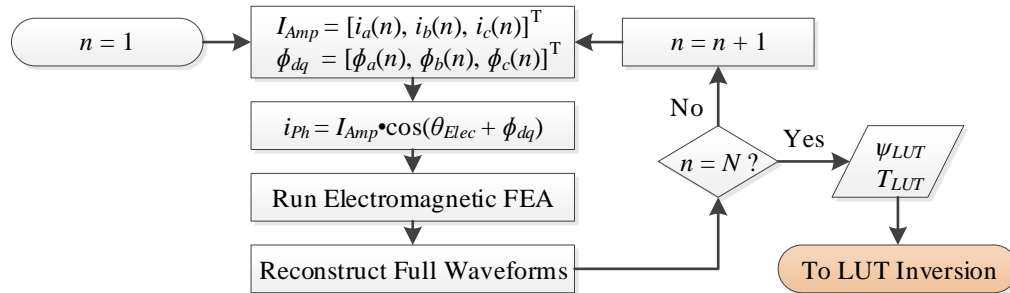


Fig. 3.6 MCSRm FEA characterization process

Both the torque and flux-linkage vary with rotor position ( $\theta_{Elec}$ ) and phase current ( $i_{ph}$ ), like the CSRm. However, since the mutual coupling must be accounted for, the parameters vary with  $i_{ph}$  for all phases. Thus, instead of having 2D LUTs for flux-linkage and torque like the CSRm, the MCSRm requires

$(1+N_{ph})$ -dimension LUTs. Using two current points and two position points as an example, the CSRMs had a 2x2 LUT matrix. With the MCSRM, these matrices are far more complex. Considering the same scenario, if:

$$N_{ph} = 3$$

$$\boldsymbol{\theta}_{Elec} = [0, 180]$$

$$\boldsymbol{i}_{ph} = [-20, 20]$$

then the FEA simulation matrix would be much larger, as shown in TABLE 3.2.

FEA Sim. #	FEA Step #	$\theta_{Elec_1}$	$i_1$	$i_2$	$i_3$	$\psi_{PhLUT}$	$T_{PhLUT}$
1	1	0	-20,	-20,	-20,	$sim_{1,1}$	
	2	180				$sim_{1,2}$	
2	1	0	-20,	-20,	20	$sim_{2,1}$	
	2	180				$sim_{2,2}$	
3	1	0	-20,	20	-20,	$sim_{3,1}$	
	2	180				$sim_{3,2}$	
4	1	0	-20,	20	20	$sim_{4,1}$	
	2	180				$sim_{4,2}$	
5	1	0	20	-20,	-20,	$sim_{5,1}$	
	2	180				$sim_{5,2}$	
6	1	0	20	-20,	20	$sim_{6,1}$	
	2	180				$sim_{6,2}$	
7	1	0	20	20	-20,	$sim_{7,1}$	
	2	180				$sim_{7,2}$	
8	1	0	20	20	20	$sim_{8,1}$	
	2	180				$sim_{8,2}$	

TABLE 3.2 MCSRM FEA simulation matrix ( $N_{Current} = 2, N_{Angles} = 2$ )

The simulation matrix in TABLE 3.2 only reflects the use of two current levels and two positions. In practice, a matrix with 10 current levels and 60 electrical positions typically provides good fidelity. Using these constraints, the final LUTs would be 60x10x3 in size, and the number of simulation steps would be:

$$N_{Sims} = N_{Current}^{N_{Ph}}$$

$$= 1000$$

$$N_{Steps} = N_{Sims} N_{Angles}$$

$$= 6000$$

However, the simulation matrix can be simplified assuming sinusoidal current and using  $dq$ -theory. The use of  $dq$ -theory implies that the phase shift between sinusoidal phase current waveforms is fixed, which is valid considering the Y-connected phases and full-bridge inverter. This significantly reduces the number of required simulations, as the amplitude for each phase is fixed. It also allows the relation between fields to be expressed as an angle ( $dq$ -excitation angle). Thus, the  $(1+N_{Ph})$ -dimension simulation matrix becomes a 3D LUT. Considering the same 3-phase example using  $N_{Current} = 2$  and  $N_{Angles} = 2$ , the LUT size is reduced, as shown in TABLE 3.3.

FEA Sim. #	FEA Step #	$\theta_{Elec1}$	$i_d$	$i_q$	$\psi_{PhLUT}$	$T_{PhLUT}$
1	1	0	-20	-20	$sim_{1,1}$	
	2	180	-20	-20	$sim_{1,2}$	
2	1	0	-20	20	$sim_{2,1}$	
	2	180	-20	20	$sim_{2,2}$	
3	1	0	20	-20	$sim_{3,1}$	
	2	180	20	-20	$sim_{3,2}$	
4	1	0	20	20	$sim_{4,1}$	
	2	180	20	20	$sim_{4,2}$	

**TABLE 3.3 MCSRМ  $dq$  FEA simulation matrix**  
( $N_{Current} = 2, N_{Angles} = 2$ )

Using this method, if  $N_{Current} = 10$  and  $N_{Angles} = 60$ , the finalized LUTs would be  $60 \times 10 \times 2$ , and the number of simulation steps is reduced:

$$\begin{aligned} N_{Sims} &= N_{Current}^2 \\ &= 100 \end{aligned}$$

$$\begin{aligned} N_{Steps} &= N_{Sims} N_{Angles} \\ &= 600 \end{aligned}$$

Since positive and negative  $i_q$  values with the same amplitude have identical results, the simulation matrix can be further simplified, as shown in TABLE 3.4. The full  $60 \times 10 \times 2$  LUTs can then be reconstructed programmatically.

FEA Sim. #	FEA Step #	$\theta_{Elec1}$	$i_d$	$i_q$	$\psi_{PhLUT}$	$T_{PhLUT}$
1	1	0	-20	20	$sim_{1,1}$	
	2	180			$sim_{1,2}$	
2	1	0	20	20	$sim_{2,1}$	
	2	180			$sim_{2,2}$	

TABLE 3.4 MCSRM  $dq$  FEA simulation matrix - using  $i_q$  symmetry  
( $N_{Current} = 2, N_{Angles} = 2$ )

Using this method, if  $N_{Current} = 10$  and  $N_{Angles} = 60$ , the number of simulation steps is reduced:

$$\begin{aligned} N_{Sims} &= N_{Current} \left( \frac{N_{Current}}{2} \right) \\ &= 50 \end{aligned}$$

$$\begin{aligned} N_{Steps} &= N_{Sims} N_{Angles} \\ &= 300 \end{aligned}$$

If the FEA waveforms are mirrored around the aligned position instead of calculating the full electrical cycle, the number of steps is cut in half, with 150 total steps. The waveforms can then be mirrored programmatically to create the full 60x10x2 LUTs.

Since the LUTs are 3D (requiring a 4D graph), they are difficult to illustrate graphically. Therefore, the LUTs are displayed here at a fixed electrical angle, to reduce them to a 2D plots for illustration purposes only. The  $dq$  current LUTs at an arbitrary electrical angle of  $60^\circ$  are shown in Fig. 3.7, and the torque LUT is shown in Fig. 3.8.

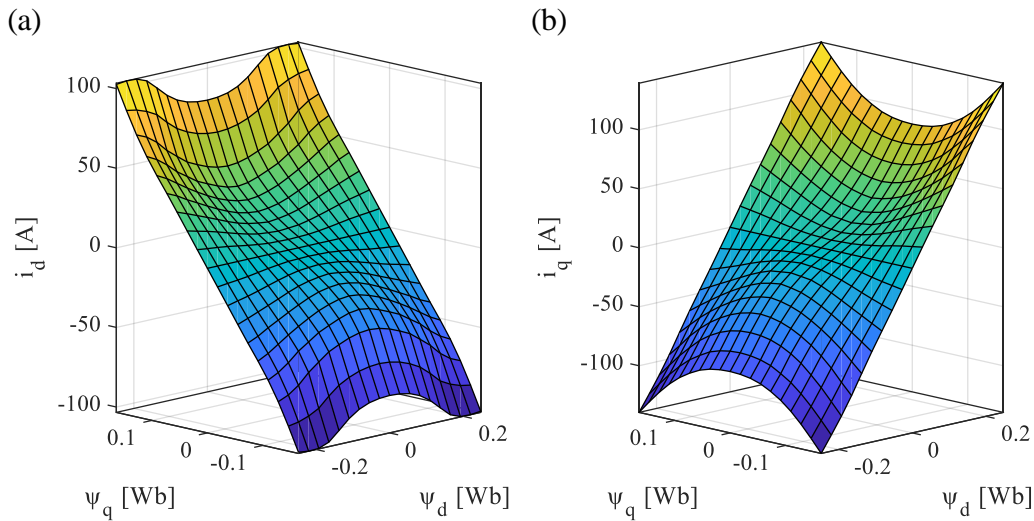


**Fig. 3.7 LUTs (sliced @  $60^\circ$  elec.): (a) d-axis current; (b) q-axis current**



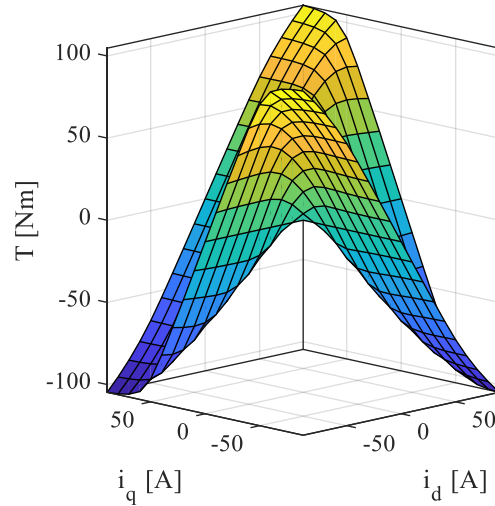


Fig. 3.8 Torque LUT (sliced @ 60° elec.)

## MCSRМ Dynamic Model

### *Equivalent Circuit*

Just like the CSRМ, the integral form of the voltage equation is used to describe the relationship between phase voltage, flux-linkage, and current:

$$\psi_{Ph} = \int (v_{Ph} - R_{Ph} i_{Ph}) dt$$

However, this equation is applied in the  $dq$ -reference frame, to simplify its implementation:

$$\psi_{dq} = \int (v_{dq} - R_{Ph} i_{dq}) dt$$

### *LUT Inversion*

The LUTs in Fig. 3.7 has been inverted in order to be effectively used in the mathematical MCSRМ model. The goal of this inversion is to complete the transformation:

$$\boldsymbol{\psi}_{dqLUT}(\boldsymbol{\theta}_{Elec}, i_d, i_q) \rightarrow \mathbf{i}_{dqLUT}(\boldsymbol{\theta}_{Elec}, \psi_d, \psi_q)$$

This process is typically conducted programmatically, and is explored in detail in [7].

### Full Model

The discrete time form of the equivalent circuit equation is:

$$\boldsymbol{\psi}_{dq}(k) = \boldsymbol{\psi}_{dq}(k-1) + [\mathbf{v}_{dq}(k) - R_{Ph}\mathbf{i}_{dqLUT}(k)]T_s$$

This equation can be implemented in an algebraic loop, using the inverted LUT  $\mathbf{i}_{dqLUT}$ , as illustrated in Fig. 3.9.

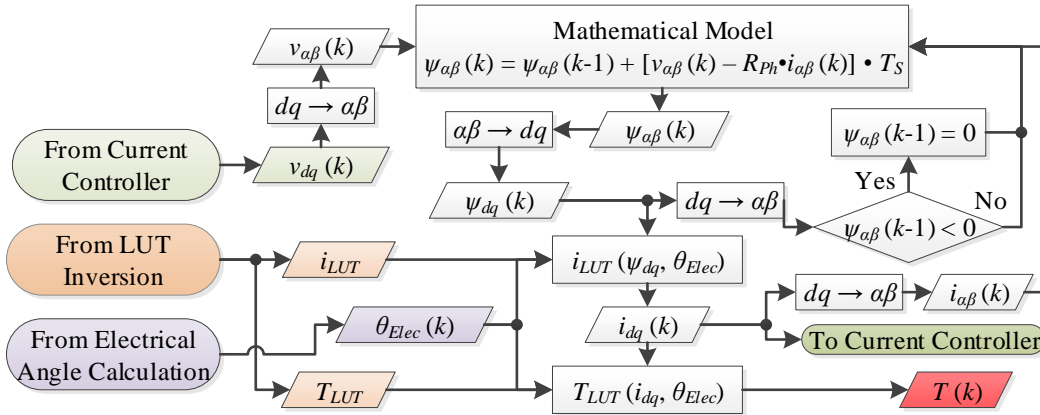


Fig. 3.9 MCSR mathematical model algebraic loop

When the full current control system (Fig. 2.22) is considered, the dynamic model acts as the plant. This full system can be modelled as shown in Fig. 3.10.

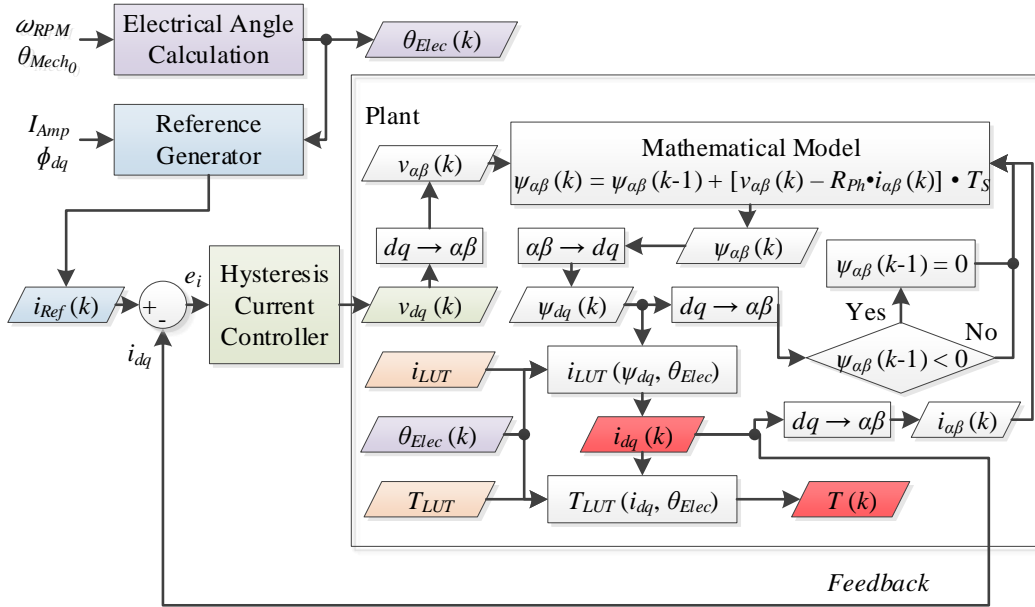


Fig. 3.10 MCSRM model implemented in control loop

## Additional Modelling

### Electrical Angle Calculation

Using the initial mechanical position ( $\theta_{Mech_0}$ ) as an input, the mechanical angle for an open-loop speed control model can be calculated:

$$\theta_{Mech}(k) = \theta_{Mech_0} + \omega_{RPM} \left( \frac{360^\circ}{60 S} \right) T_s k$$

where:

$$\theta_{Mech} = \text{mechanical angle } [^\circ]$$

$$\omega_{RPM} = \text{mechanical speed } [RPM]$$

$$T_s = \text{simulation sampling period } [s]$$

$$k = \text{simulation step \#}$$

Using  $\theta_{Mech}$ , the electrical angles can be calculated for the respective machine type, using the formulae from **Chapter 2**.

### **Current Reference Modelling**

The current reference ( $i_{Ref}$ ) must be generated to provide a target current signal for the current controller:

#### **CSRM**

*if*  $\theta_{ON} < \theta_{Elec}(k) \leq \theta_{OFF}$ :

$$\mathbf{i}_{Ref}(k) = I_{Amp}$$

*otherwise:*

$$\mathbf{i}_{Ref}(k) = 0$$

#### **MCSRM (Sine-Wave)**

$$\mathbf{i}_{Ref}(k) = I_{Amp} \sin(\theta_{Elec}(k) + \phi_{dq})$$

*where:*

$$\mathbf{i}_{Ref} = \text{reference phase current waveform}[A]$$

$$I_{Amp} = \text{reference current amplitude} [A]$$

$$k = \text{simulation step \#}$$

## Summary

In this chapter, the modelling process for SRMs and MCSRMs is explained in detail. These machines have highly non-linear behavior that necessitates the use of electromagnetic FEA to analyze them, which works well for current-source analyses. However, if the converter current control and motor dynamics are to be analyzed, a switched voltage-source FEA analysis is required, which can be impractical due to high computation time, particularly at higher sampling frequencies.

Dynamic models are developed for the CSRMs (no-mutual coupling) and MCSRMs (heavy mutual coupling) respectively, to address this challenge. FEA is only used to characterize the non-linear behavior of these motors and create both flux-linkage and torque LUTs. Once the LUTs are created, they can be used in conjunction with mathematical models, to accurately model the non-linear dynamic behavior of each machine under voltage-source control. Dynamic modelling is particularly useful when multiple current-speed points are being analyzed and for control optimization problems.

# Chapter 4

## E-Bikes and Their Propulsion

### Introduction

Switched reluctance motors are potentially suitable for several different applications, including different traction applications. However, the low torque ripple, high torque density, and high efficiencies required for traction applications provide a challenging set of requirements for a CSRSM or MCSRSM to achieve. This was desirable, as it allows for the capabilities of the CSRSM and MCSRSM to be fully evaluated at the machine limits. In this research, an external-rotor direct-drive e-bike application was chosen for the motor target for the following reasons:

- Challenging to compete with PMSM for low speed applications, due to excitation penalty
- High torque density and high efficiencies are required
- Low torque ripple is required, but not as critical as for hybrid/electric automobiles
- Must be low-cost – avoiding the use of permanent magnets is highly desirable

This chapter provides a background on the e-bike market and different e-bike types. The final section in this chapter discusses the unique requirements of e-bike motors to provide context to the different design choices made for the prototype motors.

## Electric Bicycle Market

Electric bicycles offer a low-cost personal transportation option to people around the globe. They are vastly more efficient than automobiles for transporting people, primarily because the vehicle mass is very low in comparison. Since e-bikes use electric drive systems, they do not directly create greenhouse gas emissions. If e-bikes were adopted by the general population in city centers, they could help reduce urban pollution and improve air quality. They are also much more compact and maneuverable compared to cars or motorcycles, which is highly beneficial when navigating densely populated areas. These combined factors make the e-bike an excellent option as a secondary vehicle for navigating urban areas, or as a primary vehicle for those who are looking for a low-cost personal transportation option.

The global e-bike market had a projected 35 million unit sales in 2016, most of which were in China [11]. The compound annual growth rate (CAGR) outside China is projected to be strong, at 8.2% between 2016 and 2025 [11]. However, a projected drop in sales in the Chinese market means that the global CAGR is projected to be 0.4% over the same period, as illustrated in Fig. 4.1.

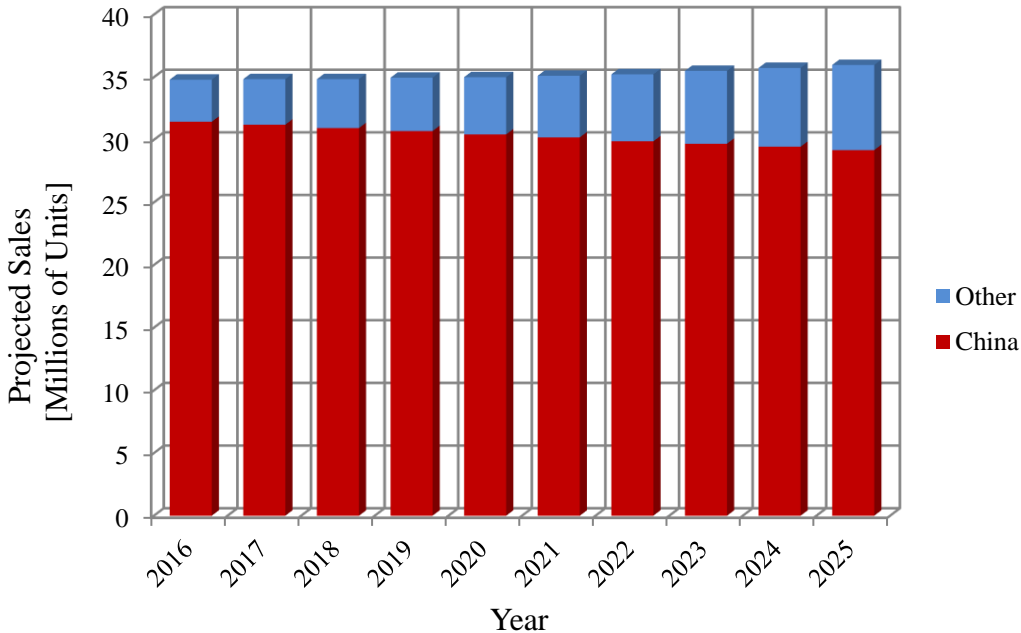


Fig. 4.1 Projected annual global e-bike sales [11]

Markets outside China appear to be largely untapped, particularly in the United States. There is significant potential for growth in several regions as e-bikes start to replace the conventional bicycle market, as shown in Fig. 4.2 [11].



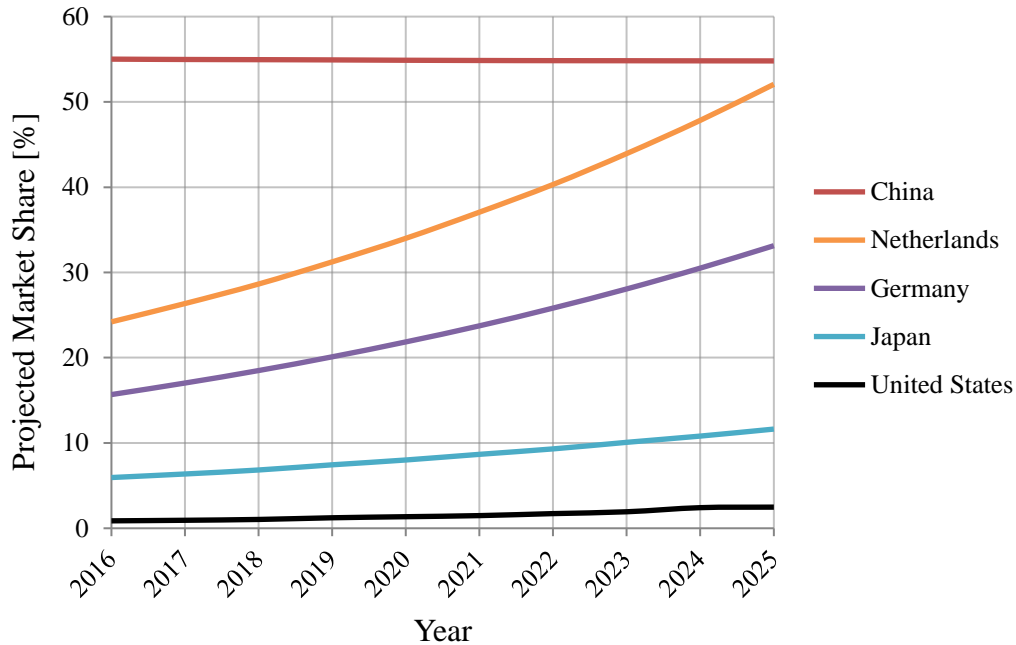


Fig. 4.2 Projected e-bike market share of bicycle market for different regions [12]

## Classification of Electric Bicycles

The official classification and regulation of e-bike specifications varies by country, but restrictions on motor power output and maximum speed are a common theme [12]. In Canada, power-assisted bicycles (e-bikes) are broadly classified under the Motor Vehicle Safety Regulations (C.R.C., c.1038) as having the following characteristics [13]:

- a) has steering handlebars and is equipped with pedals,
- b) is designed to travel on not more than three wheels in contact with the ground,
- c) is capable of being propelled by muscular power,

- d) has one or more electric motors that have, singly or in combination, the following characteristics:
- i. it has a total continuous power output rating, measured at the shaft of each motor, of **500 W** or less,
  - ii. if it is engaged by the use of muscular power, power assistance immediately ceases when the muscular power ceases,
  - iii. if it is engaged by the use of an accelerator controller, power assistance immediately ceases when the brakes are applied, and
  - iv. it is incapable of providing further assistance when the bicycle attains a speed of **32 km/h** on level ground,
- e) bears a label that is permanently affixed by the manufacturer and appears in a conspicuous location stating, in both official languages, that the vehicle is a power-assisted bicycle as defined in this subsection, and
- f) has one of the following safety features,
- i. an enabling mechanism to turn the electric motor on and off that is separate from the accelerator controller and fitted in such a manner that it is operable by the driver, or
  - ii. a mechanism that prevents the motor from being engaged before the bicycle attains a speed of 3 km/h

Note that these classification requirements are for on-road e-bike use, whereas off-road use is not regulated.

## **Types of Power Assist**

E-bike classification varies by country, but fundamentally, there are two types:

### ***1) Pedal Assist (Pedelec)***

With pedal assist systems (PAS), motor power assist is provided when the driver starts pedaling, either in response to pedal torque, pedal speed, or both [14]. This power assist can be applied using different control strategies, each with their own benefits and downsides. Depending on the system, the amount of assist provided in response to the user can also be boosted using an additional throttle [14]. Since pedal assist systems require additional sensors to measure human pedaling input, the systems are more complex and expensive than throttle-on-demand systems.

### ***2) Throttle on Demand***

Throttle-on-demand systems have a separate throttle control that controls motor power output directly.

## **Motor Configurations**

Regardless of the type of e-bike, the drive configuration can be either a mid-drive type, or hub type. In order to illustrate the differences between these setups, a standard bicycle setup without power-assist is presented as a baseline setup (see Fig. 4.3).

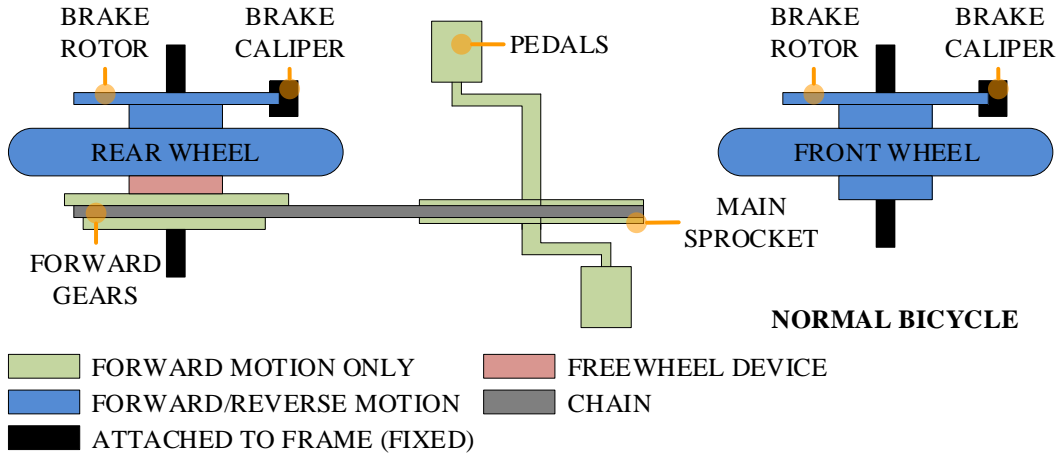


Fig. 4.3 Conventional bicycle layout, with gears, brakes, and freewheel (simplified, top view)

### Mid-Drive Motor Placement

Mid-drive systems may be internally geared and typically attach to the primary pedal sprocket. Additional gears and a derailleur system may be omitted or retained, depending on the intended use of the bike. Fig. 4.4 shows a mid-drive setup with the gearing system retained.

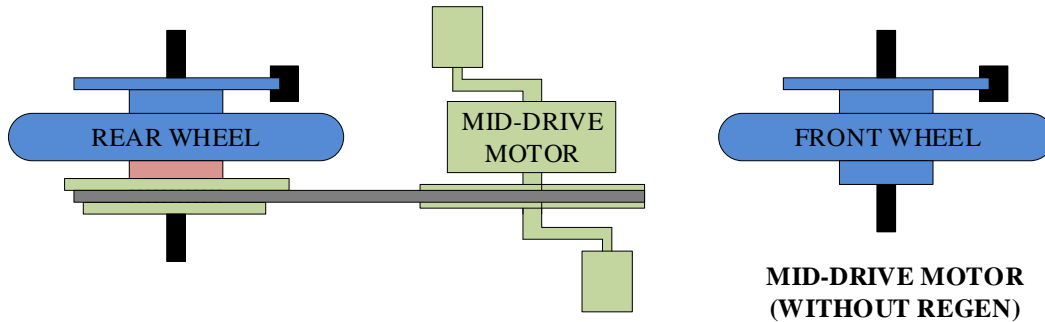


Fig. 4.4 Typical mid-drive e-bike layout, without regen capability (simplified, top view)

Mid-drive setups may use PAS, throttle-on demand, or both. One benefit from this setup is that manufacturers may include the gearing setup, controller, and any sensors required for PAS system in one unit, as shown in Fig. 4.5.

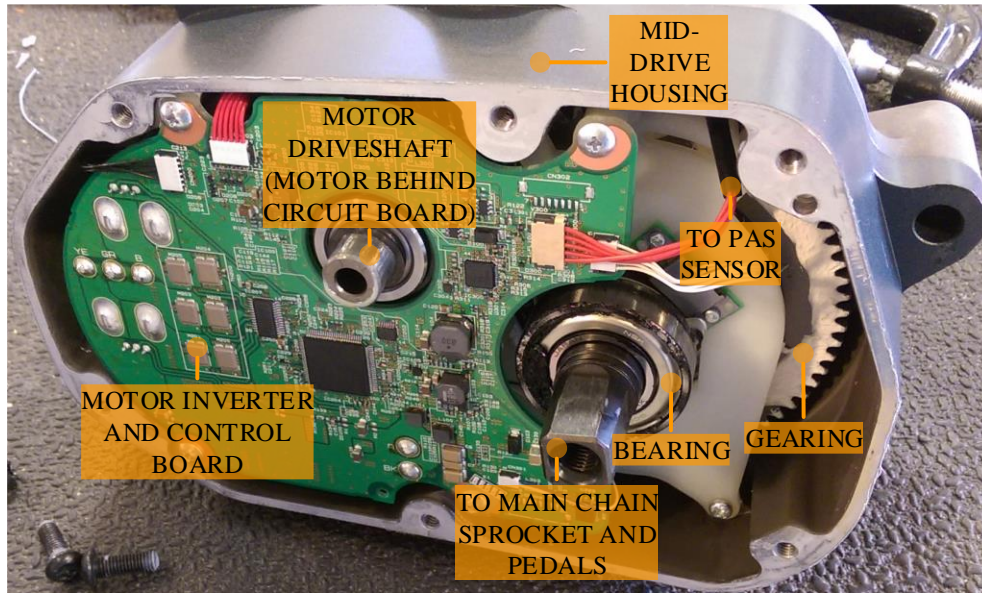


Fig. 4.5 Shimano STEPS mid-drive setup - disassembled

### *Hub Motor Placement*

In contrast, hub-type systems are directly attached to one of the wheels, as shown in Fig. 4.6. They can have an internal planetary gearset, or can be direct-drive. However, since they replace the wheel hub, they cannot use the same gearing system used for human input.

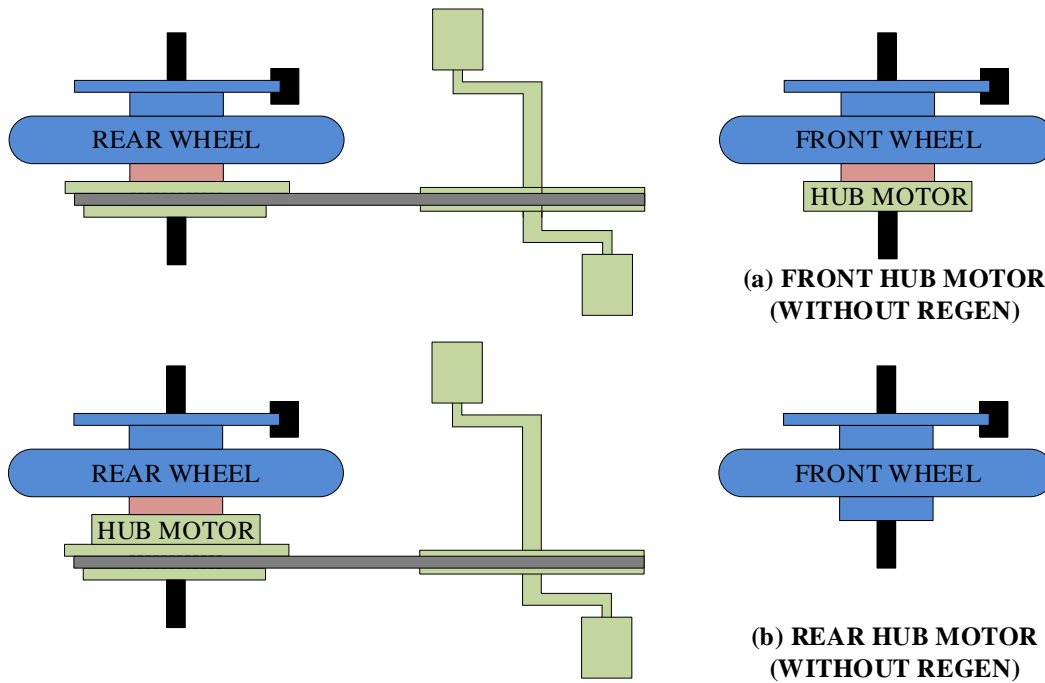


Fig. 4.6 Typical hub motor e-bike layout, without regen capability (simplified, top view): (a) front hub; (b) rear hub

### *Freewheeling and Regenerative Braking*

Most conventional bicycles have a built-in freewheel device attached to the drive wheel to prevent the pedals from spinning with the wheel after the user has stopped forward pedaling. When considering e-bikes, some setups use a freewheeling device and some do not.

If a freewheeling clutch is placed between the drive motor and the wheel, then regenerative braking will be impossible, as the motor has to be capable of being driven by the wheel when motoring torque is withdrawn. However, it is still possible to retain the benefits of a freewheeling device and regenerative braking, depending on where the freewheeling device is placed, as shown in Fig. 4.7.

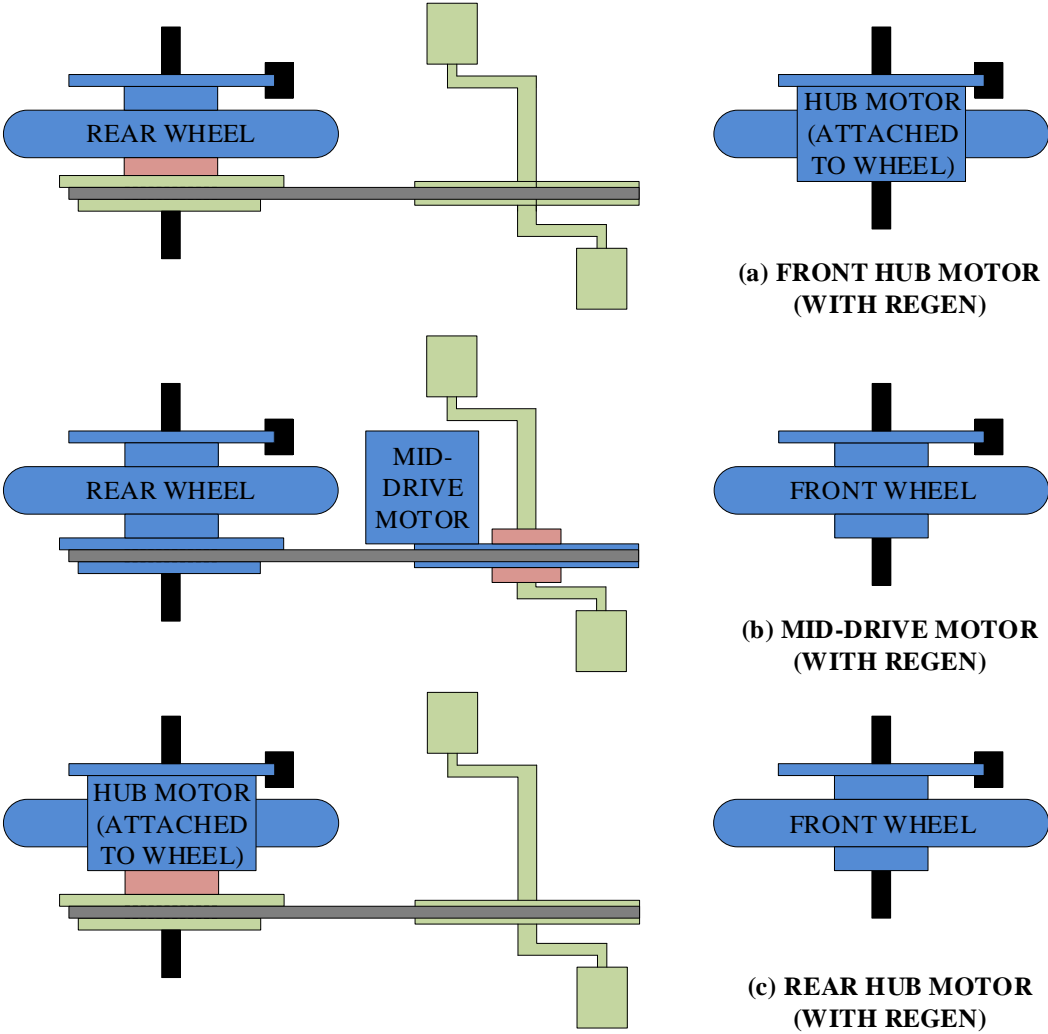


Fig. 4.7 E-bike layouts, with regen capability (simplified, top view): (a) front hub; (b) mid-drive; (c) rear hub

## Motors in Electric Bicycles

### Geared Motors

The use of a gearing system allows the setup to produce the same output torque with a smaller, faster-spinning drive motor. Some of the characteristics of this setup are as follows:

- compact, reduced motor mass
- gearing setup adds cost, but motor cost can be reduced
- complex assembly – more parts
- high speed, low torque motor:
  - lower current and turns - lower copper loss
  - higher iron loss due to a high magnetization frequency at high speed– thinner laminations may be required
  - favors motors with a wide constant power region and high top speed, but lower peak torque
  - if a permanent magnet (PM) motor is used, the required volume of magnets will be reduced; decreasing motor cost (not system cost)

Interior permanent magnet (IPM) motors, such as the “spoke-type” IPM shown in Fig. 4.8, are well suited for this application. Depending on how the power assist is implemented, the IPM can be designed to have a large constant power region, or a large constant torque region. The IPM in Fig. 4.8 is designed to provide constant torque assist for a mid-drive setup, with a small constant-power region.



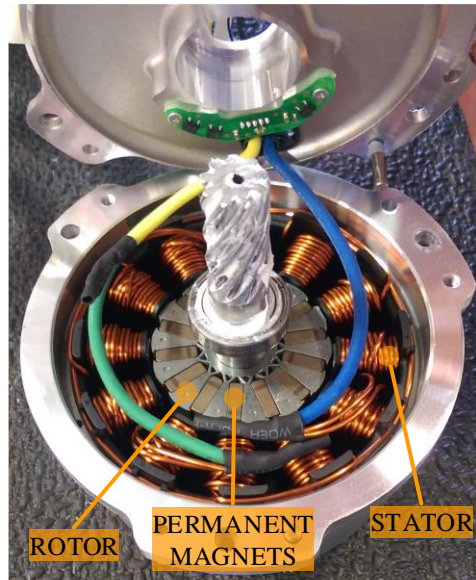


Fig. 4.8 “Spoke-type” IPM motor from Shimano STEPS mid-drive

IPM machines typically provide high torque density for a compact package, but also have the potential for an extended speed range capability due to additional reluctance torque afforded by burying the permanent magnets in the rotor. Therefore, an IPM can also be designed to have a large constant power region, which is beneficial for hub setups, as it helps eliminate the requirement for multiple forward gears at high speed. In addition, if a high gearing ratio is used, the large constant power region can allow for a smaller motor to meet torque requirements at lower speeds. This type of setup would also be a particularly good application for switched reluctance motors, due to their excellent high speed torque production capabilities and wide constant power range.

## Direct-Drive Motors

Direct-drive motors are usually fairly large in diameter to provide high starting torque without a gearing system. They have the following characteristics:

- large, but only one moving part
- low speed, high torque motor:
  - higher current or more turns to increase torque – higher copper loss
  - low iron loss – thicker laminations acceptable
  - favors motors with a narrow constant power region and top speed, but a high stall torque, for hill starts/acceleration
  - high torque quality required – little mechanical damping

This is a suitable application for surface permanent magnet (SPM) motors, since a wide constant power range is not required, and they have good torque quality. An example e-bike SPM motor is shown in Fig. 4.9.

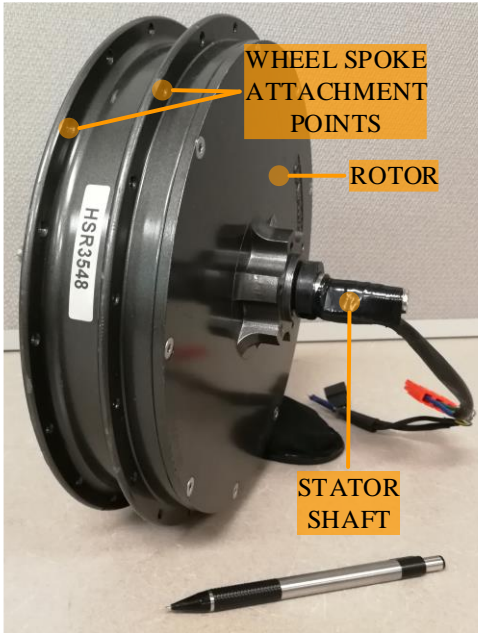


Fig. 4.9 Direct-drive SPM e-bike motor - Crystalyte HS3548

However, the use of a SPM motor for this application typically requires a significant amount of rare earth PM material, as shown in Fig. 4.10. This can increase motor cost, which is a critical factor for e-bikes.

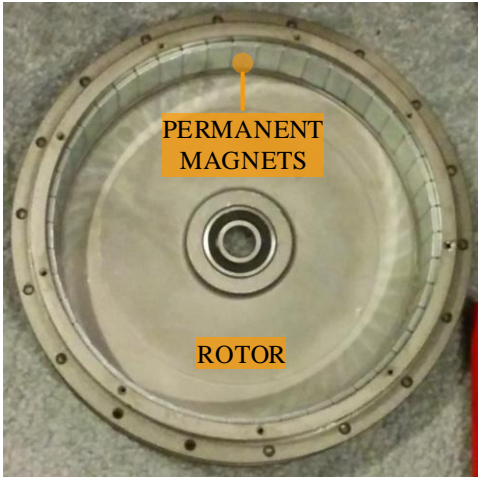


Fig. 4.10 Permanent magnet material in SPM rotor - Crystalyte HS3548

Switched reluctance motors offer a low-cost alternative for this application, as the rare earth permanent magnets are eliminated. However, an SRM would have to be very carefully designed to meet the torque density and torque ripple requirements of this application.

The mutually coupled switched reluctance motor shares the same torque ripple challenges as the CSRSM, but has the potential to produce a higher stall torque at the expense of high speed torque performance. Considering this, it may be better suited for this application than the conventional SRM. In addition, it can be fed with conventional inverters that are already commonly available for the e-bike market.

## Summary

In this chapter, the e-bike market is outlined, showing slow global growth rate, but good growth potential for markets outside China. E-bikes are expected to gradually replace conventional bicycles in several markets.

The classification of e-bikes is outlined, along with e-bike restrictions as defined by Canadian legislation. Among other requirements, Canadian legislation limits the maximum e-bike speed to 32 km/h, and the maximum sustained motor power to 500W. The differences between pedal assist and throttle on demand systems are discussed as a means to classify e-bikes.

Several different e-bike configurations are outlined, including general mid-drive systems and hub-drive systems, with or without gearing. The effects of freewheel placement on regenerative braking capability are also illustrated. Finally, basic motor characteristics for both geared and direct-drive setups are summarized.

# Chapter 5

## Target Definition: Commercial Surface-Mounted Permanent Magnet E-Bike Motors

### Introduction

In order to provide a benchmark to compare the CSRSM and MCSRM designs to, a commercially available exterior-rotor direct-drive surface permanent magnet synchronous motor (SPMSM) was purchased. This is a Crystalyte HS3548 motor, which was purchased from Grin Technologies, along with a matched inverter. Grin Technologies provides detailed motor performance information, but the motor was subjected to additional analysis and testing to ensure that the performance benchmark is accurate. In this chapter, the results from the distributor specifications, 2D electromagnetic FEA, and dynamometer testing are analyzed and compared.

### OEM Specifications

The distributor's motor performance specifications are detailed in TABLE 5.1 and the OEM inverter specifications are outlined in TABLE 5.2.

<b>PMSM Parameters</b>	
Manufacturer	Crystalyte
Model	M3548R (HS3548)
Retailer	Grin Technologies
Weight [kg]	7.47
Flange Spoke Diameter [mm]	232
Motor EMF [RPM/V]	13
Phase Resistance [ $\Omega$ ]	0.084
Magnetic Pole Pairs	23
Magnet Width [mm]	35
Temperature Monitoring	Thermistor
Speed Sensor	Hall Effect

**TABLE 5.1** Crystalyte HS3548 motor - distributor specifications [15]

<b>PMSM Controller Parameters</b>	
Manufacturer	Grin Technologies
Model	C7225-NC 25A
Retailer	Grin Technologies
Dimensions [mm]	105 x 68 x 32
MOSFETs	6 x IRFB4110
Source Voltage [V]	36-72
Source Current [A]	25

**TABLE 5.2** Grin Technologies C7225-NC-25A inverter - OEM specifications [16]–[17]

The distributor of the HS3548 motor provides an online tool [18] to illustrate the torque output, phase current, and efficiency under different speeds and loading conditions (shown in Fig. 5.1).

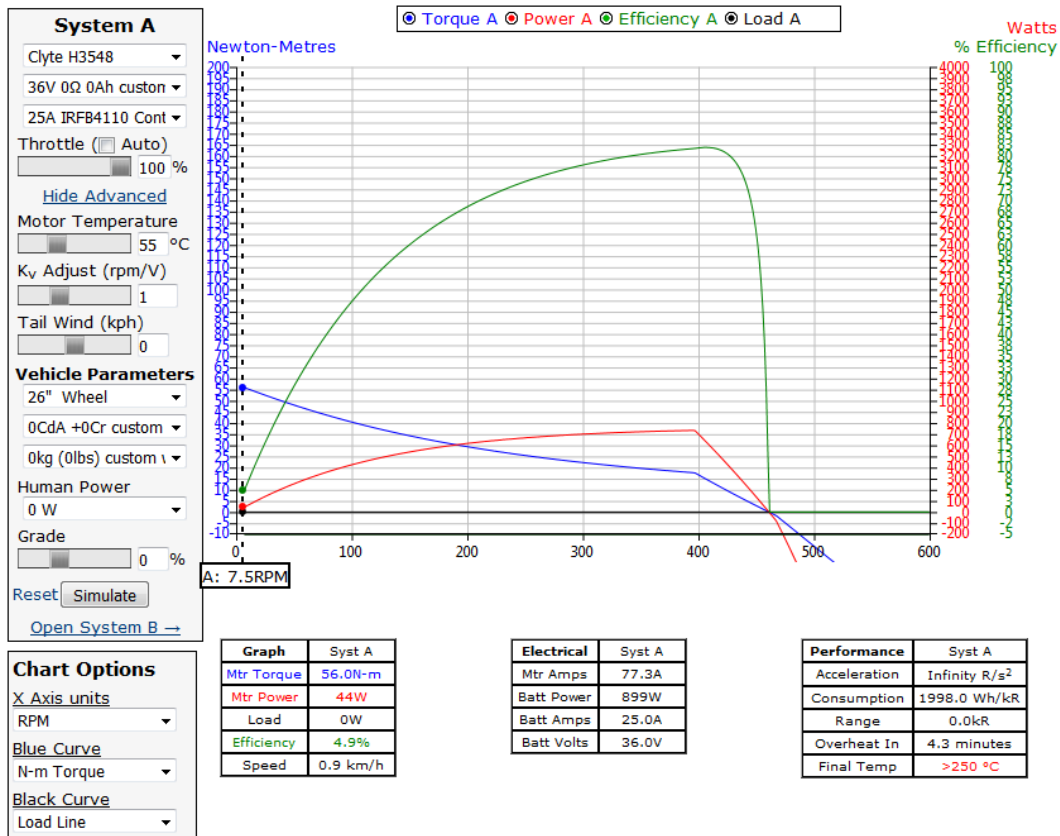


Fig. 5.1 Grin Technologies motor simulator (setup for HS3548) [18]

This tool has been used to recreate the torque-speed map of the PMSM, as detailed in the *Results* section.

## Electromagnetic FEA Modelling

The HS3548 was also disassembled, reverse engineered, and modelled using 2D JMAG electromagnetic FEA. Fig. 5.2 shows the stator of the machine with two phases removed.



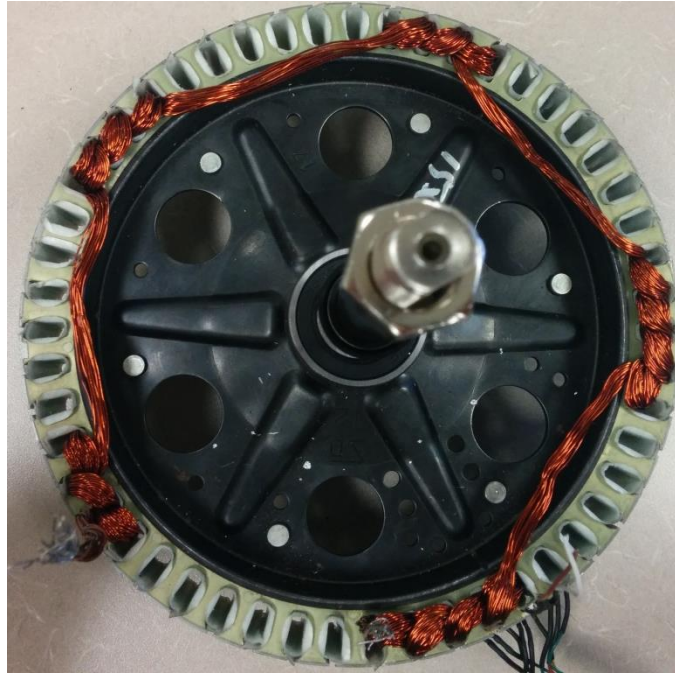


Fig. 5.2 Crystalyte HS3548 PMSM stator (2 phases removed)

The FEA analysis was conducted using sinusoidal current source excitation, at a  $dq$ -excitation angle of  $45^\circ$ . Since this is a current-source analysis, it can only validate the torque output for a given current amplitude. Therefore, the current amplitudes provided by the distributor were input at each speed point to reflect the field weakening performance of this motor. The simulation simplifies the winding so every pole has 3 turns. The rotor/magnet materials that gave the best fit with the distributor curves were selected. Iron loss is neglected for this analysis. The FEA model at maximum current is shown in Fig. 5.3.

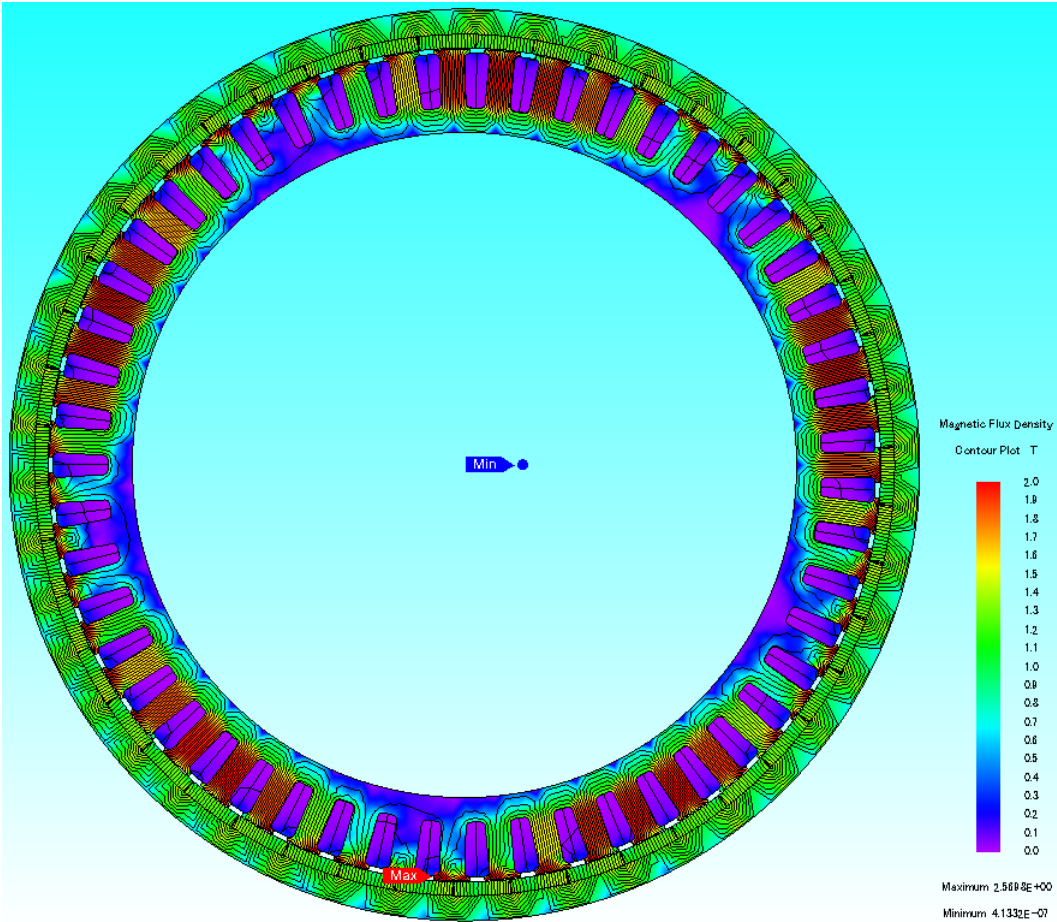


Fig. 5.3 Simplified 2D JMAG FEA model of the Crystalyte HS3548 motor

The results of the 2D FEA analysis are compared against the OEM and dynamometer results, in the *Results* section.

## Dynamometer Testing

### Dynamometer Specifications

The PMSM was tested using a custom dynamometer setup, as shown in Fig. 5.4 and Fig. 5.5.

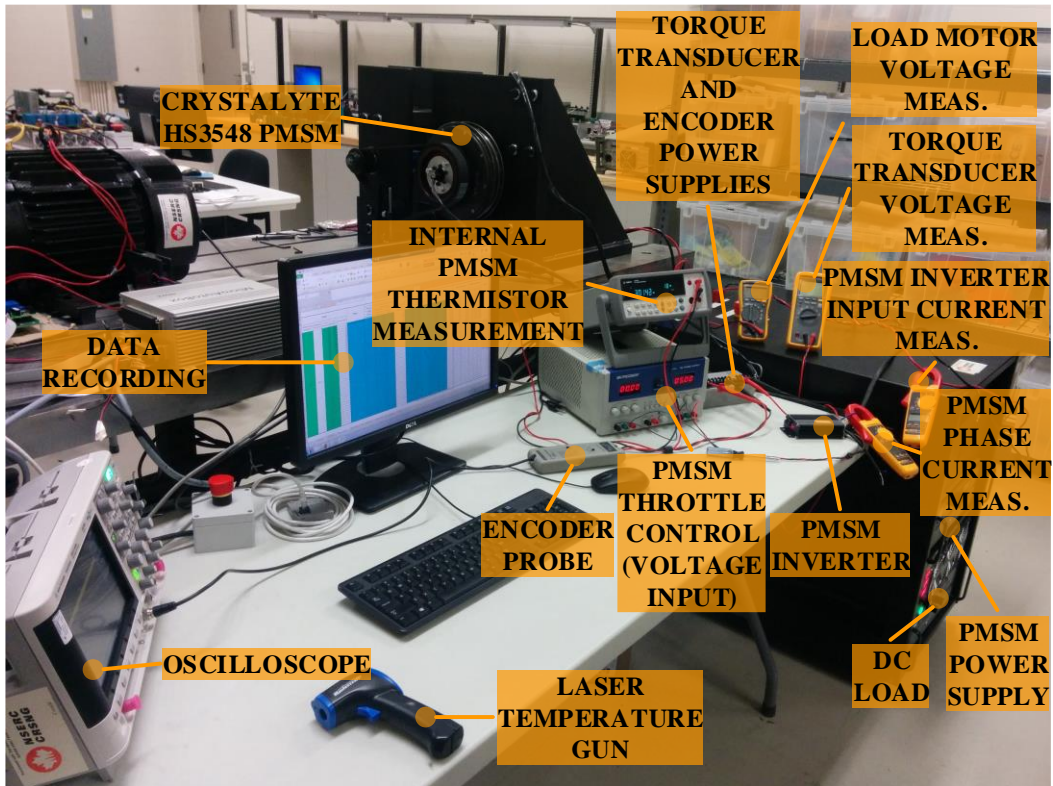


Fig. 5.4 PMSM dynamometer testing setup

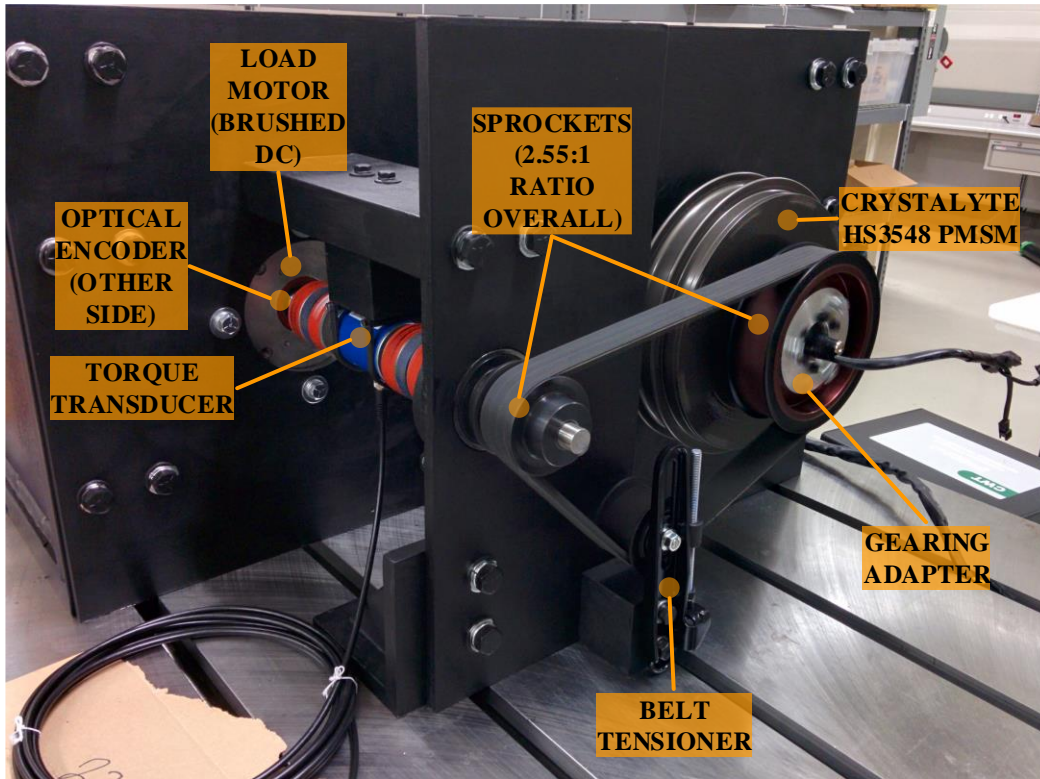


Fig. 5.5 PMSM dynamometer testing setup - detail view

### Testing Procedure (Condensed)

- 1) Record torque sensor reference voltage with the motor turned off.
- 2) Calibrate laser temperature gun emissivity with thermocouple (against PMSM exterior surface).
- 3) Note cold motor internal thermistor resistance and temperature from external hand-held thermocouple in ambient air. This is used as the initial temperature for the motor interior (assumed to be ambient).
- 4) Supply PMSM inverter with 36 V (constant) and limit current draw to 25 A.

- 5) Run PMSM at maximum throttle voltage (maximum speed) until the internal temperature has reached steady state; note this value.
- 6) Apply constant current DC load to brushed DC machine (dynamometer) load.
- 7) Wait for speed to reach steady state.
- 8) Record encoder pulse frequency, torque sensor output voltage, PMSM inverter supply current, and PMSM RMS phase current. Use laser temperature gun to record external surface temperature of PMSM and DC machine. Also record thermistor resistance (not steady state, as high loads will continue to heat up the coils).
- 9) Remove DC load.
- 10) Wait for PMSM to cool off and reach within  $+10^{\circ}\text{C}$  of steady state temperature.
- 11) Repeat steps 7-10 until the entire torque speed map is recorded. The DC load current is increased in 5 A increments until the motor stalls.

## **Calibration and Sources of Error**

The torque sensor is known to have a drifting reference voltage if the setup is bumped or otherwise disturbed. Therefore, it is important to calibrate the sensor if the absolute torque output is to be relied upon. The transducer is calibrated from the factory, but it is still advisable to check the calibration before dynamometer testing. This helps estimate the friction losses in the dynamometer setup itself. One method of testing is to use a calibrated torque wrench on the PMSM side of the

dynamometer setup, at the center of the rotation axis. The static friction torque can then be measured, but the dynamic friction may be much less. Nonetheless this allows a bound to be placed on the error, giving a range of certainty on the results. The torque wrench used for this purpose was able to read a minimum torque value of approximately 6 Nm.

Another point to note is that the center of rotation axis was not the location where the torque wrench was applied; it is slightly offset to make room for the fixed shaft (as this is an exterior rotor machine). However, the overall length of the torque wrench is far larger than this offset, so it is neglected. The machine started to rotate before the torque wrench indicated its minimum torque value of 6 Nm, and thus the total absolute torque sensor error is assumed to be no larger than 6 Nm.

The encoder would ideally have been calibrated with a laser tachometer; however, this was not available at the time. As the optical encoder design is generally robust, any error comes down to signal distortion from cable inductance and EM interference, or may also be due to oscilloscope probe accuracy. These sources of error were found to be small in practice. Though frequency did fluctuate slightly at each speed point, the overall error is small.

A laser temperature gun was used to measure the motor exterior temperature. The emissivity was calibrated to the motor surface finish, by use of a thermocouple that was known to be accurate. The internal motor temperature is measured using a factory-installed thermistor (Fig. 5.6). The initial reference



temperature for the internal thermistor is calibrated against another thermocouple that was known to be accurate.



Fig. 5.6 Factory-installed thermistor location

If the motor internal temperature surpassed the steady state temperature by a maximum of around  $10^{\circ}\text{C}$ , then it was allowed to cool off, as shown in Fig. 5.7. This prevented the phase resistance from changing significantly, affecting the phase voltage drop, and thus reducing the maximum speed of the motor during testing.

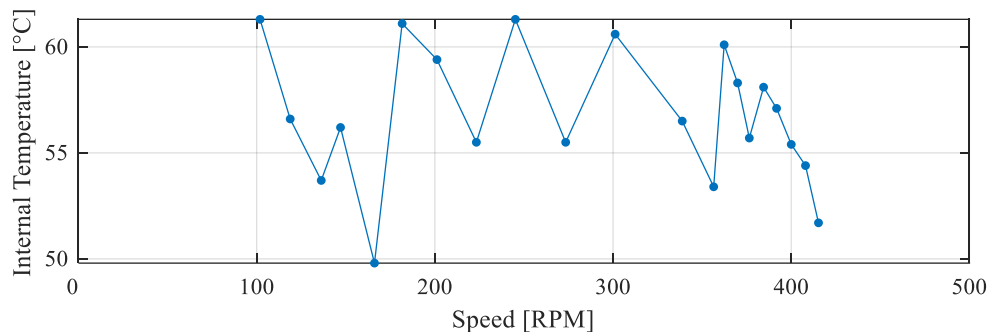


Fig. 5.7 Temperature calculated from internal thermistor

## Results

The dynamometer test results are summarized in this section. Values are compared against distributor specifications (labeled “OE-Spec” in the following figures) and the FEA results, to illustrate and help explain any discrepancies.

As illustrated in Fig. 5.8, the output torque of the PMSM is lower than expected. Both the measured absolute and delta torque values have been plotted in order to illustrate any steady state offset in the torque sensor readings, which may be caused by dynamometer setup losses or mis-calibration. The delta value is referenced to the maximum-speed no-load torque reading. This value was found to be less than the 6 Nm static torque error bound discussed in the *Calibration and Sources of Error* section. This makes sense, as the dynamic friction torque should be smaller than the static friction torque. Since the delta value does not need to be calibrated, it can be relied upon as a known lower bound on the measured torque. The actual PMSM torque is the delta plus any losses in the dynamometer setup between the PMSM and torque transducer, which should remain less than 6 Nm. Thus, we can be reasonably certain that the absolute value is within a few Nm of its true value.



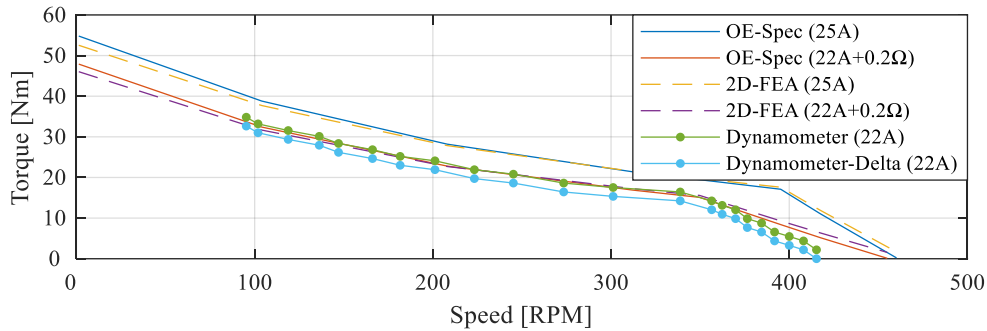


Fig. 5.8 PMSM torque-speed map (with OEM [18], FEA, and experimental curves)

The distributor-supplied data matches with the FEA results well, but the experimental results, while being parallel to these curves, has both a lower base speed and lower torque in general. A critical point to note is that the controller only drew a maximum of 22 A of DC current; not the full 25 A that it was rated at, despite the supply being capable of feeding a much higher current (see Fig. 5.9).

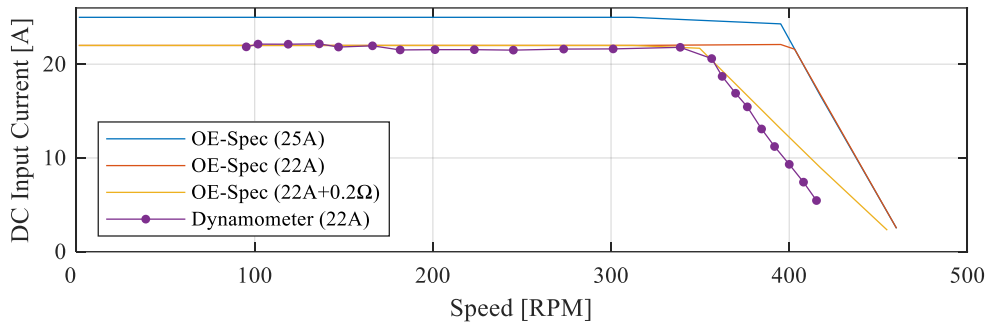


Fig. 5.9 PMSM inverter DC input current (with OEM [18] and experimental curves)

In order to examine the effect of the reduced inverter input current, the distributor results and FEA tests were also run for the reduced input value. The reduction in inverter input current was shown to drop the torque output significantly, and the base speed was now almost identical to the experimental results, but the torque was still higher than the experimental results (see Fig. 5.8).

As the only other factor outside of the manufacturer’s design was the lead cables to the controller, and the connections themselves, a small resistance (0.2 ohm), was added and the results were compared between distributor, FEA, and experimental. After this, the distributor and FEA results matched up well to the test results; though the maximum speed was somewhat lower (partially due to the fact that it was not possible to actually test a zero-torque case – the dynamometer setup does have some parasitic losses).

The motor phase current comparison is shown in Fig. 5.10 and mechanical output power is compared in Fig. 5.11.

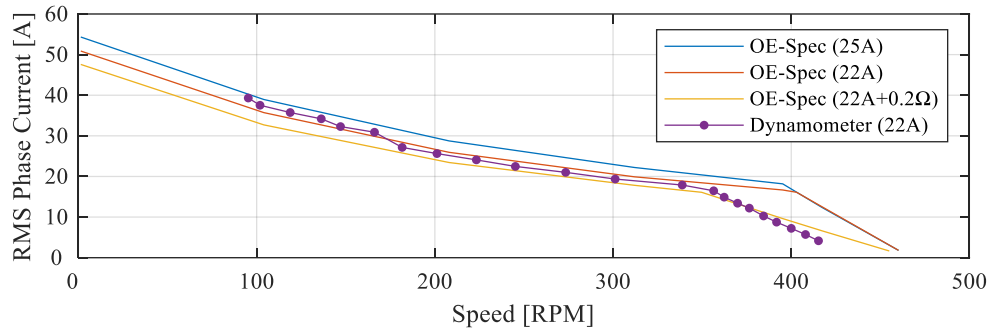


Fig. 5.10 PMSM RMS phase current (with OEM [18] and experimental curves)

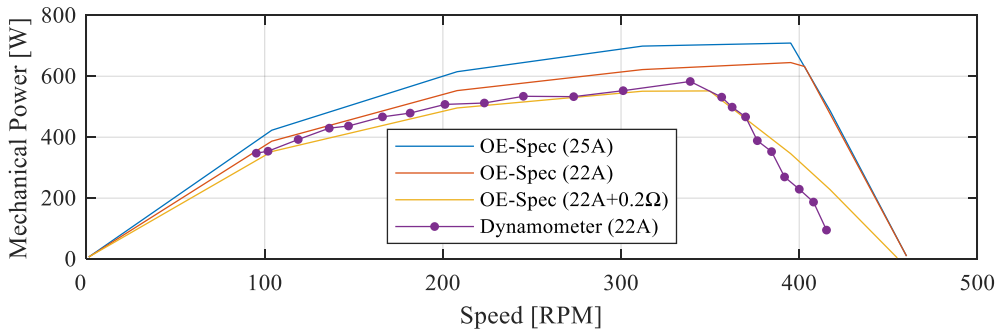


Fig. 5.11 PMSM mechanical output power (with OEM [18] and experimental curves)

Unfortunately, motor testing was terminated before the entire torque-speed map could be recorded. The DC load was not able to pull more than 105 A of current from the load motor, even though it was rated for much more than this. This issue could probably have been resolved, but shortly after hitting this limit, the phase connectors between the PMSM and inverter completely melted due to the high phase current (roughly 40A RMS). The Anderson Powerpole PP45 connectors used from the factory are rated for up to 55A (45A continuous), which seems to indicate that the phase connections were poor from the factory, resulting in excessively high resistance and the melting of the connectors. It does seem that they were sized correctly, as the motor was projected to reach a peak RMS phase current of 55A (from the distributor specifications, see Fig. 5.10). Ultimately, this is the likely cause of the lower machine base speed and torque when compared to that of the 22A FEA results and the results from the distributor.

## Finalized Design Targets

### Torque-Speed Requirements

Although there are discrepancies between the manufacturer specifications and the experimental results, the experimental curves are parallel to the manufacturer and FEA curves. It is expected that, under a given current and phase resistance, the motor would match the respective torque specifications supplied by the motor distributor. Thus, rather than designing to the experimental data, the SRM will be designed to the best-case PMSM performance curves; those provided by the motor distributor (see Fig. 5.12).

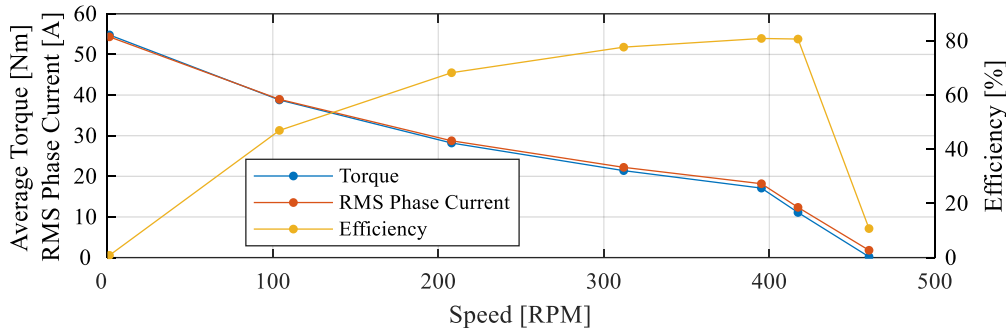


Fig. 5.12 Finalized torque-speed outline design targets [18]

In addition to the torque-speed, RMS current, and efficiency design targets, it is also important to determine the torque ripple design targets throughout the operating range. The current-source FEA model discussed in the *Results* section was also used to create a target RMS net torque ripple map shown in Fig. 5.13. Since a current-source analysis was used, it is important to note that this analysis assumes idealized sinusoidal current waveforms with a constant  $dq$ -excitation

angle of  $45^\circ$ . This is typically the case at low speed, where the motor EMF is low enough that current can be controlled accurately.

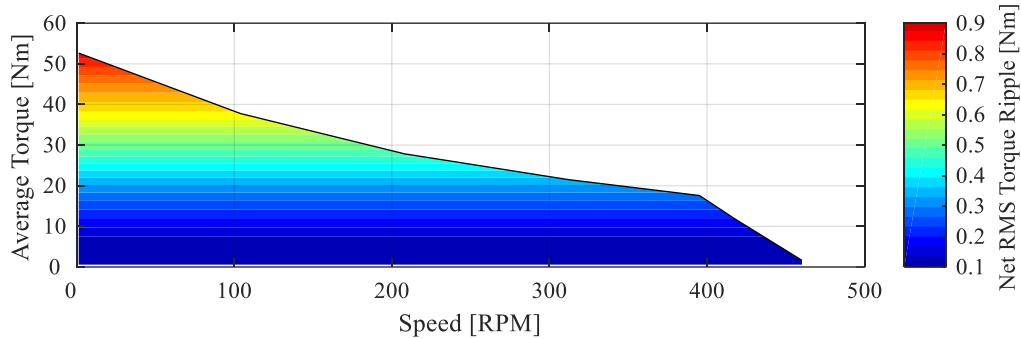


Fig. 5.13 PMSM torque ripple map

### Input Current and Voltage Requirements

Since the SRM is being designed to replace the commercially available PMSM, this completely defines the target specifications. The controller is fed by a DC battery pack, and thus the voltage and current are kept constant between the designs (36 V and 25 A respectively). However, since the PMSM uses a full-bridge converter (Y-configuration), the phase current limit under bucking action is different for the PMSM and SRM. In order to draw a fair and even comparison, the maximum RMS phase current is constrained to be the same (55 Arms), with the DC link voltage set at a constant 36 V.

## Packaging Requirements

The SRM design is constrained to have the same outside dimensions as the PMSM; not only is the volume fixed, but the aspect ratio is as well. The measured PMSM dimensions are summarized in TABLE 5.3.

Measurement	Value [mm]
Machine Type	Exterior Rotor
Exterior Diameter	220
Exterior Axial Length	58
Shaft Diameter (for Stator)	16.5
End Plate Thickness @ Back Iron	4
End Plate Thickness @ Coils	2.75
Axial Length – Rotor Iron	50
Axial Length – Magnets	35
Axial Length – Stator Iron	34.1
Axial Length – Stator Iron + Coils	45
Max Interior Axial Length (Iron)	50
Max Interior Axial Length (Coils)	52.5

TABLE 5.3 Measured HS3548 machine dimensions

One point of note is that the PMSM rotor yoke is made of non-laminated iron, and the rotor end caps are bolted into the back iron (see Fig. 5.14). The rotor stack length is larger than the stator stack length, but the magnets on the rotor are roughly the same length as the stator stack.

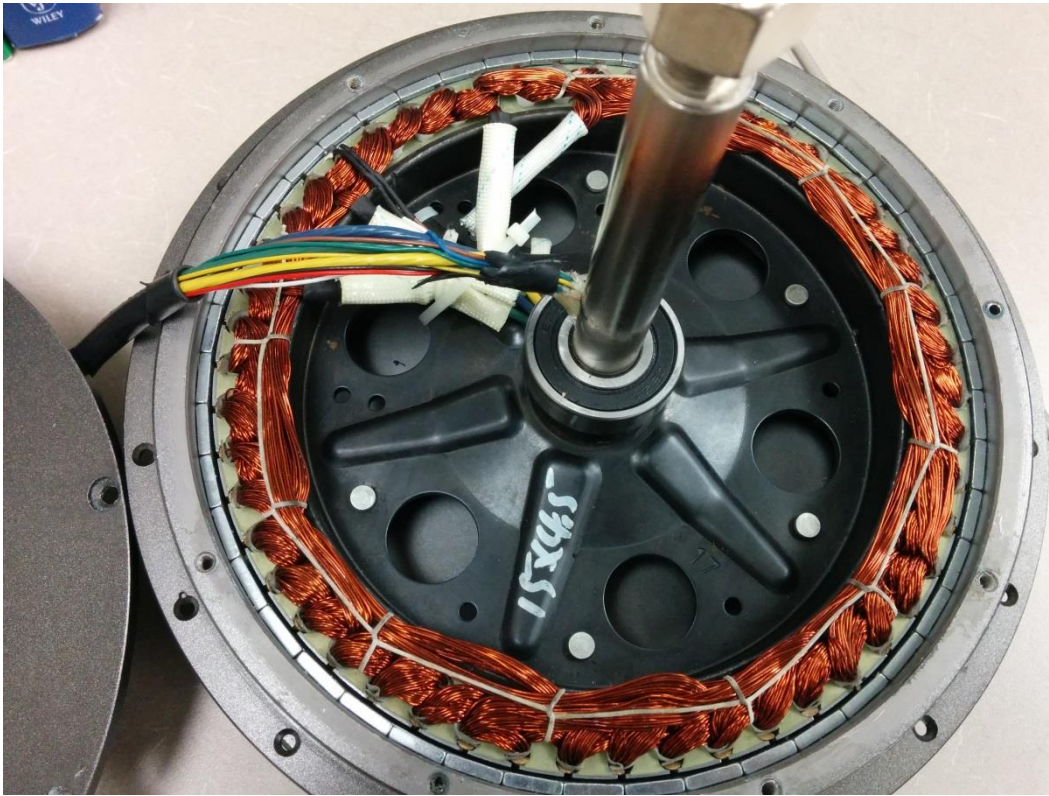


Fig. 5.14 Disassembled Crystalyte HS3548 PMSM

The manufacturer was able to use solid material for the rotor yoke because the rotor flux distribution is dominated by the permanent magnets which are affixed to the back iron; thus the losses are not significantly affected.

In the SRM design, it is desirable to have the highest rotor outside diameter possible and thus this area uses the same laminated iron material as the stator. The use of laminated steel does prevent the rotor from being made of one piece, as the bike spoke supports must be attached to the back iron, but this is not considered to be a major concern.

The finalized geometry constraints for the CSRSM and MCSRSM designs are summarized in TABLE 5.4. It is important to note that the SRM iron stack length

is allowed to exceed that of the PMSM design, as long as the outside dimensions of the machine are fixed. Preliminary analysis did show that the SRM could compete with the PMSM using the same stack length, but the efficiency was able to be significantly improved by using a longer stack length. It was possible to use a longer stack length in the SRM without breaching the packaging constraints, by modifying the shaft and endcap design.

<b>Constraint</b>	<b>Max Value [mm]</b>	<b>Justification</b>
Rotor OD	220	rotor case diameter will use laminated steel (must be drilled for end cap bolts)
Stator ID	16.5	matches shaft diameter
Iron Axial Length	50	maximum allowable inside length of case @ rotor
Iron + Copper Axial Length	52.5	maximum allowable inside length of case @ stator

**TABLE 5.4** Finalized geometry constraints for SRM and MCSRM designs



## Assumptions

As this is for an e-bike application, manufacturing costs must be reasonable, and thus excessively small tolerances (i.e. small airgap) are not feasible. However, some extra manufacturing and material cost is allowable due to the lack of expensive permanent magnets. The cooling strategy must be air cooling as a liquid cooling setup is not feasible for a low-cost e-bike application. All additional assumptions that are used as constraints for the SRM and MCSRM designs are summarized in TABLE 5.5.

Assumption	Value	Justification
Airgap	0.4 mm	excessive manufacturing cost and stiffness requirements if made smaller
Wire Fill Factor	0.6	highest reasonable value (includes wire insulation)
Stacking Factor	0.96	Reasonable, if conservative, given thick laminations
Maximum Coil Wire Strain	0.4	small wire, strain limit of copper should not limit bend radius – tooth geometry should
Coil Connections	Series	high torque, low speed motor – wanted higher current in winding

TABLE 5.5 Additional constraints for SRM and MCSRM designs

## Summary

In this chapter, the torque and RMS current performance of a commercially available exterior rotor e-bike PMSM was analyzed. Two identical motors were purchased, with one being reverse-engineered and modelled in 2D electromagnetic FEA. The other was tested on a dynamometer setup to ascertain the true torque performance of the motor. Both the 2D FEA and dynamometer results were compared against the distributor-supplied performance curves to produce the required performance targets for the SRM and MCSRMs designs.

In addition to the performance targets, the disassembled PMSM was measured to determine the geometry constraints for the motor designs. The iron axial length is allowed to surpass that of the PMSM, but the exterior motor dimensions are not. Finally, any other assumptions made during the motor design process are summarized and justified.

# Chapter 6

## Design of a Non-Coupled Switched Reluctance E-Bike Motor

### Introduction

The non-linear nature of the conventional SRM (CSRSM) makes it challenging to design and a large number of design iterations are typically required. In addition, the non-linearity necessitates the use of computationally expensive finite element analysis for the design process. In *Chapter 3*, methods of modelling the dynamic behavior of these motors were discussed. However, the use of FEA and dynamic modelling for the design process has not yet been discussed. This chapter will outline a general design procedure for both the motor geometry and current control. In addition, the effects of each design parameter will be discussed, and a detailed performance analysis of the final design will be presented.

### Electromagnetics Design

#### Motor Design Process

The design for the conventional SRM was conducted using a design-space exploration method, where each geometry parameter combination was swept. Since it would be computationally expensive to evaluate the dynamic performance of each design case, the first step in the design process uses a series of static 2D FEA analyses. In these static analyses, one phase is excited with constant current at a

fixed rotation speed to determine phase torque and voltage at this speed. This gives the phase torque profile of the motor and a rough indication of the base speed.

The static designs can then be filtered down to a smaller subset of highest performing designs, and a dynamic-current analysis (switched voltage source) can be conducted on those designs using a dynamic model, as shown in Fig. 6.1. The dynamic analysis gives the total torque and phase voltage when phase overlap is accounted for. The result depends on the phase firing angles and accurately reflects the flux weakening behavior under different levels of saturation. The dynamic results can then be compared to determine the best design candidates for each pole configuration. Finally, a sensitivity analysis was conducted on the best dynamically performing design in order to “fine-tune” the parameters.

The pole-arc angles were swept in increments of  $1^\circ$ , rotor pole height was swept in increments of 1 mm, and stator pole height was swept in increments of 25 mm. The rotor back iron thickness ( $b_R$ ) and stator back iron thickness ( $b_S$ ) were conservatively chosen so that the yokes did not significantly saturate during phase excitation overlap. The wire size ( $N_{AWG}$ ) was chosen so that the impact of small geometry changes (i.e. small stator pole-arc angle differences) could be reflected by the number of strands. The number of strands is maximized for each individual design while maintaining a target number of turns and a maximum wire fill factor of 0.6. The number of coil turns ( $N_{Turns}$ ) was varied for all designs, in

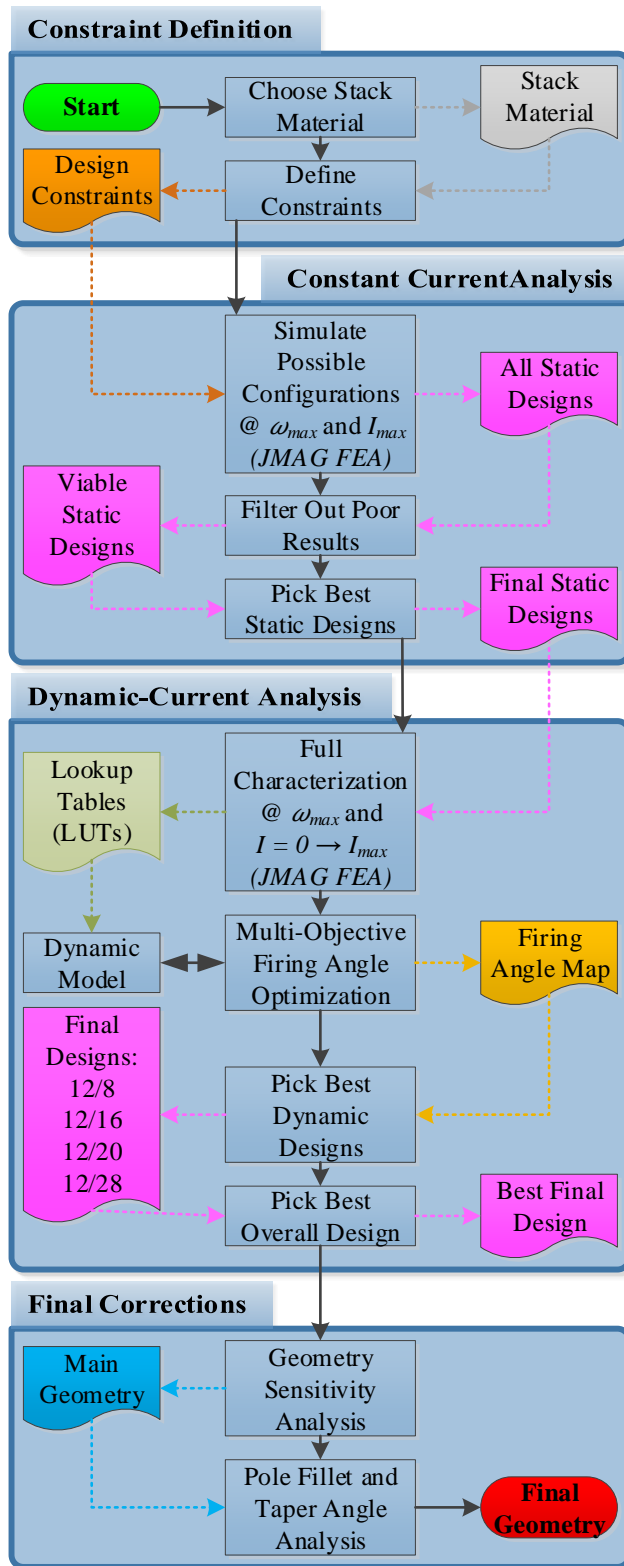


Fig. 6.1 CSRM electromagnetic design process

increments of 10 turns, to find the correct balance between copper loss, EMF, and power factor. These parameter sweep constraints are summarized in TABLE 6.1 and the parameters are identified in Fig. 6.2.

<b>Parameter</b>	<b>12/8</b>	<b>12/16</b>	<b>12/20</b>	<b>12/28</b>
$\beta_R$	4°→15°	4°→11°	4°→9°	4°→6°
$\beta_S$	$\beta_S = \beta_R - 1^\circ ; \beta_S = \beta_R$			
$h_R$	4 mm →10 mm			
$h_S$	25 mm, 35 mm, 45 mm			
$b_R$	17 mm	15 mm	13 mm	11 mm
$b_S$	25 mm			
$\alpha_R$	0°			
$\alpha_S$	0°			
$\zeta_R$	0 mm			
$\zeta_S$	0 mm			
$\gamma_R$	0 mm			
$\gamma_S$	0 mm			
$N_{AWG}$	22 AWG			
$N_{Turns}$	40, 50, 60			
$N_{Strands}$	Maximized for 60% wire fill			
$l_{stack}$	39.5 mm			
$l_{Airgap}$	0.4 mm			
Material	Cogent (Sura) M470-50A			

**TABLE 6.1** CSRM initial geometric parameter sweep ranges

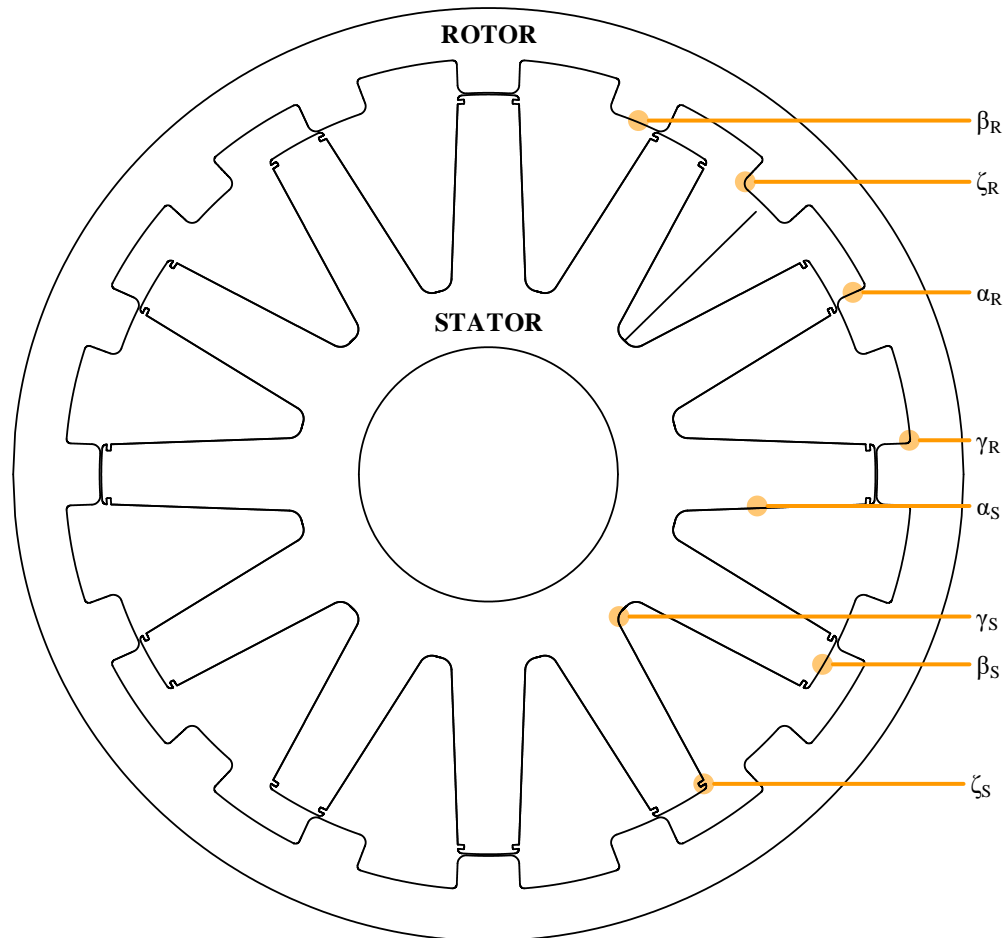


Fig. 6.2 CSR geometry parameter definition

When a given parameter is swept, all other parameters are kept constant, allowing every possible combination within the sweeping ranges to be evaluated. The parameter sweep ranges were bounded depending on geometry constraints and self-starting capabilities. The ranges were also limited to realistic values. For example, the pole-arc angle can only be so narrow before it is over-saturated and impacts aligned flux-linkage, so there is a realistic limit that exists. These limits were confirmed through the parameter sweep analysis itself. The sweeping bounds

of each parameter were set wide enough so that there was a clear performance gradient as each parameter was independently swept.

Pole fillets/tapering were omitted and the stack length, airgap, and iron material were all kept constant between the initial static designs to simplify the comparison of the other parameters. The lamination material was chosen for its flux density and torque characteristics as opposed to iron loss performance, considering the low speed nature of the machine.

### **Stator Pole-Arc Angle**

The finalized stator pole-arc angle is  $9^\circ$ . Increasing  $\beta_S$  can significantly reduce magnetic flux density in the stator poles; affecting the power factor while also reducing coil space. A larger  $\beta_S$  can also increase the aligned flux-linkage and widens the torque production angle of the machine for each torque pulse, which can lead to lower torque ripple. On the other hand, if the poles are too wide, the saliency can be reduced, which decreases the peak torque. Peak torque, RMS torque, power factor, and efficiency must all be balanced when choosing the stator pole-arc angle. The impacts of changing the stator and rotor pole-arc angles together are illustrated in Fig. 6.3.



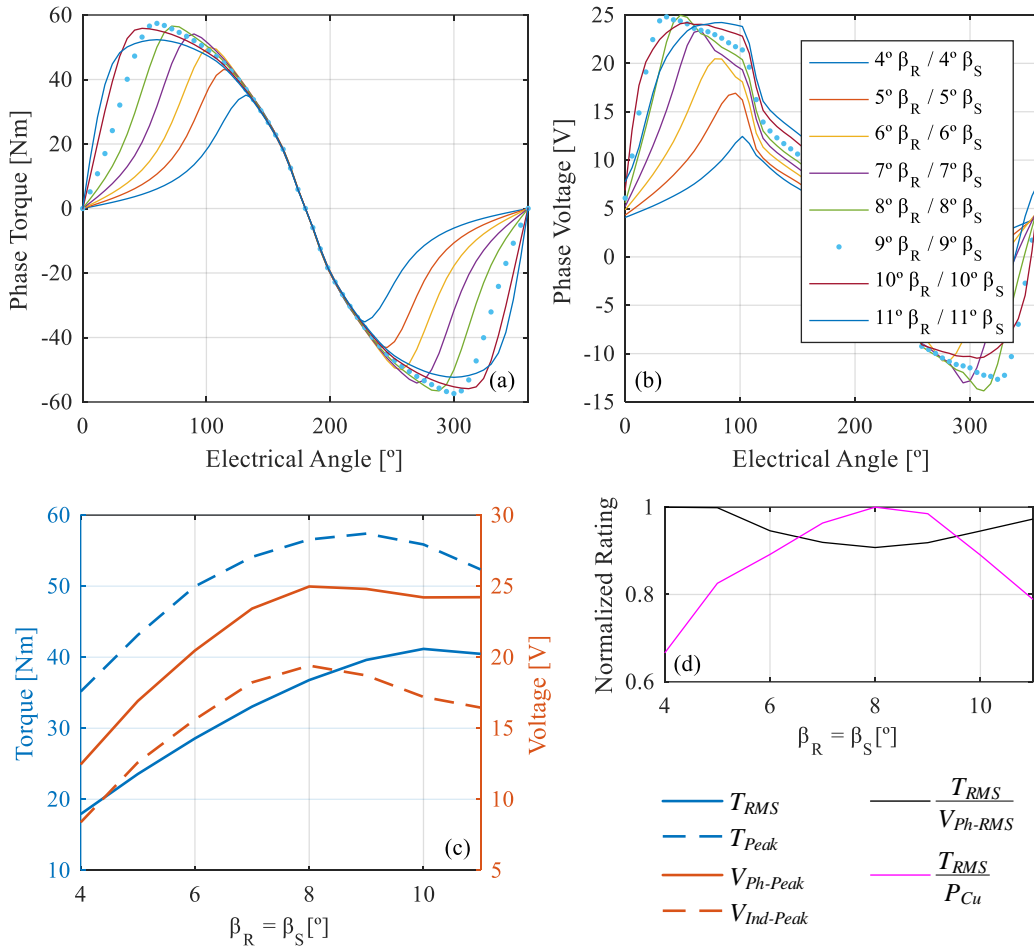


**Fig. 6.3** Effect of varying  $\beta_R$  and  $\beta_S$  (final 12/16 design, 75 A constant current):  
 (a)  $T$  effects; (b)  $V_{Ph}$  effects; (c) peak and RMS comparison; (d) normalized voltage and loss performance rating

When  $\beta_S$  increases, phase torque quality improves, and the aligned flux-linkage increases significantly due to reduced pole saturation. This generally means that the static RMS torque-per-amp performance improves as pole width increases, until the unaligned flux-linkage increases enough to significantly affect the saliency. However, the induced voltage will also be higher due to reduced pole saturation and the copper loss may increase due to decreased space for coil strands.

In contrast, if the stator pole is narrow, the pole saturation will be higher, reducing the induced voltage and improving the power-factor. A narrower pole will typically reduce both the unaligned and aligned flux-linkage for a given current, while also reducing phase torque quality. The increase in saliency can improve peak torque, but the static RMS torque-per-amp performance will typically reduce. In order to achieve the same RMS torque with narrower poles, a stronger MMF source is required to increase the aligned flux-linkage, but this will increase the copper loss due to either an increase in turns or an increase in phase current.

In summary, the stator pole-arc angle affects not only the pole saturation level, but also the machine saliency. Thus,  $\beta_S$  has a complex relationship with torque and voltage due to the non-linear SRM characteristics. Considering this, if the coil current or number of turns change, then the pole saturation level will be impacted, and  $\beta_S$  will typically need to be modified to obtain a good performance balance.

Up to this point, only the effects of varying the stator pole-arc angle near the angular limits have been discussed. The maximum stator pole-arc angle limit is considered to be the unaligned angular space between rotor poles, while the minimum limit is considered to be the point where the iron permeability reaches that of air and ceases to guide flux. Depending on the pole configuration and rotor pole-arc angles, the unaligned angular space between rotor poles can be much wider than it is practical to make the stator pole. In this case, increasing or decreasing the

stator pole width will not significantly impact the unaligned flux-linkage, simplifying the behavior as the pole-arc angle is varied.

The impacts of this are particularly clear in the 12/8 machine. This configuration allows for the poles to be significantly wider than the other configurations, as there is more space available per pole. The wide poles give better peak torque capabilities, relatively speaking, but for this design narrower poles were ultimately chosen to enable adequate saturation without requiring a large number of turns to do so (RMS current is fixed). This dropped the induced voltage down to an acceptable level without having the high copper losses associated with more turns.

In contrast, the other pole configurations had narrower poles due to higher pole counts, which did not require as many turns to saturate for a given RMS current. Therefore, the power factor benefit of higher saturation levels could be utilized without having high copper losses. These designs therefore, had a better balance between average torque, induced voltage, and efficiency, while also offering higher torque quality when compared to the 12/8 configuration.

### **Rotor Pole-Arc Angle**

The finalized rotor pole-arc angle is  $9^\circ$ . Increasing  $\beta_R$  can improve both peak and RMS torque as it allows for a higher aligned flux-linkage, but excessive  $\beta_R$  can reduce saliency and torque production capability. It was found that the rotor poles do not need to be saturated to improve power factor like the stator poles do, and thus,  $\beta_R$  can be slightly larger than  $\beta_S$  to increase the aligned

flux-linkage (thus, torque) and potentially reduce rotor iron loss, as long as self-starting capabilities are maintained.

This capability was utilized in the design of the 12/8 machine specifically, as there was plenty of available angular space per pole to increase the rotor pole-arc angle without increasing the unaligned flux-linkage. If  $\beta_R$  is larger than  $\beta_S$  then a dead-zone is created in the center of the phase torque waveform, as shown in Fig. 6.4.

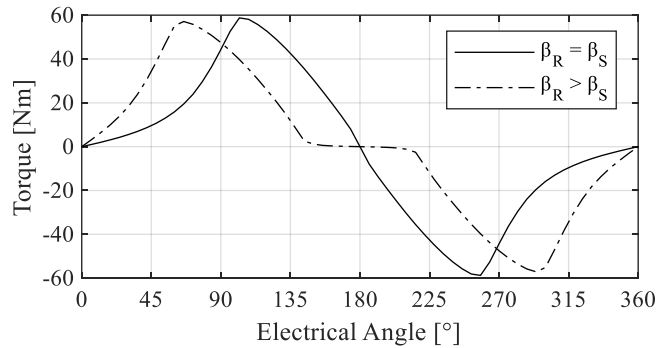


Fig. 6.4 Static torque waveforms for  $\beta_R > \beta_S$  vs.  $\beta_R = \beta_S$  (12/8 example)

However, since all phase torque waveforms are shifted by the same degree, this would not prevent self-starting or increase torque ripple (see Fig. 6.5 and Fig. 6.6). In fact, the dead-zone can potentially aid in the control of the machine by giving phases more time to turn off without risking negative torque.

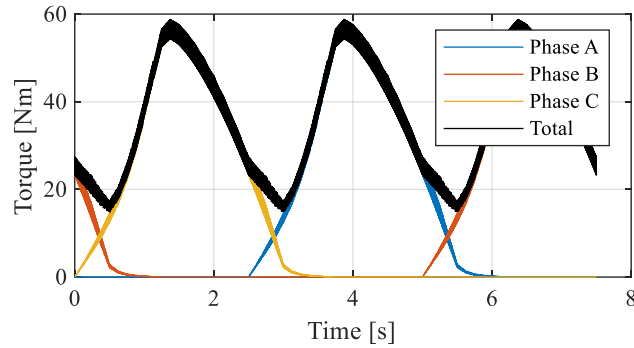


Fig. 6.5 Dynamic torque waveforms @ 1 RPM for  $\beta_R > \beta_S$  (12/8 example)

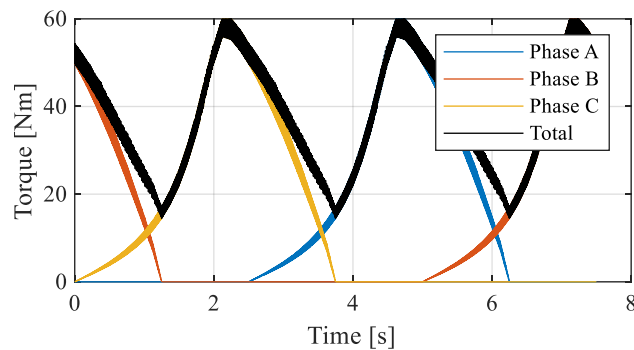
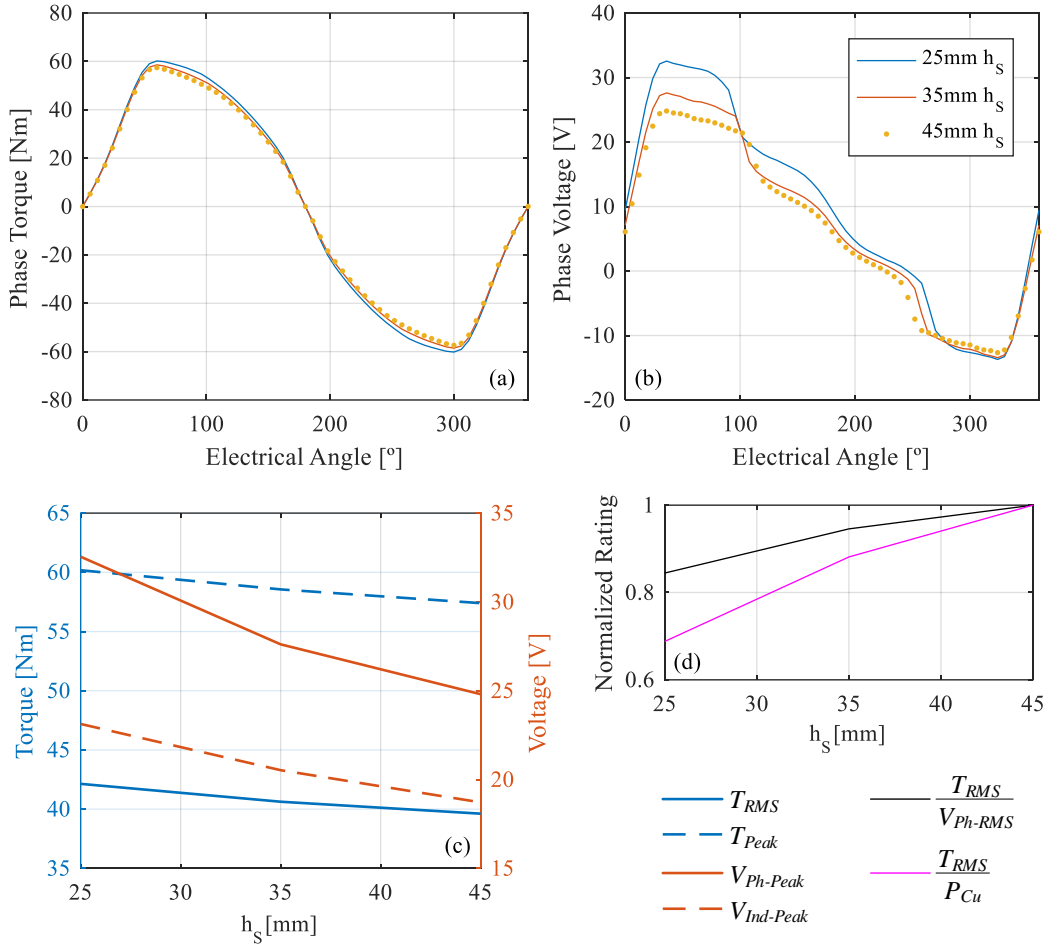


Fig. 6.6 Dynamic torque waveforms @ 1 RPM for  $\beta_R = \beta_S$  (12/8 example)

## Stator Pole Height

The finalized stator pole height was 45 mm. A smaller  $h_s$  reduces coil space, which can increase copper loss (fewer strands), but also means that a lower MMF is needed to produce the same airgap flux density, as there is less leakage. This translates into more torque with a smaller stator pole height, but also a higher voltage, as shown in Fig. 6.7.



**Fig. 6.7 Effect of varying  $h_s$  (final 12/16 design, 75 A constant current):**  
 (a)  $T$  effects; (b)  $V_{Ph}$  effects; (c) peak and RMS comparison; (d) normalized voltage and loss performance rating

Shorter poles also reduce the volume of heavily saturated iron, potentially decreasing core loss. However, since the e-bike SRM is a low speed machine, the stator pole height did not impact total losses significantly.

## Rotor Pole Height

The finalized rotor pole height was 8 mm. Increasing  $h_R$  can increase torque and induced voltage by decreasing the unaligned flux-linkage. This is true until the

pole height is large enough that flux does not link with the rotor back iron in the unaligned position, as illustrated in Fig. 6.8. The effect is most pronounced if there are a small number of rotor poles, as the flux will typically link with the rotor back iron before it links with the adjacent rotor teeth in the unaligned position.

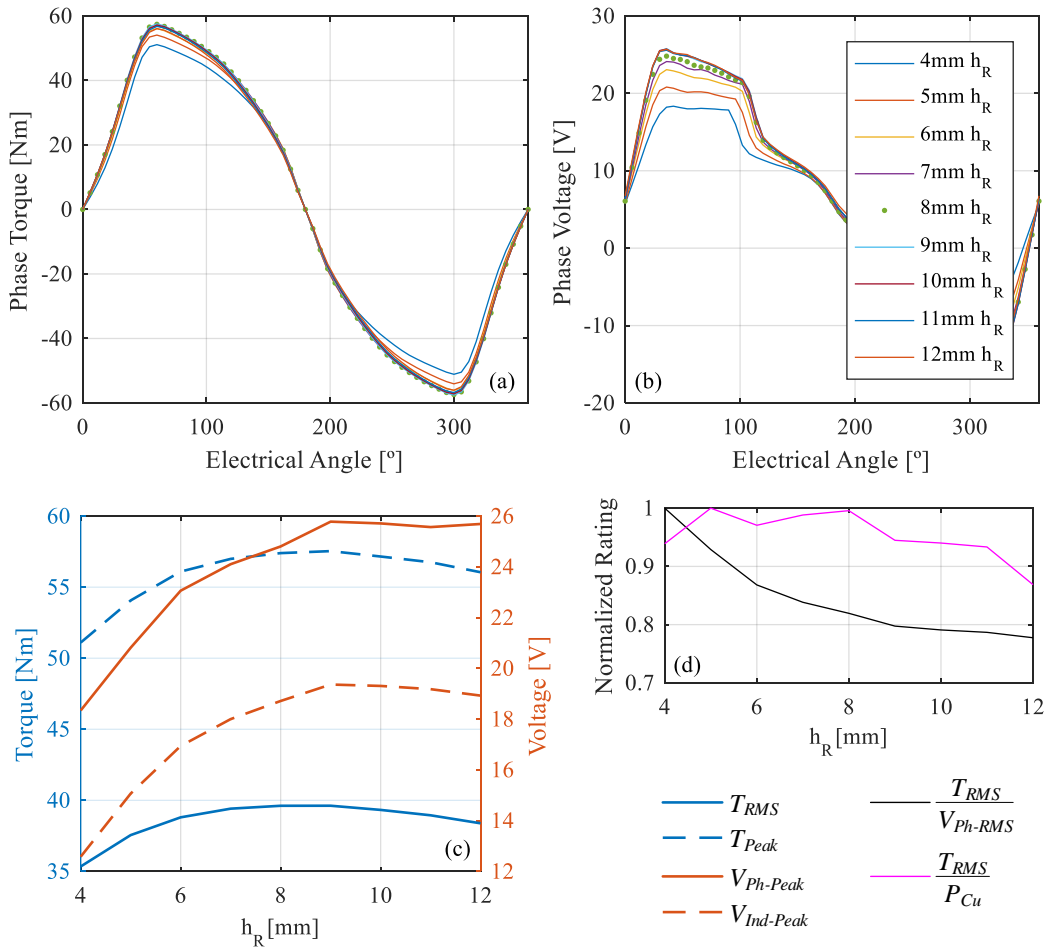


**Fig. 6.8 Effect of varying  $h_R$  (final 12/16 design, 75 A constant current):**  
 (a)  $T$  effects; (b)  $V_{Ph}$  effects; (c) peak and RMS comparison; (d) normalized voltage and loss performance rating

If the interior and exterior machine radii are fixed, then  $h_R$  can also decrease the coil space and decrease the bore (airgap) radius, reducing torque slightly.

## Yoke Thickness

The finalized yoke thickness was 15 mm for the stator and 12 mm for the rotor. A higher yoke thickness can reduce yoke saturation levels and thus decrease iron loss, while also increasing machine stiffness which can increase the machine natural frequencies and affect the NVH performance. However, if the inner and outer machine diameters are fixed, yoke thickness can also impact the airgap radius and space for strands. If the yokes are too thin, they can hamper the torque performance of the machine by restricting the flux circuit. Yoke saturation was not found to be beneficial in any way – only stator pole saturation improves power factor.

The torque and voltage impacts of changing the stator yoke thickness ( $b_S$ ) are shown in Fig. 6.9 and impacts of changing the rotor yoke thickness ( $b_R$ ) are shown in Fig. 6.10.



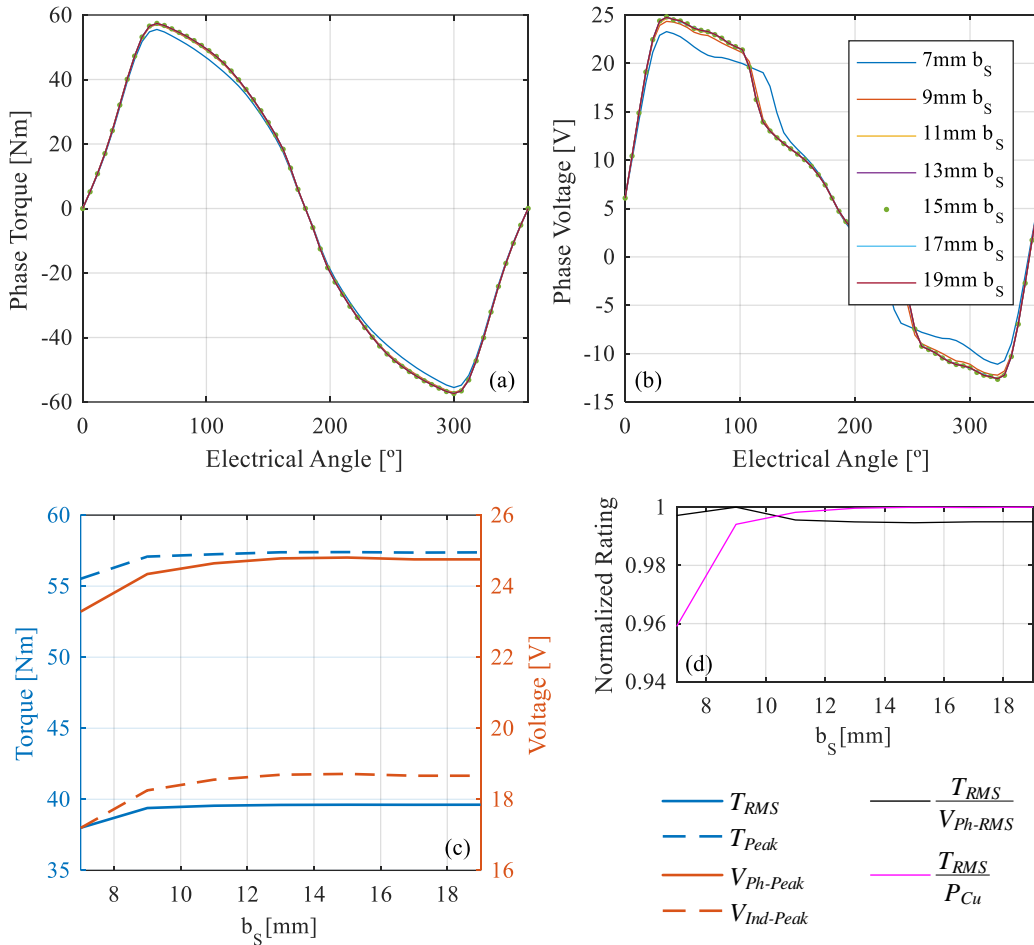


**Fig. 6.9 Effect of varying  $b_s$  (final 12/16 design, 75 A constant current):**  
 (a)  $T$  effects; (b)  $V_{Ph}$  effects; (c) peak and RMS comparison; (d) normalized voltage and loss performance rating

It is apparent from Fig. 6.9 that  $b_s$  is oversized during single phase excitation, as phase voltage and torque are the same for all values of  $b_s > 9$  mm. Since the stator shaft diameter was flexible, it was possible to oversize the stator yoke to reduce iron loss and increase rigidity without any negative impacts.

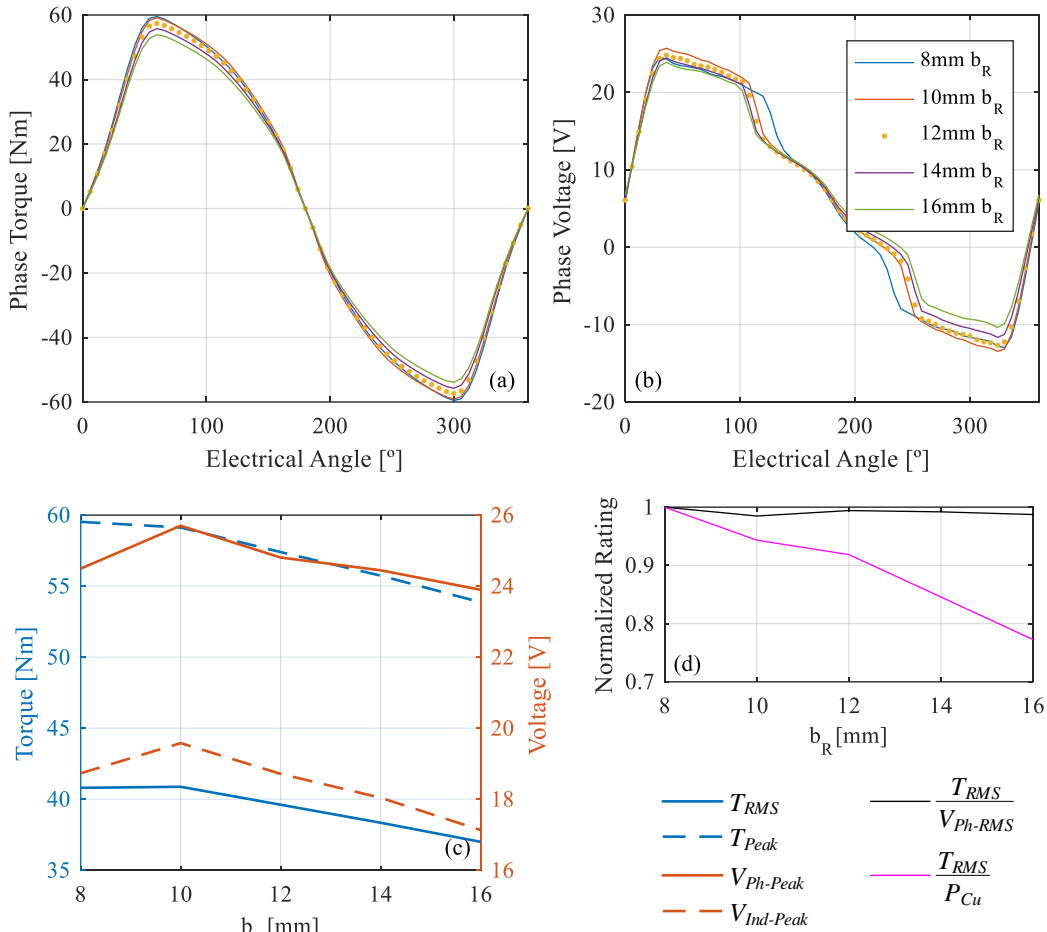


**Fig. 6.10 Effect of varying  $b_R$  (final 12/16 design, 75 A constant current):**  
 (a)  $T$  effects; (b)  $V_{Ph}$  effects; (c) peak and RMS comparison; (d) normalized voltage and loss performance rating

Observing Fig. 6.10, it appears that the rotor yoke thickness is slightly oversized for the reference design, as the torque and voltage waveforms are not significantly impacted by decreasing yoke thickness. However, it is important to note that these plots represent isolated phase values under constant current excitation. When firing angles and the other phases are accounted for in the analysis, there is typically a small amount of phase overlap where some mutual coupling is prevalent. This can increase the yoke flux density during phase

commutation. Thus, the yoke thickness was increased to avoid saturation under these conditions.

## Coil Design

### Wire Size Selection

Since the e-bike motor is a relatively low speed machine, the excitation frequency is quite low. Therefore, it is expected that AC copper loss effects such as skin effect and proximity effect do not have a significant impact on total loss. For example, at the maximum motor speed of 400 RPM, a 12/16 SRM will have a fundamental excitation frequency of:

$$f_{Mech} = \frac{400 \text{ rev}}{\text{min}} \cdot \frac{1 \text{ min}}{60 \text{ sec}} = 6.67 \text{ Hz}$$

$$f_{Elec} = N_R * f_{Mech} = 16 \cdot 6.67 = 106.67 \text{ Hz}$$

If we assume the wire permeability,  $\mu = 4\pi \times 10^{-7} \frac{H}{m}$  and the conductivity of copper,  $\sigma = 5.814 \times 10^7 \frac{S}{m}$  then the skin depth can be calculated as discussed in

### Chapter 2.

$$\begin{aligned} \delta_{skin} &= \frac{1}{\sqrt{\pi f_{Elec} \mu \sigma}} \\ &= \frac{1}{\sqrt{\pi (106.67) (4\pi \times 10^{-7}) (5.814 \times 10^7)}} \\ &= 0.0064 \text{ m} \end{aligned}$$

With a skin depth of 6.4 mm, it is clear that none of the conductors analyzed should experience AC resistance due to skin effect. Therefore, the primary concern

when selecting wire size is the copper to insulation ratio in the slot – or the effective copper area – which is reflected by the DC phase resistance. Using an analytical coil resistance estimation algorithm that accounts for the placement of each turn in the slot, it was possible to compare the resistance impacts of implementing each wire size with the finalized stator geometry. The results are compared in TABLE 6.2, where  $d_{Cu}$  represents the nominal copper diameter and  $R_{Ph}$  is the estimated resistance at 25°C.

$N_{AWG}$	$d_{Cu}$ [mm]	$N_{Turns}$	$N_{Strands}$	$R_{Ph}$ [mΩ]
12	2.0523	43	1	115.7
14	1.6281		2	92.7
16	1.2903		4	76.0
18	1.0236		6	79.7
20	0.8128		10	76.2
22	0.6426		16	76.3
24	0.5105		25	77.3
26	0.4039		39	79.2
28	0.3200		60	81.3

**TABLE 6.2** Wire size impact on phase resistance (for final 12/16 geometry)

Through this analysis, it is clear that 16 AWG, 20 AWG, and 22 AWG have similar phase resistance for the final design geometry. Since the AC resistance effects are negligible, it is desirable to have the largest wire diameter to simplify the winding process during production. However, thicker wire is more difficult to bend and it is possible to damage the wire insulation if the wire bend radius is too low. Ultimately, 22 AWG wire was selected as the analytical axial length

calculations for the coils were not yet validated by a prototype. Considering this, the smaller 22AWG wire was chosen because it allowed for some flexibility during the production process. This turned out to be quite helpful, as some strands did need to be removed during production to fit the coil axial length constraints.

### *Number of Strands*

The number of strands was maximized for the design geometry based on a slot wire fill factor constraint of 0.6. It is also important to account for an end turn fill factor of 0.6 in order to accurately estimate the total axial length of the coils. Considering the tight axial space constraints for this specific E-Bike motor and the 12-stator pole configuration utilized for the design, it was found that the axial length constraint was the limiting factor for coil design rather than the slot fill factor. As the number of stator poles increases, the copper is more evenly distributed around the airgap, meaning that the coil axial length can be reduced. However, only 12-stator pole designs were investigated for this analysis.

### Number of Turns

The final design used 43 turns per stator coil. Selecting  $N_{Turns}$  is arguably the most challenging step in the design process. Increasing the number of turns increases the flux density in the poles just as increasing phase current does. As the machine saturates, static torque will continue increasing (see Fig. 6.11) as long as:

- 1) The relative permeability of the core is greater than one.
- 2) There is still a difference between unaligned and aligned inductances to create torque.

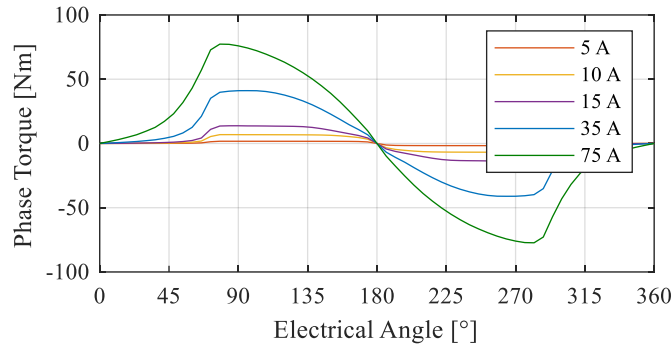


Fig. 6.11 Static-current phase torque vs. position (12/8 example)

The airgap and stator pole flux densities for the same conditions are shown in Fig. 6.12 and Fig. 6.13 respectively.

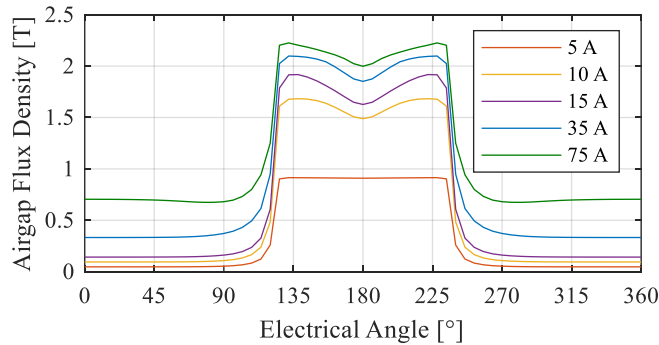


Fig. 6.12 Static-current airgap flux density vs. position (12/8 example)

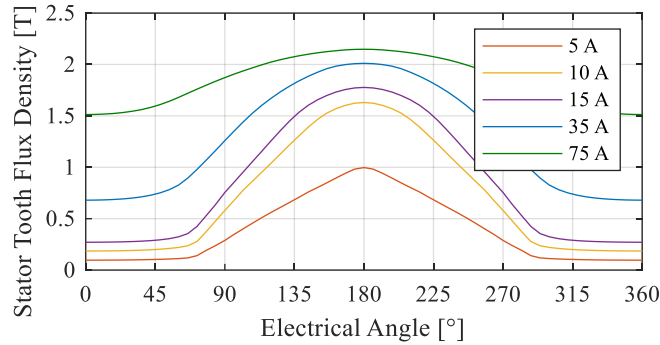


Fig. 6.13 Static-current stator pole flux density vs. position (12/8 example)

The increase in saturation level (with increasing MMF) reduces the induced voltage, as shown in Fig. 6.14. This is due to improved power factor that is achieved when the magnetic co-energy starts to surpass the stored magnetic field energy. However, this can increase iron loss, and considering the given slot area and fill factor constraints, increasing  $N_{Turns}$  also reduces space for strands; resulting in higher voltage drop and copper loss.

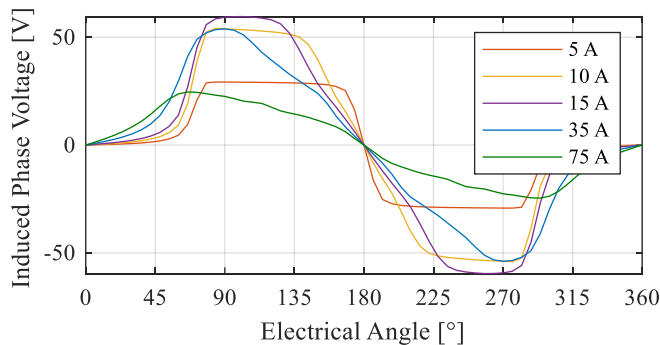
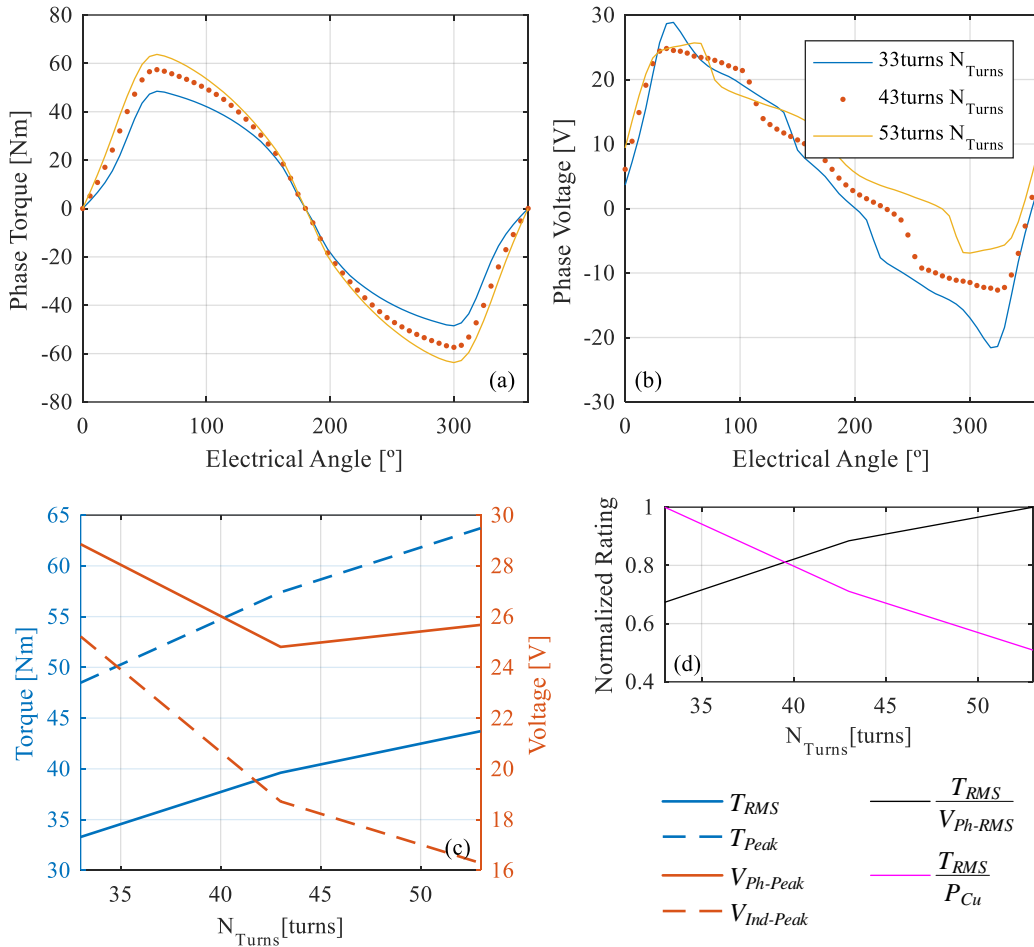


Fig. 6.14 Static-current induced phase voltage vs. position (12/8 example)

These effects are also illustrated for the 12/16 design in Fig. 6.15.



**Fig. 6.15 Effect of varying  $N_{Turns}$  (final 12/16 design, 75 A constant current):**  
 (a)  $T$  effects; (b)  $V_{Ph}$  effects; (c) peak and RMS comparison; (d) normalized voltage and loss performance rating

Though this behavior is relatively straightforward for the static case, the dynamic case is much more complex. Below the base speed, the motor will behave similarly to the static case. However, once the base speed is reached, the machine cannot build up enough current in the windings to saturate the poles and improve the power factor. Therefore, the EMF increases not only due to the increasing speed, but also due to a reduction in saturation.



This effect can be delayed (the base speed can be increased) by advancing firing angles to inject more current into the windings to effectively saturate the core. The current can be injected when the phase induced voltage is low, regardless of current (i.e. at  $0^\circ$ elec. in Fig. 6.14). With fewer rotor poles, there is a larger phase torque dead-zone, and thus a larger phase voltage dead-zone, meaning the machine may respond better to phase advance (this effect is shown in the next section).

Since the EMF at a given speed depends on the core saturation level, but the saturation level depends on  $N_{Turns}$  (and phase current), the ideal number of turns can be difficult to choose – it is a non-linear problem. This challenge can be illustrated by looking at constant conduction operation of the motor. If a non-zero minimum current is kept in the coils for the whole electrical cycle, then this will partially saturate the core, reducing EMF so that a higher peak current can be achieved later in the electrical cycle. This can significantly extend the maximum speed and constant power operation range of the motor, but also significantly increases copper losses and torque ripple. In this dissertation, constant conduction operation was avoided for all designs by applying non-linear constraints in the firing angle optimization.

In summary, it is typically desirable to only use as many turns as necessary to achieve the desired torque requirements at low speed, and the correct voltage to produce enough torque at high speed. This will help keep voltage drop and copper loss as low as possible. Since the non-linear saturation effects are significant, a

dynamic analysis must be performed when analyzing the effect of the number of turns on high speed performance (above the base speed).

### **Pole Tapering**

The finalized pole taper angle was  $2^\circ$  for the rotor and  $2^\circ$  for the stator. Increasing the rotor pole taper angle,  $\alpha_R$  can decrease saturation levels, and thus increase aligned inductance, but can also increase unaligned inductance if there is little space between stator and rotor poles in the unaligned position. In the 12/16 case, the small taper angles tested did not have a significant impact (see Fig. 6.16).

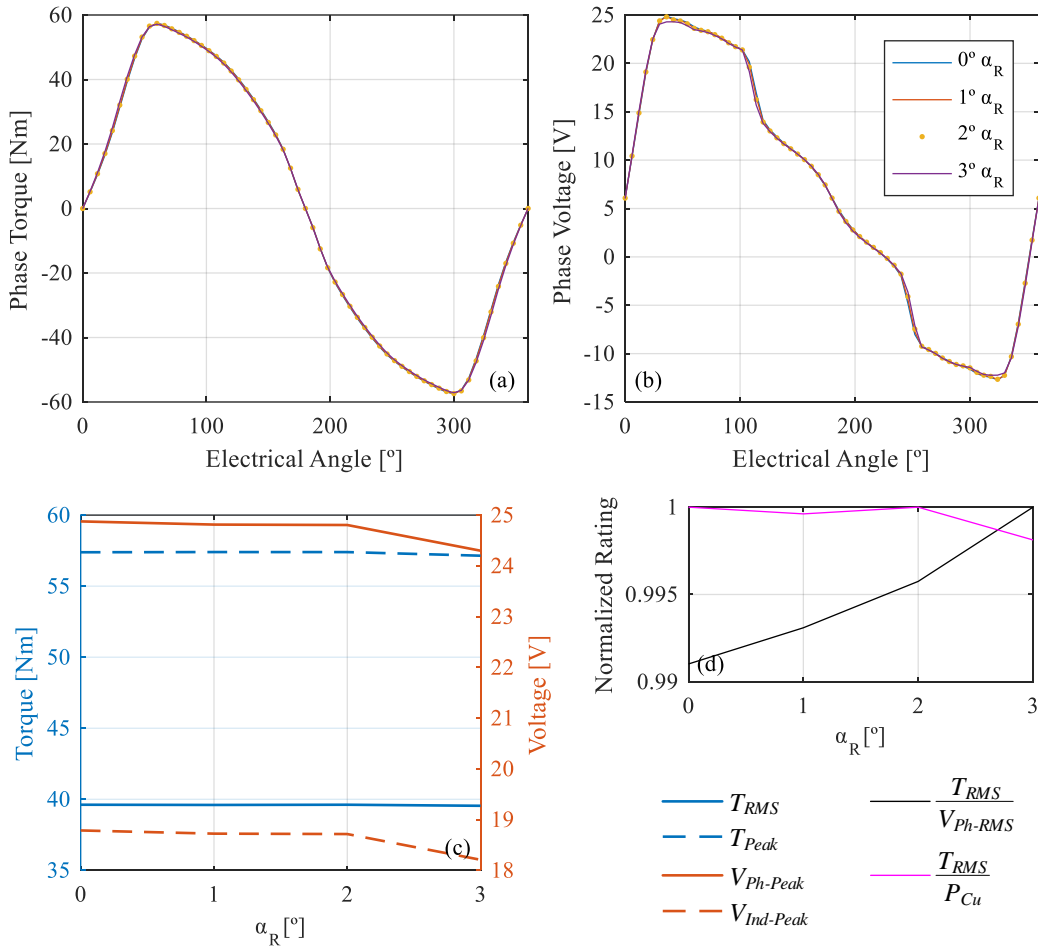


**Fig. 6.16 Effect of varying  $\alpha_R$  (final 12/16 design, 75 A constant current):**  
 (a)  $T$  effects; (b)  $V_{Ph}$  effects; (c) peak and RMS comparison; (d) normalized voltage and loss performance rating

Increasing the stator pole taper angle  $\alpha_S$  has similar effects, but they were much more pronounced than for  $\alpha_R$ , as shown in Fig. 6.17. This is due to the higher saturation levels found in the stator poles. However, tapering the stator poles can also make winding and coil retention during manufacturing more difficult, as the concentrated coils have a tendency to slide off if the taper angle is too large.

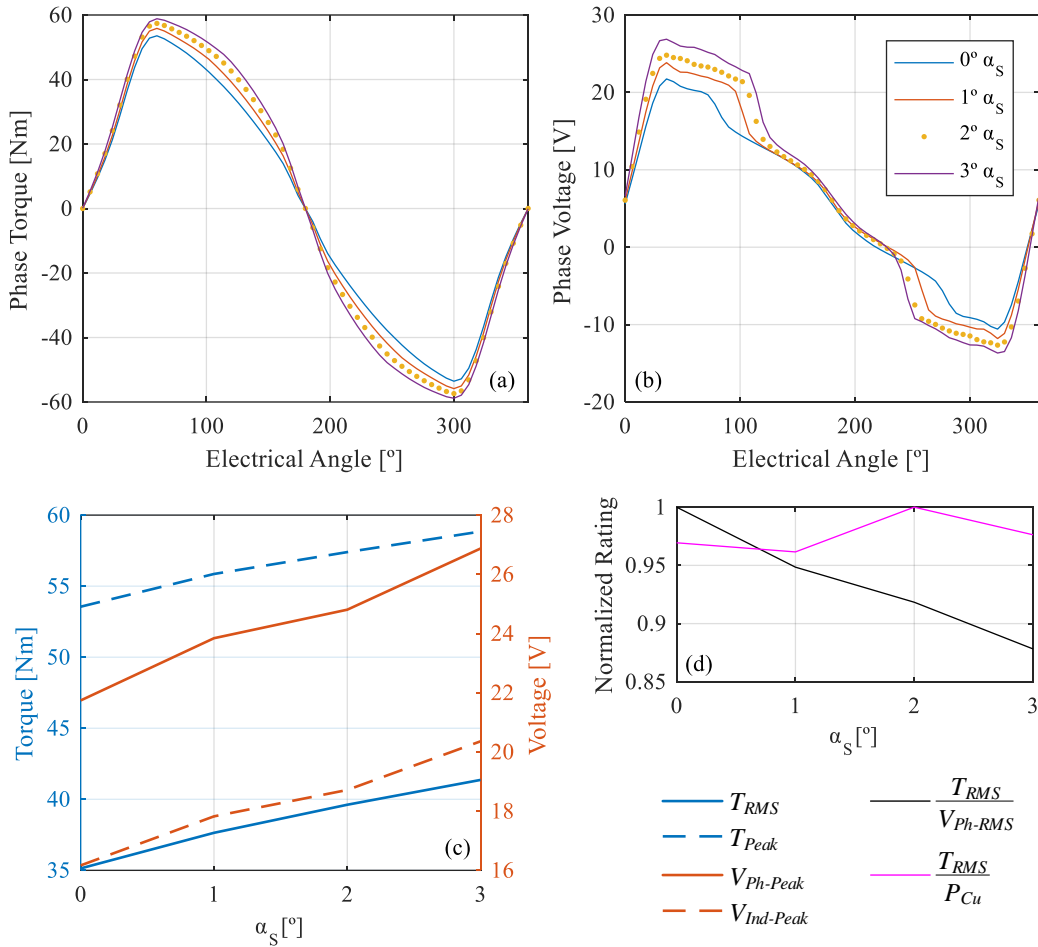


**Fig. 6.17 Effect of varying  $\alpha_s$  (final 12/16 design, 75 A constant current):**  
 (a)  $T$  effects; (b)  $V_{Ph}$  effects; (c) peak and RMS comparison; (d) normalized voltage and loss performance rating

## Pole Tip Fillets

The finalized pole tip fillet radius is 2 mm for the rotor and 1 mm for the stator. Small fillets on the tips of the rotor and stator teeth can have significant impacts on torque and voltage as these modifications affect saliency and saturation in the machine.

Adding rotor pole tip fillets can increase saliency and saturation levels. While the extra saturation can increase iron loss, the additional saliency reduces

unaligned inductance without significantly decreasing aligned inductance, resulting in more torque. This can be useful if angular space in the unaligned position is limited and a wide pole-arc angle is desired for torque quality or a high aligned flux-linkage. Torque and voltage impacts of varying  $\zeta_R$  are illustrated in Fig. 6.18.

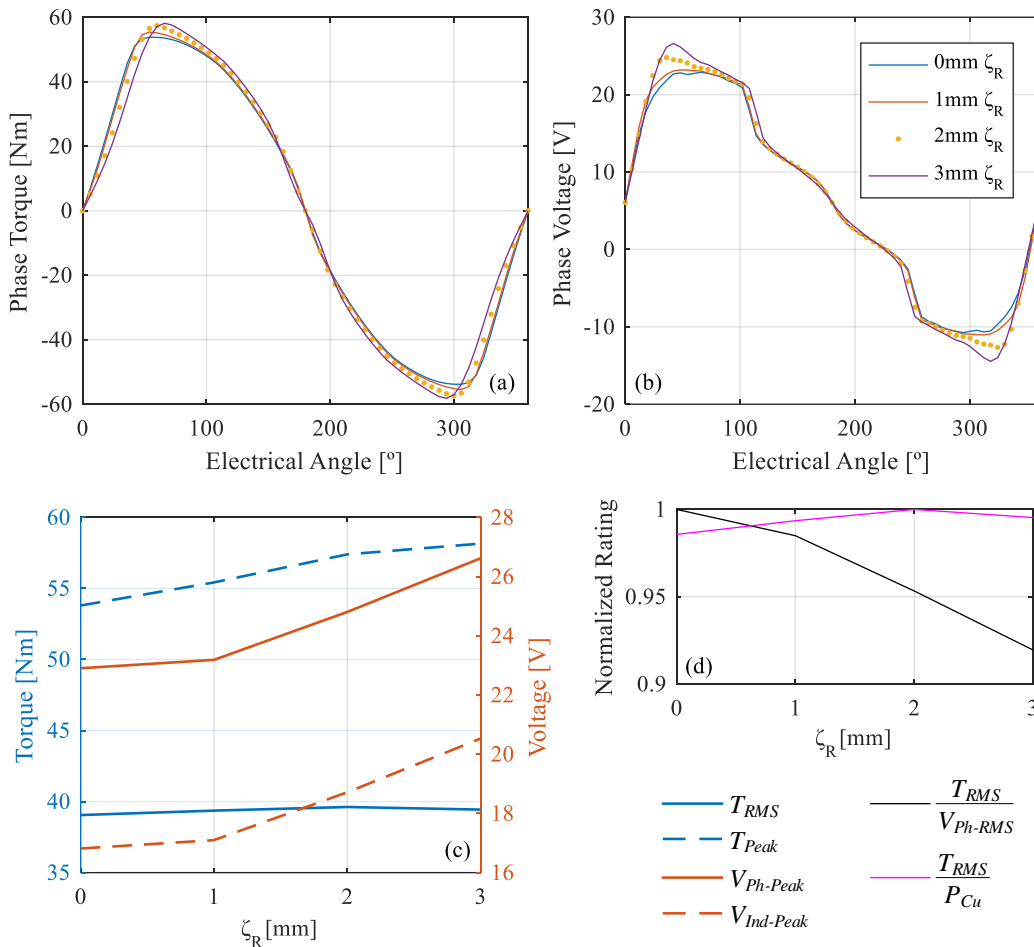


**Fig. 6.18 Effect of varying  $\zeta_R$  (final 12/16 design, 75 A constant current):**  
 (a)  $T$  effects; (b)  $V_{Ph}$  effects; (c) peak and RMS comparison; (d) normalized voltage and loss performance rating

Stator pole tip fillets have a similar effect as rotor pole tip fillets (see Fig. 6.19). The primary difference is that the stator poles typically have a higher flux

density than the rotor poles. Therefore, adding tip fillets can cause additional pole saturation that may not be desired.

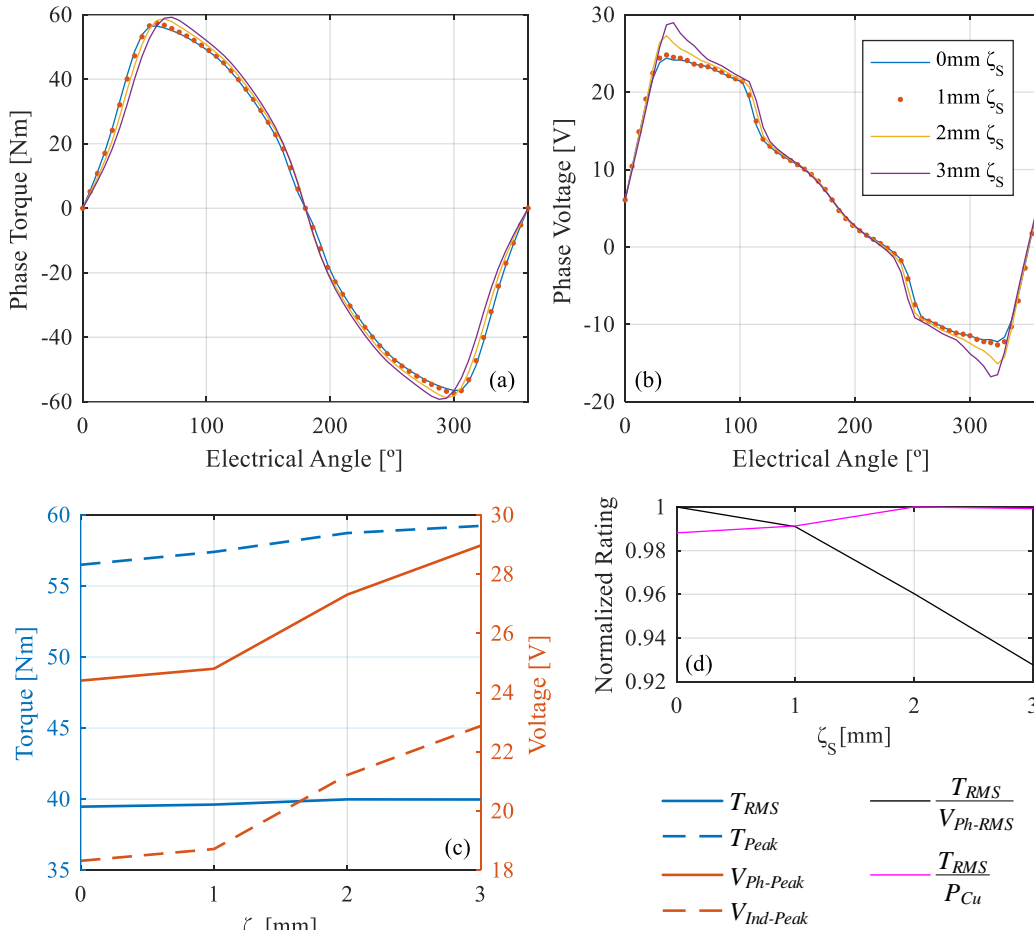


**Fig. 6.19** Effect of varying  $\zeta_s$  (final 12/16 design, 75 A constant current):  
 (a)  $T$  effects; (b)  $V_{Ph}$  effects; (c) peak and RMS comparison; (d) normalized voltage and loss performance rating

## Pole Base Fillets

The finalized pole base fillet radius is 1 mm for the rotor and 3 mm for the stator. Adding small fillets to the pole base had negligible impacts on machine performance for the 12/16 topology tested, as shown in Fig. 6.20 and Fig. 6.21. This may differ depending on the slot area, pole geometry, and fillet size.

Depending on the pole configuration, if the fillets are large, the unaligned flux-linkage could be increased, similar to increasing pole taper angles.

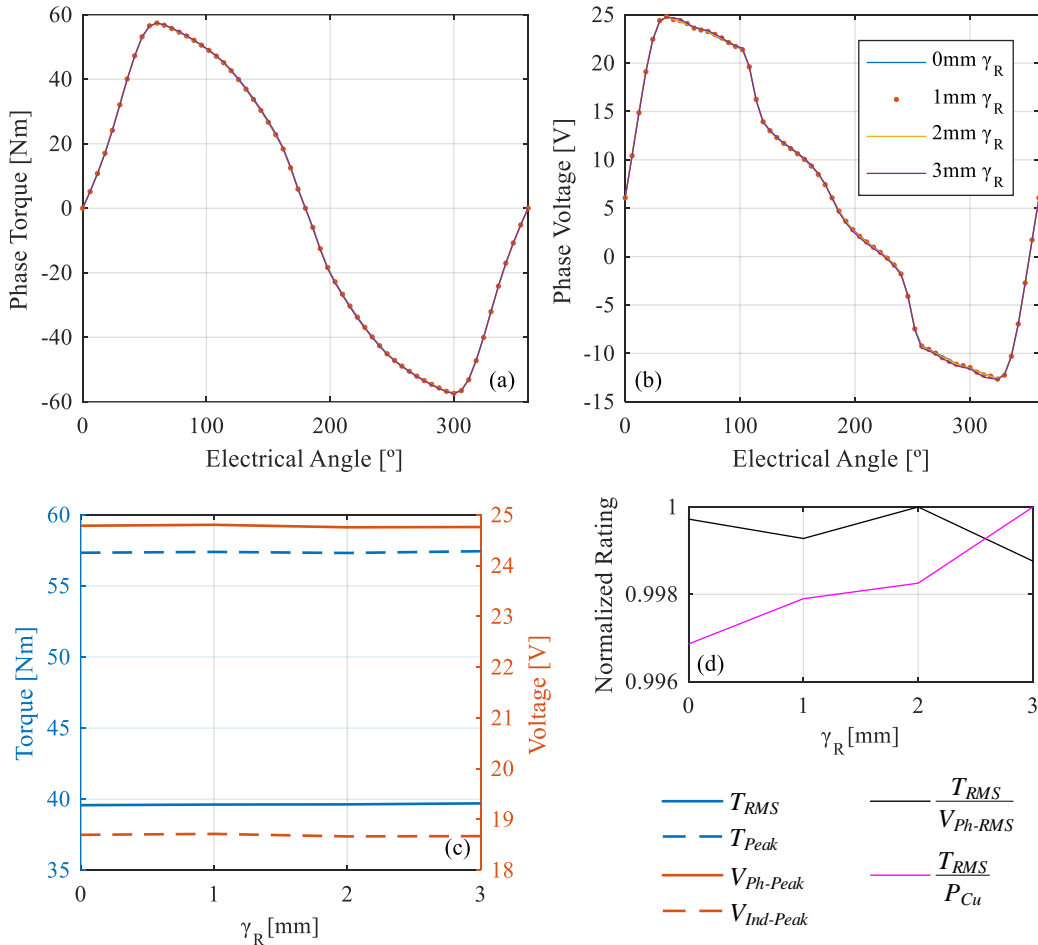


**Fig. 6.20 Effect of varying  $\gamma_R$  (final 12/16 design, 75 A constant current):**  
 (a)  $T$  effects; (b)  $V_{Ph}$  effects; (c) peak and RMS comparison; (d) normalized voltage and loss performance rating

In the case of the stator pole base fillets, they can reduce coil space, and may also make winding more difficult, depending on the slot geometry.

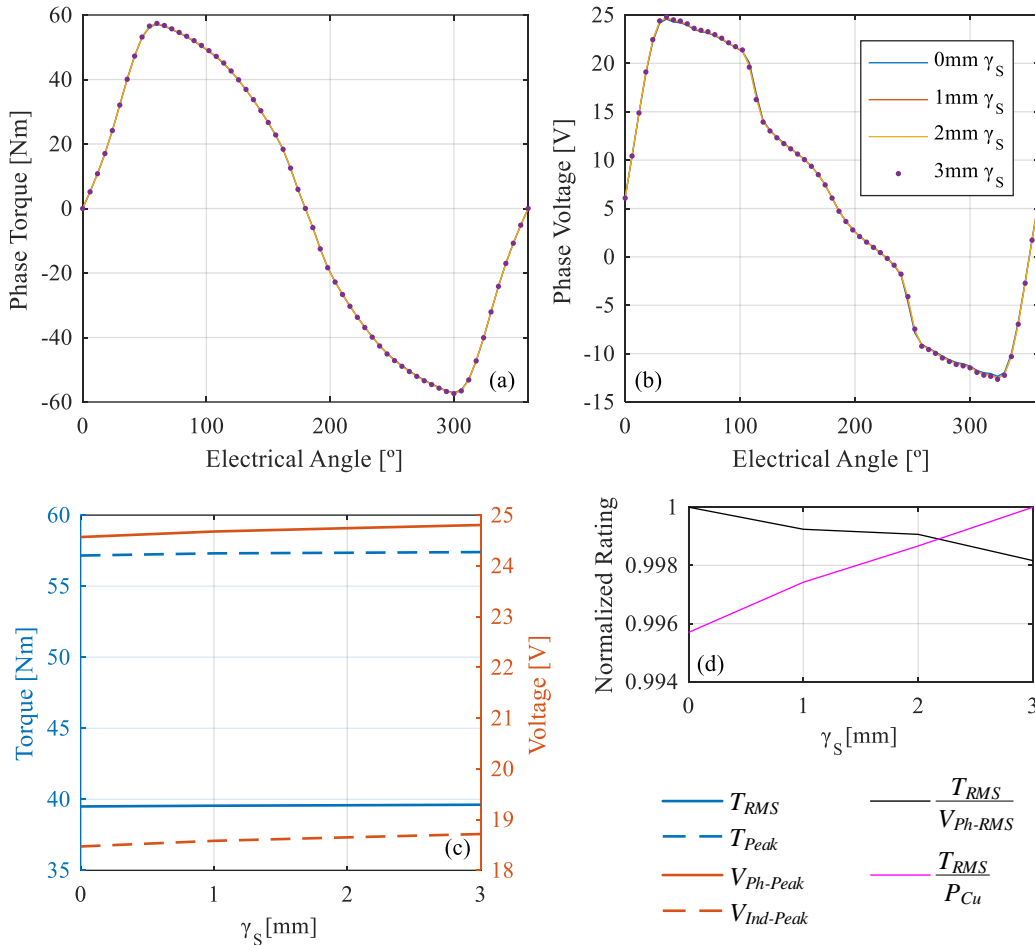


**Fig. 6.21 Effect of varying  $\gamma_S$  (final 12/16 design, 75 A constant current):**  
 (a)  $T$  effects; (b)  $V_{Ph}$  effects; (c) peak and RMS comparison; (d) normalized voltage and loss performance rating

## Stack Length

The stack length for the final design was set at 39.5 mm. The stack length does not impact saturation levels through the machine, and thus it can be modified at the end of the design without affecting the non-linear design. Increasing stack length increases torque and induced voltage linearly, while also increasing voltage drop and copper loss slightly due to the longer coil turns. This is illustrated in Fig. 6.22.



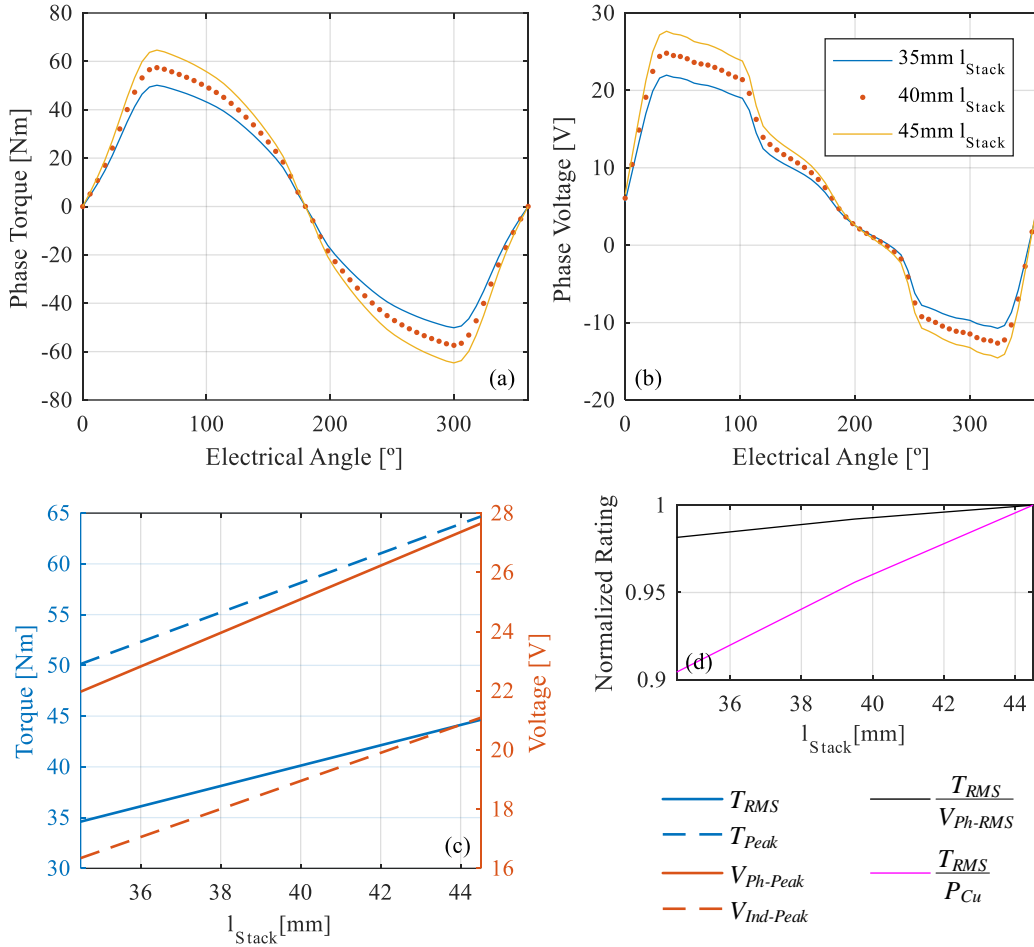


**Fig. 6.22** Effect of varying  $l_{Stack}$  (final 12/16 design, 75 A constant current):  
 (a)  $T$  effects; (b)  $V_{Ph}$  effects; (c) peak and RMS comparison; (d) normalized voltage and loss performance rating

## Airgap

The finalized airgap was set at 0.4mm. Increasing the airgap ( $l_{Airgap}$ ) will reduce torque output, increase induced voltage, and reduce efficiency in the motor, because there is more leakage in the magnetic circuit. If the airgap is reduced, the manufacturing cost can be increased significantly, as tighter tolerances have to be used to eliminate play and misalignment in the mechanical system. At small airgap lengths, the mechanical system must be rigid enough to avoid contact between the

rotor and stator when subjected to the high radial forces experienced during phase excitation. The torque and voltage impacts of varying  $l_{Airgap}$  are summarized in Fig. 6.23.

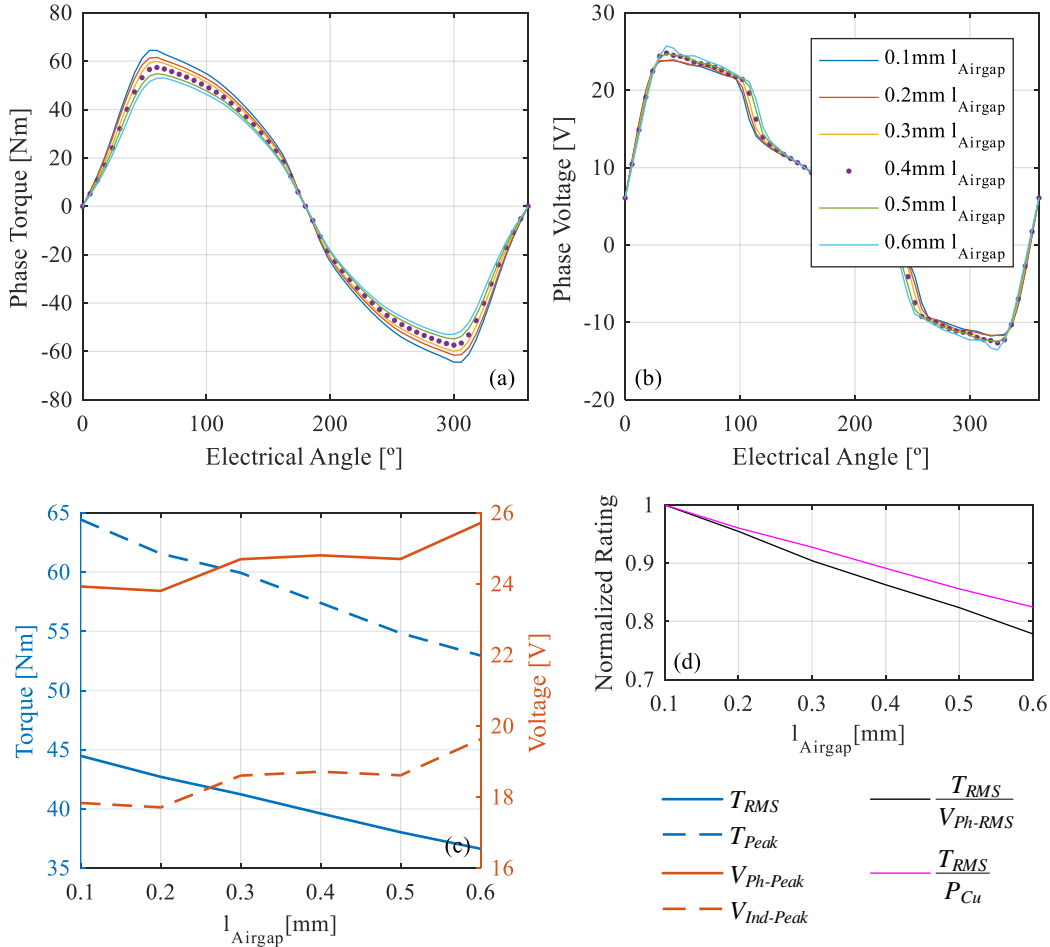


**Fig. 6.23 Effect of varying  $l_{Airgap}$  (final 12/16 design, 75 A constant current):**  
 (a)  $T$  effects; (b)  $V_{Ph}$  effects (c) peak and RMS comparison; (d) normalized voltage and loss performance rating

## Selection of Pole Configuration

The use of a 12-stator-pole configuration over a 6-pole configuration was justified for two primary reasons:

- 1) Axial length is significantly reduced when moving to 12 stator poles – flux is distributed around the airgap more. In addition, since there are more stator poles, the pole-arc angles are smaller, and thus a lower MMF is required to adequately saturate them and improve power factor.
- 2) Radial forces are more balanced for 12 stator poles. There are four main flux loops for 3-phase 12-stator-pole designs, and only two for 3-phase 6-stator-pole designs. This means that the flux must pass the airgap more times, but for NVH considerations, more balanced forces were preferred.

As discussed in the *Motor Design Process* section, the static design procedure was conducted for four different pole configurations; 12/8, 12/16, 12/20, and 12/28. The best static designs for each pole configuration (see Fig. 6.24) are compared using dynamic analyses in this section. Rotor/stator pole fillets and tapering are omitted for this comparison. As in all engineering challenges, the “best” design depends on a series of compromises with the weightings of each performance target defined by the application. In the case of E-bikes, a high enough torque density to meet the target requirements was required, but the highest torque designs were not chosen due to the losses and/or high voltages associated with them. The performance metrics were defined as follows:

- 1) Within  $T_{RMS}$  requirement

2) Within  $V_{Ph}$  requirement @ 400 RPM

3)  $\max\left(\frac{T_{RMS}}{P_{Cu_{est}}}\right)$ , where

$$P_{Cu_{est}} = N_{Ph}(I_{RMS}^2 R_{Ph})$$

where  $N_{Ph}$  is the number of phases,  $I_{RMS}$  is the maximum RMS current (55Arms),  $R_{Ph}$  is the estimated phase resistance for the given geometry,  $T_{RMS}$  is the RMS phase torque, and  $V_{Ph}$  is the phase voltage (induced + resistive voltage drop).

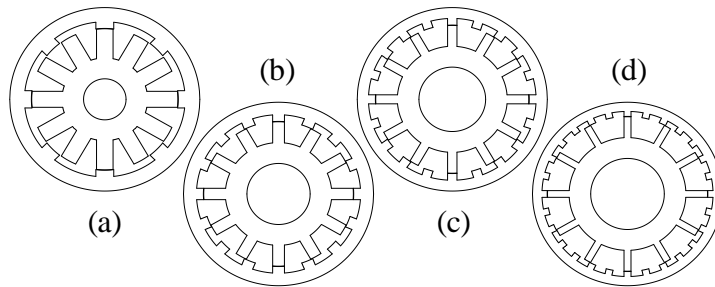


Fig. 6.24 Final exterior rotor design cross-sections (without tapering/filletts):  
(a) 12/8; (b) 12/16; (c) 12/20; (d) 12/28

### *Performance Comparison of Different Pole Configurations*

A genetic algorithm (GA) optimization method (detailed in the **Current Control** section) was used to find the firing angles at each current/speed point. The optimal firing angles are used in the dynamic model (discussed in **Chapter 3**) to create the excitation current waveforms.

The torque waveforms from the dynamic model at maximum RMS current are compared in Fig. 6.25 and the co-energy at low and high speed are compared for each machine in Fig. 6.26.

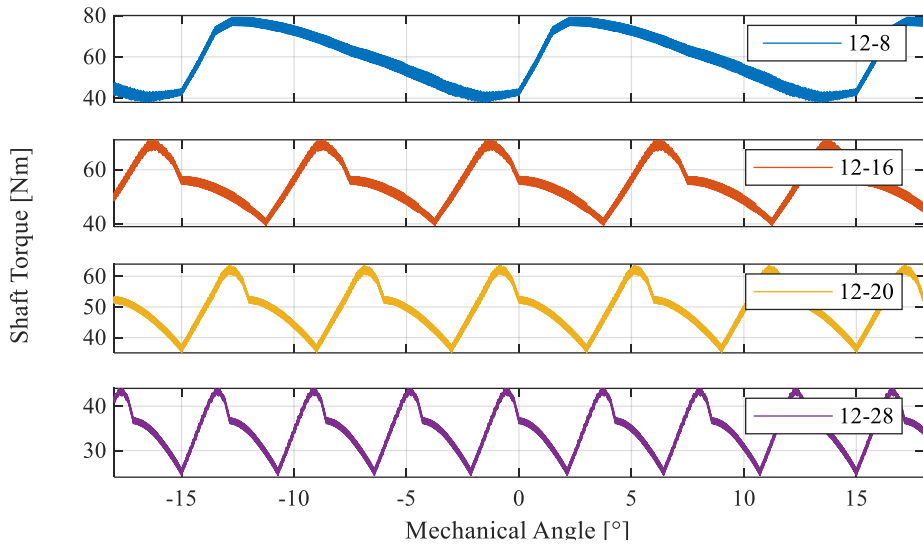


Fig. 6.25 Torque waveform comparison below base speed (max current)

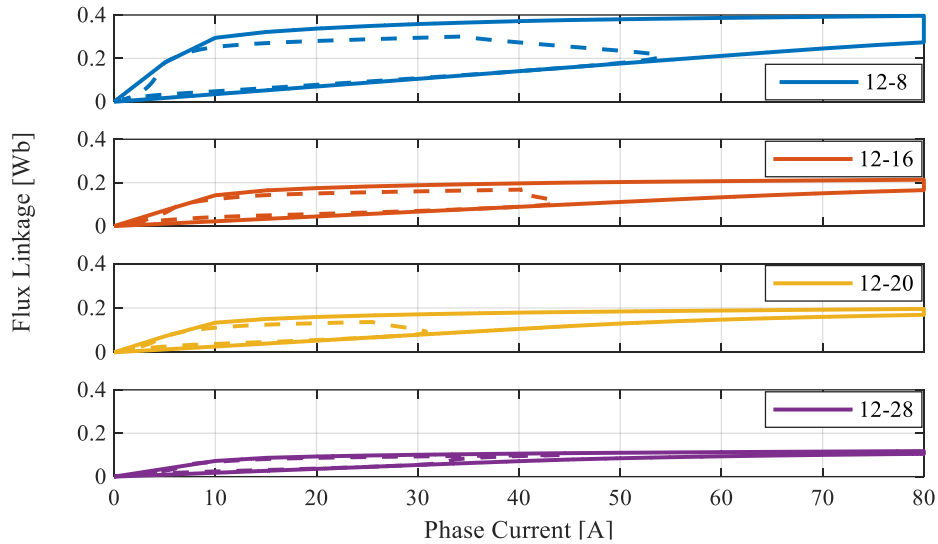


Fig. 6.26  $\psi/i$  comparison – capability limits (solid) & 400 RPM (dotted)

Next, the current waveforms generated by the dynamic model were fed into JMAG electromagnetic FEA software at each operating point to calculate the iron losses, and the copper loss was calculated from the RMS current and estimated

phase resistance at 40°C. The loss analysis is detailed in the *Loss and Efficiency Analysis* section of this chapter.

The copper losses for each design are compared in Fig. 6.27, iron loss in Fig. 6.28, RMS current in Fig. 6.29, and finally the efficiency maps are compared in Fig. 6.30.

The 12/8 design has the highest torque output and a significant constant power range, but the copper losses are much larger than other pole configurations. This is due to the high number of turns required to saturate the wider poles. However, the wider poles are necessary to obtain higher peak torque so that the average torque requirements can be met with fewer strokes. This effect is highlighted in Fig. 6.25, which shows the higher phase torque values, for a similar average torque.

Fig. 6.26 shows that the 12/8 SRM has the highest phase co-energy compared to the other machines, but it is important to consider that the total energy converted in one mechanical rotation depends on the number of electrical cycles and thus the rotor pole count. It is also clear that the 12/8 design could utilize more turns or a higher peak current to produce more torque, as the unaligned flux-linkage at maximum current is still lower than the aligned flux-linkage. This capability was not utilized as it would have further increased the copper loss.

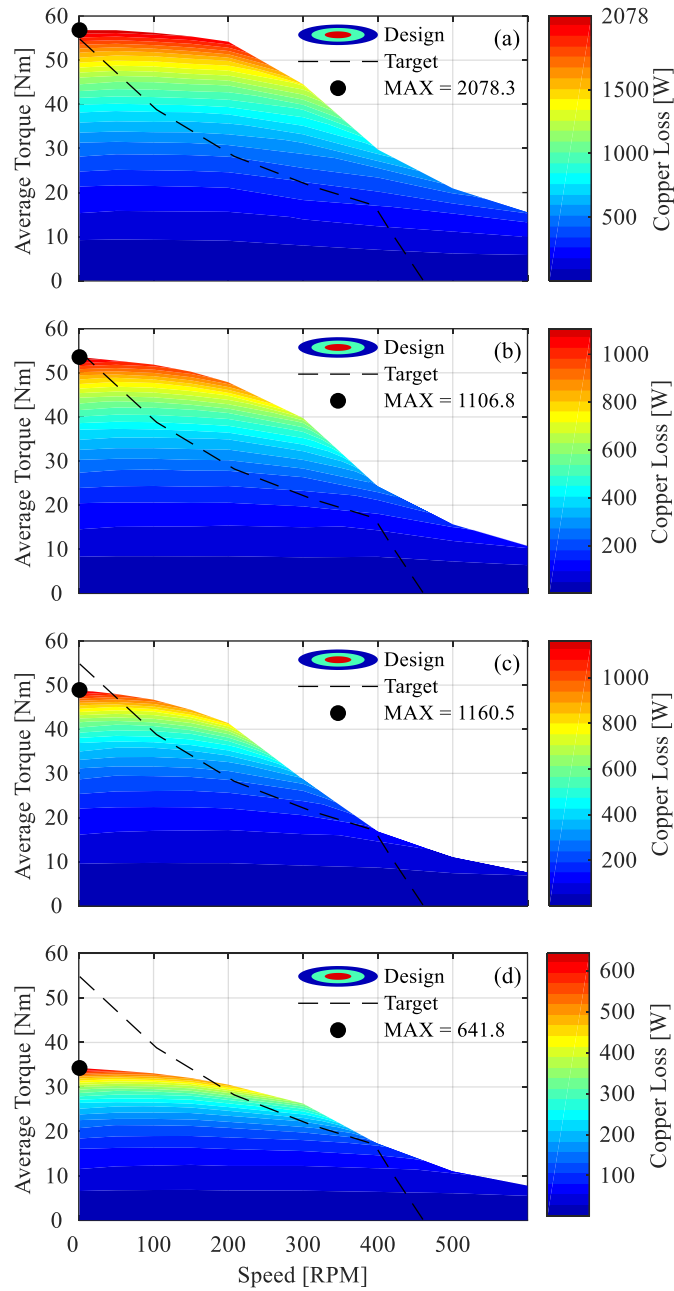


Fig. 6.27 Copper loss maps: (a) 12/8; (b) 12/16; (c) 12/20; (d) 12/28

The 12/16 design provides the best balance between average torque, torque ripple, and losses. Even though the torque ripple frequency is lower than the 12/20, the torque performance of the 12/16 at high speed is superior, with similar overall

copper losses throughout the torque-speed range. Compared to the 12/8, the torque ripple and peak copper losses of the 12/16 are lower, but the high speed torque output is also reduced.

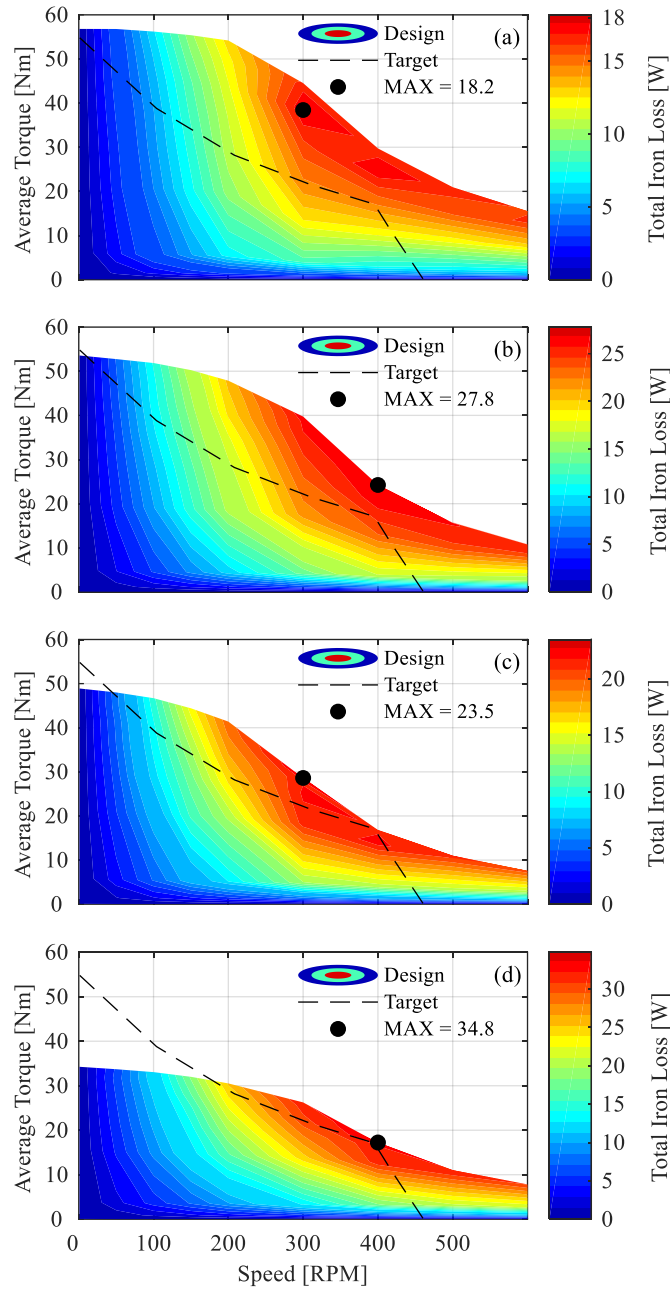


Fig. 6.28 Iron loss maps: (a) 12/8; (b) 12/16; (c) 12/20; (d) 12/28



It can be seen from Fig. 6.25 that the torque ripple amplitude at low speed decreases as the number of rotor poles increases, which is intuitive. In addition, ripple frequency obviously increases with the number of poles. Depending on the application, it may be beneficial to choose one pole configuration over the other based on the fundamental excitation frequency, to avoid resonating with the mechanical system. The 12/16 has more overall co-energy area than the 12/20, since it has both slightly more saliency (fewer poles) and a higher aligned flux-linkage (wider poles).

While the torque output of the 12/8, 12/16, and 12/20 designs is relatively close, the 12/28 has a significantly reduced peak torque capacity. This outlines the effect of adding more rotor poles: the torque quality improves, but the co-energy area decreases since the motor saturates more easily and has less saliency.

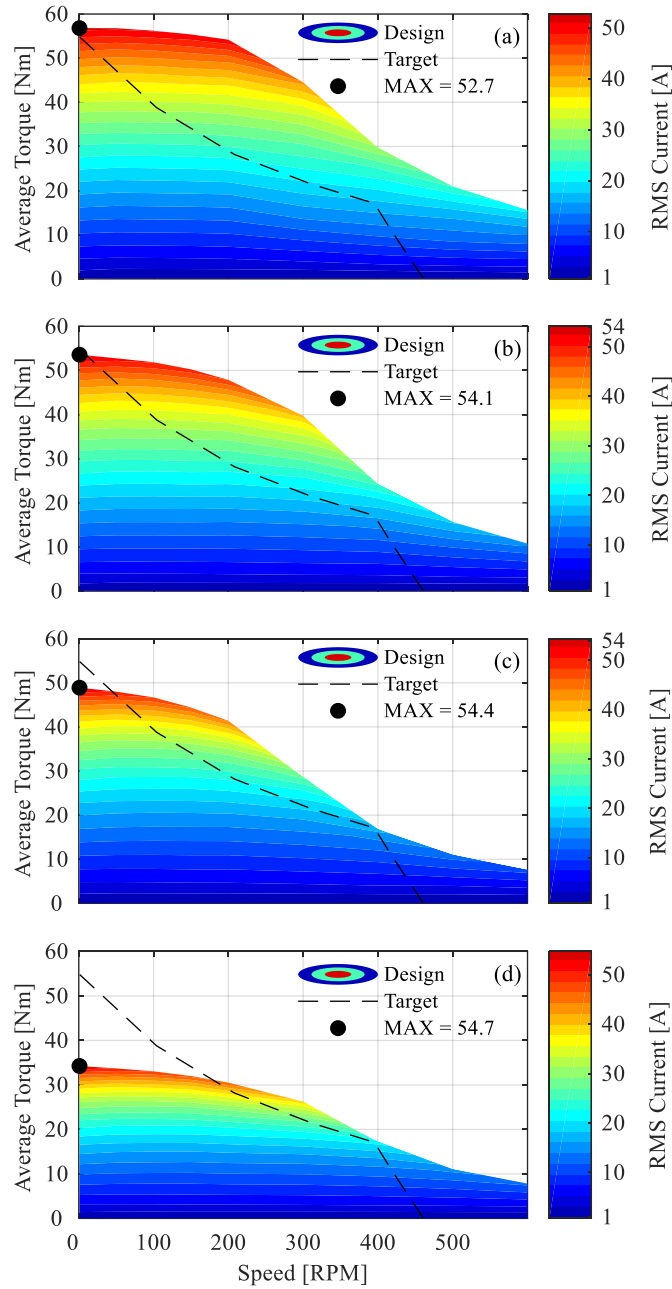


Fig. 6.29 RMS current maps: (a) 12/8; (b) 12/16; (c) 12/20; (d) 12/28

The original PMSM design had a peak efficiency at full load of roughly 81% at approximately 400 RPM [13]. Due to the additional copper strands, the

efficiency is comparable for the SRM designs. At higher speeds, the SRM efficiency is superior due to reduced RMS current.

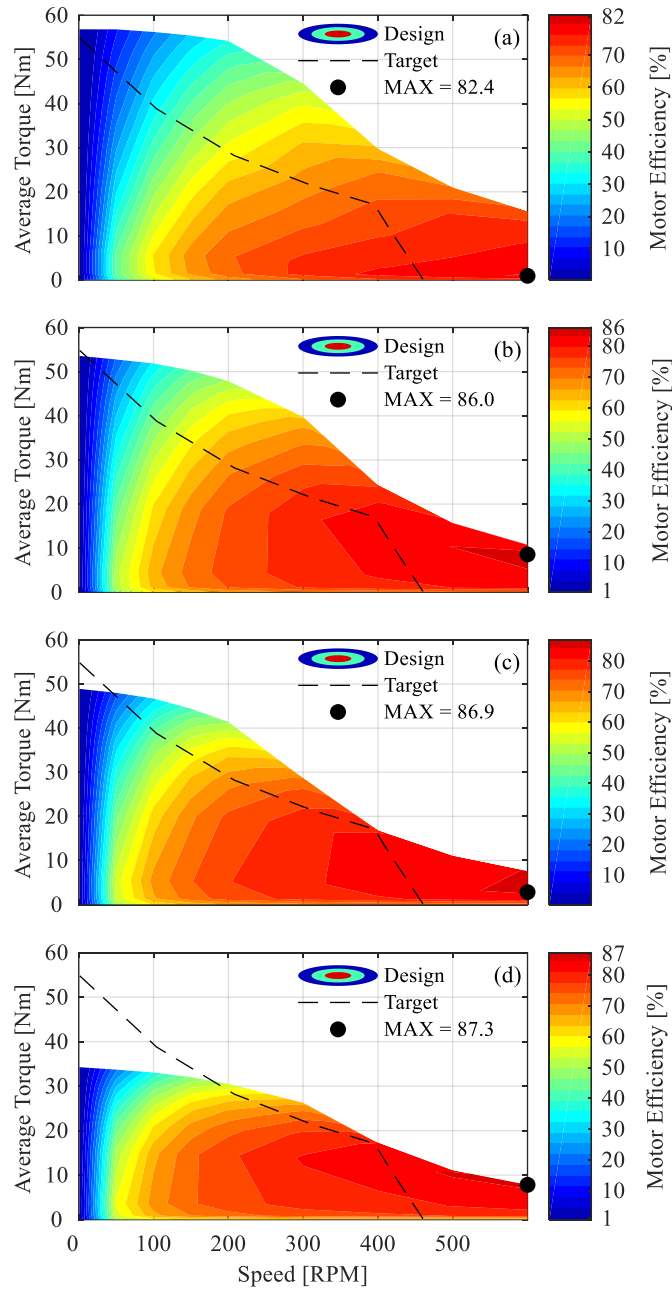


Fig. 6.30 Efficiency maps: (a) 12/8; (b) 12/16; (c) 12/20; (d) 12/28

### Coil Retention – Wedges vs. Shoes

The finalized design requires that the coils be retained in some fashion. This was particularly important due to the tapered design of the stator poles. Since any change to the pole geometry will affect the electromagnetic performance of the motor, the torque and voltage performance of both slot wedges and slot shoes were compared. The comparison of different slot retention methods is summarized in TABLE 6.3.

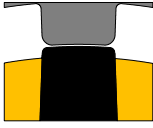
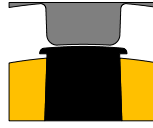
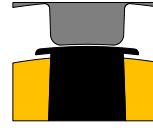
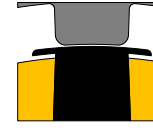
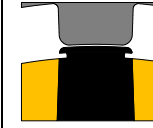
Case	1	2	3	4	5
<i>Wedges / Shoes</i>	None	Shoes ( $\theta_S + 2^\circ$ )	Shoes ( $\theta_S + 4^\circ$ )	Shoes ( $\theta_S + 6^\circ$ )	Wedges
$\zeta_S$	1 mm				
<i>Strands</i>	11				
<i>Wire Fill</i>	0.42	0.42			0.42
<i>Other Notes</i>		Thickness = 1mm			Thickness = 1mm Inset = 1.5°/side
<i>Image</i>					

TABLE 6.3 Coil retention comparison cases (final 12/16 design)

The radial thickness is the same for both the wedges and shoes. When considering the wedge case, the slot wedges are inserted into cutouts on the stator poles and are retained by friction. The cutout intrusion angle into the stator pole is

defined as the inset angle,  $1.5^\circ$  for this case. Ideally the inset angle is minimal to prevent magnetic impacts. However, the inset cannot be too small otherwise the wedges will not be properly supported. The choice of both inset angle and radial thickness is supported by ANSYS structural FEA analysis, as detailed in the *Structural Analysis* section. Both the shoes and wedges are placed as close to the airgap as possible; for the shoes there is no gap, as the pole tip fillet angle ( $\zeta_S$ ) is applied on the shoe itself. Since the wedge requires some material for retention, and it is undesirable to modify the tip fillet geometry, it is placed after the tip fillet. The performance of each case is compared in Fig. 6.31.

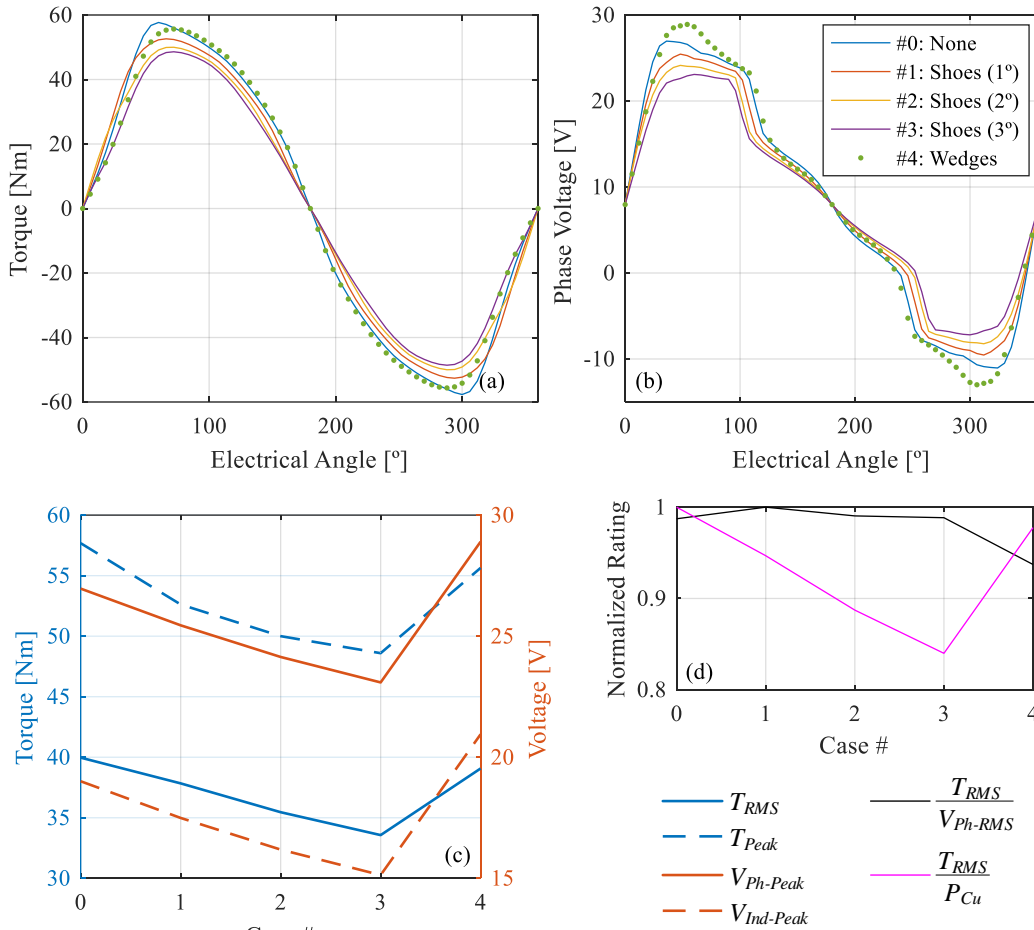


Fig. 6.31 Coil retention method comparison (final 12/16 design)

Pole shoes significantly reduced motor saliency, and thus the torque and voltage were strongly impacted, as illustrated in Fig. 6.31. Slot wedges increase pole tip saturation slightly, but the performance was found to be better than adding pole shoes, and thus they were utilized in the prototype design.

## Current Control

Up until this point in the chapter, SRM geometric design and pole configuration selection have been discussed. Dynamic analyses were conducted to produce the performance maps in the pole configuration section, but were not discussed in detail. The dynamic and structural analyses for the final design are discussed in detail for the rest of this chapter. This section outlines the dynamic model current-control strategy used to generate the current waveforms for each point in the torque-speed performance maps. A voltage source hysteresis current controller is fed with GA optimized firing angles to create these current waveforms. The firing angle optimization strategy is discussed in this section.

### Genetic Algorithm Firing Angle Optimization

A multi-objective Genetic Algorithm optimization was used to determine the firing angles for the torque-speed map. The “*gamultiobj*” function in Matlab was used to run the GA optimization, but the overall algorithm is based on the one discussed in [1] – though it has been expanded upon significantly. The two optimization objectives are:

- 1)  $\max(T_{Ave})$
- 2)  $\min(T_{Ripple})$

These are calculated using the following formulae:

$$T_{Ave} = mean(T_{Dynamic}) = \frac{1}{N_{Steps}} \sum_{k=1}^{N_{Steps}} T_{Dynamic_k}$$

$$\begin{aligned}
 T_{Ripple} &= rms(\mathbf{T}_{Dynamic} - T_{Ave}) \\
 &= \sqrt{\frac{1}{N} \sum_{n=1}^N |T_{Dynamic_n}|^2} - \frac{1}{N} \sum_{n=1}^N T_{Dynamic_n}
 \end{aligned}$$

where:

$k$  = optimization model time step

$N_{Steps}$  = number of optimization model time steps

$T_{Ave}$  = average torque [Nm]

$T_{Ripple}$  = net RMS torque ripple [Nm]

The parameters used for the optimization are shown in TABLE 6.4. The two objectives for the optimizer fitness function require a dynamic model (see **Chapter 3**) to evaluate. In this table,  $N_{Cycles}$  represents the number of electrical cycles to be run in the dynamic model for each point. All but the last electrical cycle is discarded to account for transient behavior. The number of discrete simulation steps per electrical cycle is represented as  $N_{Steps}$ . The total number of simulation steps evaluated by the dynamic model for each fitness function evaluation is therefore  $N_{Cycles} \cdot N_{Steps}$ . The current sampling frequency ( $f_{Current}$ ) is set at 100 kHz.



Parameter	Value
$N_{Cycles}$	10
$N_{Steps}$	5000
$f_{Current}$	100 kHz
Population Size	150
Elite Count	50
Stall Generation Limit	20
Convergence Tolerance	0.001

TABLE 6.4 Optimizer and model parameters

The torque speed maps were run for the following speed ( $\omega_{RPM}$ ) range:

$$\omega_{RPM} = [1 \quad 50 \quad 100 \quad 150 \quad 200 \quad 300 \quad 400 \quad 500]$$

and the following reference current amplitude ( $I_{Amp}$ ) range:

$$I_{Amp} = [80 \quad 75 \quad 65 \quad 55 \quad 45 \quad 35 \quad 25 \quad 10 \quad 5 \quad 1]^T$$

In order to ensure efficient convergence, several linear and non-linear constraints were used in the optimization process. Some of these constraints are updated depending on the  $I_{Amp}$  index ( $c$ ) and  $\omega_{RPM}$  index ( $s$ ).

### **Linear Constraints**

The first constraint is always enforced, to ensure torque production in the motor:

$$\theta_{ON_{c,s}} < \theta_{OFF_{c,s}}$$

The next set of constraints is updated as the map is generated. They are used to ensure that the firing angles advance as the motor speed increases.

$$\text{for } c = 1 \text{ or } s = 1:$$

$$-90^\circ \leq \theta_{ON_{c,s}} \leq 90^\circ$$

$$90^\circ \leq \theta_{OFF_{c,s}} \leq 180^\circ$$

*otherwise:*

$$-90^\circ \leq \theta_{ON_{c,s}} \leq (0.9 \cdot \theta_{ON_{c,s-1}})$$

$$90^\circ \leq \theta_{OFF_{c,s}} \leq (1.1 \cdot \theta_{OFF_{c,s-1}})$$

### ***Non-Linear Constraints***

The first set of non-linear constraints prevents constant conduction operation to improve motor efficiency:

$$\left[ \min(\mathbf{i}_{ph}) - \frac{I_{Rated}}{100} \right] \leq 0$$

*where:*

$$\mathbf{i}_{ph} = \text{phase current time array}[A]$$

$$I_{Rated} = \text{motor rated current } [A]$$

The final set of non-linear constraints ensures that torque increases as current increases to ensure optimizer consistency:

$$T_{Ave_{c-1,s}} - T_{Ave_{c,s}} \leq 0$$

In addition to updating the constraints as each torque-speed point is solved, the population size is also doubled for the following cases, to ensure that the first set of firing angles are properly converged before using them as the initial constraints:

$$c = 1, s = 1: \text{end}$$

$$s = 1, c = 1: \text{end}$$

### Control Maps

The firing maps shown in Fig. 6.32 were generated after running optimizations for each point in the torque-speed map.

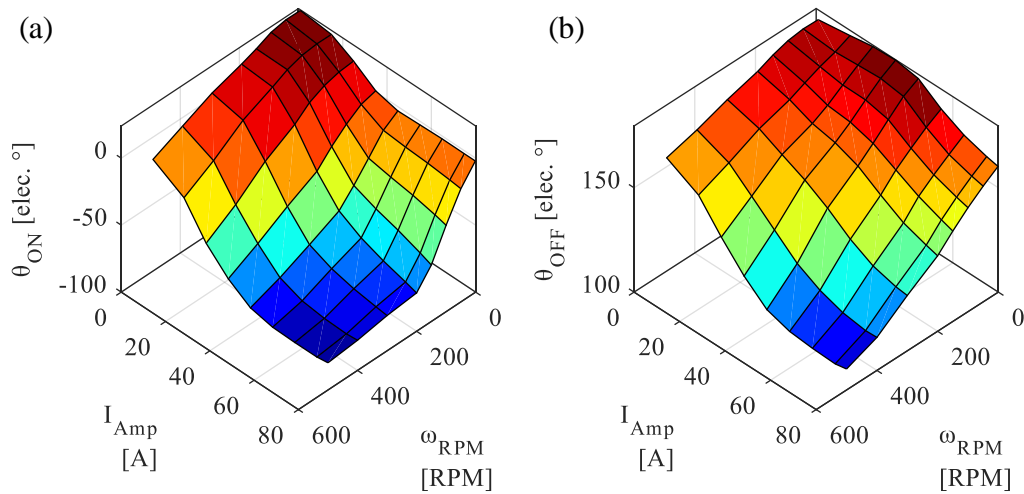


Fig. 6.32 Optimized firing tables for finalized 12/16 design: (a) turn-on; (b) turn-off

## Loss and Efficiency Analysis

Once the firing angle map has been generated, the phase current waveforms from the dynamic model can be used to conduct a loss analysis. The iron losses for each point in the map are calculated using JMAG electromagnetics FEA software, which uses the dynamic model current waveforms as an input.

The FEA analysis accounts for pole wedge geometry, but treats the shaft as air, omits the rotor lamination bolts (which are non-magnetic), and also assumes no 3D leakage effects. Further analysis has shown negligible magnetic impact from the shaft and rotor lamination bolts, but 3D effects do have measurable torque

impacts. However, due to the computational complexity of 3D loss analyses, 2D analyses were necessary.

The sampling frequency for the hysteresis control is set at 100 kHz, but the JMAG model uses down-sampled current waveforms due to computation time constraints. Therefore, the iron loss analysis specifically accounts for changes in the current waveform harmonics caused by the geometry and firing angles. Copper losses are estimated from the RMS phase current and estimated phase resistance, using the following formula:

$$P_{Cu} = N_{Ph} \cdot I_{RMS}^2 \cdot R_{Ph}$$

The torque-speed map versus peak command current is shown in Fig. 6.33.

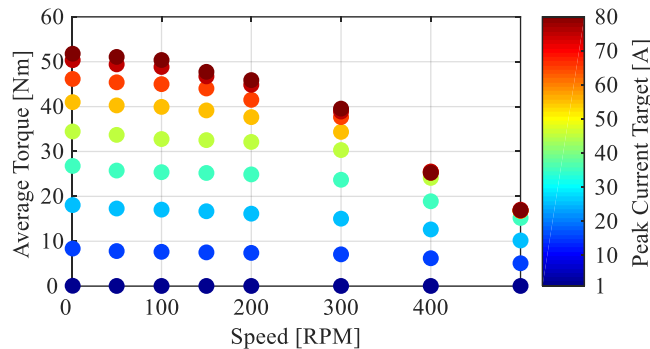
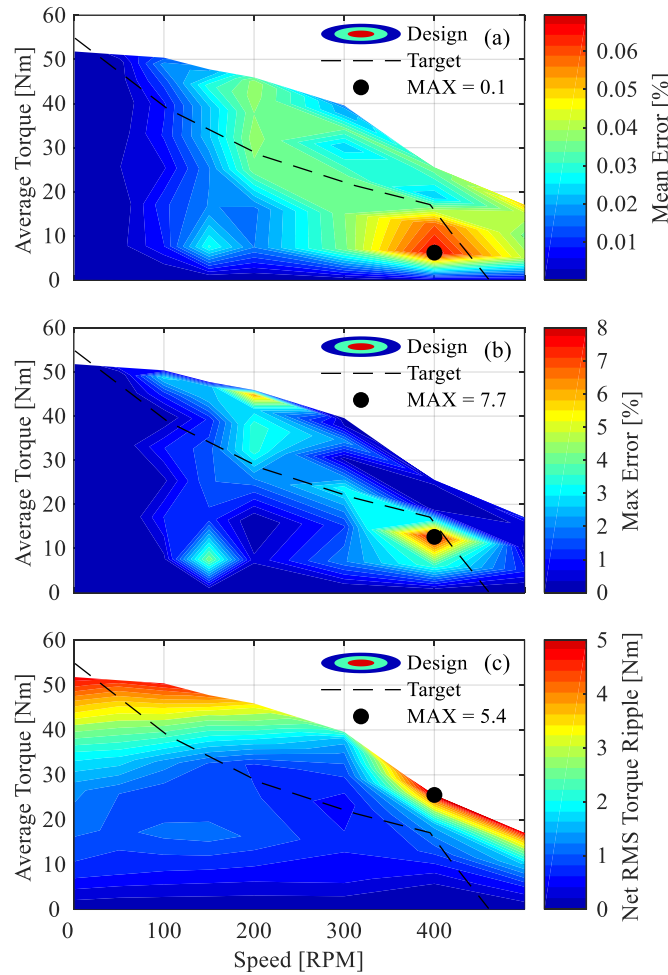


Fig. 6.33 Analyzed torque-speed points (final 12/16 design)

### Torque-Speed – Efficiency Maps

The dynamic model is also validated during the FEA iron loss calculation, to show the torque error for each calculation point, as in Fig. 6.34(a)-(b). The torque ripple is calculated from the FEA torque results in Fig. 6.34(c). The peak torque ripple for the CSRSM is significantly higher than the PMSM (see Fig. 5.13); particularly at high load and low speed. At stall torque, the net RMS torque ripple

is roughly 4.8 Nm for the CSRSM, versus roughly 0.8 Nm for the PMSM machine. At higher speeds, the results are much closer; for example, at 300 RPM at maximum PMSM load, the SRM has about 0.51 Nm net RMS torque ripple, where the PMSM has about 0.35 Nm. It is important to note that the CSRSM torque ripple is calculated based on a voltage source analysis, whereas the PMSM uses a current source analysis. Thus, it is possible that the torque quality of the PMSM at high speed may actually be worse than illustrated in Fig. 5.13.



**Fig. 6.34 Torque-speed maps (final 12/16 design) - with:**  
(a) mean dynamic model vs. FEA error contours; (b) peak dynamic model vs. FEA error contours; (c)  
Net RMS torque ripple contours

FEA iron loss results are summarized in Fig. 6.35; with the maximum iron loss occurring at peak load around 400 RPM.

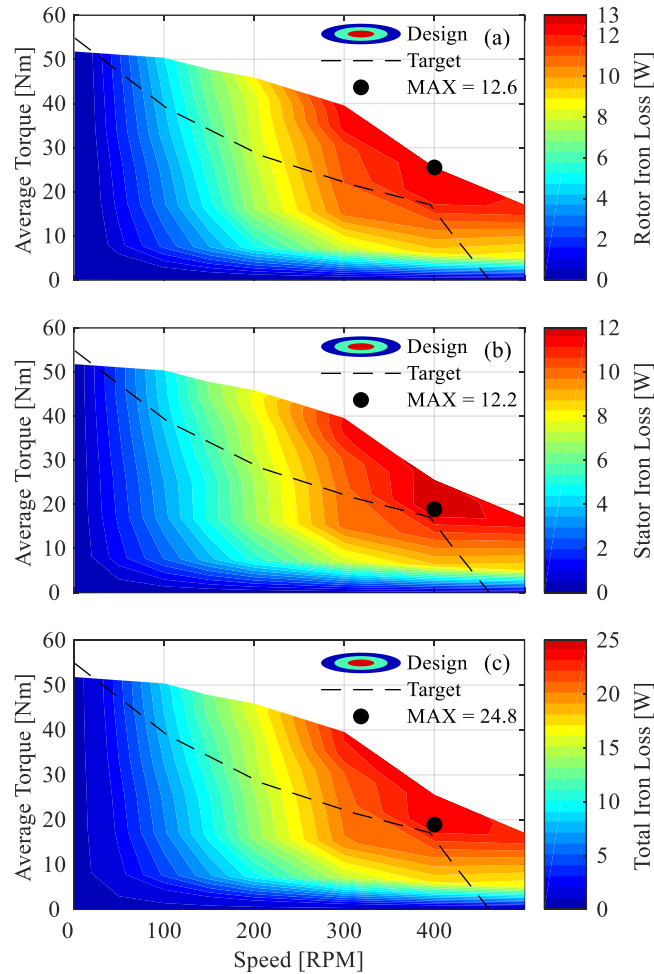


**Fig. 6.35 Torque-speed maps (final 12/16 design) - with:**  
(a) rotor iron loss contours; (b) stator iron loss contours; (c) total iron loss contours

The RMS current and copper loss maps are shown in Fig. 6.36. As is expected, both graphs have the worst losses at peak load and low speed. When comparing Fig. 6.35 and Fig. 6.36, it is clear that copper loss dominates for this low speed e-bike application.

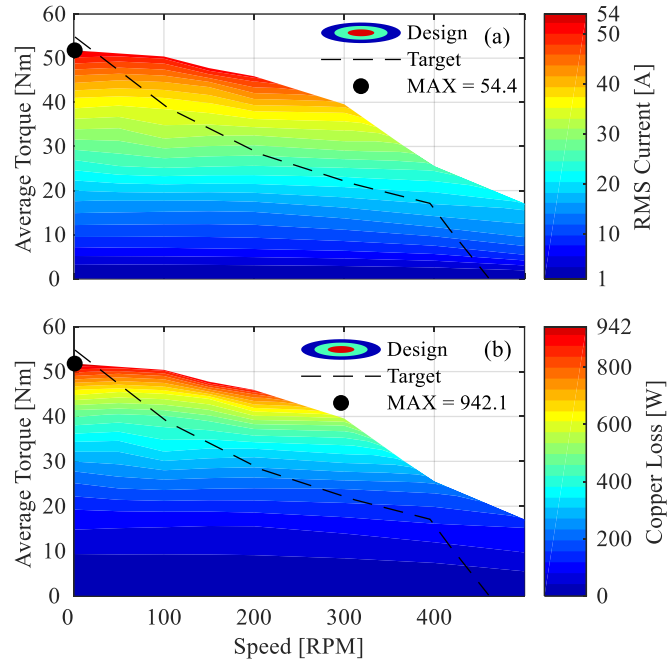


**Fig. 6.36 Torque-speed maps (final 12/16 design) - with:**  
**(a) RMS phase current contours; (b) copper loss contours**

Finally, the total loss and efficiency maps are shown in Fig. 6.37. With a peak motor efficiency of 85.4%, this motor has a higher efficiency than the PMSM target machine at high speed, and the efficiency is comparable at the maximum speed of 400 RPM.

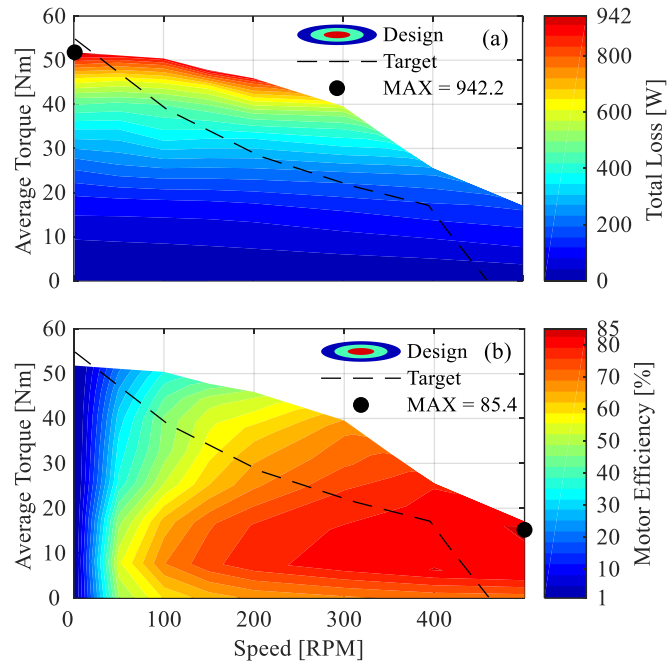


Fig. 6.37 Torque-speed maps (final 12/16 design) – with:  
(a) total loss contours; (b) motor efficiency contours

## Thermal Analysis

The thermal limitations of an SRM are determined by the class of coil insulation; where different insulation types have different peak temperature limitations. Magnet wire rated for 200°C (“Class K”) is cost effective and commonly available, but this analysis considers the use of “Class E” wire rated for 120°C to give a healthy safety margin for this analysis [19].

This thermal analysis uses the loss analysis results for the finalized 12/16 design, as discussed in the *Loss and Efficiency Analysis* section. Observing Fig. 6.36, it is clear that copper loss is dominant for the majority of the operating range. Considering that the SRM suffers from an excitation penalty and that this is a relatively low speed application, this is to be expected.



MotorCAD software uses a lumped parameter thermal network (LPTN) to solve for thermal behavior in a number of typical machine types. The model uses MotorCAD's default values for contact resistances for conduction heat transfer and correlation functions for convection heat transfer. The motor is only cooled by airgap convection (through windage) and airflow around the housing. Fig. 6.38 and Fig. 6.39 show the simplified radial and axial geometry, as modelled in MotorCAD, respectively.

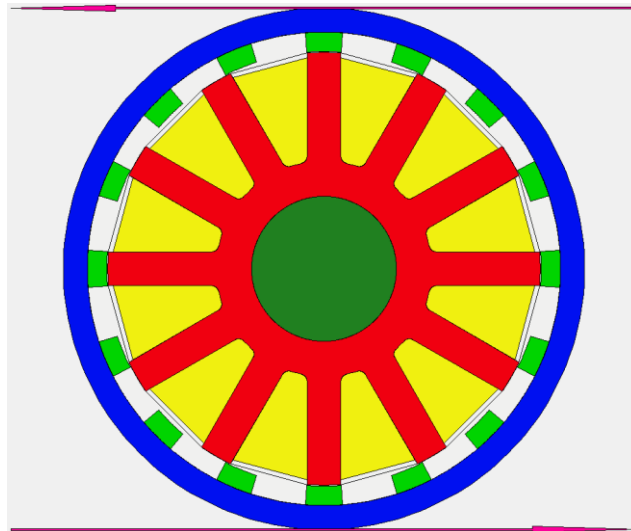


Fig. 6.38 Radial geometry representation in MotorCAD (final 12/16 design)

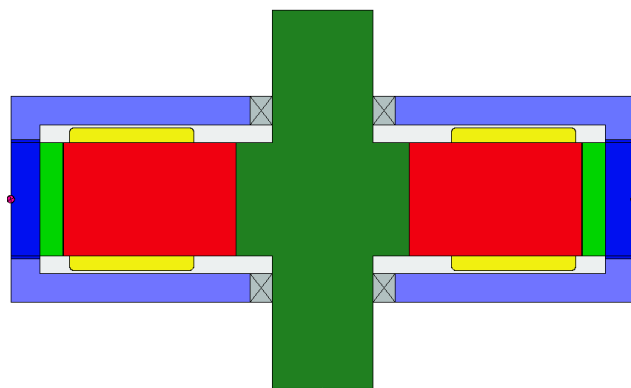
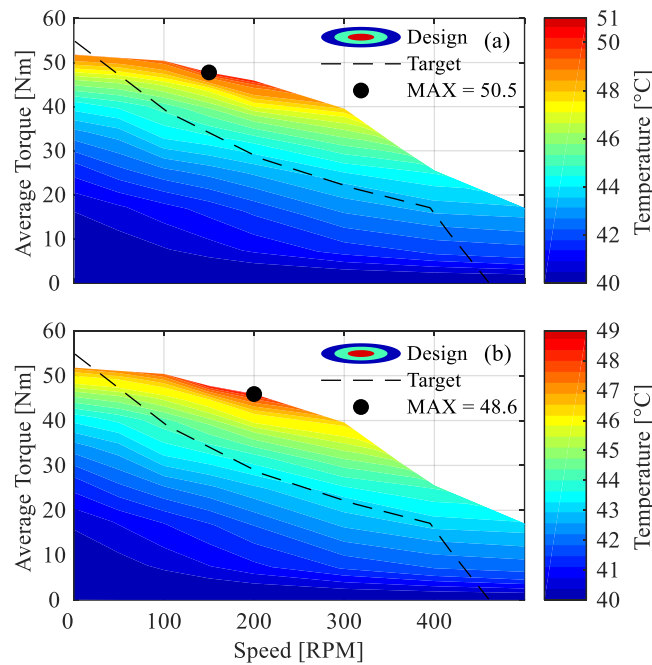


Fig. 6.39 Axial geometry representation in MotorCAD - rotated (final 12/16 design)

## Torque-Speed – Transient Thermal Maps

Using MotorCAD’s ActiveX scripting options it was possible to import the losses at a discrete set of torque-speed operating points in order to characterize the full thermal performance of the motor under steady-state speed conditions, with an assumed ambient temperature of 40°C.

In Fig. 6.40 to Fig. 6.42, the transient thermal performance of different motor components is shown for discrete motor operating points inside the motor torque-speed envelope. These maps were generated by subjecting the motor to a 5-minute transient thermal analysis at each point.



**Fig. 6.40 Rotor transient thermal performance maps after 5 minutes (final 12/16 design):**  
(a) pole; (b) yoke

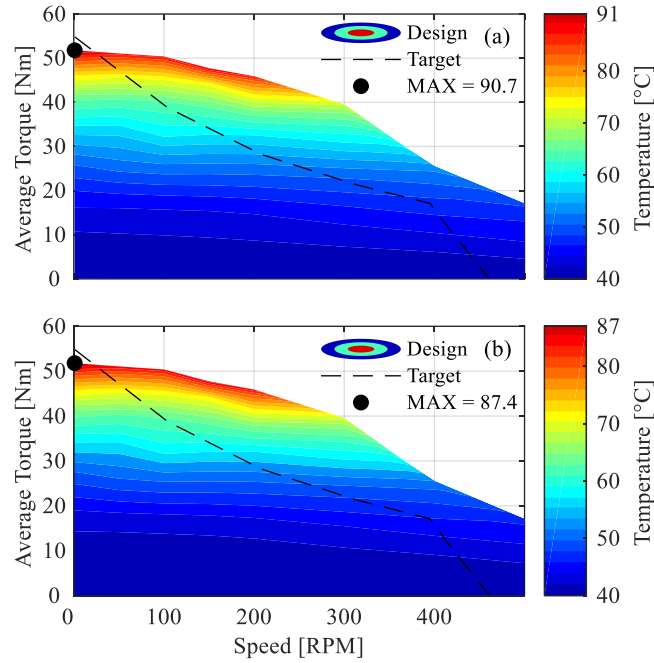


Fig. 6.41 Stator transient thermal performance maps after 5 minutes (final 12/16 design):  
(a) pole; (b) yoke

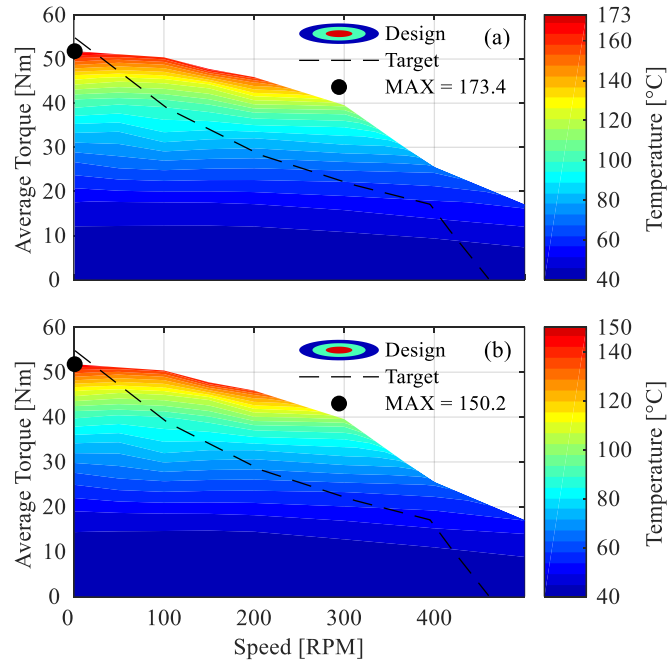


Fig. 6.42 Winding transient thermal performance map after 5 minutes (final 12/16 design):  
(a) peak; (b) average

The time required to reach the winding thermal class for each discrete torque-speed operating point is shown in Fig. 6.43.

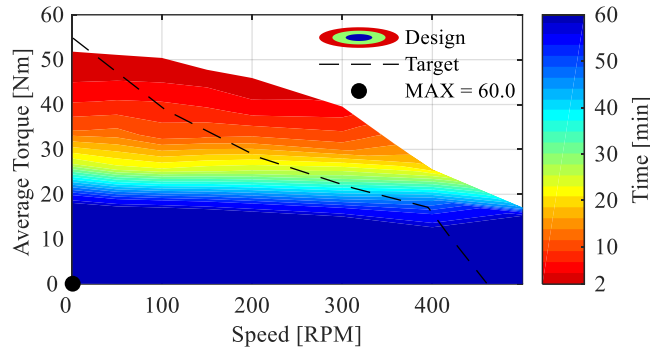


Fig. 6.43 Time to 120°C peak winding temperature (final 12/16 design)

This map was generated by running a 60-minute transient thermal analysis for each operating point, and finding the point where the peak winding temperature reaches 120°C. If the motor does not reach this temperature in 60 minutes, it is assumed to have reached steady state.

If the temperature distributions are compared to the losses in Fig. 6.36, it can be seen that the stator temperature is much more influenced by copper loss than iron loss. The most inefficient region for the motor is at very low speeds, under high load, where the copper loss is high. Under these load conditions the motor windings can still stay below 120°C for at least five minutes, as shown in Fig. 6.43.

## Drive Cycle Response

The analysis up to this point assumes steady state motoring at each operation point within the torque-speed envelope. However, during actual operation, the manner in which the e-bike is driven will have a significant effect on the motor thermal response. Therefore, a 20-minute transient drive cycle (shown in Fig. 6.44) was used to illustrate the real-world thermal performance of the SRM.

The commercial SPMSM is advertised for a maximum speed of roughly 48 km/h, which translates to 461 RPM with a 22-inch wheel. The same wheel size is used for this analysis (see TABLE 6.5). Unlike the PM machine however, the SRM is capable of producing torque at far higher operating speeds.

Parameter	Value	Unit
Wheel Size	22	inches
	0.559	meters
Max. Motor Speed	712	RPM
Wheel Speed	75	km/h
Weight (Vehicle)	50	lbs
Weight (Driver)	200	lbs
Total Mass	113.4	kg
Max. Torque	55	Nm

TABLE 6.5 Drive cycle parameters

Therefore, the drive cycle is scaled so that the SRM can operate at a peak speed of 712 RPM (75 km/h) to illustrate the thermal performance throughout the whole operating envelope. The majority of the drive cycle consists of more realistic speeds under 32 km/h, which is the speed limit for e-bikes in Ontario, Canada [13].

The drive cycle does not account for inertia, so the motor must work to both accelerate and decelerate the e-bike. Driving cycles based on measured road conditions would allow the bike to coast during deceleration instead of continually using regenerative braking; thus this drive cycle is a conservative representation.

Once the drive cycle was specified, the loss for each component during each time interval was determined by interpolating between the discrete torque-speed operating points (see Fig. 6.33). Motor efficiency profiles for motoring and generating are assumed to be identical for thermal considerations. If the drive cycle demands torque that the motor is incapable of achieving, the closest achievable torque was chosen.

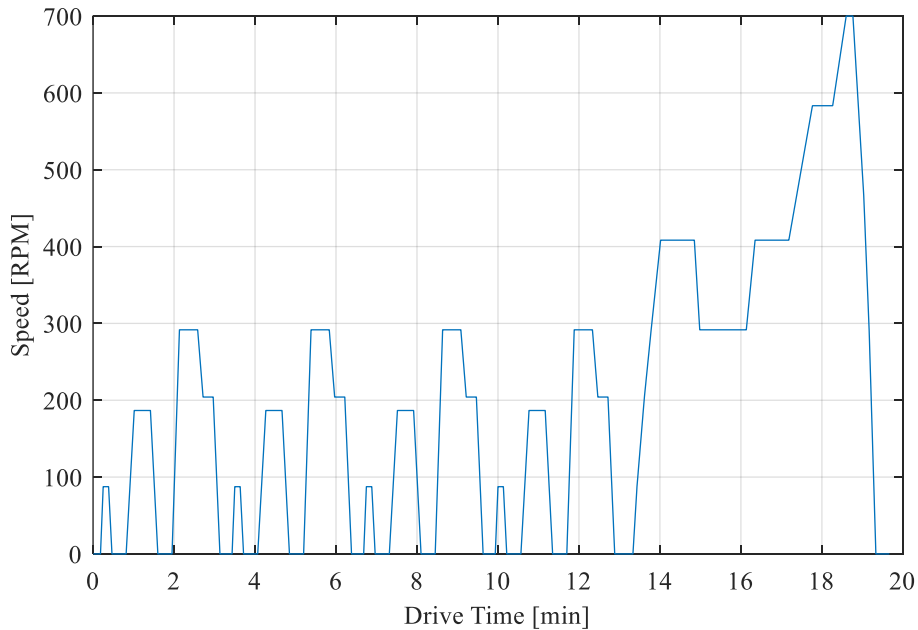


Fig. 6.44 Speed-time e-bike drive cycle

In Fig. 6.45, the torque demanded for the drive cycle exceeds the motor's capabilities near the end of each cycle. This is expected since this region was designed to test the thermal response when the motor is pushed to its limits.

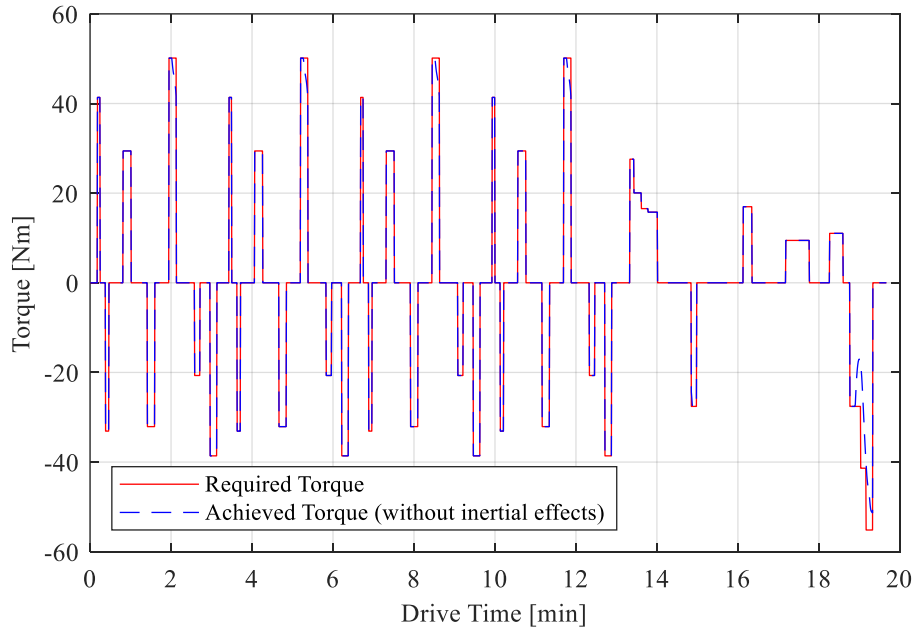


Fig. 6.45 Torque-time e-bike drive cycle

Fig. 6.46 shows the drive cycle transient thermal response of the motor. The high torque, low speed region of the torque-speed map is the most inefficient region for this motor. In the drive cycle, the motor operates largely within this region and thus we would expect poor thermal performance. Yet, the temperature response over 20 minutes shows a maximum winding temperature well below the 120°C limit. As the maximum temperatures remain approximately 40°C below the wire rating, the motor lifetime should benefit.

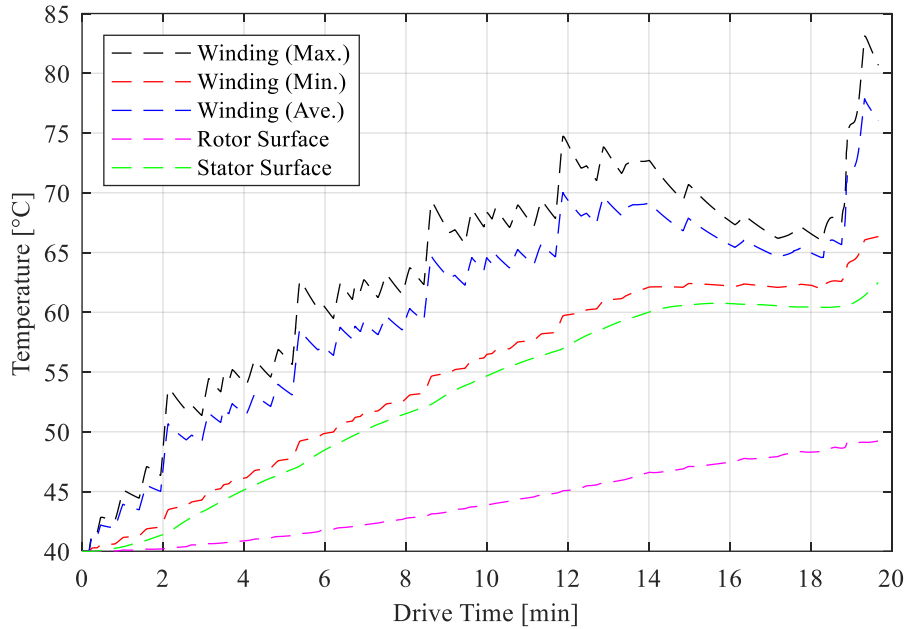


Fig. 6.46 Drive-cycle transient thermal response (final 12/16 design)

The windings are the highest temperature components since copper losses contribute the most to losses in this motor. What is notable is that without any added cooling techniques, and with few available heat transport paths from the stator, the motor still presents good thermal performance. For a short commute, or trip around town it is likely the motor would not experience a temperature rise any greater than the results here indicate. Therefore, the finalized 12/16 geometry with no additional thermal management is considered to be viable, from a thermal perspective.



## FEA Validation

In order to ensure that the dynamic modelling to this point has been accurate, two sample torque-speed points were validated using a switched-voltage electromagnetic FEA analysis in JMAG. This was accomplished by entering the switched voltage waveforms from the dynamic model into JMAG FEA and then comparing the current and torque results.

### 2D Switched Voltage FEA Validation – Critical Points

The first validation point is at 10 RPM and maximum load – where saturation and mutual coupling have significant impacts. Induced voltage is also low, and thus there is significant switching action at this point. The switched voltage waveforms input into JMAG are shown in Fig. 6.47. A 500 Hz maximum switching frequency was used, to decrease the number of time steps required in the FEA analysis.

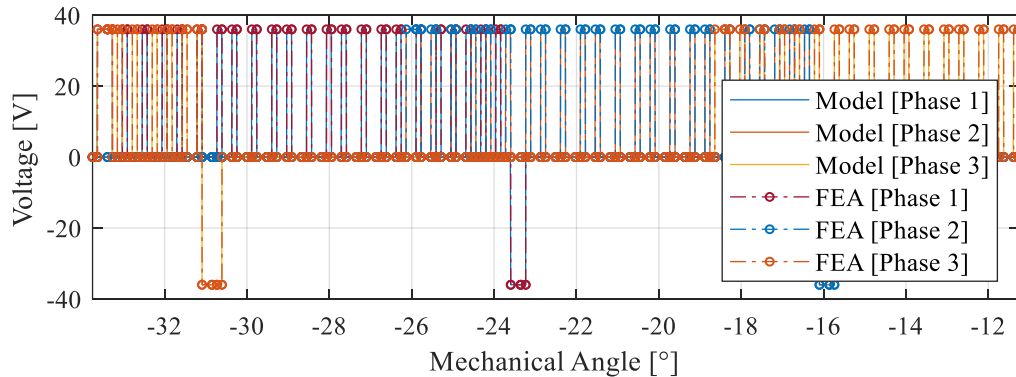


Fig. 6.47 Switched voltage waveforms @ 10 RPM, 75 A reference (final 12/16 design)

Fig. 6.48 shows the torque, current, and flux-linkage validation results, showing good agreement.

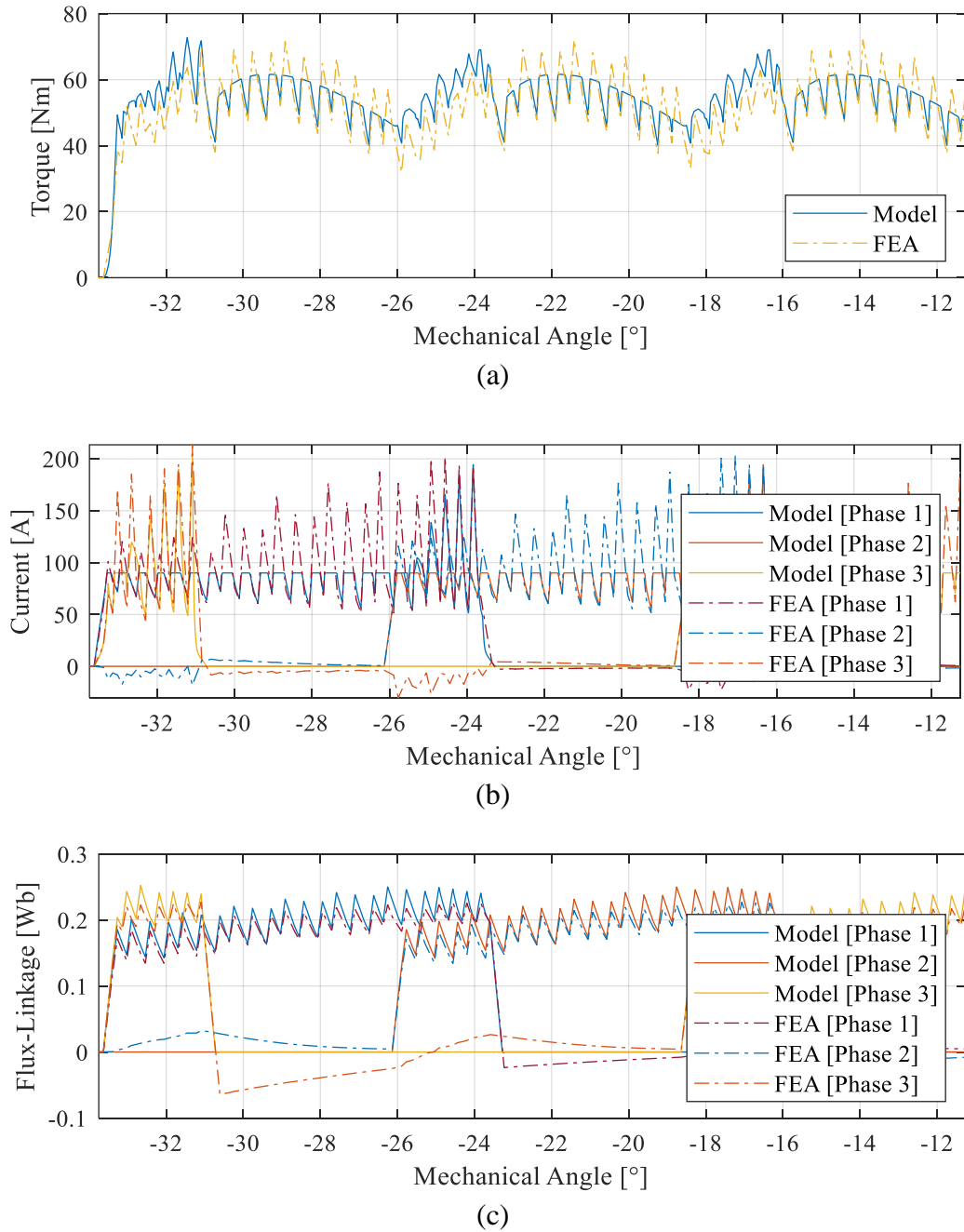


Fig. 6.48 2D switched voltage FEA validation @ 10 RPM, 75 A reference (final 12/16 design):  
(a) torque; (b) phase current; (c) phase flux-linkage

The final validation point is at the maximum PMSM speed of roughly 400 RPM and maximum load, where phase advance is significant and less switching occurs. The switched voltage waveforms input into JMAG are shown in Fig. 6.49. A 100 kHz maximum switching frequency was used.

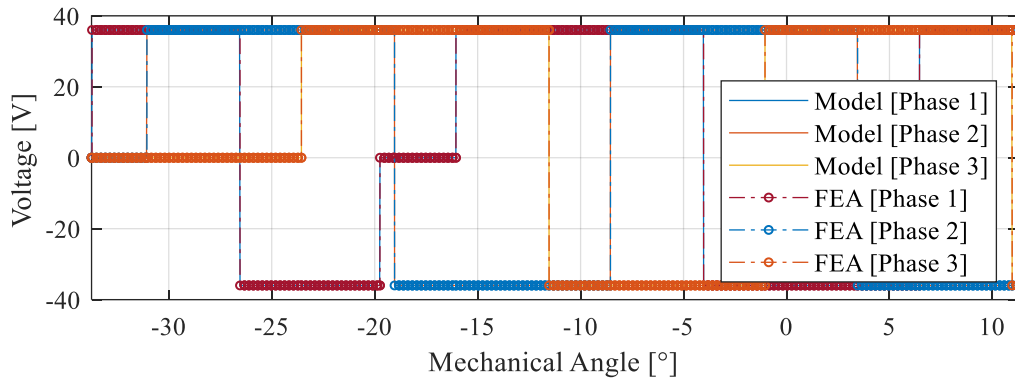


Fig. 6.49 Switched voltage waveforms @ 400 RPM, 75A reference (final 12/16 design)

Fig. 6.50 shows the torque, current, and flux-linkage validation results, showing excellent agreement.

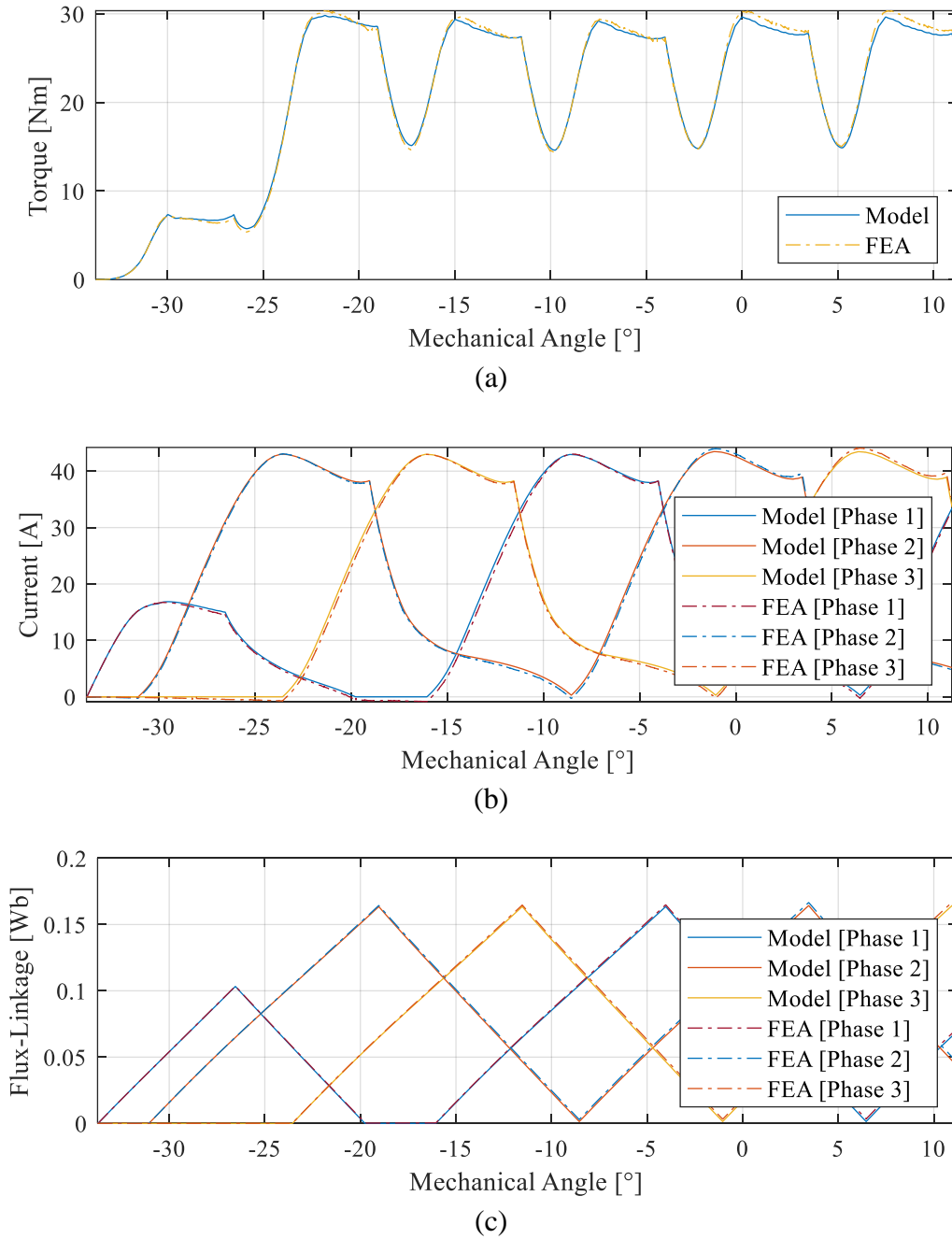


Fig. 6.50 2D switched voltage FEA validation @ 400 RPM, 75 A reference (final 12/16 design):  
(a) torque; (b) phase current; (c) phase flux-linkage

## Structural Analysis

The prototype SRM and commercial PMSM have the same overall package dimensions, but the interior of the SRM was designed to maximize coil space and it also utilized a different shaft design to accomplish this. Since these parts have been re-designed, a structural analysis has been conducted to demonstrate the feasibility of the designs. Static finite element mechanical stress analyses were conducted on the critical components of the final 12/16 prototype motor; namely the end-caps and shaft, using ANSYS Mechanical FEA. This analysis is detailed in *Appendix B*.

## Summary

A novel exterior-rotor switched reluctance motor was engineered using a design space exploration method, where each geometry parameter was varied to find the best performing design. 12/8, 12/16, 12/20, and 12/28 pole configurations were analyzed and compared. The 12/16 design was found to be most suitable for this application, as it fits the torque speed requirements well while also balancing torque ripple and efficiency more effectively than the 12/8 design.

After the electromagnetic design, the finalized motor was analyzed in depth; and the firing angle optimization, loss analysis, thermal analysis, and structural analysis were discussed in detail. The finalized motor was found to have a peak motor efficiency of 85.4%, which is higher than the PMSM machine. The torque performance is comparable with the PMSM machine at low speed, and superior at high speed when considering 2D electromagnetic effects. The torque ripple was found to be higher than the PMSM at low speed, but similar at higher speeds when comparing the same torque-speed points. Both thermal and structural analyses support the feasibility of the design. Finally, the dynamic modelling used for the control optimization was validated against 2D JMAG FEA, and was shown to be accurate.

# Chapter 7

## Experimental Verification: Non-Coupled 12/16 Switched Reluctance Motor

### Introduction

The finalized design of the non-coupled switched reluctance motor was validated experimentally to ensure that the analyses accurately reflected its performance capabilities. It is important to note that the motor prototype was built with validation purposes in mind, and thus the mechanical design was not optimized for mass commercial manufacturing. This chapter discusses the manufacturing tolerances, assembly process, assembly testing, and dynamometer performance testing of the prototype motor.

### Additional Design Considerations

In addition to the magnetic, thermal, and structural analyses conducted on the prototype motor, as discussed in *Chapter 6*, there are additional design decisions that have to be made to finalize the prototype motor. These design decisions include the assembly component selection and tolerance choices, which directly affect the manufacturing complexity and cost of the motor. The components of the final motor prototype are detailed in Fig. 7.1 and the manufactured prototype is detailed in Fig. 7.2.

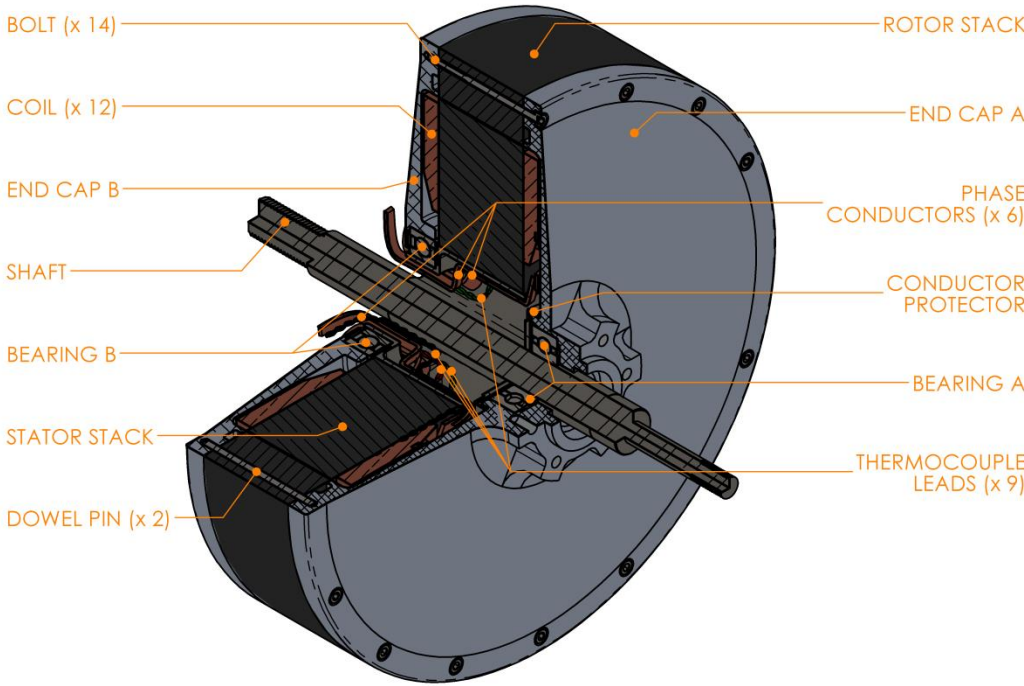


Fig. 7.1 Assembly component detail (12/16 CSR prototype)

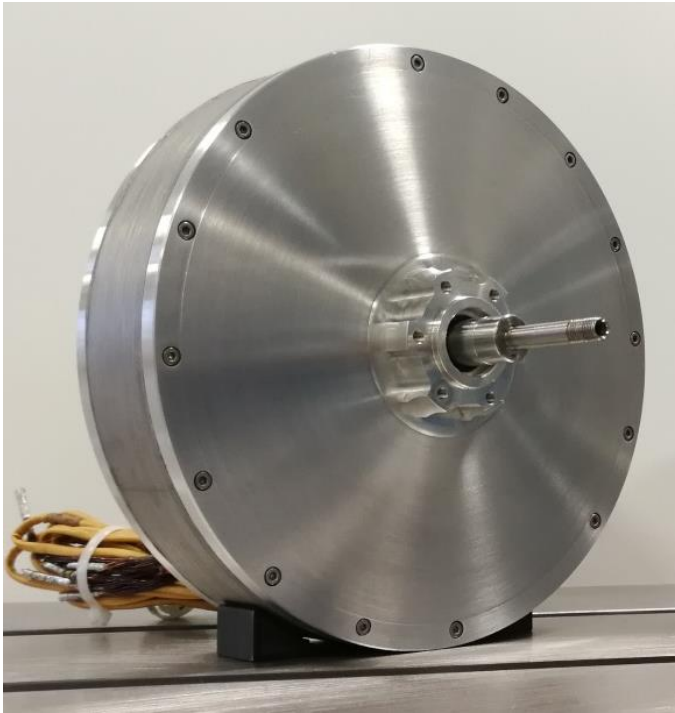


Fig. 7.2 Manufactured prototype 12/16 CSR



## Main Bearing Selection

There are several different types of ball and roller bearings suitable for the main bearings of the motor; each with their inherent advantages and disadvantages. Deep groove radial ball bearings were selected as the main bearings for this motor for several reasons:

- a) Suitable speed and radial loading capabilities
- b) Good resistance to axial loading
- c) Does not have stringent preloading requirements (unlike angular contact ball bearings, for example)
- d) Widely available, used in the commercial PMSM

In the final prototype design, the phase conductors pass through the center of the stator shaft, just as they do for the commercial PMSM. However, unlike the PMSM, there are two conductors per phase (asymmetric-bridge), the effective cross-sectional area of the phase conductors is larger (to decrease copper loss), and additional thermocouple wires were added (for validation and future research). The original PMSM passed all the conductors through a keyway in the shaft, but this was not possible due to these aforementioned factors. In order to accommodate the larger conductor bundle, the shaft design was modified so that the bearing on one side is larger than the other side, as shown in Fig. 7.3.

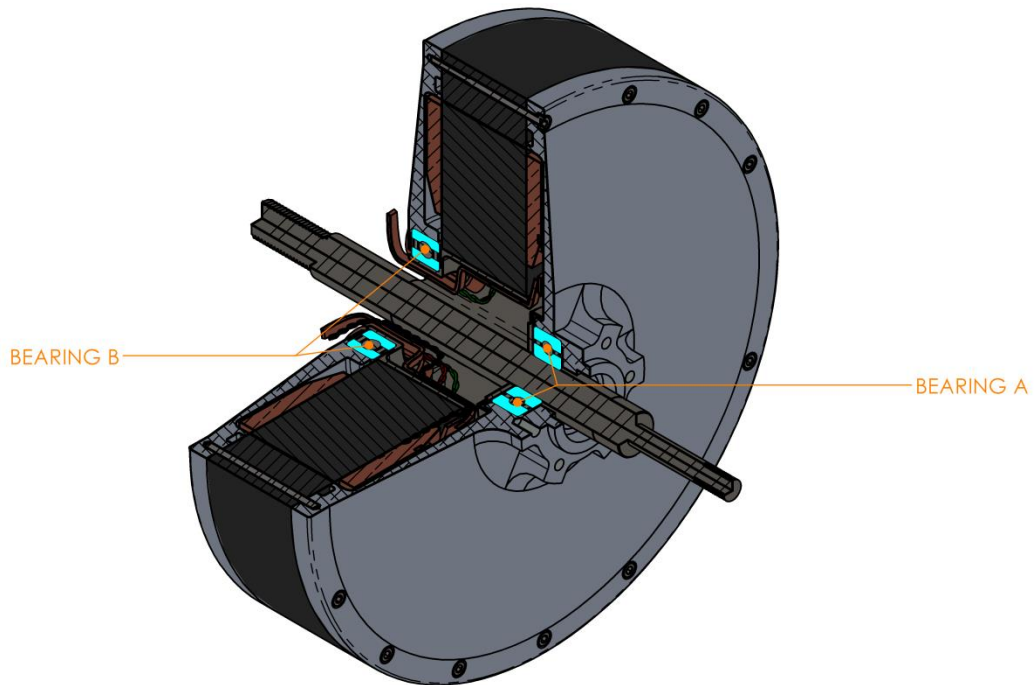


Fig. 7.3 Main bearings – cross-section highlighted in cyan (12/16 CSRМ prototype)

This allows for the same mounting flange to be used on one side, while leaving plenty of room for the phase conductors to exit the machine. The bearing specifications are summarized in TABLE 7.1, which is adapted from the bearing datasheets [20] and [21]:

<b>Bearing</b>	<b>A</b>	<b>B</b>
Bore Diameter [mm]	17	40
Outer Diameter [mm]	40	62
Static Radial Load [N]	1050	2250
Dynamic Radial Load [N]	2200	3050
Maximum Speed [RPM]	12000	11000
Clearance Designation	C3	C0
Seals	Double Sealed	Double Sealed

TABLE 7.1 Main bearing specifications

### **Bearing Preload**

The bearings were preloaded axially using a wave-spring washer for two primary reasons:

- a) Compensate for axial tolerance deviation
- b) Compensate for play in bearing to improve bearing life

The inner race of each bearing has a sliding fit on the shaft, so that the rotor “floats” on the shaft and can slide axially by a small degree. A wave spring washer was chosen over other washer types due to the constant spring coefficient (unlike Belleville washers, for example), force capabilities, and spring coefficient selection. The washer itself was chosen for its allowable deformation and spring coefficient, to ensure that the bearings are sufficiently preloaded. A rough estimation of the amount of preload required for deep groove radial ball bearings is based on the following formula [22]:

$$F_{Preload} = 4d \text{ to } 8d$$

where:

$$F_{Preload} = \text{preload force [N]}$$

$$d = \text{nominal bearing bore diameter [mm]}$$

The required preload force for each bearing is summarized in TABLE 7.2.

<b>Bearing</b>	<b>A</b>	<b>B</b>
Bore Diameter, $d$ [mm]	17	40
Minimum $F_{Preload}$ [N]	68	160
Maximum $F_{Preload}$ [N]	136	320

TABLE 7.2 Bearing preload guidelines

However, for this prototype, the axial preload force was reduced, as the motor was not going to be subjected to significant axial loading under test conditions. The primary reason for this was to reduce friction in the testing setup, as this was not accounted for in the motor modelling.

## Rotor Assembly

The rotor assembly consists of the rotor lamination stack, endcaps, rotor lamination slot fillers, and connecting hardware, as shown in Fig. 7.4.

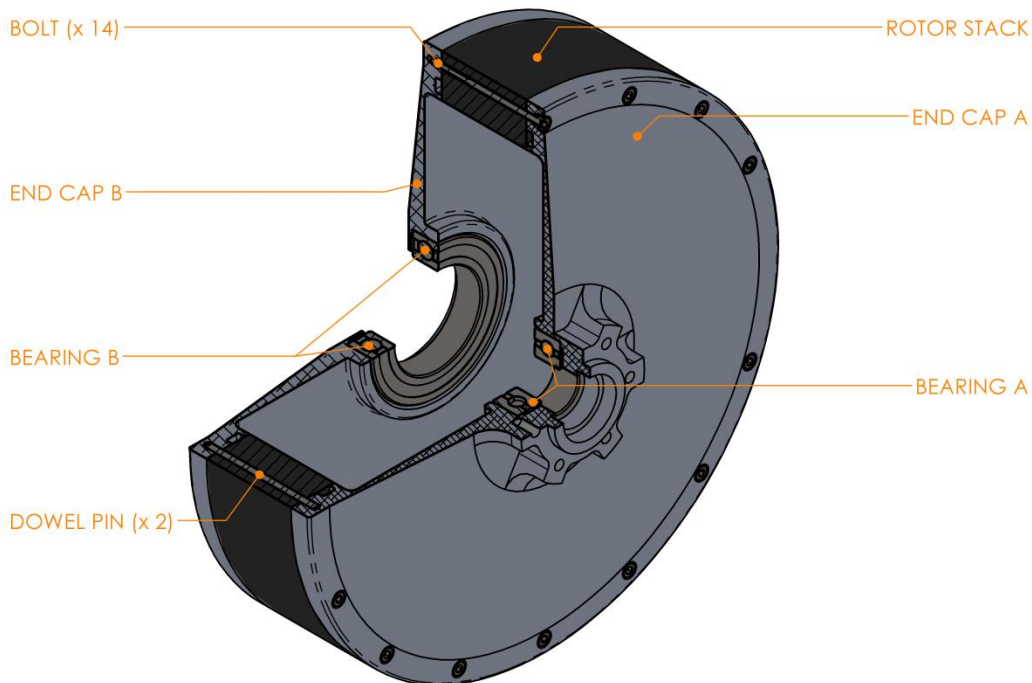


Fig. 7.4 Rotor assembly detail (12/16 CSR prototype)

The two dowel pins are used to align the rotor stack and endcaps, while the bolts retain the assembly axially. Non-magnetic stainless steel bolts and dowel pins were used to avoid magnetic impacts, and JMAG electromagnetic FEA analyses showed negligible torque and voltage impacts from adding the through holes in the rotor stack.

Filler material was added to the rotor slots to reduce windage loss and noise. Silicone rubber material was used for this purpose, as it is low cost, has a high enough temperature resistance (maximum 260°C as per the product specifications

[23]), and can easily conform to the rotor shape with minimal manufacturing work required. The thermal expansion coefficient of the material is also low to ensure that it does not expand and breach the airgap when the motor heats up. Finally, the material is not hydroscopic like some of the alternative plastic materials are. The rotor slot filler material is retained by grooves in each endcap. The manufactured rotor assembly, with slot fillers installed, is shown in Fig. 7.5.

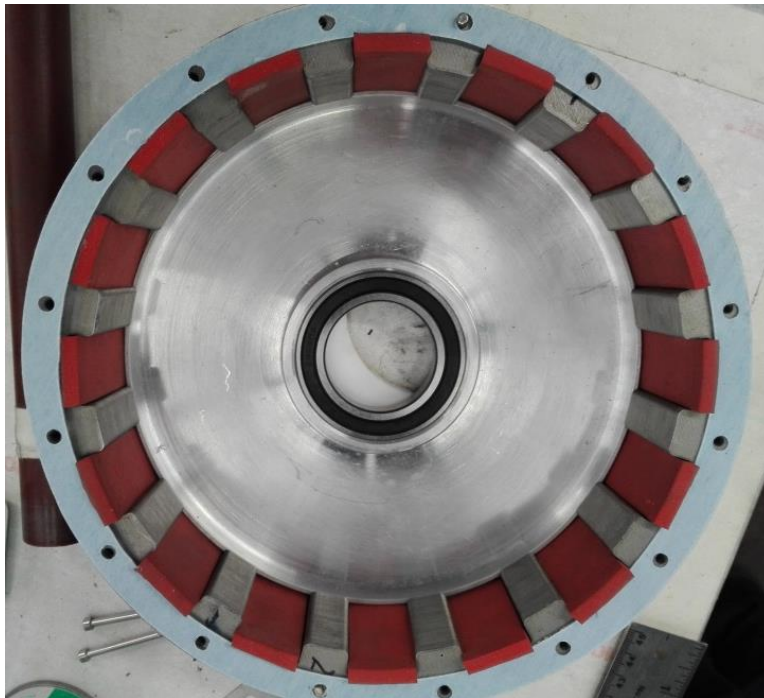


Fig. 7.5 Manufactured rotor assembly (end cover A removed for inspection)

## Stator Assembly

The stator assembly consists of the stator lamination stack, shaft, coils, insulation, thermocouples, conductor protector, and slot wedges, as shown in Fig. 7.6.

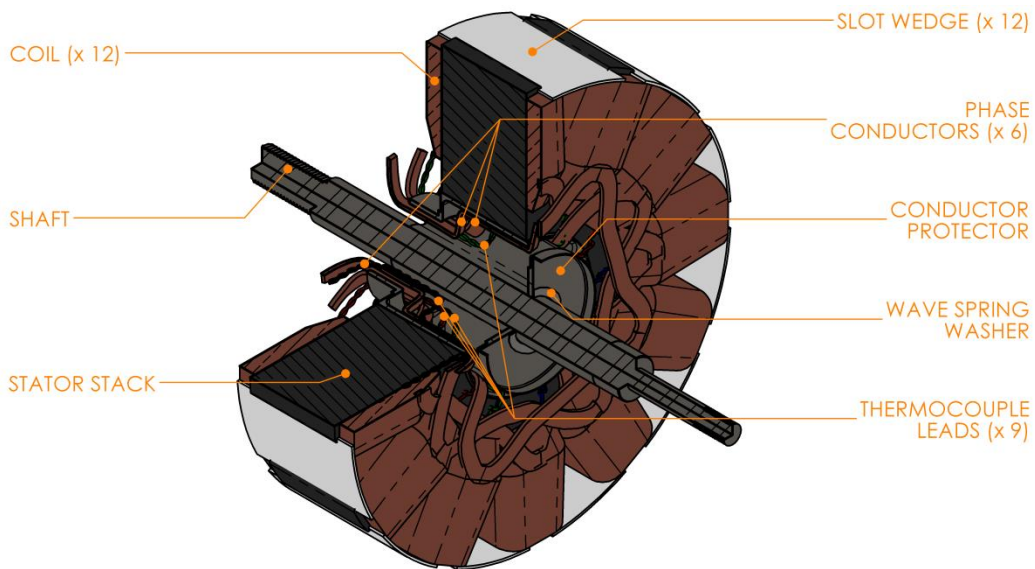


Fig. 7.6 Stator assembly detail (12/16 CSR prototype)

Since this is an external rotor motor, the shaft supports the main bearings and rotor assembly and is press fit into the center of the stator stack. The coils are retained using rigid slot wedges and Nomex insulation is used to insulate the coils from the stator stack. Each coil is retained using rigid slot wedges. The stator assembly with coils was vacuum resin infused to enhance vibration resistance and motor reliability, as just as the PMSM stator was.

There is less space inside the SRM housing compared to the PMSM. Therefore, the “conductor protector” part was machined to protect the phase

conductors from the rotating surfaces of the motor. The phase conductors and thermocouples were fixed in place using epoxy.

The insulation and finished stator assembly (before thermocouple insertion) are shown in Fig. 7.7.

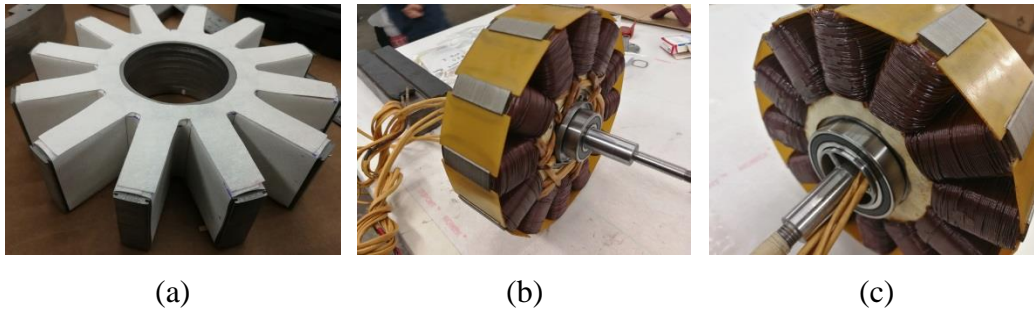


Fig. 7.7 Manufactured stator assembly: (a) insulation; (b) side A; (c) side B.

### *Thermal Measurement*

There are nine thermocouples placed at different locations on each phase of the motor winding. Each phase has one thermocouple at the axial center of the coil, as close to the airgap as possible. The next thermocouple is placed at the axial and radial center of the coil, while the final thermocouple is placed at the base of the coil, on the one side of the motor. This placement gives a good idea of the temperature distribution of the coils, for thermal model validation.

Each phase has the same relative positioning, so that temperatures for a given thermocouple can be checked against the same thermocouple position for the other phases. If the motor and thermocouples are operating correctly, the three phases should have identical temperatures at the same position for each phase. The



positions of each thermocouple for the manufactured prototype are highlighted in Fig. 7.8.

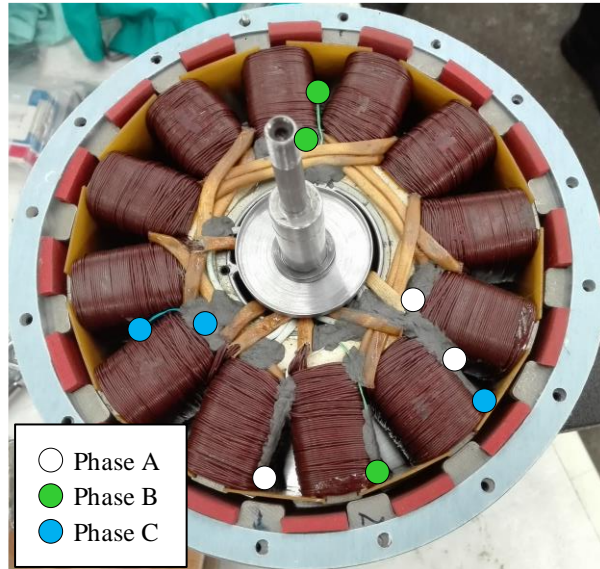
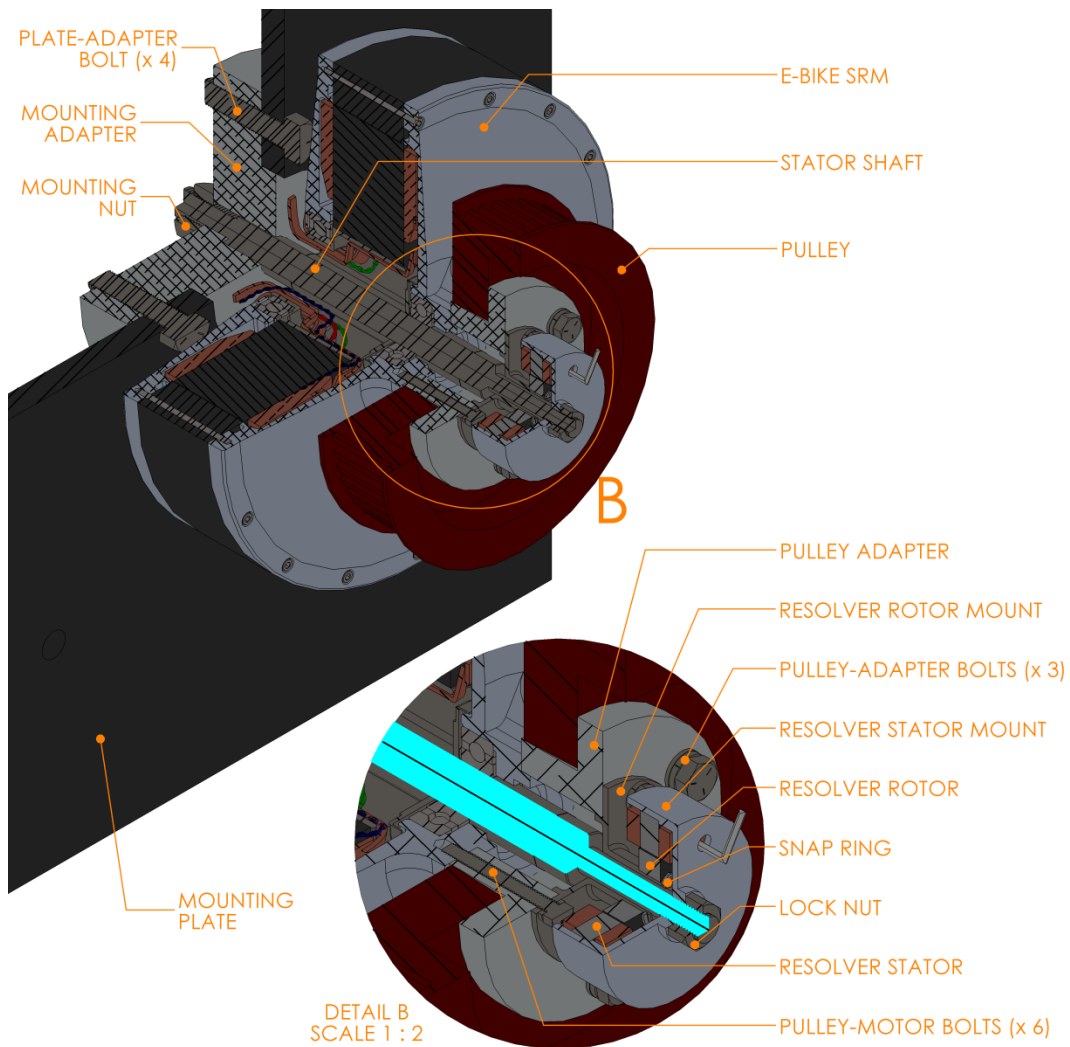


Fig. 7.8 Prototype thermocouple positions (3 per phase)

Originally, twelve thermocouples were to be used in the prototype. The thermocouples of each phase have the same relative positioning, as shown in Fig. 7.8. Using twelve thermocouples, two thermocouples in each phase would be placed at the same position. This would have allowed the thermocouple readings for one location to be double checked to ensure proper thermocouple functioning (independent of checking for motor faults). However, this required the thermocouples to be installed before finishing the winding process due to the limited space for cable routing. The motor assembler did not follow this assembly order, and thus it was not possible to install the extra thermocouples. This was not an issue, as the thermocouples were checked for proper functioning before finalizing the assembly.

## Additional Components

In addition to the motor itself, some components needed to be designed to attach the resolver and to mount the motor assembly to the dynamometer setup, as detailed in Fig. 7.9.



**Fig. 7.9 Resolver, gearing, and mounting detail – shaft cross-section highlighted in cyan (12/16 CSRM prototype)**

Most of these components are the same ones used in the PMSM dynamometer testing setup. The primary difference is that a resolver was added for

the SRM, which required a unique mounting strategy due to the exterior rotor motor design. Ideally, an external rotor resolver would be used for this purpose, but one with suitable dimensions was not able to be sourced. Therefore, a hollow resolver rotor mount is attached to the pulley adapter to hold the resolver rotor, while the shaft on one side of the SRM is extended and threaded to support the resolver stator mount, as highlighted in Fig. 7.9.

The manufactured resolver-rotor/pulley assembly (rotating) is detailed in Fig. 7.10 (a), and the resolver-stator assembly (stationary) is shown in Fig. 7.10 (b).

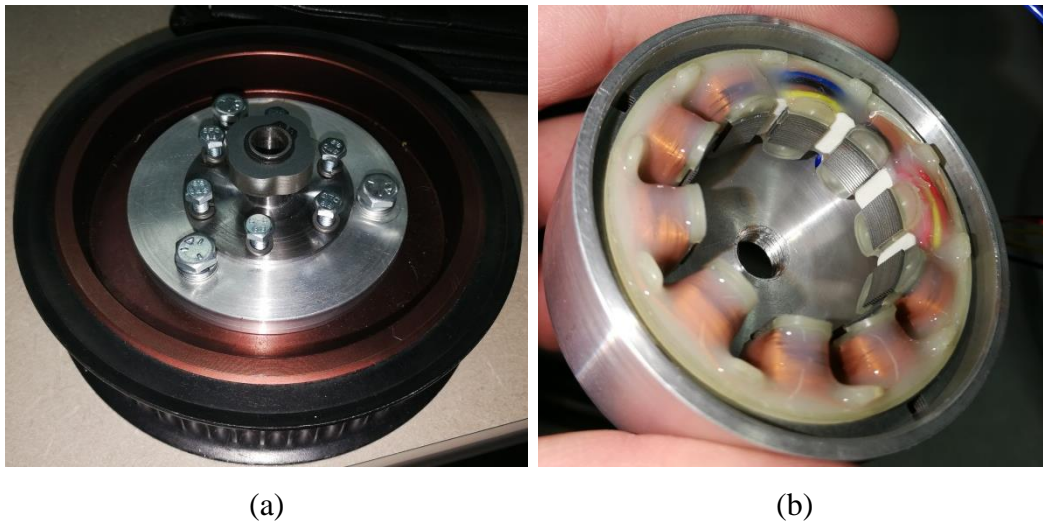
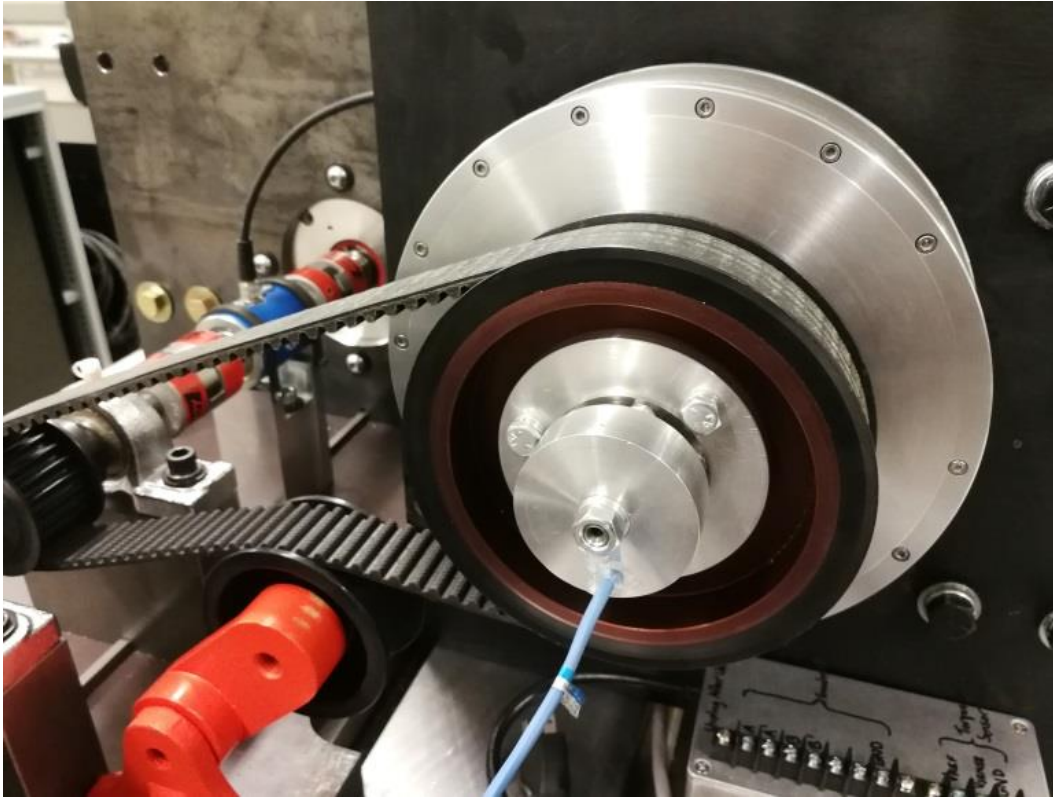


**Fig. 7.10 Additional components: (a) resolver-rotor/pulley assembly; (b) resolver-stator assembly**

Fig. 7.11 shows the entire setup once fully assembled and mounted to the testing bench.



\*

Fig. 7.11 Full assembly, with resolver and gearing system attached (12/16 CSRМ prototype)

## Manufacturing Tolerances

Each part of the finalized design was modeled in Solidworks, and engineering drawings were created to illustrate the manufacturing and assembly requirements for each part. Since the motor was relatively low speed and the airgap was reasonable at 0.4 mm, the tolerances did not need to be excessively tight, but they still needed to be selected correctly to ensure the prototype met expectations. Note: In this section, “OD” represents “outside diameter” and “ID” represents “inside diameter”.

### Bearing Fits

The bearings use standard ISO limits and fits that were selected based on the NTN bearing manufacturer recommendations [22]. Typically, when selecting bearing fits, either the inner or outer race is selected as a tighter fit, while one is a looser fit. Since the bearings must also slide axially to accept the axial wave-spring preload, the looser race should have tolerances that permit a sliding fit.

#### *Inner Race Fit*

The recommended shaft (bearing inside diameter interface) fits for cylindrical-bore radial ball bearings as detailed by NTN in [22] are summarized in TABLE 7.3.

Load Conditions	Load Class	Nominal Shaft OD (Bearing Bore) [mm]	Recommended Shaft Fit
Rotating inner race  OR  Indeterminate direction loading	Light OR variable	< 18	h5
		18 to 100	js6
		100 to 200	k6
		> 200	N/A for ball bearings
	Normal to heavy	< 18	js5
		18 to 100	k5
		100 to 140	m5
140 to 200		m6	
200 to 280		n6	
> 280	N/A for ball bearings		
Very heavy OR shock	> 50	N/A for ball bearings	
Static inner race	Axially sliding	ALL	g6
	Axially fixed	ALL	h6

**TABLE 7.3 Recommended shaft fits for cylindrical-bore radial ball bearings (adapted from Table 7.2 in [22]) – final selection highlighted.**

In the e-bike SRM design, the outer race of each bearing is pressed into its respective aluminum endcap, while the inner races slide axially on the shaft. The shaft was chosen as the sliding fit as it is less wear-prone than aluminum and is not rotating with the e-bike wheel.

When considering the inner race of each bearing, a “g6” shaft OD tolerance is selected from TABLE 7.3. This is due to the need for a sliding fit, and the fact that the shaft is the stationary part in the setup.

***Outer Race Fit***

The recommended housing (bearing outside diameter interface) fits for radial ball bearings as detailed by NTN in [22] are summarized in TABLE 7.4.

Housing Type	Load Conditions	Load Class	Recommended Housing Fit
Solid OR Split	Static outer race	ALL	H7
		Heat conducted through shaft	G7
Solid	Indeterminate direction loading	Light to normal	JS7
		Normal to heavy	K7
		Heavy shock	M7
	Rotating outer race	Light OR variable	M7
		Normal to heavy	N7
Heavy (thin wall housing) OR heavy shock load	P7		

**TABLE 7.4 Recommended housing fits for radial ball bearings (adapted from Table 7.2 in [22]) – final selection highlighted.**

Since the outer race is the one subjected to loading, it is necessary to calculate the load range to select the correct fit. NTN defines the load ranges as [22]:

$$\begin{array}{ll} \text{Light Load} & P_r \leq 0.06C_r \\ \text{Normal Load} & 0.06C_r < P_r \leq 0.12C_r \\ \text{Heavy Load} & P_r > 0.12C_r \end{array}$$

where:

$P_r$  = bearing equivalent load (radial)

$C_r$  = basic dynamic load rating (radial)

As discussed in the *Structural Analysis* section, the continuous radial load experienced by the bearings under driving conditions is 686.7 N (1g load). It is assumed that this will be the primary loading case. In reality, the bearings will be subjected to axial loading during cornering and occasional shock loading. However, when considering fits, these will not be the nominal loading conditions, and thus are not used for the load calculations. Special cases like shock loading are separately accounted for, as shown in TABLE 7.4.

The two main bearings share the applied load and the wheel is loaded at the center of the two bearings, meaning that  $P_r$  for each bearing is half the applied radial load (343.35 N per bearing). Based on the dynamic radial load rating for each bearing (TABLE 7.1), the load class for each bearing can be calculated as shown in TABLE 7.5.



Bearing	A	B
$P_r$ [N]	343.35	343.35
$C_r$ [N]	2200	3050
Load Class	$P_r > 0.12C_r$ $343 > 264$ (Heavy)	$0.06C_r < P_r \leq 0.12C_r$ $183 < 343 \leq 366$ (Normal)

**TABLE 7.5 Bearing load conditions for tolerance selection**

After determining the load class, TABLE 7.4 can be used to select the housing fit for each bearing. Since the outer race is rotating, and subjected to normal-heavy load, an “N7” housing ID fit is chosen. Another important note is that the NTN specifications assume steel housings for the bearing, where aluminum is used for this machine. Since aluminum is not as rigid as steel and the thermal expansion with temperature is also higher than steel, a tighter fit can be necessary when the bearing is pressed into aluminum.

When considering production, it would make more sense to use a “P7” fit for each bearing outer race to account for the alloy housing and heavy shock loads experienced when traversing potholes, etc. However, for the prototype an “N7” fit is already tight enough, considering that the bearings will experience very little radial load in the testing environment.

## **Bolt and Dowel Fits**

The rotor stack is retained by the two end caps using fourteen bolts and two dowel pins. The dowel pins are used to accurately align the stack and endcaps, while the bolts retain the assembly axially.

### ***Dowel Pin Fits***

A locational clearance fit was desired for the dowel pins, to provide an accurate, snug fit, while still remaining removable. However, since the dowels do not use ISO standard fits, an equivalent fit was approximated, as calculated in

### ***Appendix F***

### ***Bolt Fits***

A sliding fit was desired for the bolts so they could be easily removed and a snug fit was not required, as the dowel pins already provide angular alignment for the assembly. Since the bolts do not use a standard ISO tolerance, an equivalent fit was approximated, as calculated in *Appendix F*.

### ***Dowel and Bolt Positioning***

The positioning of each dowel pin and bolt is constrained relative to the bearing housing surface datum for each endcap, and relative to the airgap datum for the rotor stack. The positional accuracy was chosen based on industry experience; with a limit of 0.1 mm for the dowels and 0.2 mm for the bolts.

The absolute required positional accuracy can also be calculated depending on the selected fits, by considering the maximum offset for a given fit. For example,

in Fig. 7.12 a clearance fit is desired, and thus the shaft center position can only be offset until the maximum shaft OD reaches the minimum hole ID.

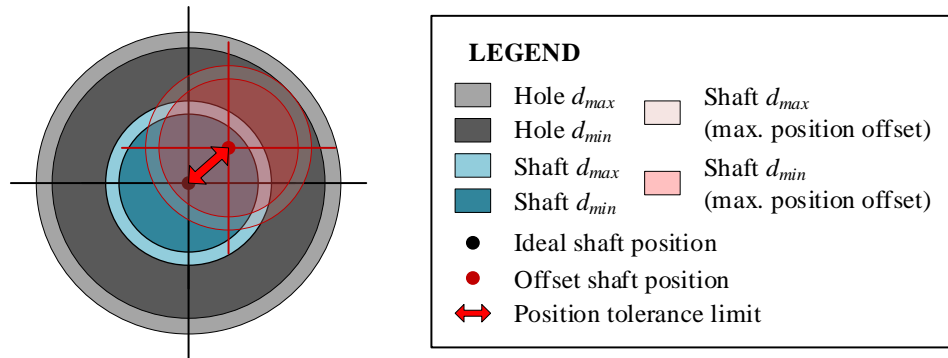


Fig. 7.12 Dowel and bolt positional accuracy tolerance concept

## Resolver Press Fit

### *Stator*

The stator of the Tamagawa TS2225N114E102 resolver is press fit into a custom housing, as illustrated in Fig. 7.9. Since the press-fit is the only means of retaining the resolver stator, it is important that the fits are correctly selected. It was desired to have a locational interference fit for this purpose, but the resolver stator does not use a standard ISO tolerance. Therefore, the required fit to achieve an acceptable amount of clearance was calculated (see *Appendix F*).

## Radial Tolerances

The different radial tolerances and critical dimensions are illustrated in Fig. 7.13.

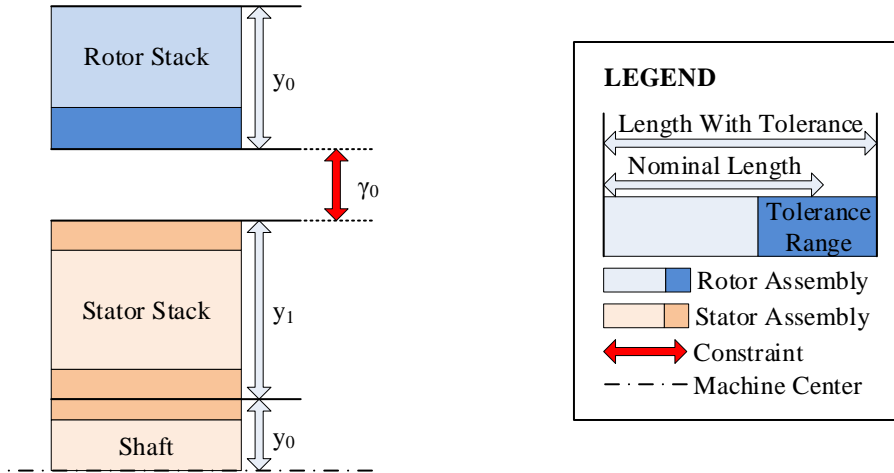


Fig. 7.13 Radial tolerances (12/16 CSR prototype)

### *Shaft-Stator*

The radial tolerances are set using standard fits. The stator stack is attached to the shaft by an interference fit. However, any retained stress in the stator laminations from a heavy interference fit will negatively affect the magnetic performance, and thus it was desired to use as little interference as possible while still retaining the stack. A hole-basis locational interference fit (H7/p6) was chosen for this purpose.

In order to reduce the pressing forces required and to ensure the pressing process did not misalign the stator stack, the stator ID was heated using an induction heater (Fig. 7.14) and the shaft was cooled before being pressed into the stator (Fig.

7.15). It was also necessary to reduce pressing forces because the shaft was not installed before winding the stator stack.



Fig. 7.14 Stator heating using induction heater (12/16 prototype)



Fig. 7.15 Shaft cooling before insertion (12/16 prototype)

The pressing procedure is detailed in Fig. 7.16.



Fig. 7.16 Shaft insertion procedure

In addition to the fit itself, the shaft was originally going to be spot welded in three places to ensure stack retention. However, this required the shaft to be installed before winding the stator and this assembly order was not followed. Therefore, a small set screw was tapped on the edge of the stator-shaft interface to ensure that the stack does not slip at the motor's maximum torque output.

### *Airgap*

In order to provide an accurate, consistent airgap length, and accurate pole geometry at an airgap, a profile tolerance of 0.05 mm applied to the stator pole tip geometry at the airgap. This ensures that the entire pole tip geometry is within 0.05mm of deviation from the design geometry, at any location. This is the most stringent tolerance used in the entire motor, but is necessary to ensure balanced magnetic pull, to avoid eccentricity, and to ensure optimal machine performance.

This is typically accomplished by grinding the airgap surface after assembly, to account for any deflection from pressing the shaft into the stator stack.

The rotor pole tips have the same 0.05 mm profile tolerance applied, for the same reasons as the stator. Though the profile tolerance constrains the entire pole tip profile (not just the diameter), it can still be used to calculate the airgap tolerance bounds, as discussed in *Appendix F*.

### **Axial Tolerances**

The axial tolerances were determined using a tolerance stack-up, allowing individual feature tolerances to be selected so that lumped dimensions are within a specific tolerance range. This is critical to ensure that assembled parts fit together correctly. Since the motor has an interior stator and exterior rotor, the tolerance stack-up must be performed on each subassembly separately. An axial pre-load spring is used to accommodate for the difference in axial length between the rotor and stator assemblies (as illustrated in Fig. 7.17).

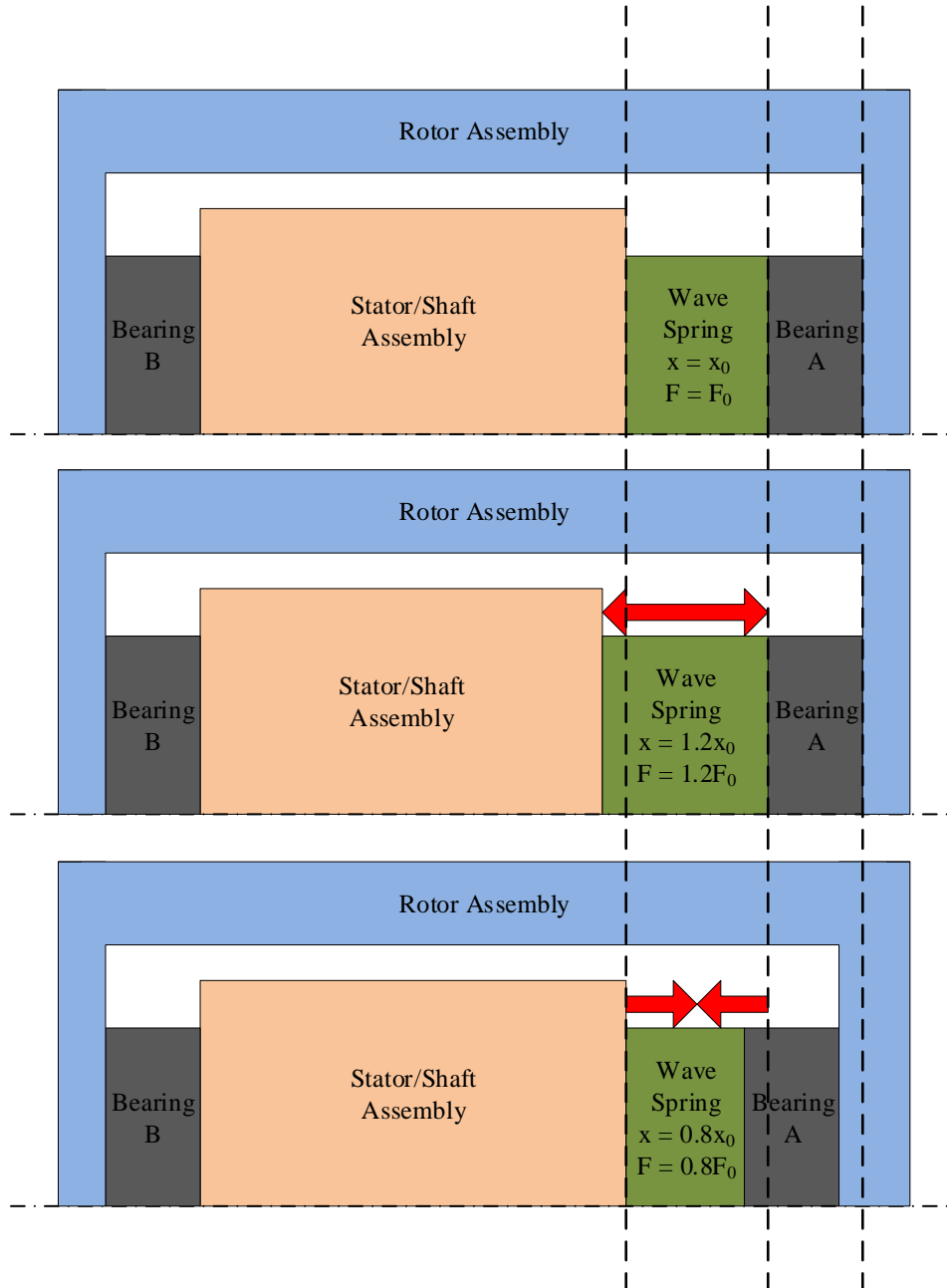


Fig. 7.17 Axial pre-load spring operating principle (12/16 CSRSM prototype)

In this case, the sum of all the rotor axial tolerances between the bearing mounting faces will constrain the axial distance between bearings. Ideally, this distance is equivalent to the sum of the axial tolerances for all the stator components



between the bearings. However, in reality this will vary, since each part has a tolerance range. It is important to ensure that there is enough inter-bearing axial space for the stator assembly, so the stator axial tolerances are chosen to limit the maximum axial length of the stator stack. Then the axial preload spring can be used to take up any remaining axial space.

In addition to simply ensuring that the parts fit together, it is also critical to ensure that the rotor and stator stacks are axially centered relative to each other, to prevent torque loss. Finally, as the stator assembly shifts axially relative to the rotor assembly, the axial pre-load spring will expand or contract. This will affect the preload force, and this must be accounted for.

When considering all factors, there are six critical reference positions for the tolerance stack-up:

- 1) Bearing A (outer race – left edge)
- 2) Rotor Stack (left edge)
- 3) Stator Stack (left edge)
- 4) Stator Stack (right edge)
- 5) Rotor Stack (right edge)
- 6) Bearing B (outer race – right edge)
- 7) Pre-load spring (right edge)

The interaction between motor axial dimensions is detailed in the axial tolerance stack-up illustrated in Fig. 7.18.

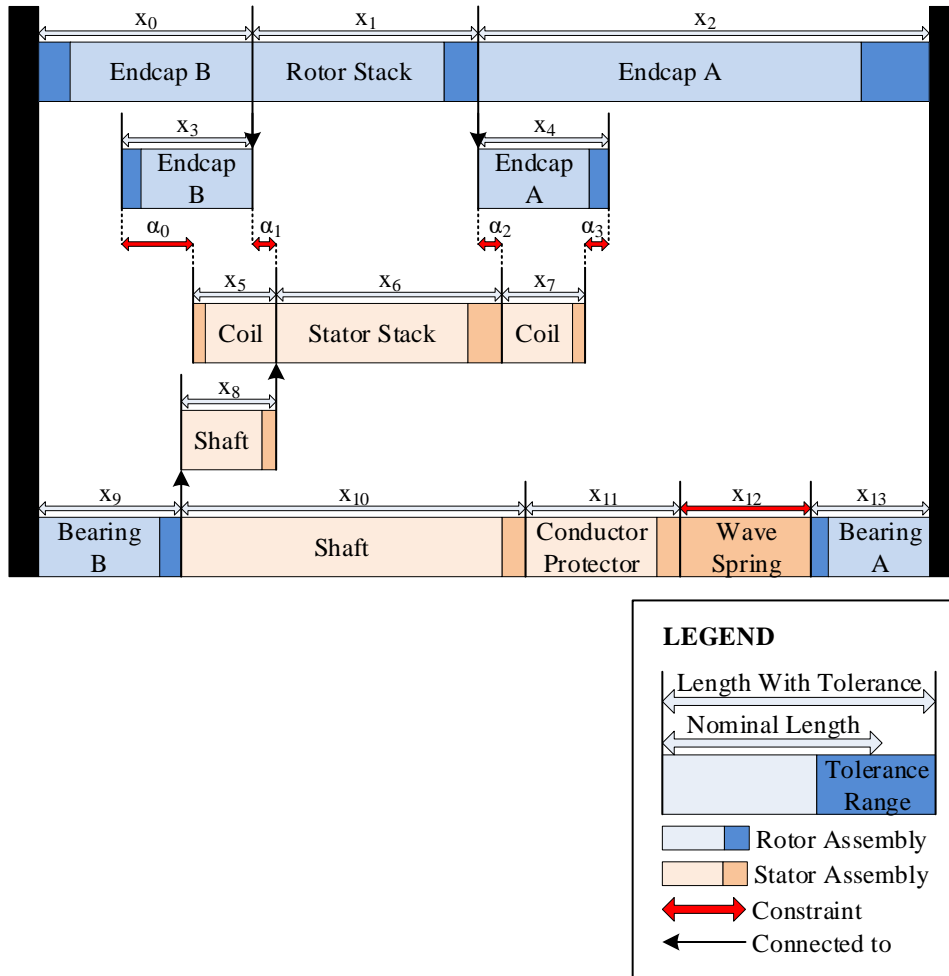


Fig. 7.18 Axial tolerance stack-up (12/16 CSR motor prototype)

The stack-up illustrated in Fig. 7.18 was input into a Microsoft Excel spreadsheet, to visualize the effects of the axial tolerance for each component on the stack alignment, coil-endcap clearance, and bearing preload. These calculations are summarized in *Appendix F*. Note: all dimensions are relative to the motor left side (side “B”) bearing face, and the individual component length symbols are defined in Fig. 7.18.

## Testing

After the prototype assembly, several tests were conducted before delivery and dynamometer performance validation. These tests were conducted to ensure that the major motor performance parameters were within a reasonable range of the expected results.

### Stacking Factor

The stacking factor used for the motor design process was assumed to be 0.96 for the Cogent (Sura) M470-50A material, based on the minimum stacking factor for competitor materials (i.e. JFE 50JNA500) [24], since detailed information was not available from the manufacturer. The stacking factor can be calculated as follows:

$$\text{stacking factor} = \frac{l_{Fe_1} \cdot N_{Lam}}{l_{Stack}}$$

or, alternatively:

$$\text{stacking factor} = \frac{m_{Fe_1} \cdot N_{Lam}}{m_{Stack}}$$

where:

$l_{Fe_1}$  = thickness of one lamination (steel only) [mm]

$l_{Stack}$  = thickness of entire stack (steel + insulation) [mm]

$m_{Fe_1}$  = mass of one lamination (steel only) [mm]

$m_{Stack}$  = mass of entire stack (steel + insulation) [mm]

$N_{Lam}$  = number of laminations in the stack

A close-up image of the stator stack has been included here for illustration purposes (see Fig. 7.19).

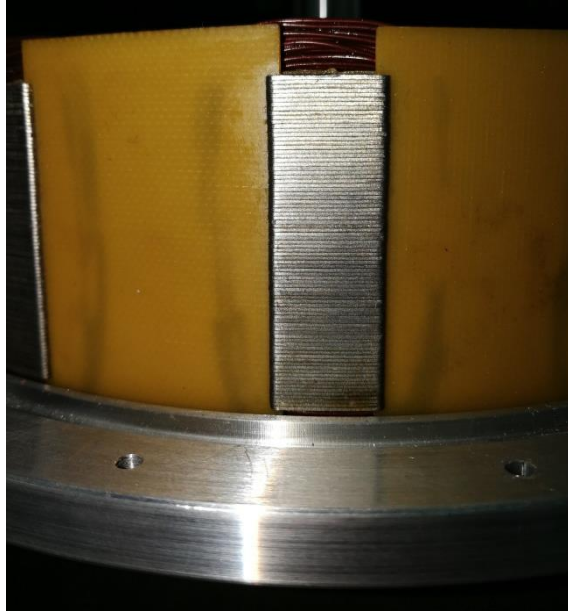


Fig. 7.19 Prototype stator stack (83 laminations for stator– 78 for rotor)

### Axial Stack Alignment

The axial stack alignment was checked and verified to be within one lamination thickness. An image of the stack alignment is provided in Fig. 7.20.



Fig. 7.20 Axial stack alignment (12/16 prototype)

## Internal Clearances

Since the e-bike motor has tight internal clearances between the coils and endcaps, it was important to check that the minimum gap of 1 mm was not violated. A Plastigauge was used to test the minimum internal clearance, as illustrated in Fig. 7.21.



Fig. 7.21 Plastigauge testing of internal clearances (side “A” shown – side “B” circled)

The minimum clearance for each side is summarized in TABLE 7.6.

Side	A	B
Minimum Clearance [mm]	1.25	1.25

TABLE 7.6 Minimum internal clearance between endcaps and windings

## Winding Testing

### *Sequential Excitation Test*

This is a basic test used to ensure that all coils are wound in the correct direction. The firing order for this e-bike machine is A, B, C. Exciting the phases with a constant current in this order should cause the motor to rotate in the counter-clockwise direction. The motor phases were excited in sequence for one mechanical rotation, with a total of 48 steps in one rotation. This matches the number of machine strokes, verifying that the coil winding directions are correct.

### *Phase Resistance/Inductance Test*

This is a basic test to ensure that the phase resistances and inductances are similar for all phases. The procedure for this test is as follows:

- 1) Connect the negative phase leads in Y-configuration
- 2) Slowly rotate motor (without exciting it)
- 3) Measure phase-to-phase inductance,  $L$

The results of the test are summarized in TABLE 7.7. The maximum inductance variation is 0.09 mH showing that all phases exhibit a very similar performance.

	<b>Phase A to B</b>	<b>Phase B to C</b>	<b>Phase C to A</b>
$L$ [mH]	6.20 ~ 10.11	6.20~10.13	6.29~10.11

TABLE 7.7 Measured line-line inductance variation with position

In addition to the inductance test, the individual phase resistances (not y-connected) were measured using a milliohm meter at room temperature (roughly

23°C), and the results are summarized in TABLE 7.8. The maximum deviation between phases is 0.00148  $\Omega$ , showing that the phases are well balanced.

	Phase A	Phase B	Phase C
$R_{Ph} [m\Omega]$	128.90	129.98	128.51

TABLE 7.8 Measured phase resistance at room temperature

### ***500V Mega-Ohm Test (Phase-Ground Insulation Test)***

This test is used to verify that there are no shorts between the phases and ground (the stator laminations), by measuring the resistance between both. More information on this testing methodology can be found in the IEEE Standard 43-2013 [25].

The measured resistance for each phase was found to be over 10 G $\Omega$ . The IEEE standard stipulates a minimum permissible resistance of 5 M $\Omega$  for machines rated below 1 kV [25], so it is clear that insulation quality between the phases and ground is excellent for the manufactured prototype.

### ***1000V Voltage Impulse Test (Turn-Turn and Phase-Phase Insulation Test)***

Otherwise known as a Baker Surge Comparison Test, this test is used to verify that there are no insulation weaknesses between coil turns or shorts between phases. An impulse voltage is injected between each pair of Y-connected phases, creating a decaying sinusoidal voltage in the windings. If there are significant differences in the voltage waveform for different phase pairs, this signifies a fault [26].

The maximum difference between phases was measured to be approximately 4%. Considering this is below 5%, it is clear that the turn-turn and phase-phase insulation is intact.

### Rotating Assembly Balancing

The motor was balanced to an ISO G2.5 quality grade, as specified in the ISO 1940-1 standard. According to the standard, this balancing grade is suitable for most motor drives operating over 950 RPM, with the tighter G1.0 grade used for higher precision drives [27]. Since targeted maximum motor speed is 400 RPM, this is more than acceptable. Fig. 7.22 shows the prototype motor balancing setup.

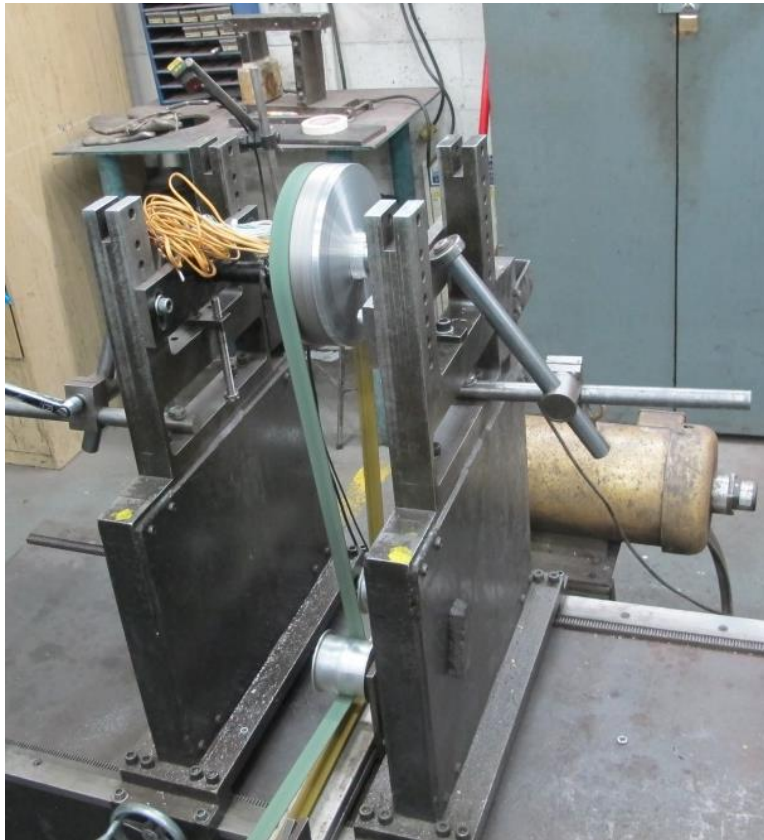


Fig. 7.22 Prototype motor - balancing setup



With a G2.5 balance quality grade,  $\varepsilon = 1.0 \frac{mm}{s}$  [27], the maximum permissible residual unbalance ( $U_{per}$ ) can be calculated [27]:

$$U_{per} = 1000 \left( \frac{\varepsilon \cdot m}{\omega} \right)$$

where:

$$U_{per} = \text{permissible residual unbalance [g} \cdot \text{mm]}$$

$$\varepsilon = \text{unbalance magnitude constant } \left[ \frac{mm}{s} \right]$$

$$m = \text{rotating assembly mass [kg]}$$

$$\omega = \text{angular velocity } \left[ \frac{rad}{s} \right]$$

The motor balancing test report is shown in Fig. 7.23.

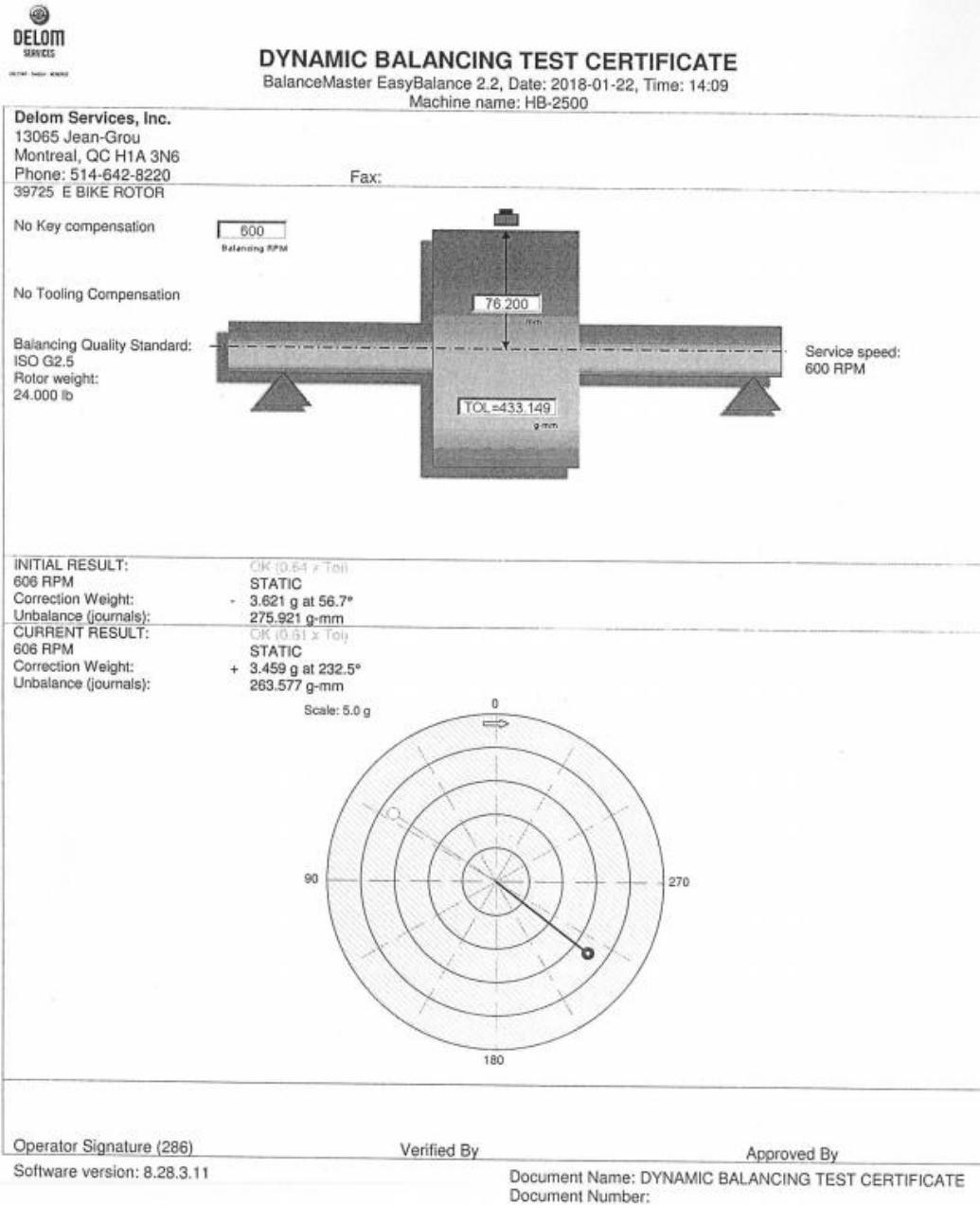


Fig. 7.23 Prototype motor - balancing test report

## Validation

A dynamometer setup is used to validate the performance of the final prototype motor. There are two fundamental tests that are conducted to validate the electromagnetic performance of the motor: a static flux-linkage test, and a dynamic torque-speed test.

### Dynamometer Setup

A dynamometer was used to validate the CSRSM design. The motor is connected through a gearing setup and torque transducer, to a brushed DC motor that acts as a dynamic load which can be varied at each speed point using a variable resistive power sink (DC load). The rotor position and speed is calculated using a resolver on the SRM side of the setup. An indexer is setup to lock the SRM rotor at different positions for the static flux-linkage tests. The SRM itself is powered by asymmetric-bridge converter which is controlled using a digital signal processor (DSP) board, programmed in C language. Both the current control and speed control logic (if applicable) are handled by the DSP, as illustrated in Fig. 7.24.

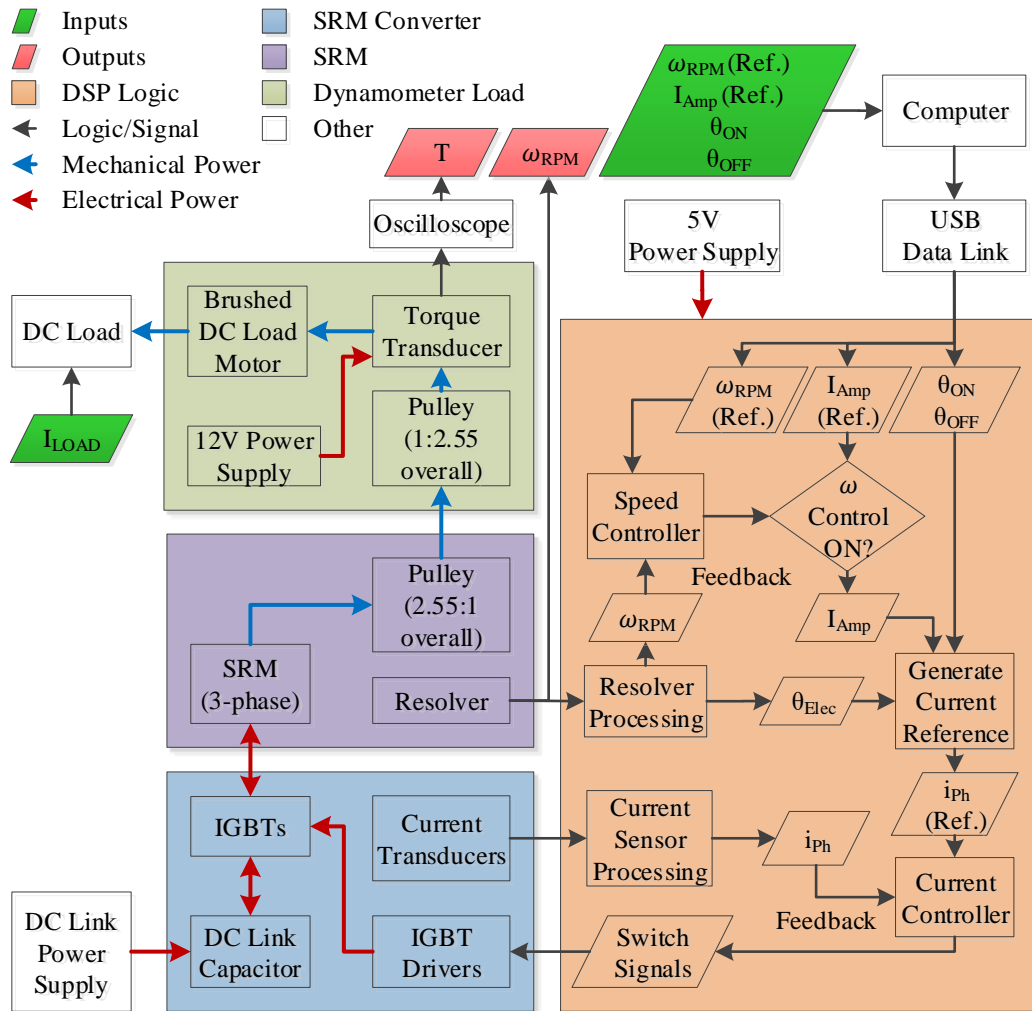


Fig. 7.24 DSP - converter block diagram as used in dynamometer setup

Fig. 7.25 shows a picture of the same experimental setup detailed in Fig. 7.24. In this image, the DC-load and liquid inverter cooling are not connected, as the motor is undergoing static flux-linkage tests.

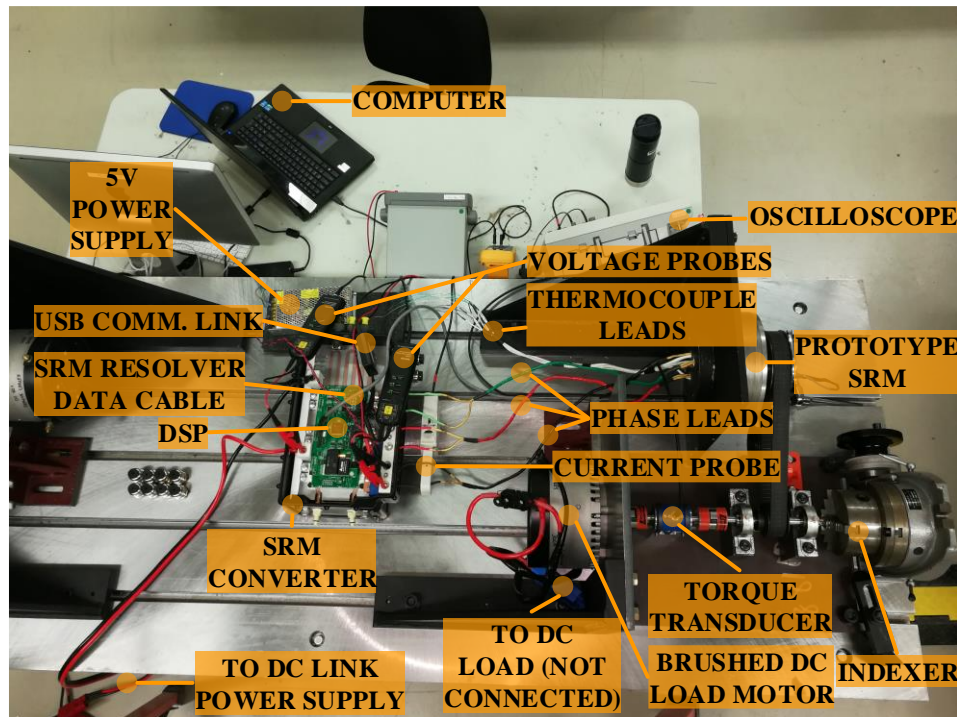


Fig. 7.25 Full dynamometer testing setup

## Current Transducer Calibration

The phase current transducers must be calibrated to ensure that they produce the correct measurements for the operating current range.

### *Procedure*

- 1) With the SRM converter switches open, record the zero-current offset for each of the phase current transducers.
- 2) Short the phase terminals from the SRM converter for a given phase, using a short, wide diameter conductor.
- 3) Connect the DC link power supply to the converter. Set the supply voltage to be larger than the voltage drop through the converter (10 V is

sufficient), and the supply current to the maximum motor phase current.

Enable the power supply as a constant-current source.

- 4) Adjust the adjust the phase current scaling value so that the value from the DSP matches the supply current reading.
- 5) Check for different current levels to ensure that the calibration is accurate for the full current range.
- 6) Turn off and disconnect the power supply.
- 7) Repeat steps 2 to 6 for each phase.

## Resolver Calibration

In this prototype, the resolver is the only position feedback available, and it must be accurate to ensure that current is injected at accurate firing angles. If the firing angles are inaccurate, the torque output, torque ripple, power factor, and efficiency will also be inaccurate. As the number of rotor poles increases, so does the importance of accurate position measurement. The position error for each stroke can be assembled into a LUT, as shown in Fig. 7.26.

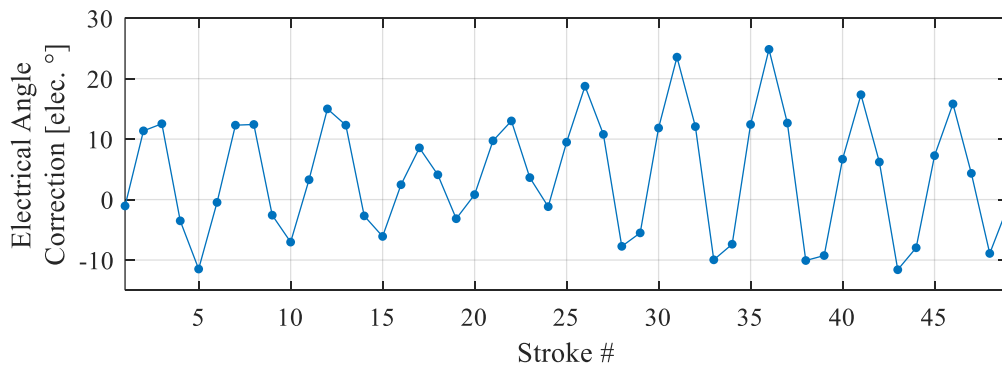


Fig. 7.26 Position error vs. stroke #

Observing Fig. 7.26, the position error is clearly cyclical, and depending on the stroke, the deviation from the mean can be significant. In order to compensate for this error, a position correction LUT is implemented in the DSP code (with linear interpolation), to adjust the resolver electrical position depending on the current stroke number. This method will also account for manufacturing error as it pertains to pole positioning.

### ***Procedure***

- 1) Excite the SRM phases with moderate constant current and in sequence for the rotation direction that will be used for testing. This will rotate the SRM like a stepper motor, with each step being a new stroke.
- 2) At each new stroke, with the corresponding phase still excited, record the difference between corresponding phase electrical position (from the resolver) and the aligned position ( $180^\circ$  elec.).
- 3) Repeat steps 1 to 2 for each stroke
- 4) Repeat steps 1 to 3 to ensure that results are repeatable.

## Static Flux-Linkage Validation

The static flux-linkage test is conducted to validate the flux-linkage look-up-tables (LUTs). As explained in *Chapter 6*, these LUTs are generated using 2D JMAG electromagnetic FEA; however there are still several assumptions which need to be validated:

- 1) 3D leakage affects are negligible; where this may not be the case in reality
- 2) Material properties used as an input to the FEA analysis are perfect. In reality, they will not account for changes in magnetic properties due to structural stress and changes of the microstructure during cutting of the laminations.

Since the phase voltage of the SRM is:

$$v_{Ph} = R_{Ph}i_{Ph} + \frac{d\psi_{Ph}(i_{Ph}, \theta_{Elec})}{dt}$$

where:

$$v_{Ph} = \text{phase voltage (averaged over test)} [V]$$

$$R_{Ph} = \text{phase resistance } [\Omega]$$

$$i_{Ph} = \text{phase current (averaged over test)} [A]$$

$$\psi_{Ph} = \text{phase flux linkage } [Wb]$$

$$t = \text{time } [s]$$

$$\theta_{Elec} = \text{rotor electrical position } [^\circ]$$



and considering  $R_{Ph}$ ,  $v_{Ph}$ ,  $dt$ , and  $i_{Ph}$  can be measured, it is possible to calculate  $\psi_{Ph}$  by rearranging the voltage equation:

$$d\psi_{Ph} = (v_{Ph} - R_{Ph}i_{Ph})dt$$

$$\left(\psi_{Ph_{t_2}} - \psi_{Ph_{t_1}}\right) = (v_{Ph} - R_{Ph}i_{Ph}) (t_2 - t_1)$$

Since there is no current at the start of the test,  $\psi_{t_1} = 0$ , so:

$$\left(\psi_{Ph_{t_2}} - 0\right) = (v_{Ph} - R_{Ph}i_{Ph}) (t_2 - 0)$$

$$\psi_{Ph_{t_2}} = (v_{Ph} - R_{Ph}i_{Ph})t_2$$

If this equation is solved at each individual position and peak current point, then the flux-linkage LUT can be validated. These points are defined as follows:

$$\theta_{Elec} = [0, 36, 72, 108, 144, 180]$$

$$\theta_{Mech} = [0, 2.25, 4.50, 6.75, 9.00, 11.25]$$

$$i_{Ph} = I_{Amp} = [0 \ 5 \ 10 \ 20 \ 30 \ 40 \ 50 \ 60 \ 70 \ 75]^T$$

### ***Procedure***

- 1) SETUP: Use an oscilloscope record the current and voltage of phase “A”.

The voltage probe should be measured at the converter phase terminals.

Set a trigger on the phase “A” current probe, to allow the oscilloscope to record only the amount of data required (and obtain an accurate excitation time measurement).

- 2) With the DC-link disconnected (open), measure  $R_{Ph}$  at the converter terminals, using a micro-ohmmeter (see Fig. 7.27). This will account for additional resistance due to long phase leads and connections.



Fig. 7.27 Phase resistance measurement

- 3) Since current is applied for such a short time, the winding temperature is roughly constant, and it is assumed that the resistance does not change during the rest of the procedure. Observe the phase resistance or winding temperature to verify this assumption.
- 4) Fix the rotor of the prototype motor at the first  $\theta_{Mech}$  position, using an indexer, as shown in Fig. 7.28.

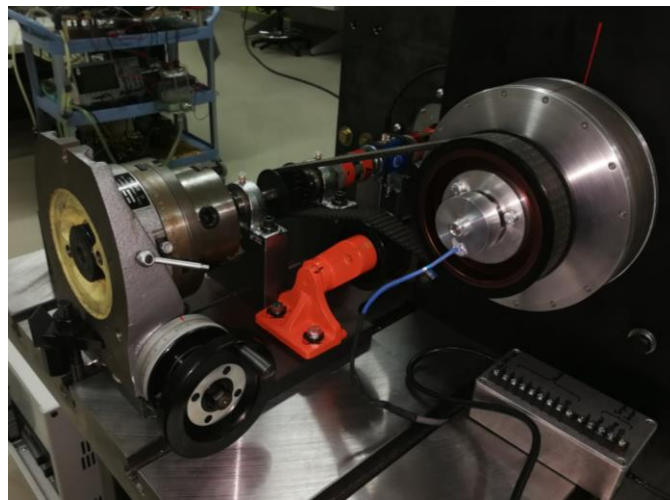


Fig. 7.28 Flux-linkage testing - with indexer visible

- 5) Apply a constant voltage on phase A until the phase current reaches the first  $I_{Amp}$  level (this is automated using closed loop current control).  
During this step, observe the CSRSM resolver position to ensure that the position has not changed during the test. This can occur due to insufficient belt tension or due to slippage at the indexer chuck. If the position changes during the test, the position must be reset, belt and chuck tension must be checked, and the test at the current data point must be re-run.
- 6) Record the triggered voltage and current waveforms versus time, as shown in Fig. 7.29.

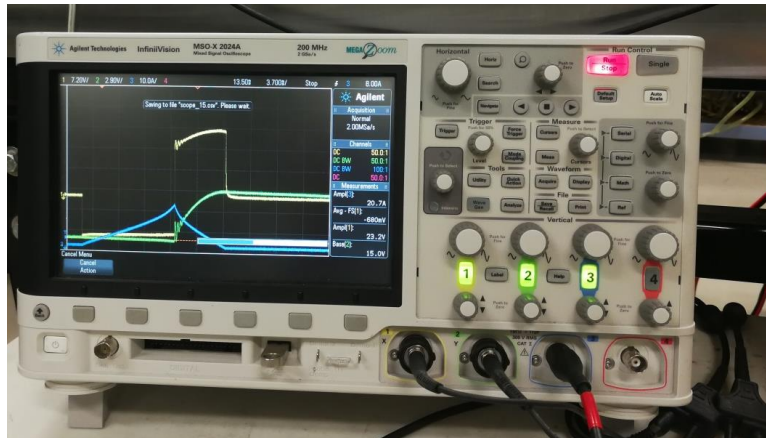
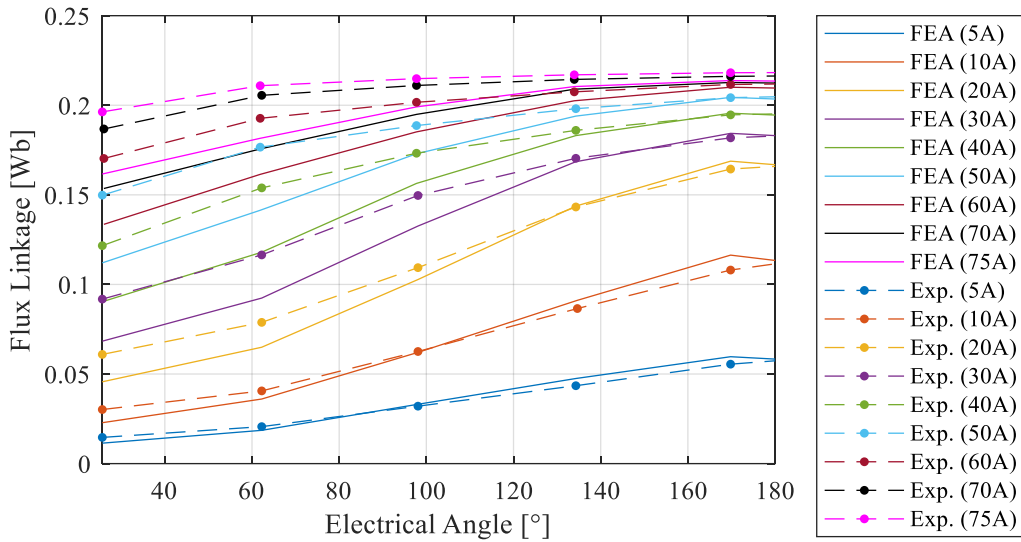


Fig. 7.29 Capturing phase current and voltage waveforms using oscilloscope

- 7) Calculate  $\psi_{Ph}$  and record the value.
- 8) Repeat steps 4 to 7 for each  $I_{Amp}$  and  $\theta_{Mech}$  position.

**Results**

The 2D FEA and experimental flux-linkage LUT maps are compared in Fig. 7.30 and Fig. 7.31. In this comparison, the FEA phase resistance is set to the measured value, and the stacking factor was increased to 0.99.



**Fig. 7.30 Flux-linkage validation  $\psi$ - $\theta$  (12/16 CSRSM prototype)**

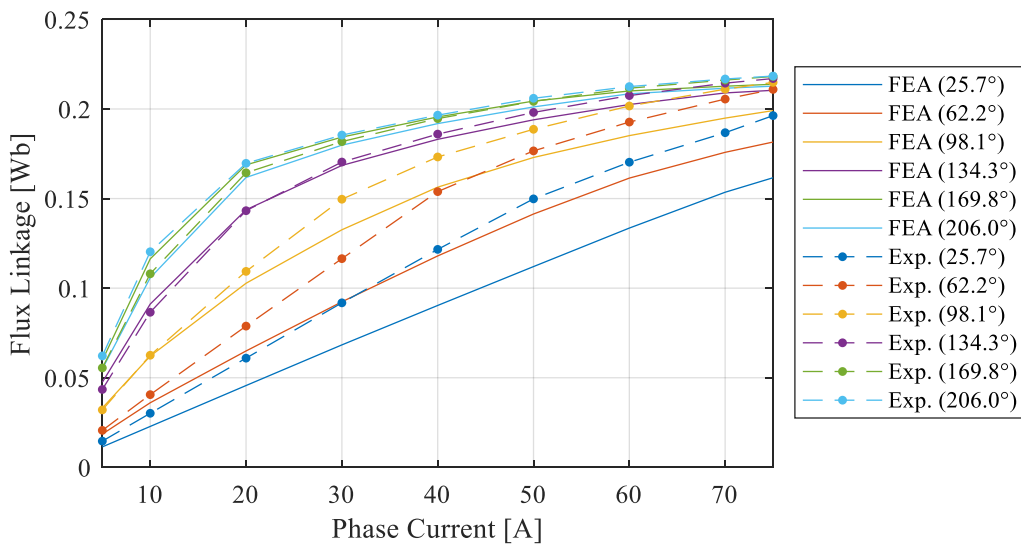


**Fig. 7.31 Flux-linkage validation  $\psi$ - $i$  (12/16 CSRSM prototype)**

The experimental flux linkage results in Fig. 7.30 and Fig. 7.31 show deviation from the FEA results, particularly when moving from the aligned position to the unaligned position. This is primarily due to flex in the dynamometer belt assembly during each torque pulse, which shifts the position slightly during each test. Since there is theoretically zero torque at the aligned position, the results at 180° electrical are expected to be accurate.

At high current values, the aligned flux linkage is higher than predicted, which suggests that the prototype CSRMM saturates at a slightly higher current than expected from the FEA simulations. There are several possible causes for this:

- Slightly wider rotor and/or stator pole-arc angle(s), due to manufacturing deviations, which would require more current to saturate. This is plausible because wider poles would also explain the high un-aligned flux linkage.
- Magnetic properties of the steel are superior to those supplied by the manufacturer
- Since this is a 3-phase 12-stator pole motor, there are four flux paths. When a given phase is excited, inaccurate positioning of the flux-carrying poles can cause flux to link differently for each pole. This can affect the un-aligned and aligned flux linkage for the phase.
- The coil center may be different than that modeled in FEA. In FEA, coil is modelled assuming an analytically estimated coil shape for the given number of turns, strands, and fill factor. The actual coil geometry differs from this shape slightly, which can have a small effect on flux linkage.

## Dynamic Torque-Speed Validation

The dynamic torque-speed validation ensures that the calculated torque-speed map for the motor is accurate. Recall from *Chapter 6* that the torque speed maps are generated by simulating the dynamic performance at each torque-speed point. Verifying the torque-speed map experimentally allows for all assumptions and simplifications in the electromagnetic design/analysis process to be validated as a whole. The run points used to validate the torque-speed map are outlined below:

$$\omega_{RPM} = [50, 100, 150, 200, 300, 400]$$

$$I_{Amp} = [15, 25, 35, 45, 55, 65, 75]^T$$

### *Procedure*

- 1) Setup an oscilloscope or power analyzer to record the phase current, phase voltage, and torque sensor voltage. The phase voltage probes should be connected at the converter phase terminals.
- 2) Measure the phase resistance through the converter phase terminals (switches open). This phase resistance value will be used as an input to the FEA resistance values, and accounts for the phase lead and connection resistances. If the resistance between the SRM converter supply and the DC link is not negligible, then measure this and add it to the phase resistance value.
- 3) The converter itself has an internal voltage drop at the IGBTs ( $V_{IGBT}$ ), which can be measured by shorting the phase terminals for a given switch,

closing the switch, and running constant current through it. If the DC link supply cables are sized large enough (their resistance is negligible), then the voltage drop measured by the supply will indicate the IGBT voltage drop. This voltage drop can also be found in the IGBT datasheet, and it is assumed to be constant (regardless of current).

- 4) Connect the SRM converter to the power supply and set it as a  $(36\text{ V} + V_{IGBT})$  voltage source. Since  $V_{IGBT}$  is assumed to be constant, this should compensate for the inverter phase voltage effects.
- 5) Connect the brushed DC load machine to the DC load, but do not apply any load.
- 6) A multi-meter can be connected to the internal motor thermistor leads – to measure temperature. Alternatively, a multi-port I/O unit can be used to record all thermistor values simultaneously. Due to the positioning of the thermistors for the CSRSM prototype, this allows for the temperature distribution to be verified, and for the temperature of each phase to be compared against the other phases. This is useful for identifying coil faults.
- 7) Set the converter phase current amplitude to the first  $I_{Amp}$  value. A speed PI is not used as it can cause current waveform perturbations. The firing angles are automatically selected depending on speed and current, using LUTs (with linear interpolation) implemented in the converter DSP code.

This ensures that the correct firing angles are used, regardless of any speed variations.

- 8) Apply load to the SRM by setting the DC load to draw a low current from the brushed DC machine. Increase this current load until the SRM starts to slow down to the next  $\omega_{RPM}$  point.
- 9) Record the torque output. If the efficiency is being calculated, record the phase voltage waveforms, phase current waveforms, and torque sensor readings, on the same axis (using a power analyzer).
- 10) Allow the motor to cool to ensure that the phase resistance doesn't significantly change.
- 11) Repeat steps 8 to 10 for each  $\omega_{RPM}$  point.
- 12) Set the converter phase current amplitude to the next  $I_{Amp}$  point.
- 13) Repeat steps 8 to 12 for each  $I_{Amp}$  point.



### Sources of Error

There are several potential causes of error in the torque-speed map:

- Wider rotor and/or stator poles can reduce motor saturation levels and decrease power factor. In addition, wider poles can decrease saliency (increase un-aligned flux linkage) and reduce the average torque output.
- In-accurate angular positioning of the rotor and/or stator poles, which can affect how the phase torque waveforms interact and contribute to shaft torque.
- The dynamometer setup has some friction and inertia losses. In order to account for these losses, the DC load motor can be used to rotate the SRM prototype at different speeds (SRM is not excited). This allows for all torque losses on the SRM side of the torque transducer to be measured, as shown in Fig. 7.32.

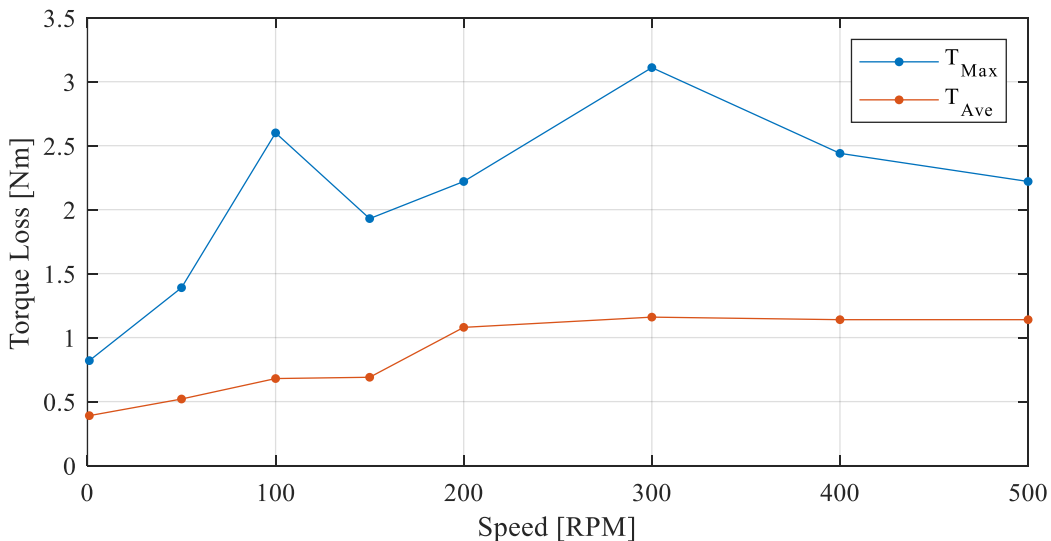


Fig. 7.32 Dynamometer Torque Loss vs. Speed

In Fig. 7.32, the torque reading from the torque transducer varies over time, and thus both the maximum and average values have been presented.

- The motor is allowed to cool down between tests, but during testing, the coils still heat up (quickly at high currents). The FEA analysis uses the measured motor phase resistance, adjusted to 40°C. However, if the actual phase temperature varies outside this temperature, the phase resistance can be impacted, affecting the base speed.
- Finally, all the FEA analyses up to this point have been 2D, and thus 3D flux leakage effects have not been accounted for. These effects can have a noticeable impact in torque (a range of roughly 5-10% torque-reduction was observed during preliminary analysis).

## Summary

A prototype non-coupled 12/16 SRM was manufactured to validate the analyses conducted in *Chapter 6*. Additional design considerations for manufacturing and mounting the assembly in the experimental setup have been examined. Detailed information on bearing selection and preloading has also been discussed, along with the thermal measurement system utilized in the motor.

Motor manufacturing considerations, such as the chosen limits and fits have been analyzed in detail and justified. Any differences between the engineering design and the manufactured prototype have also been noted.

The tests conducted on the assembled prototype motor have been detailed. The major motor parameters, such as phase balance, are shown to be within expected ranges for the prototype.

Finally, the prototype testing setup is detailed, and the static phase flux-linkage characteristics are compared against the 2D FEA maps used in *Chapter 6*. The flux linkage characteristics show good agreement at the aligned position, with the experimental CSRSM prototype saturating at a slightly higher current than expected. The experimental flux linkage results deviate as the rotor position approaches the un-aligned position. This is expected to be primarily due to manufacturing deviation of the pole geometry and pole positioning, as well as 3D flux-leakage effects.

# Chapter 8

## Design of a Mutually Coupled Switched Reluctance E-Bike Motor

### Introduction

Mutually coupled switched reluctance motors (MCSRMs) follow similar torque-production principles as conventional switched reluctance motors (CSRMs). However, phases are excited together rather than separately, which allows for a standard 3-phase AC inverter to be used instead of an asymmetric-bridge converter.

The MCSRMs produce reluctance torque as the CSRMs do, but the co-energy area can be increased by utilizing mutual flux-linkage effects between phases (as discussed in *Chapter 2*). Thus, the MCSRMs can have a high torque production potential, but since more than one phase is excited at a time, the machine uses more of the iron at a given time, making it more difficult to saturate. This is beneficial at low speed, as it can improve torque output, but at high speed, it becomes difficult to saturate the core effectively to improve the power factor, without having high copper losses.

The high speed performance of the MCSRMs is further impacted by the total number of effective turns excited at a given moment. In the CSRMs only one phase is excited at a time, whereas the MCSRMs excite more than one phase at a time; increasing the EMF for a given current at high speed. In order to design a

competitive MCSRMs, choice of pole configuration is highly important, and the geometry must be highly optimized, as detailed in this chapter.

## Electromagnetics Design

### Motor Design Process

The design process for the MCSRMs is similar to that of the CSRM; each geometry parameter combination is swept independently of the others. Since it would be computationally expensive to evaluate the dynamic performance of each design case, the first step in the design process uses a series of static 2D FEA analyses. These static analyses are a bit different than for the conventional SRM, as the motor is analyzed with a 3-phase AC current source rather than exciting a single phase with constant current. This allows for the behavior under mutual coupling to be examined. It also allows for the torque output, torque ripple, and phase voltage to be accurately determined for a given phase current amplitude and  $dq$ -excitation angle ( $\phi_{dq}$ ). The  $dq$ -excitation angle is set at  $45^\circ$  for the static analysis, as this produces the maximum average torque for a current-source analysis.

Since the static analysis is a current-source analysis, it does not account for the effects of voltage limitations above the motor base speed. The phase voltage can be observed as a rough metric to compare high speed performance between designs. This assumes that full phase current can be injected at high speed, which may not be possible given the fixed DC-link voltage. However, for the initial

geometry design stages, this is sufficient to narrow down the design space to results that give sufficient low-speed torque output.

Since so many more designs and pole configurations were evaluated for the MCSR design, an additional design stage was added to give a better indication of motor performance at high speed, before resorting to dynamic analyses. Due to the DC link voltage limit, less current will be able to be injected at high speed. In order to give a metric of high speed performance to compare different designs, the torque output and phase voltage at reduced current and maximum speed can be evaluated. This effectively indicates how voltage-efficient the motor is at producing torque under the reduced saturation levels experienced at high speed.

The low/high speed static designs can then be filtered down to a smaller subset of highest performing designs, and a dynamic-current analysis (switched voltage source) can be conducted on those designs using a dynamic model, as shown in Fig. 8.1. This model is different than the one used for the conventional SRM, and uses  $dq$ -axis theory to model the 3-phase full-bridge inverter and Y-connected phases. The dynamic analysis gives the total torque and phase voltage when voltage limits are considered. The result depends on  $\phi_{dq}$  (which varies with speed and load) and accurately reflects the flux weakening behavior under different levels of saturation. The dynamic results can then be compared to determine the best overall design candidates. Finally, a sensitivity analysis was conducted on the best dynamically performing design in order to “fine-tune” the parameters.

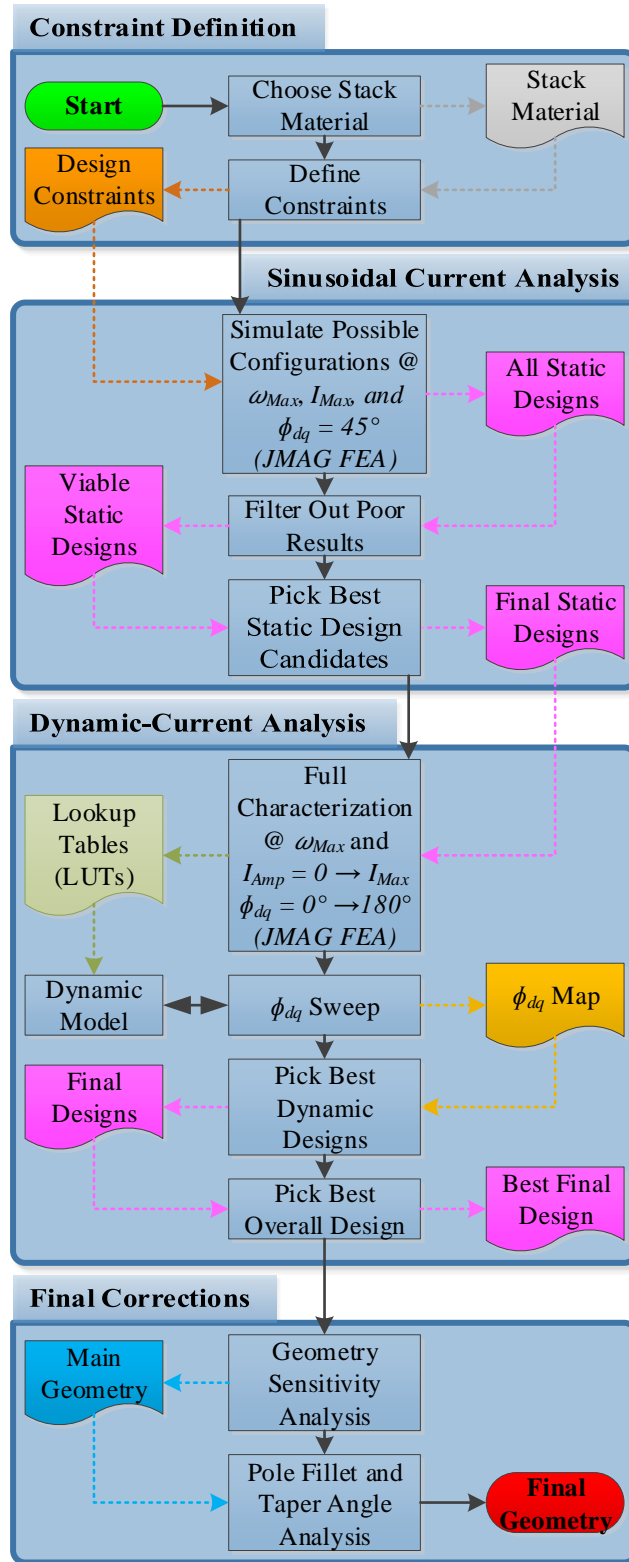


Fig. 8.1 MCSRM electromagnetic design process

The pole-arc angles were swept in increments of  $1^\circ$ , rotor pole height was swept in increments of 1mm, and stator pole height was originally fixed at 25 mm until the pole configurations were narrowed down. The rotor back iron thickness ( $\beta_R$ ) and stator back iron thickness ( $\beta_S$ ) were conservatively chosen so that the yokes did not significantly saturate during phase excitation overlap. The wire size ( $N_{AWG}$ ) was chosen so that the impact of small geometry changes (i.e. small stator pole-arc angle differences) could be reflected by the number of strands. The number of strands is maximized for each individual design while maintaining a target number of turns and a maximum wire fill factor of 0.6. The number of coil turns ( $N_{Turns}$ ) was varied for all designs to find the correct balance between copper loss, EMF, and power factor. These parameter sweep constraints are summarized in TABLE 8.1 and the parameters are identified in Fig. 8.2.

It is important to note that the ranges specified in TABLE 8.1 are only the initial ranges used to narrow down the choices of pole configurations; otherwise the number of required simulations would have been infeasible. As the pole configurations were narrowed down, additional sweeps of  $h_S$ ,  $b_R$ ,  $b_S$ , and  $N_{Turns}$  were conducted on the best-performing pole configurations.



$N_S$	12				15				21			24	
$N_R$	8	16	20	28	5	10	20	25	7	14	28	8	16
$\beta_{RLB}$	4°		3°	4°				3°					
$\beta_{RUB}$	41°	18°	14°	9°	68°	32°	14°	10°	47°	21°	9°	41°	19°
$\beta_{SLB}$	4°		3°	4°				3°					
$\beta_{SUB}$	14°	11°	9°	7°	13°		9°	7°	11°	6°	10°		
$h_{RLB}$ [mm]	7	6		4	11	6	5		4				
$h_{RUB}$ [mm]	12	11											
$h_S$	25 mm												
$b_R$	17 mm												
$b_S$	25 mm												
$\alpha_R$	0 mm												
$\alpha_S$	0 mm												
$\zeta_R$	0 mm												
$\zeta_S$	0 mm												
$\gamma_R$	0 mm												
$\gamma_S$	0 mm												
$N_{AWG}$	28 AWG												
$N_{Turns}$	40, 50, 60				32, 40, 48, 60				23, 29, 34, 60			20, 25, 30, 60	
$N_{Strands}$	Maximized for 60% wire fill												
$l_{Stack}$	39.5 mm												
$l_{Airgap}$	0.4 mm												
Mat.	Cogent (Sura) M470-50A												

**TABLE 8.1 MCSRM initial geometric parameter sweep ranges**

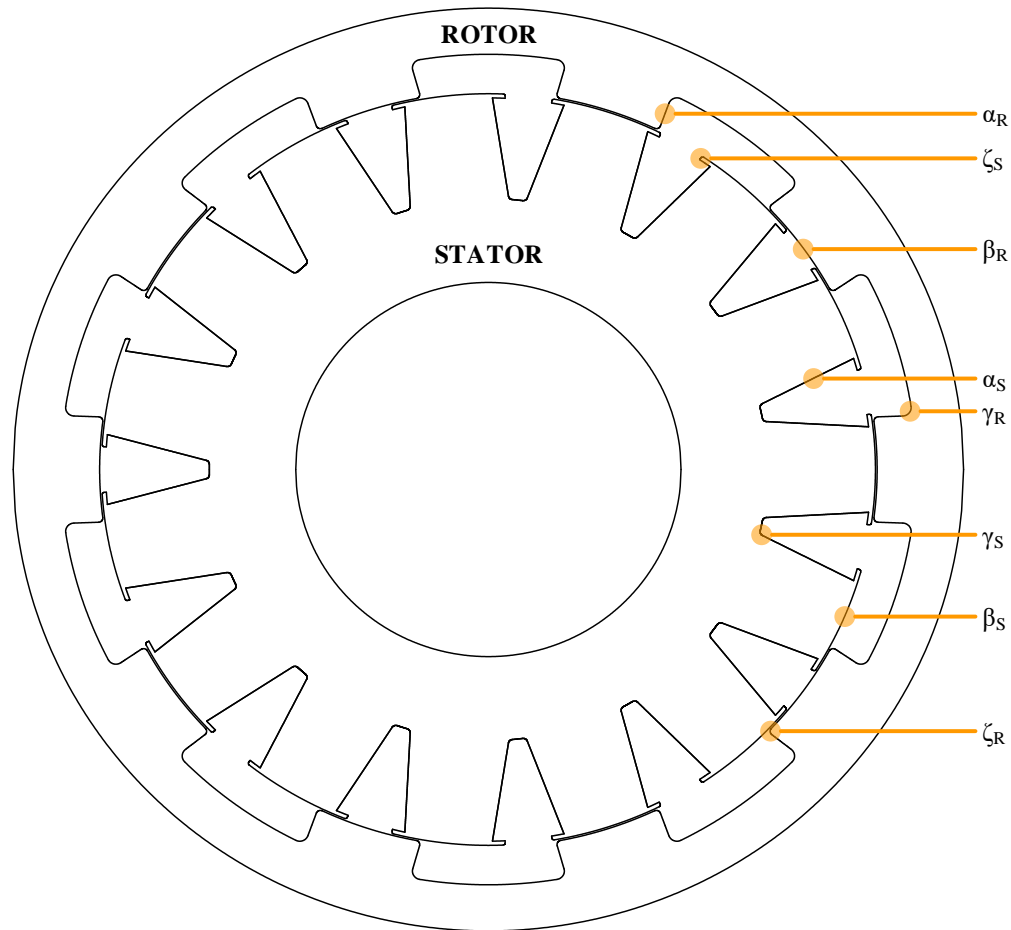


Fig. 8.2 MCSR geometry parameter definition

When a given parameter is swept, all other parameters are kept constant, allowing every possible combination within the sweeping ranges to be evaluated. The parameter sweep ranges were bounded depending on geometry constraints. Self-starting considerations are different for MCSRMs, and thus pole arc angles were far less constrained than for the CSRMs designs; resulting in many more design cases. The ranges were also limited to realistic values. For example, the pole-arc angle can only be so narrow before it is over-saturated and impacts aligned flux-linkage, so there is a realistic limit that exists. These limits were confirmed through

the parameter sweep analysis itself. The sweeping bounds of each parameter were set wide enough so that there was a clear performance gradient as each parameter was independently swept.

Pole fillets/tapering were omitted and the stack length, airgap, and iron material were kept identical to that of the CSRSM final design, for a fair comparison.

### **Stator Pole-Arc Angle**

The finalized stator pole-arc angle is  $13^\circ$  for the MCSRSM design. Increasing  $\beta_S$  will reduce the magnetic flux density in the stator poles and also reduces space for the coils, just as it does for the CSRSM. The reduction in flux density also affects power factor, but as shown in Fig. 8.3, the voltage benefit is not as noticeable as for the CSRSM. This is a critical fundamental difference between the machine types that must be considered. The ideal balance between EMF and copper losses is at a lower saturation level than the CSRSM, when considering this e-bike application. Since more than one phase is excited at a given time for the MCSRSM, twice the number of stator poles must be saturated compared to the CSRSM and the flux must bridge the airgap twice as many times. Thus, significantly more energy is required to saturate the poles meaning that for a given RMS phase current limit, more turns are required. The required increase in number of turns can increase the phase voltage drop enough to further complicate the problem (induced voltage reduces, but phase voltage increases, meaning that there are diminished returns in terms of net voltage).

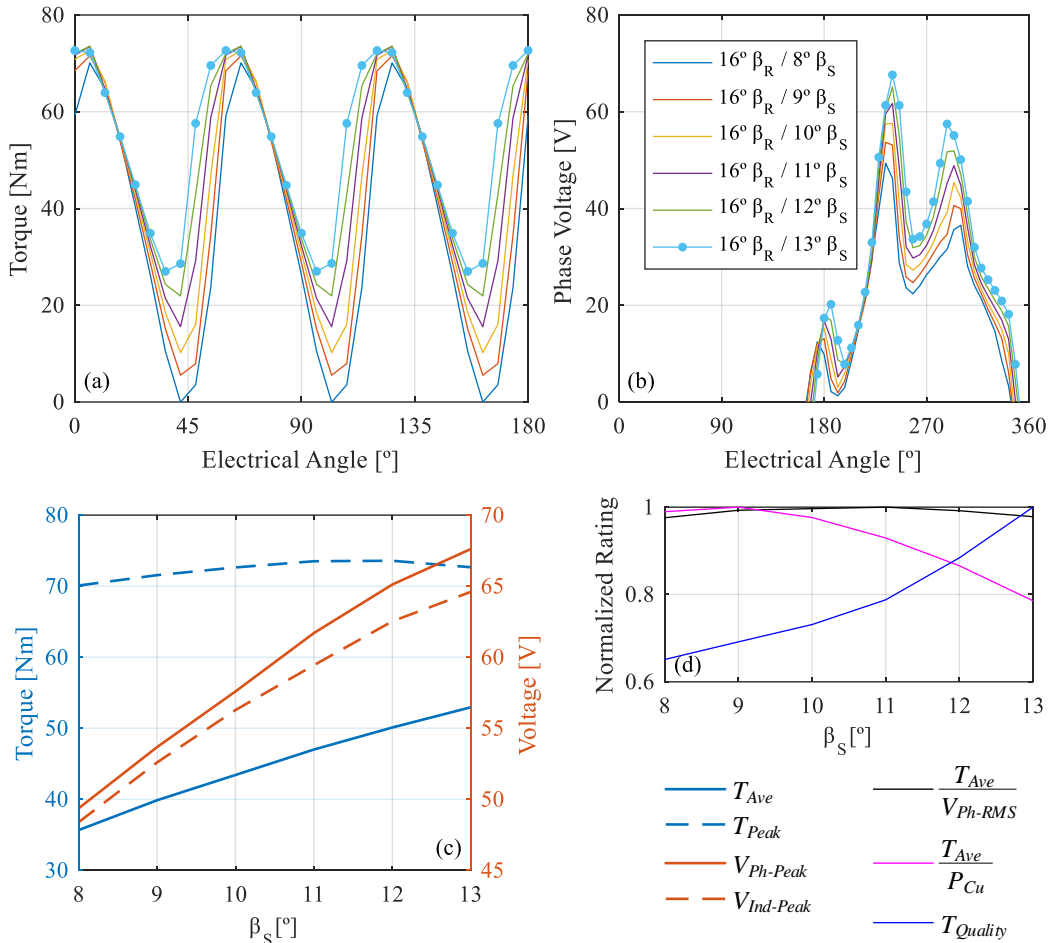


**Fig. 8.3 Effect of varying  $\beta_S$  (final 15/10 design, 3-phase AC,  $I_{Amp} = 75$  A,  $\phi_{dq} = 45^\circ$ ):**  
 (a)  $T$  effects; (b)  $V_{Ph}$  effects; (c) peak and RMS comparison; (d) normalized voltage and loss performance rating

The implications of this behavior are that the MCSRМ was saturated less than the CSRМ design, and produces a higher induced voltage at maximum speed, meaning that the high speed torque performance cannot compete with the CSRМ. However, this was necessary to avoid high copper losses and maintain reasonable efficiency.

Another major consideration in the choice of  $\beta_S$  is the impact on torque ripple, as shown in Fig. 8.3 (d). The torque ripple for the finalized MCSRМ design

is higher than the CSRМ, and it is not possible to independently control the current in each phase to reduce torque ripple using a conventional full-bridge inverter. Therefore, the most effective way to reduce torque ripple for these motors is to change the pole configuration or widen the poles. This of course makes it harder to saturate the poles, but the improvement in average torque output (due to reduced torque ripple) outweighs the downsides, even at high speed.

### **Rotor Pole-Arc Angle**

The finalized rotor pole-arc angle is  $16^\circ$ . Increasing  $\beta_R$  offers significant torque quality, voltage, and efficiency improvements until the optimal angle has been exceeded, as shown in Fig. 8.4. The ideal angle is noticeably larger than the stator pole-arc angle, since a wider  $\beta_R$  helps improve mutual coupling between phases until the optimal angle is reached.

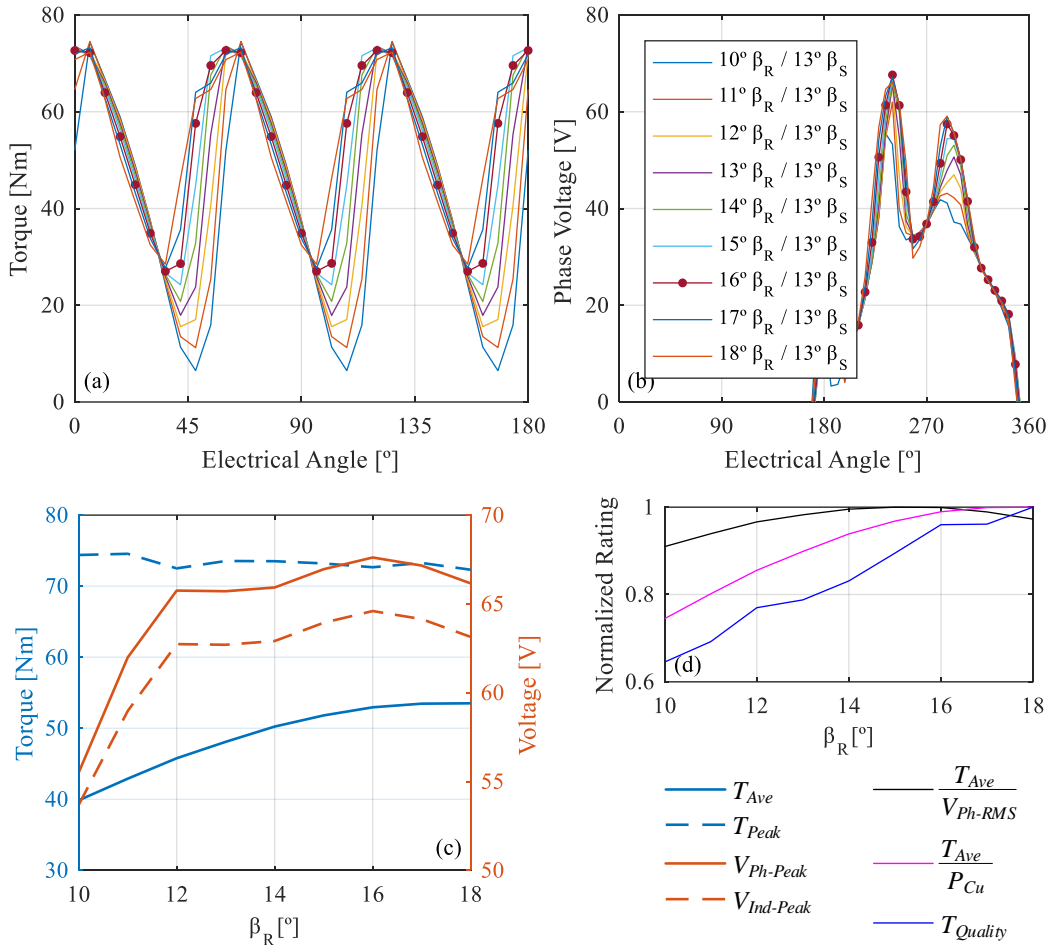


**Fig. 8.4 Effect of varying  $\beta_R$  (final 15/10 design, 3-phase AC,  $I_{Amp} = 75$  A,  $\phi_{dq} = 45^\circ$ ):**  
 (a)  $T$  effects; (b)  $V_{Ph}$  effects; (c) peak and RMS comparison; (d) normalized voltage and loss performance rating

## Stator Pole Height

The finalized stator pole height is 25 mm. A smaller  $h_s$  reduces coil space, which can lead to higher copper loss (fewer strands), but also means that less pole volume needs to be saturated. Observing Fig. 8.5, it is clear that the motor becomes more efficient as pole height is increased, due to the increase in coil space and, thus, number of strands. However, due to the wide pole angles, the pole height of 30 mm could not be exceeded. At a 30 mm pole height, due to the wide stator pole-arc

angles, the poles intersect at the base of the slot. This creates a triangular slot base, which would make the winding process challenging. Thus, a 25 mm height was chosen for the final design.

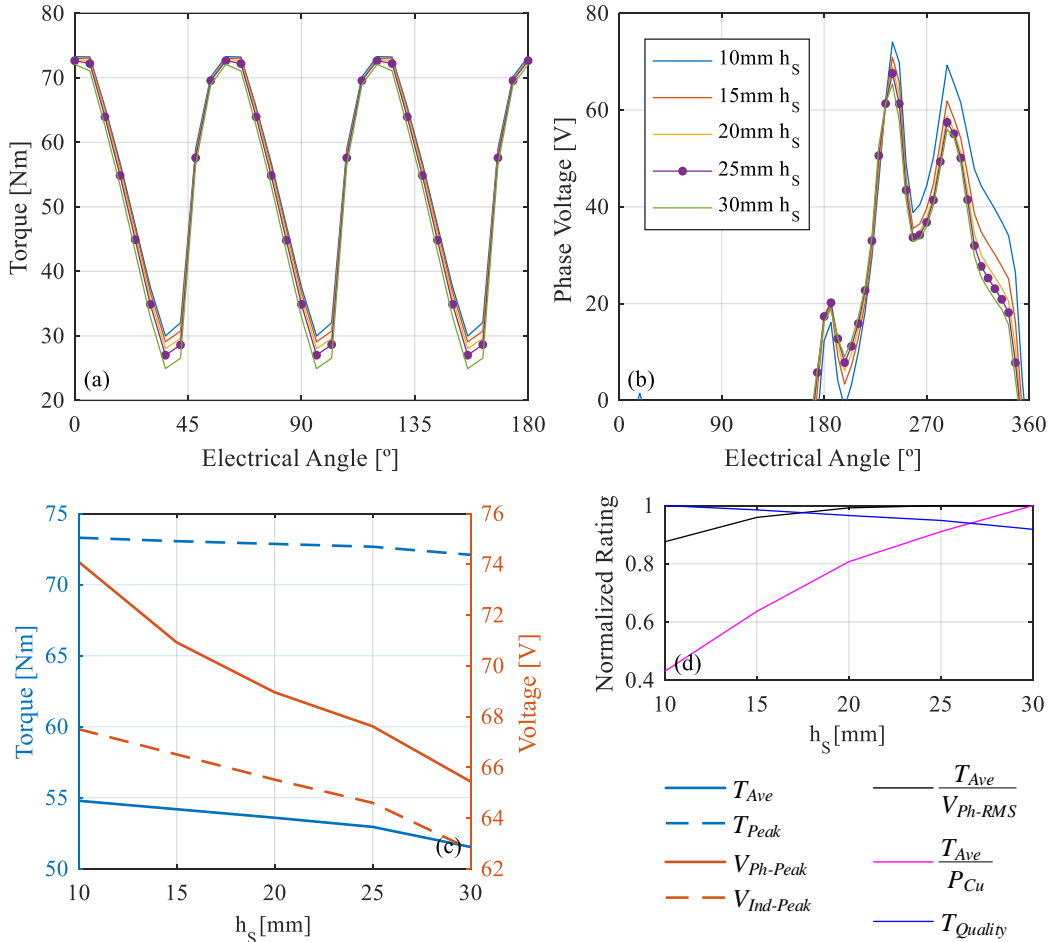


**Fig. 8.5 Effect of varying  $h_s$  (final 15/10 design, 3-phase AC,  $I_{Amp} = 75$  A,  $\phi_{dq} = 45^\circ$ ):**  
 (a)  $T$  effects; (b)  $V_{Ph}$  effects; (c) peak and RMS comparison; (d) normalized voltage and loss performance rating

## Rotor Pole Height

The finalized rotor pole height is 9 mm. Increasing  $h_R$  decreases the minimum flux-linkage when the poles are unaligned. In turn, this improves the reluctance torque. This behavior continues until the pole height is large enough that

the minimum flux-linkage is not impacted by further pole height increases, as illustrated by Fig. 8.6 (c-d). Since the outer machine diameter is fixed, increasing rotor pole height also reduces the room for coil strands (affecting efficiency), and reduces the airgap bore radius (diminishing natural torque multiplication).

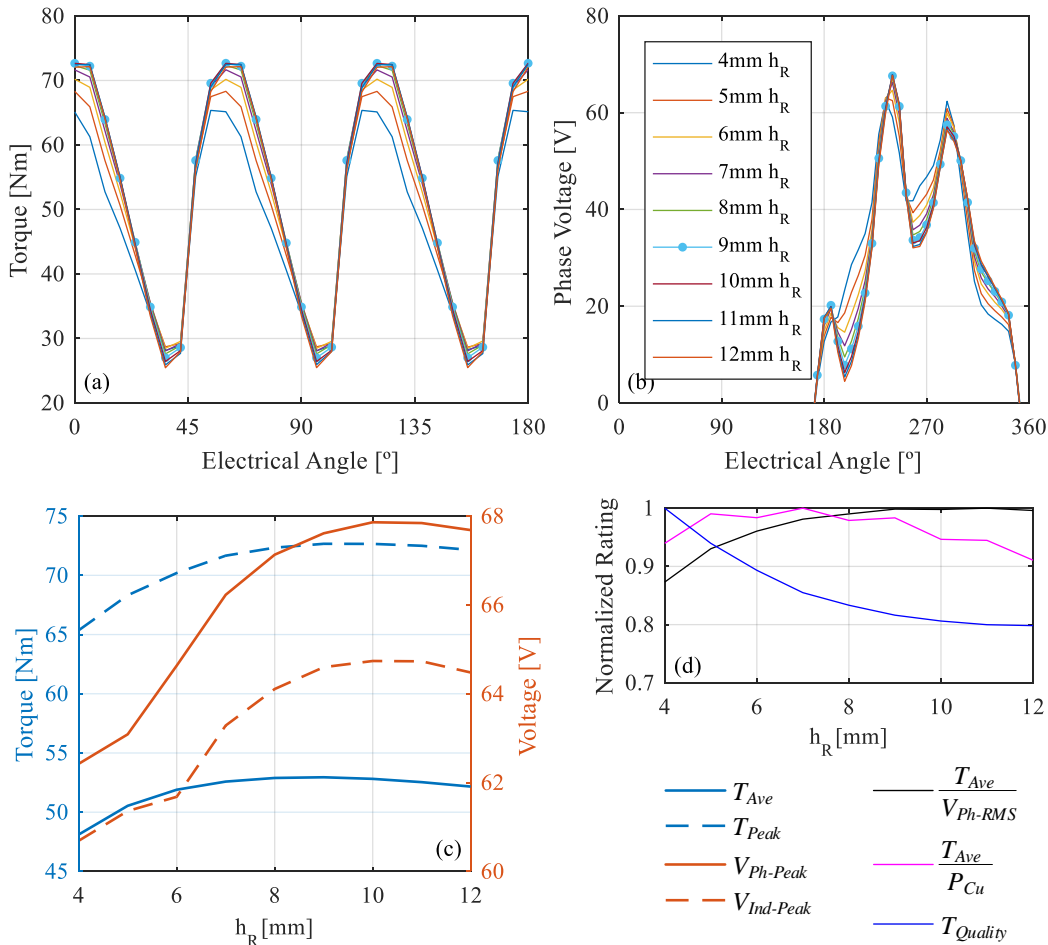


**Fig. 8.6 Effect of varying  $h_R$  (final 15/10 design, 3-phase AC,  $I_{Amp} = 75$  A,  $\phi_{dq} = 45^\circ$ ):**  
 (a)  $T$  effects; (b)  $V_{Ph}$  effects; (c) peak and RMS comparison; (d) normalized voltage and loss performance rating

Observing Fig. 8.6, the ideal pole height for a 75A analysis is closer to 7 mm, as it offers lower torque ripple, with better peak voltage performance. However, a taller pole height was finally chosen for the design, as the RMS phase



voltage performance improves slightly when the height is increased and this also allows for better machine performance if higher current amplitudes are used.

### **Yoke Thickness**

The finalized yoke thickness was 20 mm for the stator and 11 mm for the rotor. As shown in Fig. 8.7, the stator yoke thickness is oversized for this machine. As this is an external rotor machine, the stator shaft diameter and stator pole base diameter constrain the maximum yoke thickness. Given that the shaft diameter is relatively small, there was plenty of space to oversize the stator yoke. This reduces stator yoke iron losses and increases the stator stiffness, but also increases mass slightly.

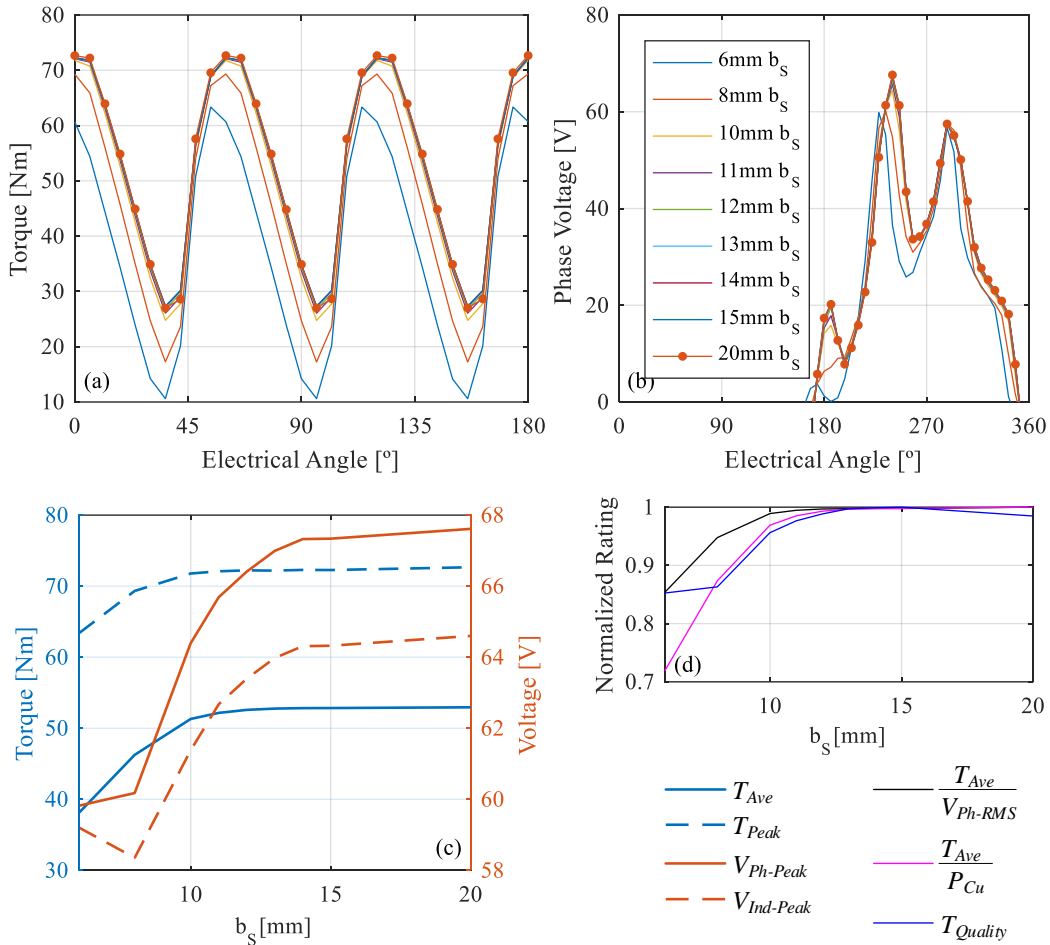


**Fig. 8.7 Effect of varying  $b_s$  (final 15/10 design, 3-phase AC,  $I_{Amp} = 75$  A,  $\phi_{dq} = 45^\circ$ ):**  
 (a)  $T$  effects; (b)  $V_{Ph}$  effects; (c) peak and RMS comparison; (d) normalized voltage and loss performance rating

Selecting the rotor yoke thickness is more critical than stator yoke thickness for this machine, as the rotor outside diameter is fixed. If the rotor pole height is fixed, increasing the rotor yoke thickness can decrease the airgap bore diameter. This can reduce the stator pole height, and the amount of coil space. It is clear from Fig. 8.8, that the finalized yoke thickness offers the best voltage performance, copper loss performance, and torque quality balance.

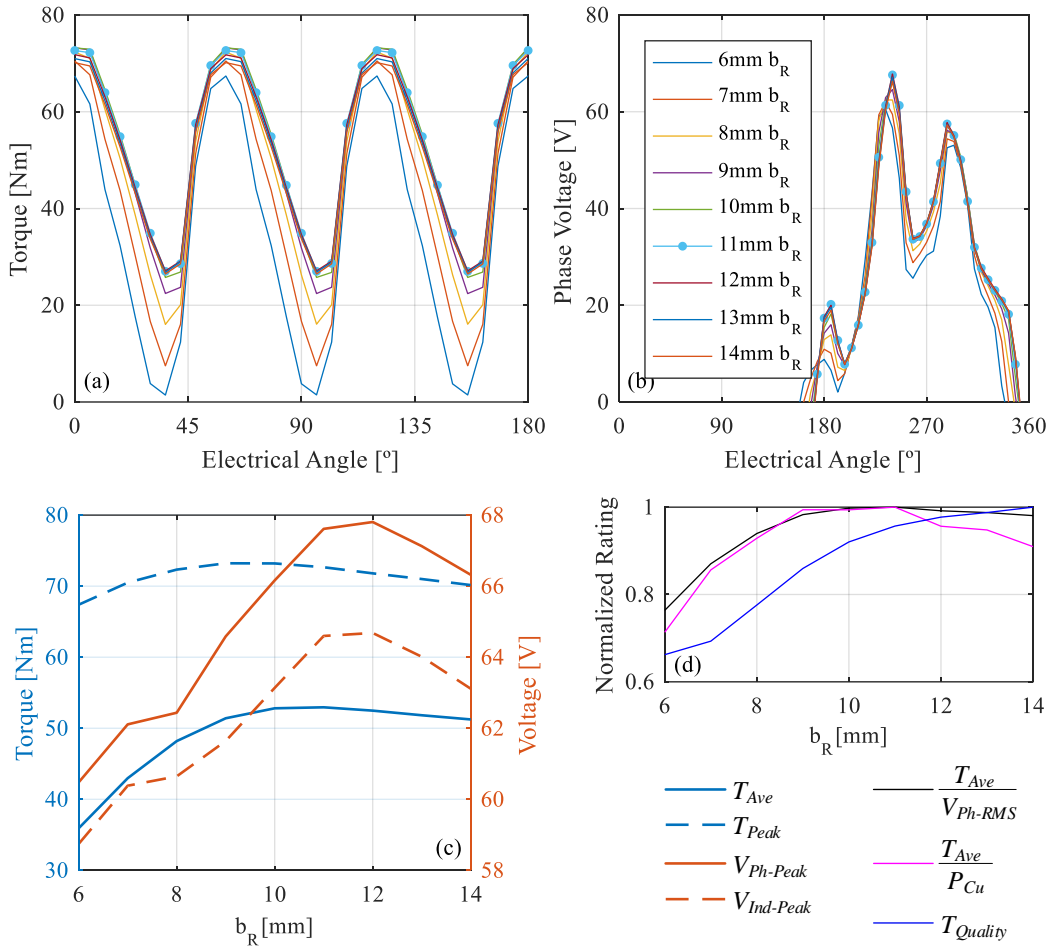


**Fig. 8.8** Effect of varying  $b_R$  (final 15/10 design, 3-phase AC,  $I_{Amp} = 75$  A,  $\phi_{dq} = 45^\circ$ ):  
 (a)  $T$  effects; (b)  $V_{Ph}$  effects; (c) peak and RMS comparison; (d) normalized voltage and loss performance rating

## Coil Design

### Wire Size Selection

As discussed in *Chapter 4*, due to the low rotation speed requirements of the e-bike motor, AC copper loss like skin effect and proximity effect do not have a significant impact on total loss. The MCSRM design has fewer rotor poles than the CSRSM design (15/10 vs. 12/16), and the electrical frequency is halved due to the AC phase current waveforms. Therefore, the fundamental excitation frequency is:

$$f_{Mech} = \frac{400 \text{ rev}}{\text{min}} \cdot \frac{1 \text{ min}}{60 \text{ sec}} = 6.67 \text{ Hz}$$

$$f_{Elec} = \left(\frac{N_R}{2}\right) * f_{Mech} = \left(\frac{10}{2}\right) \cdot 6.67 = 33.33 \text{ Hz}$$

If we assume the wire permeability,  $\mu = 4\pi \times 10^{-7} \frac{H}{m}$  and the conductivity of copper,  $\sigma = 5.814 \times 10^7 \frac{S}{m}$  then the skin depth can be calculated as discussed in *Chapter 2*.

$$\begin{aligned} \delta_{skin} &= \frac{1}{\sqrt{\pi f_{Elec} \mu \sigma}} \\ &= \frac{1}{\sqrt{\pi(33.33)(4\pi \times 10^{-7})(5.814 \times 10^7)}} \\ &= 0.0114 \text{ m} \end{aligned}$$

With a skin depth of 11.4 mm, it is clear that none of the conductors analyzed should experience AC resistance due to skin effect. Therefore, the primary concern when selecting wire size is the copper to insulation ratio in the slot – or the

effective copper area – which is reflected by the DC phase resistance. Using the same analytical coil resistance estimation algorithm used in **Chapter 6**, the phase resistance for different wire diameters is compared in TABLE 8.2, where  $d_{Cu}$  represents the nominal copper diameter and  $R_{Ph}$  is the estimated resistance at 25°C.

$N_{AWG}$	$d_{Cu}$ [mm]	$N_{Turns}$	$N_{Strands}$	$R_{Ph}$ [mΩ]
14	1.6281	28	1	154.4
16	1.2903		1	242.7
18	1.0236		2	194.9
20	0.8128		4	157.9
22	0.6426		6	166.4
24	0.5105		10	159.1
26	0.4039		17	150.6
28	0.3200		26	155.3
30	0.2540		41	157.2
32	0.2032		63	160.4

**TABLE 8.2** Wire size impact on phase resistance (for final 15/10 geometry)

This analysis shows that 26 AWG clearly gives the lowest phase resistance. Though this is a smaller wire size than the CSR design uses (22 AWG), the winding complexity is not significantly increased, because the total number of conductors in the slot is actually reduced.

### ***Number of Strands***

The number of strands was maximized for the design geometry based on a slot wire fill factor constraint of 0.6. It is important to account for an end turn fill factor of 0.6 in order to accurately estimate the total axial length of the coils. In the MCSRM design, the slot fill factor was the dominant constraint on the number of strands, not the end turn-fill factor, as was the case for the CSRSM design. This is because the additional stator poles helped distribute the copper around the machine more evenly to reduce axial length.

### ***Number of Turns***

The final design used 28 turns per stator coil. Selecting  $N_{Turns}$  is arguably the most challenging step in the design process when the machine is highly saturated. However, the lower saturation levels in the MCSRM design mean that small changes in the number of turns have a nearly linear effect on torque and voltage, as shown by Fig. 8.9.

The torque quality, voltage performance, and efficiency are all shown to decrease as  $N_{Turns}$  increases. It is expected that voltage performance will eventually start to increase if  $N_{Turns}$  was further increased, but the copper losses become so high that the high-turn designs are not feasible, and thus these results were not shown here.

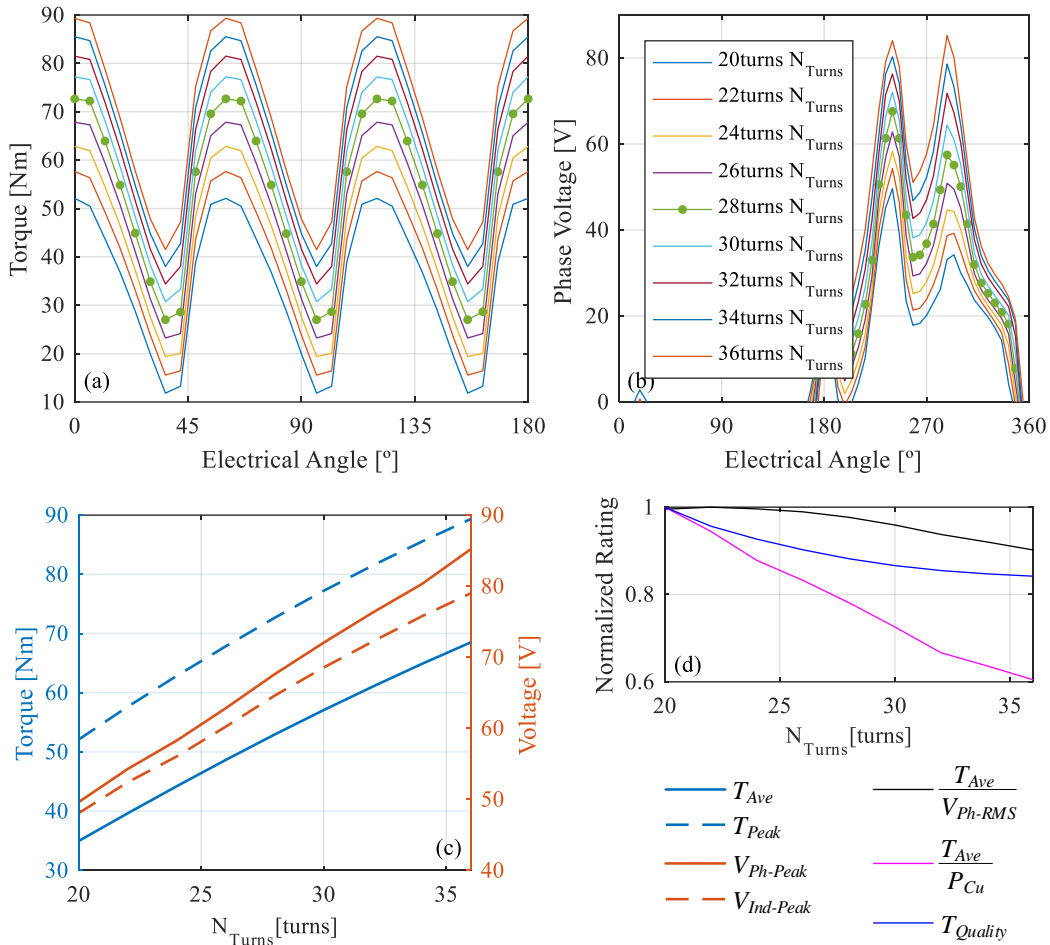


**Fig. 8.9 Effect of varying  $N_{Turns}$  (final 15/10 design, 3-phase AC,  $I_{Amp} = 75$  A,  $\phi_{dq} = 45^\circ$ ):**  
 (a)  $T$  effects; (b)  $V_{Ph}$  effects; (c) peak and RMS comparison; (d) normalized voltage and loss performance rating

## Pole Tapering

The finalized pole taper angle was  $2^\circ$  for the rotor and  $3^\circ$  for the stator. The rotor pole taper (Fig. 8.10) has negligible effects on all machine performance metrics, but a small angle was selected for the final design to increase rotor pole stiffness and to reduce the rotor pole flux density at the aligned position slightly.

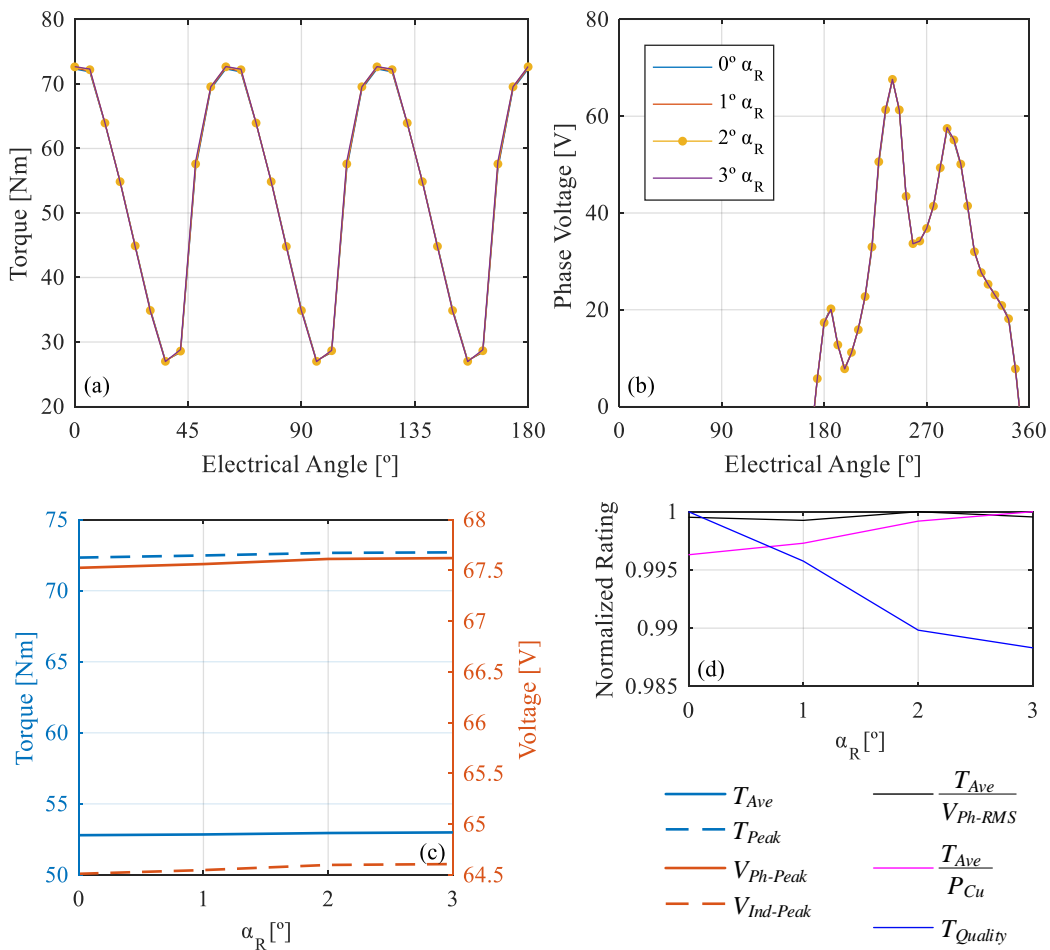


**Fig. 8.10** Effect of varying  $\alpha_R$  (final 15/10 design, 3-phase AC,  $I_{Amp} = 75$  A,  $\phi_{dq} = 45^\circ$ ):  
 (a)  $T$  effects; (b)  $V_{Ph}$  effects; (c) peak and RMS comparison; (d) normalized voltage and loss performance rating



Adding a small amount of stator pole tapering does improve the motor torque slightly (see Fig. 8.11). However, copper losses are also increased, as stator tapering reduces coil space.

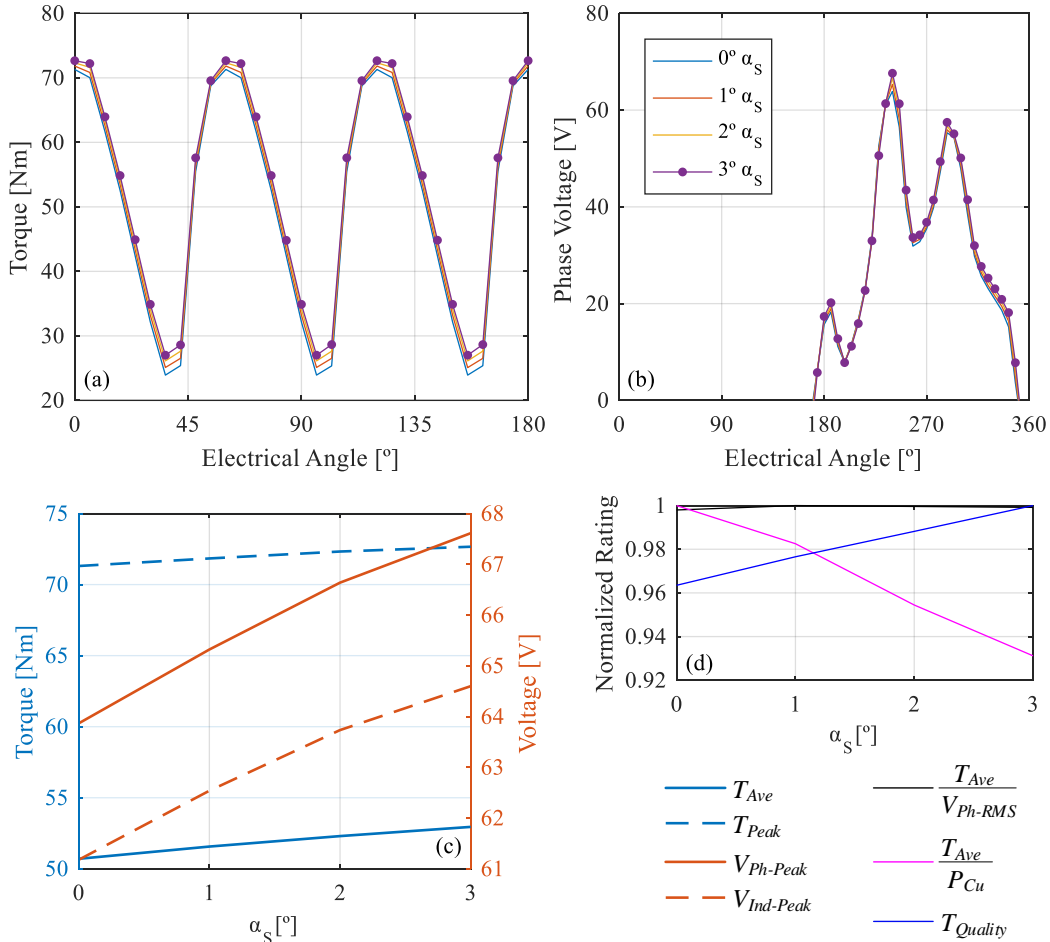


**Fig. 8.11** Effect of varying  $\alpha_s$  (final 15/10 design, 3-phase AC,  $I_{Amp} = 75$  A,  $\phi_{dq} = 45^\circ$ ):  
 (a)  $T$  effects; (b)  $V_{Ph}$  effects; (c) peak and RMS comparison; (d) normalized voltage and loss performance rating

## Pole Tip Fillets

The finalized pole tip fillet radius is 1 mm for the rotor and 0 mm for the stator. As shown in Fig. 8.12, a small rotor pole tip fillet does not significantly affect motor performance, while larger fillets reduce motor torque quality.

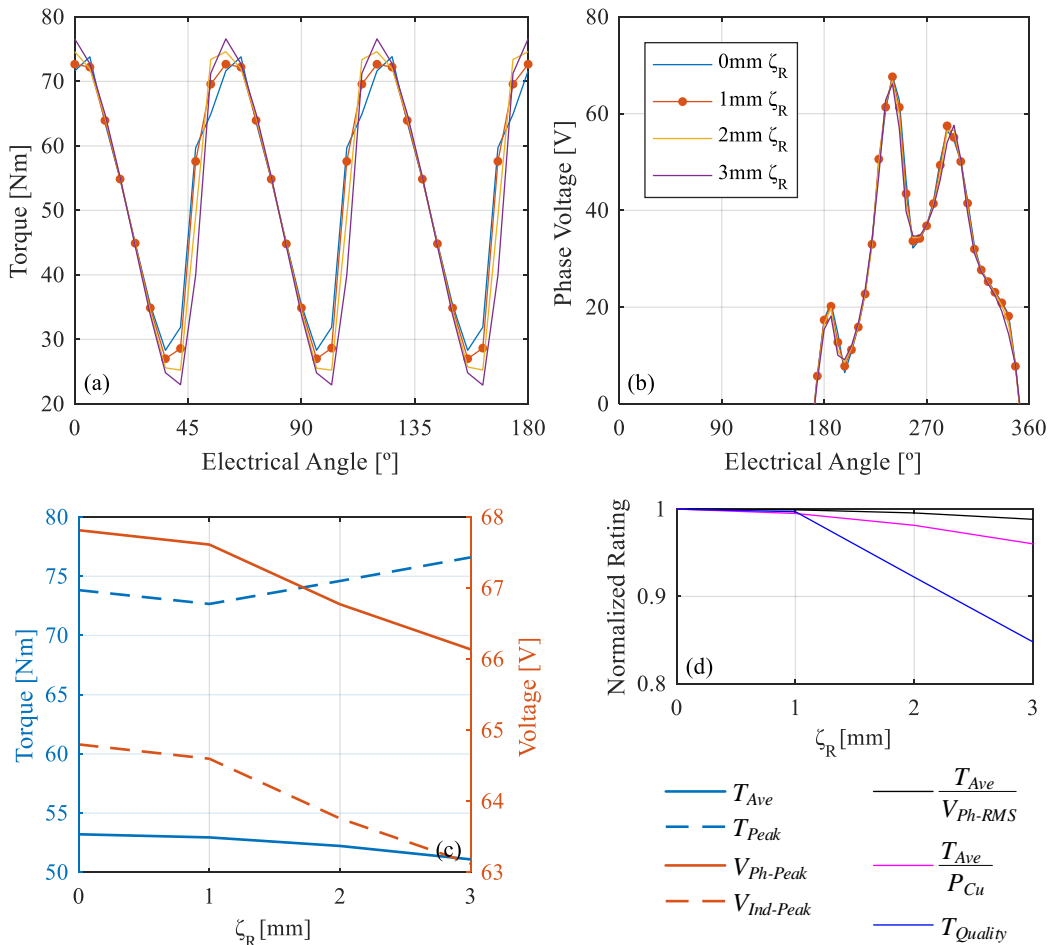


**Fig. 8.12** Effect of varying  $\zeta_R$  (final 15/10 design, 3-phase AC,  $I_{Amp} = 75$  A,  $\phi_{dq} = 45^\circ$ ):  
 (a)  $T$  effects; (b)  $V_{Ph}$  effects; (c) peak and RMS comparison; (d) normalized voltage and loss performance rating

Stator pole tip fillets have a similar impact, as shown in Fig. 8.13, but the effects are more pronounced due to the higher saturation levels.

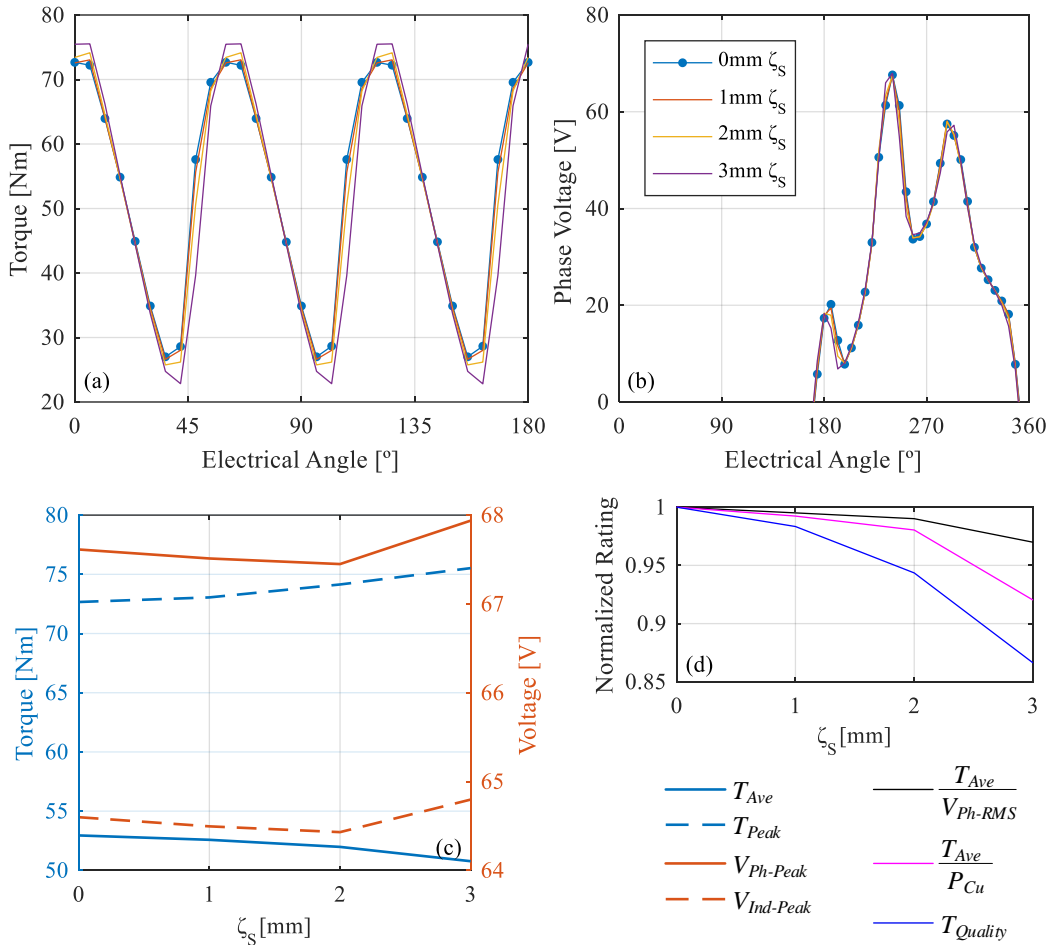


**Fig. 8.13 Effect of varying  $\zeta_S$  (final 15/10 design, 3-phase AC,  $I_{Amp} = 75$  A,  $\phi_{dq} = 45^\circ$ ):**  
 (a)  $T$  effects; (b)  $V_{Ph}$  effects; (c) peak and RMS comparison; (d) normalized voltage and loss performance rating

## Pole Base Fillets

The finalized pole base fillet radius is 2 mm for the rotor (Fig. 8.14) and 1 mm for the stator (Fig. 8.15). The primary reasoning for adding these fillets is to reduce sharp lamination edges, which would create areas of increased mechanical stress. In addition to this, adding pole base fillets increases pole stiffness slightly.

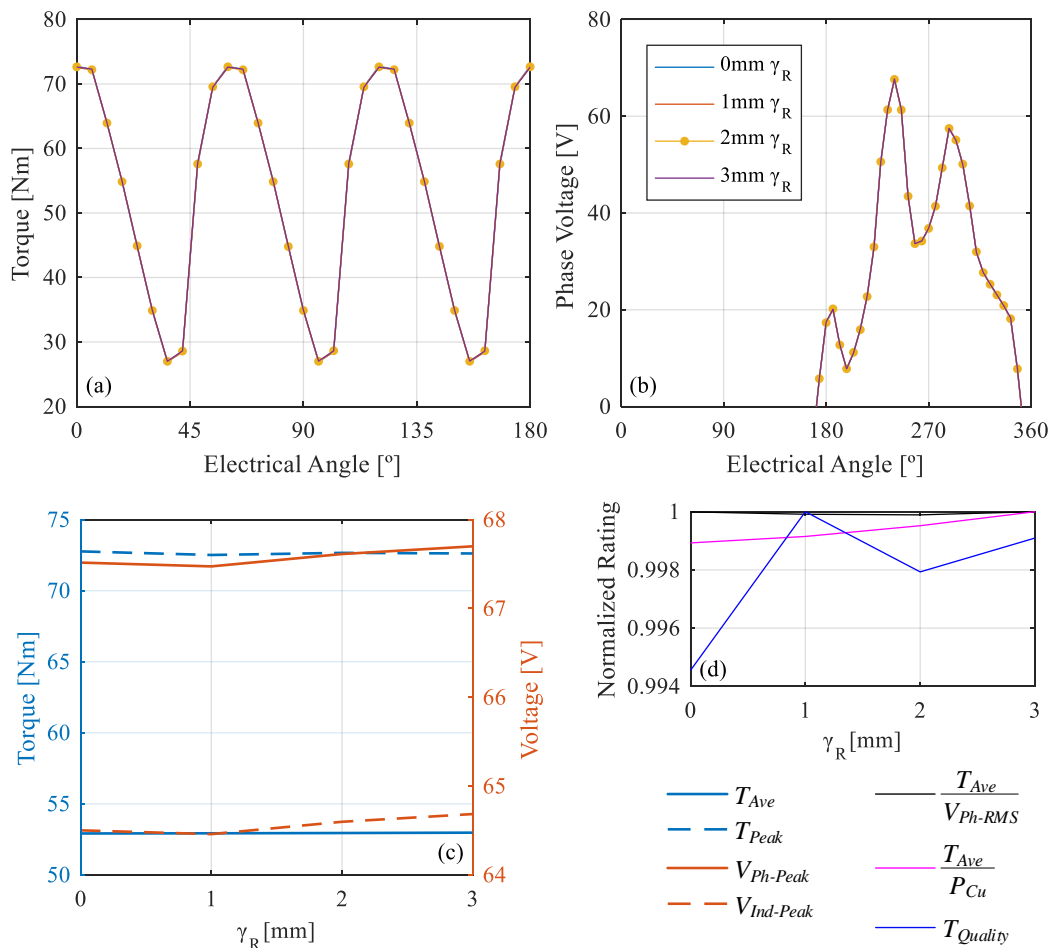


**Fig. 8.14** Effect of varying  $\gamma_R$  (final 15/10 design, 3-phase AC,  $I_{Amp} = 75$  A,  $\phi_{dq} = 45^\circ$ ):  
 (a)  $T$  effects; (b)  $V_{Ph}$  effects; (c) peak and RMS comparison; (d) normalized voltage and loss performance rating

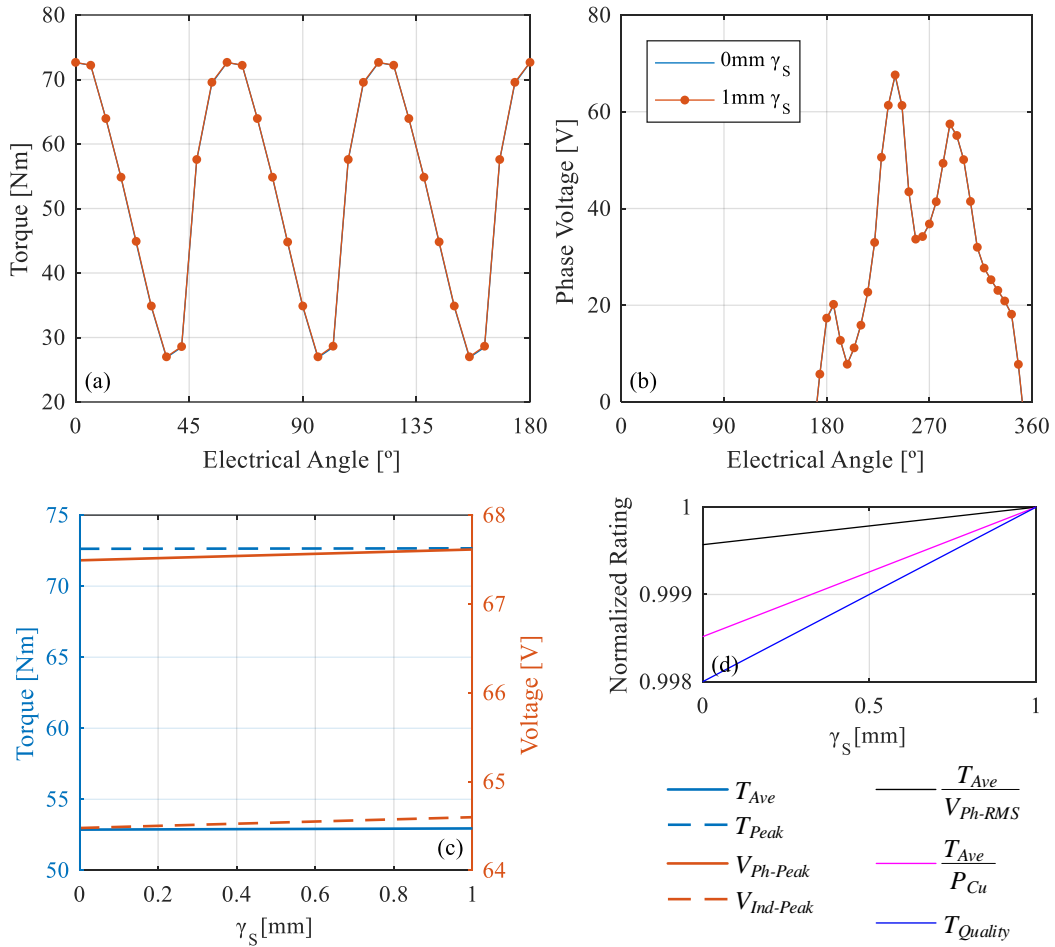


**Fig. 8.15** Effect of varying  $\gamma_S$  (final 15/10 design, 3-phase AC,  $I_{Amp} = 75$  A,  $\phi_{dq} = 45^\circ$ ):  
 (a)  $T$  effects; (b)  $V_{Ph}$  effects; (c) peak and RMS comparison; (d) normalized voltage and loss performance rating

## Stack Length

The stack length for the final design is set at 39.5 mm (same as the CSR design). This linearly affects average torque and phase voltage, and does not impact saturation levels. However, as shown in Fig. 8.16, torque ripple does increase with stack length. This is clearly due to peak torque increasing more than the minimum torque when stack length is increased.

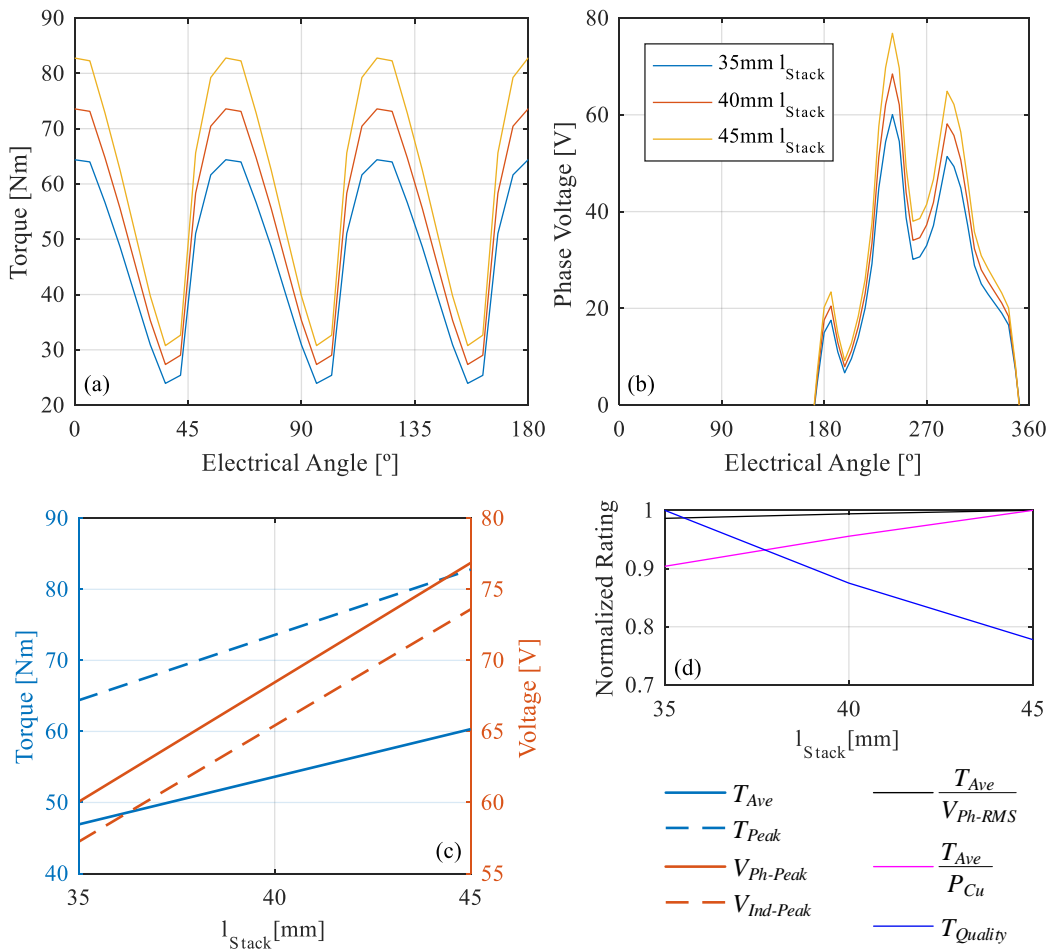


**Fig. 8.16** Effect of varying  $l_{Stack}$  (final 15/10 design, 3-phase AC,  $I_{Amp} = 75$  A,  $\phi_{dq} = 45^\circ$ ):  
 (a)  $T$  effects; (b)  $V_{Ph}$  effects; (c) peak and RMS comparison; (d) normalized voltage and loss performance rating

## Airgap

The finalized airgap was set at 0.4 mm (same as the CSRSM design). Increasing the airgap ( $l_{Airgap}$ ) will reduce torque output, increase induced voltage, and reduce efficiency in the motor, because there is more leakage in the magnetic circuit (aligned flux-linkage is reduced for the same phase MMF).

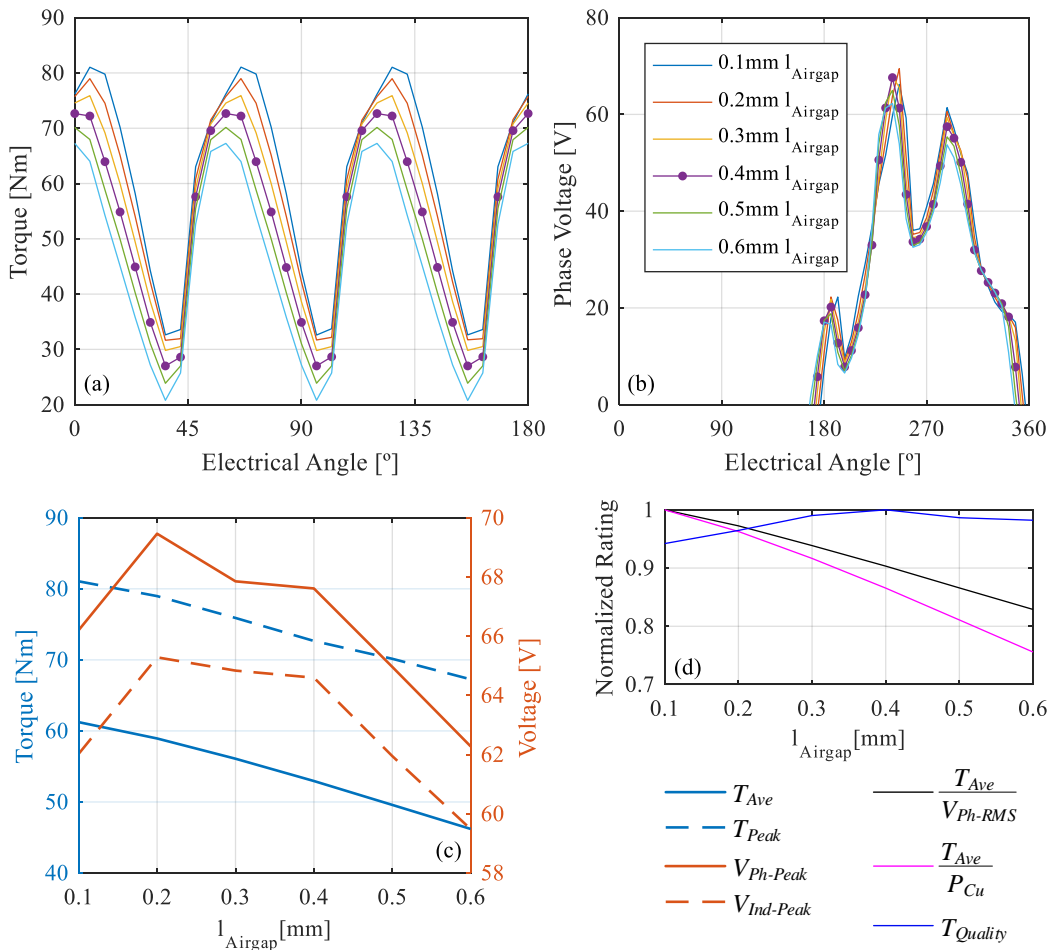


**Fig. 8.17** Effect of varying  $l_{Airgap}$  (final 15/10 design, 3-phase AC,  $I_{Amp} = 75$  A,  $\phi_{dq} = 45^\circ$ ):  
 (a)  $T$  effects; (b)  $V_{Ph}$  effects; (c) peak and RMS comparison; (d) normalized voltage and loss performance rating

## Selection of Pole Configuration

In this analysis, the 12/8, 12/16, 12/20, 12/28, 15/5, 15/10, 15/20, 15/25, 21/7, 21/14, 21/28, 24/8, and 24/16 pole configurations were analyzed to determine the best-performing configuration for this application. Rather than creating a final design with efficiency maps for each pole configuration, the static results for each configuration were analyzed to identify the most promising pole configurations for further analysis. This significantly reduced the number of required simulations. In order to give an indication of the relative performances of each pole configuration, the “best” results of the initial sweep are compared here. Since the definition of the “best” design depends on different factors, three different comparisons are shown. In all comparison tables, only designs that meet a minimum average torque of 48 Nm are shown, unless none of the evaluated designs can reach this torque output for a given pole configuration. Please note that the voltage performance metric ( $\frac{T_{Ave}}{V_{RMS}}$ ) and the copper loss performance metric ( $\frac{T_{Ave}}{P_{Cu}}$ ) are normalized for each comparison, and thus are not intended to be compared between tables.

In TABLE 8.3 the highest average torque designs for each pole configuration are compared. The 12/8, 15/10, 21/7, 21/14, and 24/28 all show promising torque output, with the 12/8 having the best voltage performance metric, but also high torque ripple. The 15/10 and 21/14 designs offer much lower torque ripple, but the voltage and copper loss performance metrics of the 21/14 are significantly worse than the 15/10.



<b>Pole Configuration</b>	$T_{Ave}$ [Nm]	$T_{Ripple}$ [%]	$V_{Peak}$ [V]	$V_{RMS}$ [V]	$\frac{T_{Ave}}{V_{RMS}}$	$\frac{T_{Ave}}{P_{Cu}}$
12/8	60	92	97	59	1.00	0.84
12/16	51	71	167	86	0.58	1.00
12/20	41	80	195	91	0.44	0.95
12/28	28	88	224	100	0.27	0.72
15/5	51	205	118	79	0.63	0.31
15/10	82	62	169	103	0.78	0.50
15/20	52	72	229	113	0.45	0.72
15/25	41	71	240	111	0.36	0.64
21/7	68	181	237	178	0.37	0.16
21/14	104	53	328	213	0.48	0.24
21/28	51	76	456	185	0.27	0.37
24/8	72	180	407	361	0.20	0.08

**TABLE 8.3 Pole configuration performance comparison (best  $T_{Ave}$  results):**  
400 RPM, 3-phase AC @  $I_{Amp} = 75$  A,  $\phi_{dq} = 45^\circ$

The designs in TABLE 8.4 are different than those in TABLE 8.3. In TABLE 8.4, the designs with the best voltage performance metric for each pole configuration are compared. The 15/10 is shown to be capable of the best voltage performance of all the pole configurations, followed by the 12/8, and finally the 21/14.

Pole Configuration	$T_{Ave}$ [Nm]	$T_{Ripple}$ [%]	$V_{Peak}$ [V]	$V_{RMS}$ [V]	$\frac{T_{Ave}}{V_{RMS}}$	$\frac{T_{Ave}}{P_{Cu}}$
12/8	53	111	69	44	0.91	0.64
12/16	49	52	137	74	0.50	0.56
12/20	30	46	72	40	0.57	1.00
12/28	20	25	87	41	0.37	0.75
15/5	51	205	118	79	0.49	0.18
15/10	49	103	62	37	1.00	0.79
15/20	50	55	206	99	0.39	0.41
15/25	27	55	70	39	0.52	0.93
21/7	61	194	184	128	0.37	0.12
21/14	49	95	67	43	0.87	0.60
21/28	50	58	370	152	0.25	0.25
24/8	57	211	194	137	0.32	0.11

**TABLE 8.4 Pole configuration performance comparison (best  $T_{Ave}/V_{RMS}$  results):  
400 RPM, 3-phase AC @  $I_{Amp} = 75$  A,  $\phi_{dq} = 45^\circ$**

The designs in TABLE 8.5 are different than those in TABLE 8.3 and TABLE 8.4. In TABLE 8.5, the designs with the best copper loss performance metric for each pole configuration are compared. When observing the designs that met the minimum average torque requirement, once again the 15/10 shows the best voltage performance, followed by the 12/8, and finally the 21/14.

Pole Configuration	$T_{Ave}$ [Nm]	$T_{Ripple}$ [%]	$V_{Peak}$ [V]	$V_{RMS}$ [V]	$\frac{T_{Ave}}{V_{RMS}}$	$\frac{T_{Ave}}{P_{Cu}}$
12/8	49	123	66	41	0.91	0.61
12/16	50	58	150	78	0.49	0.57
12/20	34	61	85	47	0.57	1.00
12/28	25	65	107	51	0.37	0.84
15/5	51	205	118	79	0.50	0.16
15/10	49	99	60	38	1.00	0.73
15/20	50	53	213	102	0.38	0.41
15/25	31	60	77	45	0.53	0.90
21/7	61	194	184	128	0.37	0.11
21/14	49	116	71	44	0.85	0.58
21/28	50	58	370	152	0.25	0.23
24/8	57	211	194	137	0.32	0.10

TABLE 8.5 Pole configuration performance comparison (best  $T_{Ave}/P_{Cu}$  results):  
400 RPM, 3-phase AC @  $I_{Amp} = 75$  A,  $\phi_{dq} = 45^\circ$

When considering the pole configurations analyzed, the 15/10, 12/8, and 21/14 configurations are shown to offer the best performance for each of the performance metrics. The 12/8 was not analyzed further due to the torque ripple, but the 15/10 and 21/14 designs were subjected to additional parameter analyses, in addition to the ranges shown in TABLE 8.1. Finally, the 15/10 design was chosen for the final design, as it is shown to provide the best balance between the average torque, torque ripple, voltage performance metric, and copper loss performance metric.

### Coil Retention – Wedges vs. Shoes

The different slot retention methods compared are summarized in TABLE

8.6.






Case	1	2	3	4	5
<i>Wedges / Shoes</i>	None	Shoes ( $\theta_S + 2^\circ$ )	Shoes ( $\theta_S + 4^\circ$ )	Shoes ( $\theta_S + 6^\circ$ )	Wedges
$\zeta_S$	0.5 mm				
<i>Strands</i>	18				
<i>Wire Fill</i>	0.60	0.60			0.64
<i>Other Notes</i>	Thickness = 1mm				Thickness = 1mm Inset = 1.5°/side
<i>Image</i>					

TABLE 8.6 Coil retention comparison cases (final 15/10 design)

Since the pole tip fillet was shown to have a negligible impact on the magnetic performance for the MCSRМ case, a small fillet was added to avoid sharp edges around the poles. The thickness and wedge inset are the same as those for the CSRМ design. The performance of each coil retention method is compared in Fig.

8.18.

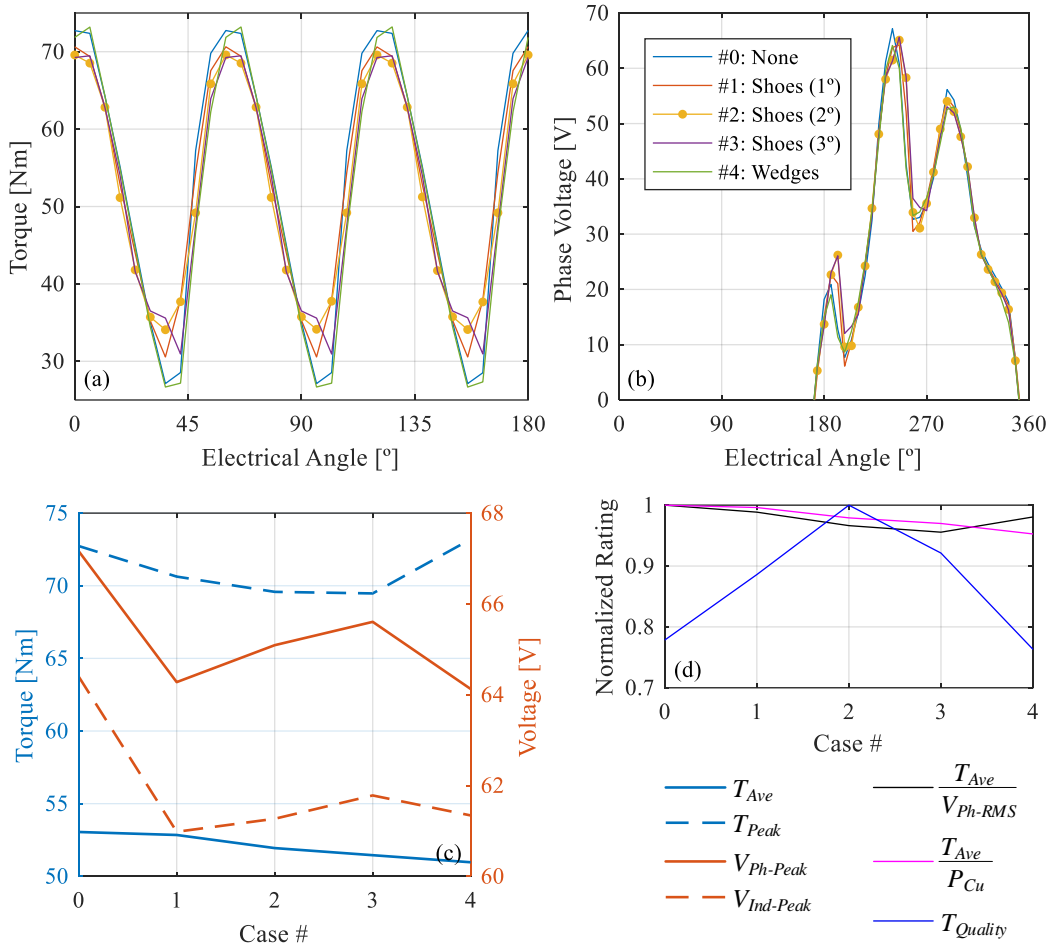


Fig. 8.18 Coil retention method comparison (final 15/10 design)

Unlike the CSR design the performance of the MCSR actually improved with the use of pole shoes. It can be seen from Fig. 8.18 that the peak torque is reduced, but the shoes improve the average torque output of the motor, without significantly affecting voltage. If the pole shoe angle is further increased, then average torque production drops and voltage performance decreases. The final design uses 2° pole shoes for these reasons.

## Current Control

In this chapter so far, the geometric design process of the MCSRМ has been discussed in detail, along with the justification for choosing the 15/10 pole configuration. All of the analyses presented to this point have been “static” analyses that assume a 3-phase sinusoidal phase current source at a fixed  $\phi_{dq}$ . The rest of the chapter presents the dynamic performance analysis of the motor, given a finite voltage source. Since the induced voltage varies depending on speed and load, the  $\phi_{dq}$  angle must be optimized for each torque-speed point to realize the best performance when considering a finite DC-link voltage. This is exactly the same reason the firing angles have to be optimized for the CSRМ case, but since a full-bridge inverter is used for the MCSRМ, there is less control over the shape of the current waveforms. Once the  $\phi_{dq}$  map has been generated, it can be fed into the MCSRМ dynamic model to create the current waveforms required for the loss analysis.

### $\phi_{dq}$ Sweep

One method of calculating the ideal  $\phi_{dq}$  for a given current amplitude and speed is through a “brute force” sweep of  $\phi_{dq}$ . This method uses the MCSRМ dynamic model to calculate torque instead of other methods that may use an analytical torque calculation with the flux-linkage LUT.

This is a less computationally efficient method of determining  $\phi_{dq}$  for a given current amplitude and speed, but in practice, it was much faster than the GA

optimization used for the CSRSM control, so this was not seen as an issue. This method also accounts for the real current waveform shape switching effects. The  $\phi_{dq}$  sweep algorithm is detailed in Fig. 8.19.

```
function  $\phi_{dq}$  = CC_Method2( $\phi_{LB}$ ,  $\phi_{UB}$ ,  $V_{DC}$ ,  $I_{Amp}$ ,  $\omega_{Elec}$ ,  $R_{Ph}$ )  
    % update the sweep range based on constraint bounds:  
     $\phi_{Range}$  =  $\phi_{LB}:1:\phi_{UB}$ ;  
  
    for i = 1:length( $\phi_{Range}$ )  
         $T_{Ave}(i)$  = RunModel( $I_{Amp}$ ,  $\phi_{Range}(i)$ ,  $\omega_{Elec}$ ,  $R_{Ph}$ ,  $V_{DC}$ );  
    end  
  
    % find the index with the maximum  $T_{Ave}$ :  
    k = find( $T_{Ave} == \max(T_{Ave})$ );  
  
    % final results for this  $\omega$ -i point:  
     $\phi_{dq}$  =  $\phi_{Range}(k)$ ;  
end
```

Fig. 8.19  $\phi_{dq}$  selection algorithm

Since a dynamic model is used for this method, the dynamic model parameters are explained in TABLE 8.7. In this table,  $N_{Cycles}$  represents the number of electrical cycles to be run in the dynamic model for each point. All but the last electrical cycle is discarded to account for transient behavior. The number of discrete simulation steps per electrical cycle is represented as  $N_{Steps}$ . The total number of simulation steps evaluated by the dynamic model for each point in the sweep range is therefore  $N_{Cycles} \cdot N_{Steps}$ . The current sampling frequency ( $f_{Current}$ ) is set at 100 kHz.

Parameter	Value
$N_{Cycles}$	10
$N_{Steps}$	5000
$f_{Current}$	100 kHz

TABLE 8.7 Sweep model parameters

The algorithm was run for the following speed ( $\omega_{RPM}$ ) range:

$$\omega_{RPM} = [1 \quad 50 \quad 100 \quad 150 \quad 200 \quad 300 \quad 400 \quad 500]$$

and the following reference current amplitude ( $I_{Amp}$ ) range:

$$I_{Amp} = [80 \quad 75 \quad 65 \quad 55 \quad 45 \quad 35 \quad 25 \quad 10 \quad 5 \quad 1]^T$$

### Constraints

In order to reduce the computation time of the parameter sweep, the sweep range of  $\phi_{dq}$  is constrained depending on the  $I_{Amp}$  index ( $c$ ) and  $\omega_{RPM}$  index ( $s$ ).

The phase advance angle  $\phi_{dq}$  is swept in increments of  $1^\circ$ elec., and the constraints are set as follows:

if  $s = 1$ :

$$0^\circ \leq \phi_{dq_{c,1}} \leq 180^\circ$$

otherwise:

$$\left(0.9 \cdot \phi_{dq_{c,s-1}}\right) \leq \phi_{dq_{c,s}} \leq 180^\circ$$

Since  $\phi_{dq}$  approaches the upper bound ( $180^\circ$ ) as the speed increases, this constraint ensures that the sweep range is reduced where possible, decreasing computation time.



### Control Map

The  $\phi_{dq}$  map shown in Fig. 8.20 was generated after running the sweep algorithm for each point in the torque-speed map.

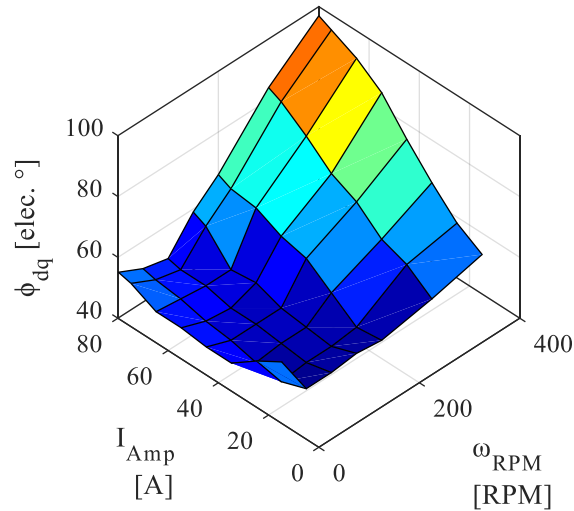


Fig. 8.20  $\phi_{dq}$  map for finalized 15/10 design

## Loss and Efficiency Analysis

Once the  $\phi_{dq}$  map has been generated, the phase current waveforms from the MCSRM dynamic model can be used to conduct a loss analysis. The loss analysis is conducted in JMAG electromagnetic FEA at each torque-speed point. The analysis accounts for pole shoe geometry, but treats the shaft as air, omits the rotor lamination bolts (which are non-magnetic), and also assumes there are no 3D effects. Further analysis has shown negligible magnetic impact from the shaft and rotor lamination bolts, but 3D effects can have torque impacts. However, due to the computational complexity of 3D loss analyses, 2D analyses were necessary.

The rest of the analysis procedure is identical to that of the CSRSM, as discussed in *Chapter 6*.

### **Torque-Speed – Efficiency Maps**

The dynamic model is also validated during the FEA iron loss calculation, to show the torque error for each calculation point, as in Fig. 8.21 (a)-(b). The torque ripple is calculated from the FEA torque results in Fig. 8.21 (c). Clearly, the MCSRM has much higher torque ripple than both the CSRSM (Fig. 6.34) and the PMSM (Fig. 5.13). This is because of negative torque generated during part of the MCSRM electrical cycle. Unlike the CSRSM where the phase is turned off when it starts to produce negative torque, the MCSRM phases cannot be independently controlled using a full-bridge inverter. In addition, since more than one phase is excited at a time for the MCSRM, it is possible to have one rotor pole contribute to positive torque while the other contributes to negative torque. Depending on the pole configuration, this effect may be more or less pronounced, but it isn't possible to completely eliminate the negative torque contribution.

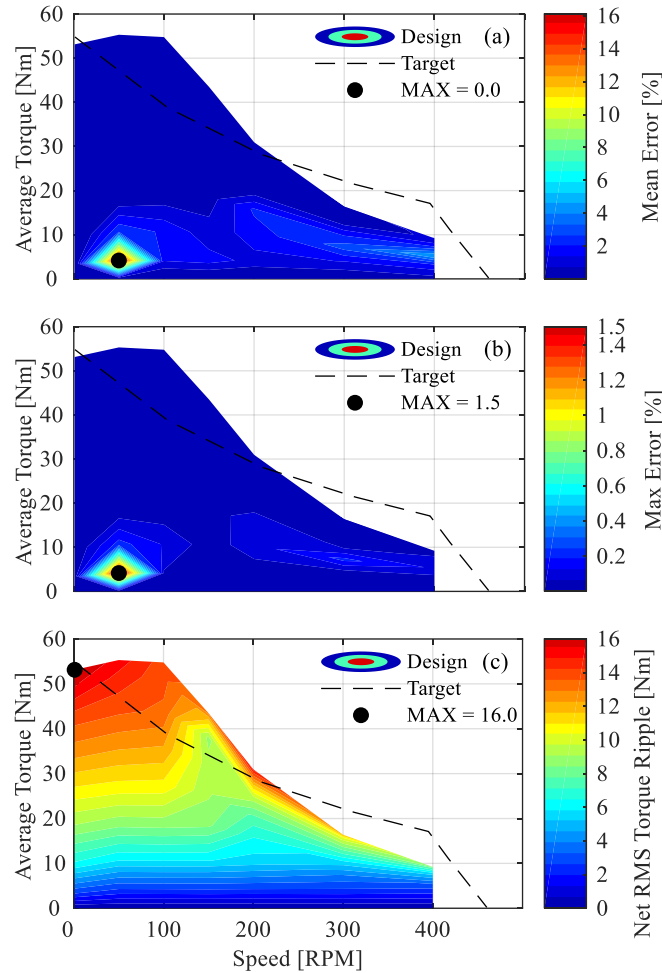


**Fig. 8.21 Torque-speed maps (final 15/10 design) - with:**  
(a) mean dynamic model vs. FEA error contours; (b) peak dynamic model vs. FEA error contours; (c)  
Net RMS torque ripple contours

FEA iron loss results are summarized in Fig. 8.22; with the maximum iron loss occurring at peak load around 400 RPM. Notably, both the maximum rotor and stator iron loss are lower for the MCSRSM when compared against the CSRSM design (Fig. 6.35), even though more iron is utilized at a given instant.

The fundamental flux density frequency for the stator poles and stator yoke is lower than the CSRSM, as is the peak flux density. The number of flux density

frequency harmonics is also lower for the MCSRM stator. These factors explain the lower stator iron loss overall for the MCSRM versus the CSRSM.

The fundamental flux density frequency for the rotor poles and rotor yoke are both higher than the CSRSM, and the peak flux density is similar between both machines. However, the number of frequency harmonics for the MCSRM is significantly reduced from the CSRSM, which explains the lower rotor iron losses.

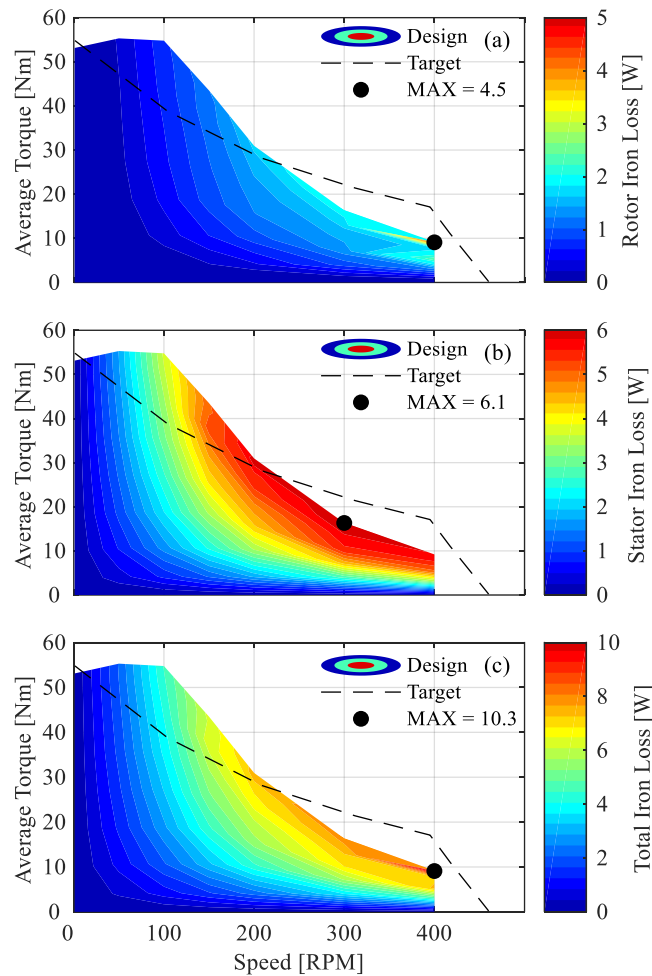
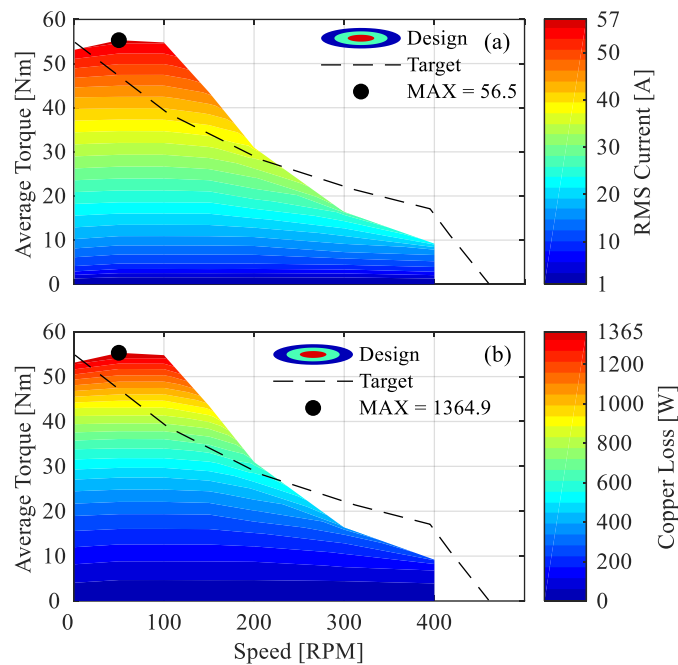


Fig. 8.22 Torque-speed maps (final 15/10 design) - with:  
(a) rotor iron loss contours; (b) stator iron loss contours; (c) total iron loss contours

The RMS current and copper loss maps are shown in Fig. 8.23. As is expected, both graphs have the worst losses at peak load and low speed. When comparing Fig. 8.22 and Fig. 8.23, it is clear that copper loss dominates for this low speed e-bike application. The MCSRМ has the same peak RMS current constraint, but higher copper losses than the CSRМ (Fig. 6.36). This is due to an increased phase resistance; estimated at  $0.142\ \Omega$  for the MCSRМ versus  $0.106\ \Omega$  for the CSRМ (at room temperature). The MCSRМ phase resistance is higher due to both the increased number of stator poles the use of much wider stator poles than the CSRМ.



**Fig. 8.23 Torque-speed maps (final 15/10 design) - with:**  
**(a) RMS phase current contours; (b) copper loss contours**

Finally, the total loss and efficiency maps are shown in Fig. 8.24. With a peak motor efficiency of 74.9%, the MCSRМ cannot meet the peak efficiency of

the PMSM or CSRSM (Fig. 6.37). This can be explained by the increased RMS current and copper loss versus the CSRSM at high speed.

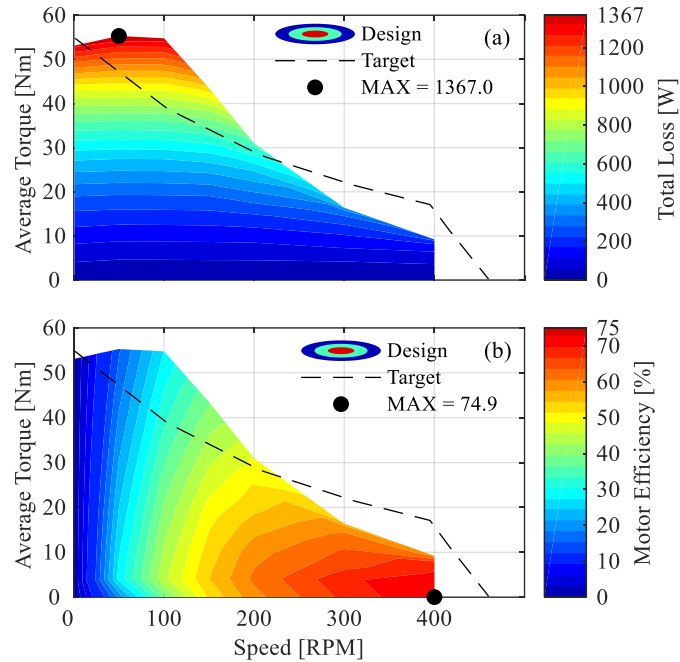


Fig. 8.24 Torque-speed maps (final 15/10 design) - with:  
(a) total loss contours; (b) motor efficiency contours

## Thermal Analysis

The thermal analysis for the MCSRSM follows the same procedure as the CSRSM, as discussed in *Chapter 6*. Since the MCSRSM has higher losses than the CSRSM, it heats up much more quickly, and thus higher temperature magnet wire must be used. Here, “Class C” polyimide-insulated magnet wire is selected for this design, which has a maximum thermal rating of 240°C [19].

This thermal analysis uses the loss analysis results for the finalized 15/10 design, as discussed in the *Loss and Efficiency Analysis* section. Observing Fig. 8.23, it is clear that copper loss is dominant for the majority of the operating range.

Considering that the MCSRМ suffers from an excitation penalty as the CSRМ does, and that this is a relatively low speed application, this is expected.

The same MotorCAD thermal analysis conducted in *Chapter 6* for the CSRМ was conducted for the MCSRМ. Fig. 8.25 and Fig. 8.26 show the simplified radial and axial geometry, as modelled in MotorCAD, respectively.

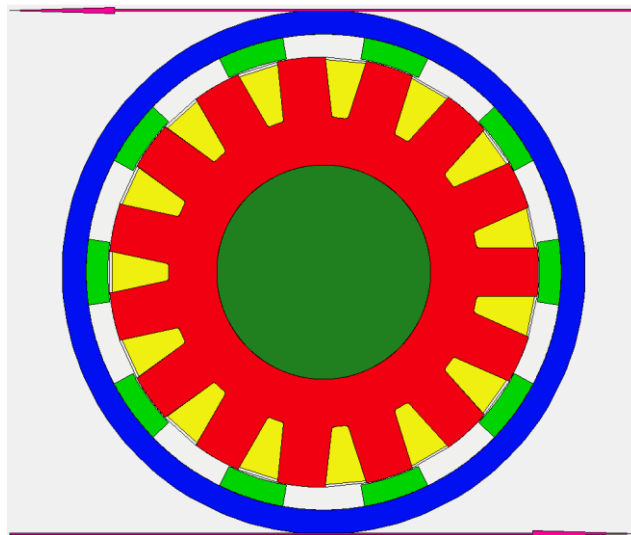


Fig. 8.25 Radial geometry representation in MotorCAD (final 15/10 design)

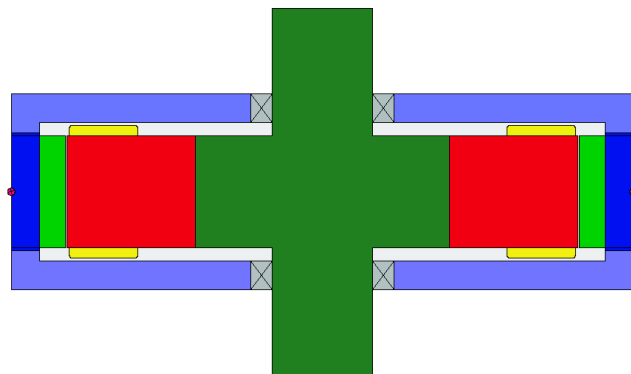


Fig. 8.26 Axial geometry representation in MotorCAD - rotated (final 15/10 design)

## Torque-Speed – Transient Thermal Maps

In Fig. 8.27 to Fig. 8.29, the transient thermal performance of different motor components is shown for discrete motor operating points inside the motor torque-speed envelope. These maps were generated by subjecting the motor to a 5-minute transient thermal analysis at each point. When comparing the results to the CSRSM (Fig. 6.40 to Fig. 6.42), the temperature is higher for each component. Considering that the housing geometry is identical between both machines, the heat paths out of the machine are the same. The higher temperatures can thus be attributed to higher machine losses.

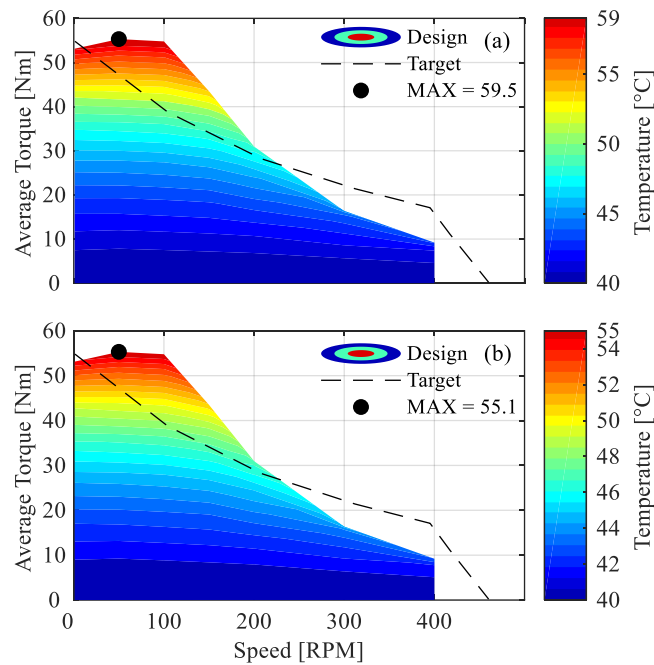


Fig. 8.27 Rotor transient thermal performance maps after 5 minutes (final 15/10 design):  
(a) pole; (b) yoke



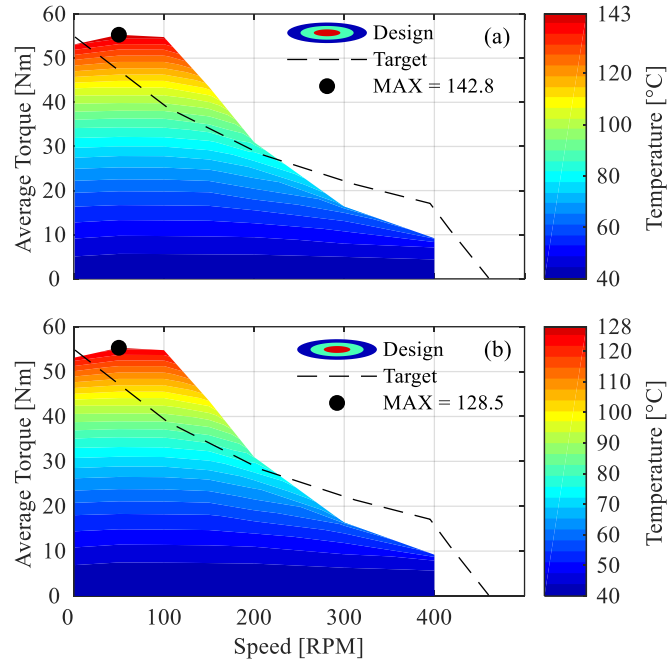


Fig. 8.28 Stator transient thermal performance maps after 5 minutes (final 15/10 design):  
(a) pole; (b) yoke

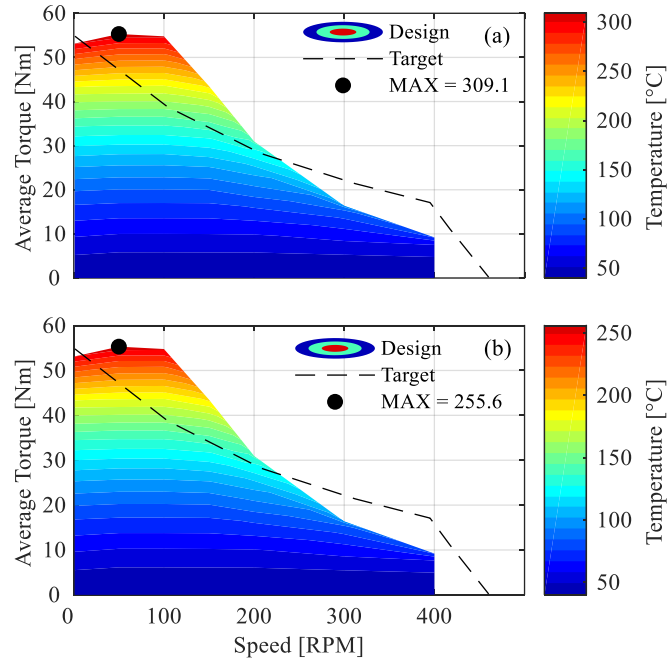


Fig. 8.29 Winding transient thermal performance map after 5 minutes (final 15/10 design)

The time required to reach the winding thermal class for each discrete torque-speed operating point is shown in Fig. 8.30. The same plot is provided for the CSRМ in Fig. 6.43.

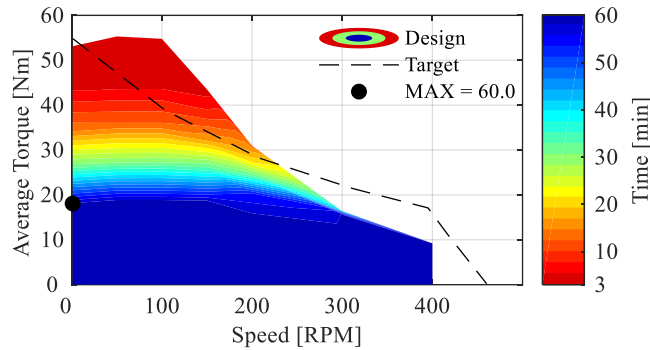


Fig. 8.30 Time to 240°C peak winding temperature (final 15/10 design)

This map was generated by running a 60-minute transient thermal analysis for each operating point, and finding the point where the peak winding temperature reaches 240°C. If the motor does not reach this temperature in 60 minutes, it is assumed to have reached steady state.

If the temperature distributions are compared to the losses in Fig. 8.23, it can be seen that the stator temperature is influenced by copper loss much more than iron loss. The most inefficient region for the motor is at very low speeds, under high load, where the copper loss is high. Under these load conditions the motor windings can still stay below 240°C for at least three minutes, as shown in Fig. 8.30.

## Drive Cycle Response

The MCSRМ was subjected to the same thermal transient drive cycle test as the CSRМ, as detailed in *Chapter 6* (see Fig. 6.44 and Fig. 6.45). However, the high speed region of this test has been omitted, as it exceeds the torque output of the MCSRМ at this range.

The finalized drive-cycle is shown in Fig. 8.31, and the torque response of the MCSRМ is shown in Fig. 8.32.

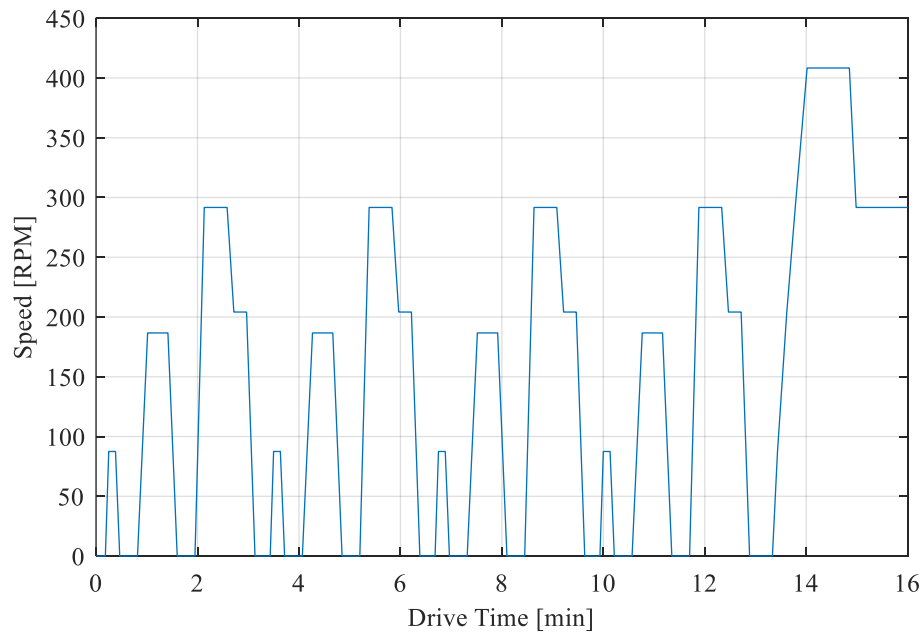


**Fig. 8.31** Speed-time e-bike drive cycle

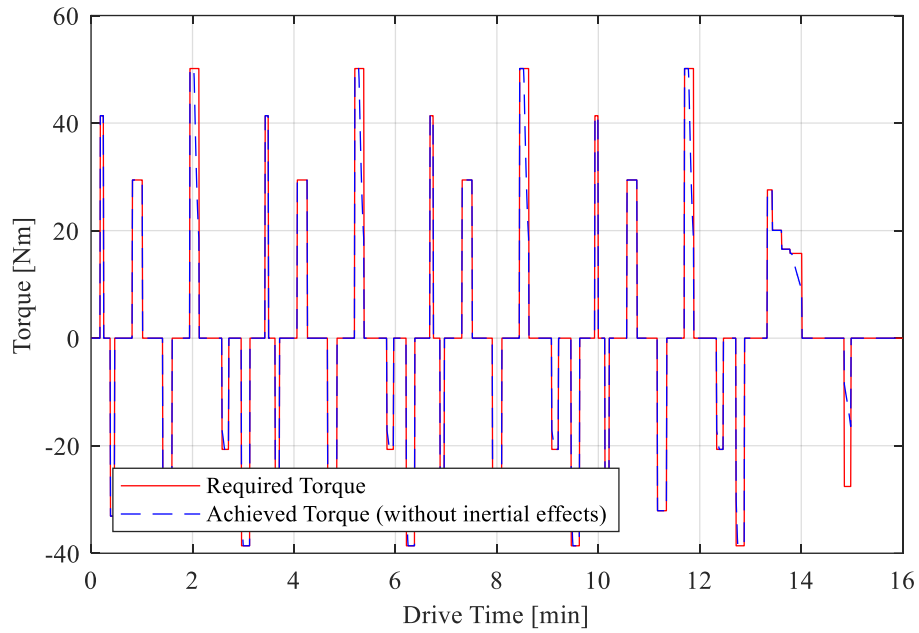


Fig. 8.32 Torque-time e-bike drive cycle

Fig. 8.33 shows the drive cycle transient thermal response of the motor.

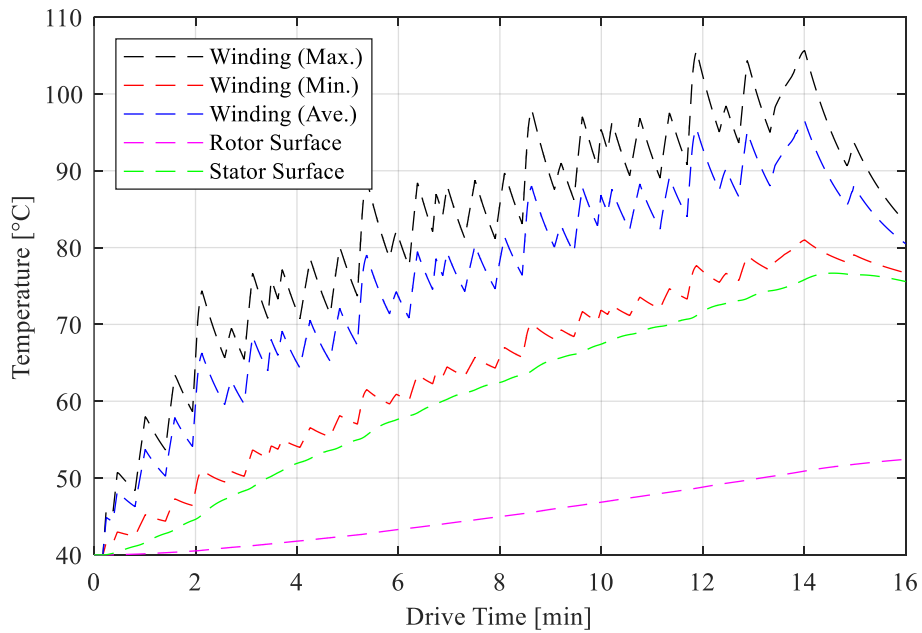


Fig. 8.33 Drive-cycle transient thermal response (final 15/10 design)

It is clear from Fig. 8.33 that the MCSRМ design heats up much more quickly than the CSRМ design does (Fig. 6.46). However, with the higher temperature magnet wire utilized in the design, the motor still offers good thermal performance for the tested drive cycle, though the wire cost may be increased.

## FEA Validation

In this section, the MCSRМ dynamic model is validated at two operating points, using a switched voltage source electromagnetic FEA analysis. This is the same validation procedure used to validate the CSRМ dynamic model, in *Chapter 6* (see Fig. 6.47 to Fig. 6.50). The same switching frequencies at each operating point are used for this analysis.

### 2D Switched Voltage FEA Validation – Critical Points

The first validation point is at 10 RPM and maximum load. The switched voltage waveforms input into JMAG are shown in Fig. 8.34.

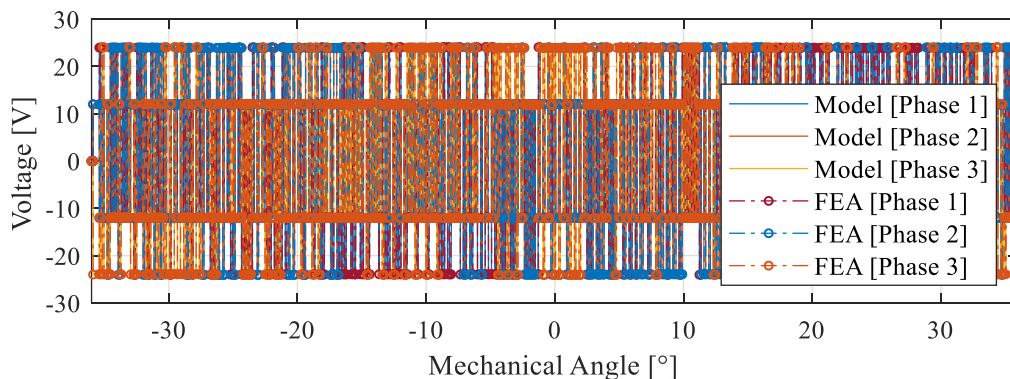


Fig. 8.34 Switched voltage waveforms @ 10 RPM, 75A reference (final 15/10 design)

Fig. 8.35 shows the torque, current, and flux-linkage validation results, showing good agreement.

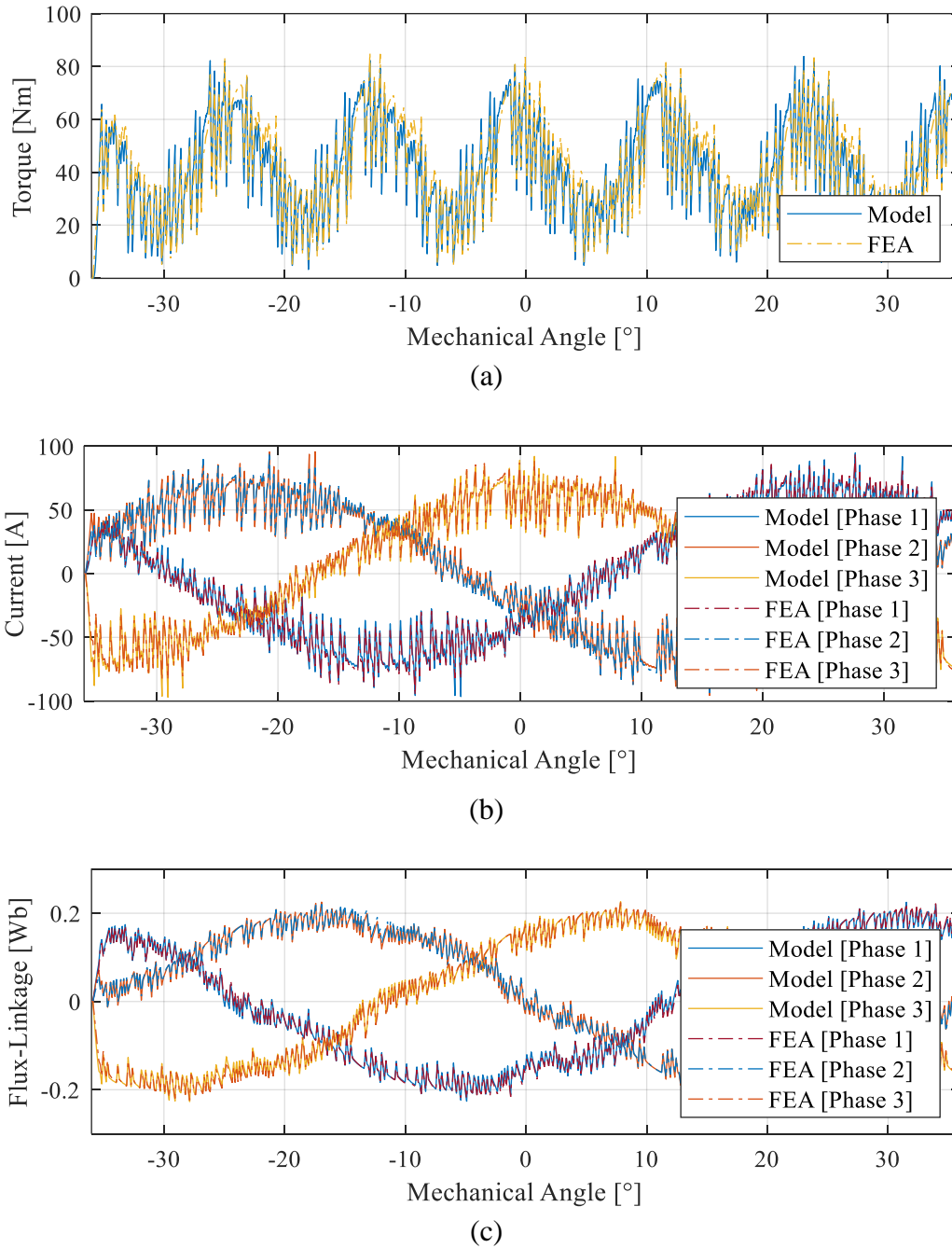


Fig. 8.35 2D switched voltage FEA validation @ 10 RPM, 75A reference (final 15/10 design):  
(a) torque; (b) phase current; (c) phase flux-linkage

The second validation point is at 400 RPM and maximum load. The switched voltage waveforms input into JMAG are shown in Fig. 8.36.

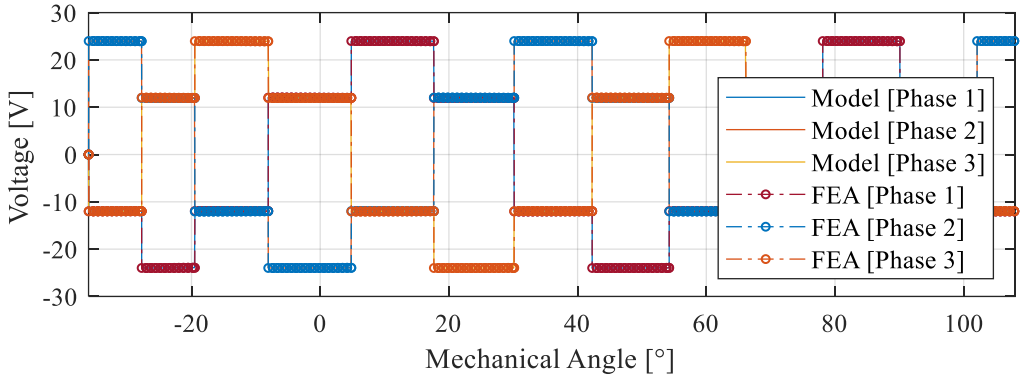
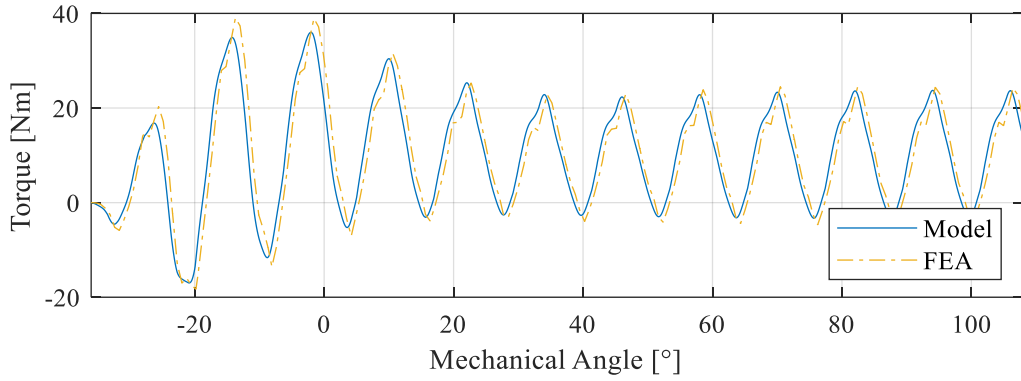
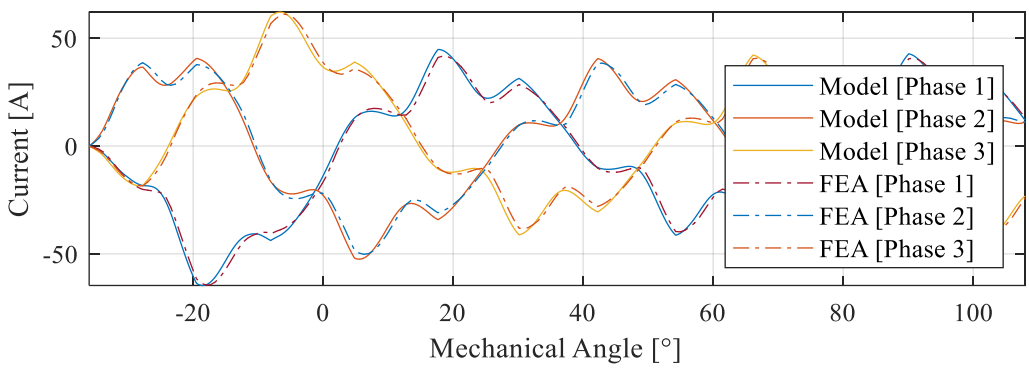


Fig. 8.36 Switched voltage waveforms @ 400 RPM, 75A reference (final 15/10 design)

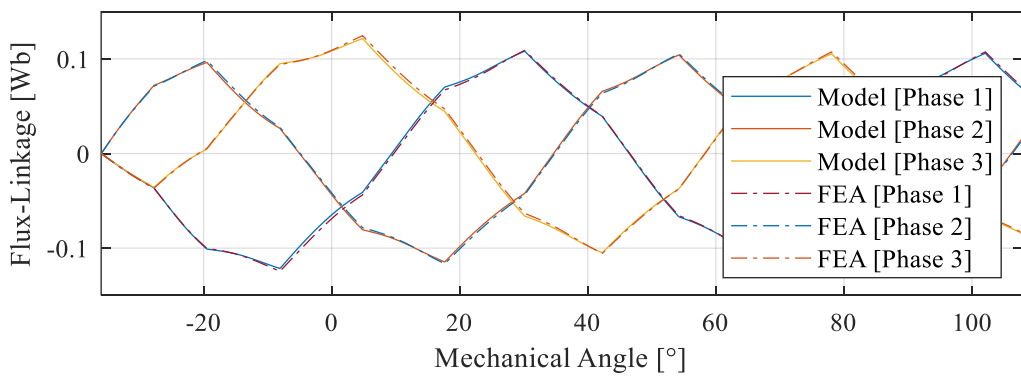
Fig. 8.37 shows the torque, current, and flux-linkage validation results, showing excellent agreement.



(a)



(b)



(c)

Fig. 8.37 2D switched voltage FEA validation @ 400 RPM, 75A reference (final 15/10 design):  
(a) torque; (b) phase current; (c) phase flux-linkage



## Summary

A novel exterior-rotor mutually coupled switched reluctance motor was engineered using a design space exploration method, where each geometry parameter was varied to find the best performing design. 12/8, 12/16, 12/20, 12/28, 15/5, 15/10, 15/20, 15/25, 21/7, 21/14, 21/28, 24/8, and 24/16 pole configurations were analyzed, and the best performing configuration was selected for further analysis. The 15/10 configuration was found to be most suitable for this application, as it fits the torque speed requirements better than the other designs while also offering reasonable motor efficiency and lower torque ripple than many of the other MCSRM designs.

After the electromagnetic design, the finalized motor was analyzed in depth; and the  $dq$ -excitation angle ( $\phi_{dq}$ ) selection, loss analysis, and thermal analysis were discussed in detail. A structural analysis was not conducted for the MCSRM, as the CSRSM structural analysis is expected to remain valid for this motor, seeing as the critical dimensions did not change.

The finalized motor was found to have a peak motor efficiency of 74.9%, which is inferior to both the CSRSM and PMSM. This is primarily due to the wide poles that were required to improve torque quality, and the reduction in coil space due to this. The minimal coil space increases copper losses significantly, reducing the efficiency. The higher copper losses also cause the motor to reach its thermal limit more quickly than the CSRSM. The iron losses were lower than the CSRSM on both the rotor and stator. On the stator, the lower losses are due to lower peak flux

densities, a lower fundamental flux density frequency, and fewer flux density harmonics. The rotor iron losses are lower primarily due to fewer flux density harmonics.

The high speed performance of the MCSRM is inferior to the CSRM and PMSM. This is due to a reduction in power factor, which has several causes. The first reason is lower saturation levels, giving less power factor improvement than the CSRM achieves. Next, the phase resistance is higher for the MCSRM, which means less voltage is available to counter the EMF at high speed. The final reason for poor high speed performance is the excitation of more than one phase at a time increasing the EMF that must be overcome by the DC-link voltage. Finally, the dynamic modelling used for the control analysis was validated against 2D JMAG FEA and was shown to be accurate.

# Chapter 9

## Conclusions

### Conclusions

This thesis discusses the design of both a conventional non-coupled SRM and a mutually-coupled SRM for an exterior rotor e-bike application. Several novel pole configurations were analyzed for each machine type, and the performance of the final CSRSM and MCSRM designs were compared for this application.

This thesis starts off with an introduction in Chapter 1, which outlines the thesis contributions and motivation for this research. In Chapter 2, the theoretical fundamentals of CSRSM and MCSRM operation are discussed. The importance of machine saturation is analyzed in detail. Due to heavy saturation, both machines are shown to be highly non-linear and cannot be designed using analytical methods. Therefore, the modelling fundamentals of each machine are outlined in Chapter 3. With the fundamentals and modelling methods outlined, Chapter 4 focuses on defining the target e-bike application; focusing on the market, regulations, and motor characteristics. Chapter 5 takes this further, where a commercial PMSM e-bike motor is purchased, reverse engineered, and validated to develop accurate target requirements for the CSRSM and MCSRM machine designs. With the design constraints defined, Chapter 6 then details the electromagnetic, control, structural, and thermal design of a non-coupled 12/16 exterior rotor SRM. The final design is

then manufactured and experimentally validated in Chapter 7. The MCSRM is then designed in Chapter 8, including the electromagnetic, control, and thermal design.

The performance and parameters of the reference PMSM, finalized 12/16 CSRSM, and finalized 15/10 MCSRM are compared in TABLE 9.1.

	<b>PMSM (HS3548)</b>	<b>CSRSM (12/16)</b>	<b>MCSRSM (15/10)</b>
$T_{Ave} (< BS)$ [Nm]	54.8	51.8	55.3
$T_{Ave}$ (400 RPM) [Nm]	17.1	25.5	9.2
$T_{Ripple} (< BS)$ [Nm rms]	0.8	4.8	16.0
$T_{Ripple}$ (300 RPM) [Nm rms]	0.35	0.51	11.6
<i>Peak Efficiency</i> [%]	80.9	85.4	74.9
<i>Phase Resistance</i> [ $\Omega$ ]	0.084	0.106	0.142
<i>Mass</i> [kg]	7.74	10.36	< 10.36
<i>Stack Length</i> [mm]	34.1	39.5	
<i>Outside Axial Length</i> [mm]	58		
<i>Outside Diameter</i> [mm]	220		
$i_{RMS}$ (max) [A rms]	~ 55		
<i>DC Link Voltage</i> [V]	36		
<i>Notes</i>	Mass has been measured unless otherwise noted. All performance specifications are theoretical. BS = base speed		

**TABLE 9.1 Performance comparison – PMSM vs. 12/16 CSRSM vs. 15/10 MCSRM**

The 12/16 CSRSM design is shown to be competitive with the PMSM when considering torque output. However, it is important to note that the stator stack length of the CSRSM is longer than the PMSM machine (39.5 mm vs. 34.1 mm),

though the outside dimensions are the same. The CSRSM is superior to the PMSM in terms of peak efficiency, and high speed torque performance, while having the potential to cost less when mass manufactured (due to the lack of rare-earth permanent magnets). The CSRSM has higher torque ripple than the PMSM does at low speed and high torque, however, the torque ripple is competitive at higher speeds.

The 15/10 MCSRM design uses a full-bridge inverter, just as the PMSM does. It has the same exterior dimensions and same stack length as the CSRSM, but its high speed torque performance is shown to be inferior to both the CSRSM and PMSM. This is due to several reasons, among which are lower power factor, multi-phase excitation, and a higher voltage drop. Torque quality is lower than the CSRSM, as is efficiency, due to higher copper loss. The MCSRM is shown to be highly resistant to saturation, which gives it the potential for high torque output at low speed, but also makes it challenging to effectively improve machine power factor through saturation; meaning that high speed torque output suffers. The MCSRM may be better suited to lower speed, high torque applications, for this reason.

## **Future Work**

This thesis is not intended to be a comprehensive analysis of the CSRSM and MCSRM for this application. There are some areas where future research may be carried out, to better understand the differences between CSRSM, MCSRM, and PMSM for this application:

- **MCSRМ - Current Shaping**

Just as current waveform shaping can be applied for the CSRM case, it can also be applied to reduce torque ripple for the MCSRМ case. The MCSRМ is shown to have a significant amount of negative torque production by one of the rotor poles, as the other pole produces positive torque, effectively reducing the total torque output. This is true both with a rotor yoke and without a yoke. If the current waveforms could be shaped, and current could be controlled independently to divert the flux paths that contribute to negative torque, then it may be possible to improve the torque output and reduce the torque ripple. However, this would likely require the use of a symmetric-bridge ('H'-bridge) converter, with independently controlled phases, making the converter more complex than both the asymmetric-bridge (CSRM) and full-bridge (MCSRМ/PMSM) converters; increasing cost.

- **MCSRМ - Removal of Rotor Yoke**

A brief analysis was conducted on the effects of removing the iron rotor yoke for the MCSRМ design (see *Appendix C*). The rotor poles can then be mounted using a thinner, non-magnetic yoke. This improves the radial space inside the exterior rotor machine, which improve coil space and help reduce copper loss. At the same time, it changes the way flux links in the magnetic circuit, and depending on the pole configuration it can improve peak torque significantly without increasing the phase voltage. The

downside is that torque ripple is nearly 100%. Without the yoke, the rotor poles act similarly to how the magnets in a SPMSM do, however the flux direction is not fixed, as the excitation is still provided by the stator. If the flux direction in the rotor poles could be controlled, then it may be possible to eliminate some of the negative phase torque and improve the overall torque ripple. Controlling the flux direction in the poles requires current shaping, as discussed below.

- **CSRM - Current Shaping**

In line with the point above, the CSRM torque ripple can be reduced (particularly at low speed, where the EMF is low), using torque sharing functions (current waveform shaping). The blending of this control strategy with conventional firing angle control could also be researched, to create a hybrid control map. This would allow the torque ripple to be compared in detail, to see if the SRM can compete on these grounds.

- **MCSRM – Prototyping and Validation**

The dynamic modelling used for the MCSRM was experimentally validated in [3], but the 15/10 MCSRM design presented in this thesis was not.

- **MCSRM – Square-Wave vs. Sine-Wave Excitation**

Sine-wave and square-wave excitation were both investigated for the finalized MCSRM, with multiple conduction angles being analyzed for the latter case (i.e. 120° to 180°). However, the performance of each

excitation type using different motor geometry was not analyzed. The difference in torque output for the final design (between 120° square-wave and sine-wave) was not significant, and the results were omitted from this thesis. However, a comprehensive analysis was never conducted, and this may be justification for future research.

- **Acoustic Noise and Vibration Analysis**

Noise and vibration analysis and modelling have been discussed and validated in [2]. However, a noise and vibration analysis was not conducted for any of the motors discussed in this thesis. If such analyses were to be conducted, it may open up further avenues for research; such as modifying the mass, stiffness, and dampening to reduce motor resonance and noise output.

- **Analysis on Pole Filler Effects**

In line with the NVH analysis, the rubber pole filler material used in the CSRSM prototype was not analyzed in detail. They were primarily added to reduce windage, but may also add mass/dampening to the rotor. It may be worth investigating if this has any impact on the overall NVH performance.



## References

- [1] J. W. Jiang, B. Bilgin, B. Howey, and A. Emadi, “Design Optimization of Switched Reluctance Machine Using Genetic Algorithm,” in *Proc. IEEE International Electric Machines and Drives Conference (IEMDC)*, Coeur d’Alene, ID, May 2015, pp. 1671–1677.
- [2] J. Dong *et al.*, “Hybrid Acoustic Noise Analysis Approach of Conventional and Mutually Coupled Switched Reluctance Motors,” *IEEE Trans. Energy Convers.*, vol. 32, no. 3, pp. 1042–1051, 2017.
- [3] J. Dong *et al.*, “Advanced Dynamic Modeling of Three-Phase Mutually-Coupled Switched Reluctance Machine,” *IEEE Trans. Energy Convers.*, vol. 33, no. 1, pp. 146–154, 2017.
- [4] B. Howey, E. Rowan, B. Bilgin, and A. Emadi, “Thermal Trade-off Analysis of an Exterior Rotor E-Bike Switched Reluctance Motor,” in *Proc. IEEE Transportation Electrification Conference and Expo (ITEC)*, Chicago, IL, Jun. 2017, pp. 605–612.
- [5] B. Howey, B. Bilgin, and A. Emadi, “Design of an External-Rotor Direct Drive E-Bike Switched Reluctance Motor,” *IEEE*, 2018.
- [6] B. Howey, B. Bilgin, and A. Emadi, “Design of a Mutually Coupled External-Rotor Direct Drive E-Bike Switched Reluctance Motor,” *IEEE*, 2018.
- [7] B. Howey and H. Li, “Operational Principles and Modeling of Switched

- Reluctance Machines,” in *Switched Reluctance Motor Drives: Fundamentals to Applications*, 1st ed., B. Bilgin, J. Jiang, and A. Emadi, Eds. Hamilton: CRC Press, 2018.
- [8] B. Bilgin, “Switched Reluctance Machines in Generating Mode,” in *Switched Reluctance Motor Drives: Fundamentals to Applications*, 1 ed., B. Bilgin, J. Jiang, and A. Emadi, Eds. Hamilton: CRC Press, 2018.
- [9] B. Bilgin, A. Emadi, and M. Krishnamurthy, “Switched reluctance generator with higher number of rotor poles than stator poles,” *IEEE Transp. Electrifi. Conf. Expo*, pp. 6–11, 2012.
- [10] F. Hensley, S. Member, A. W. Wong, S. Member, W. C. Yu, and S. Member, “Comparative Analysis of Conventional Switched Reluctance Machines and Mutually Coupled Switched Reluctance Machines,” pp. 180–185, 2017.
- [11] R. Citron and J. Gartner, “Executive Summary: Electric Bicycles Li-Ion and SLA E-Bikes: Drivetrain, Motor, and Battery Technology Trends, Competitive Landscape, and Global Market Forecasts,” 2016.
- [12] D. Hurst and J. Gartner, “Research Report - Executive Summary: Electric Bicycles,” p. 14, 2013.
- [13] Minister of Transport, *2017 Motor Vehicle Safety Regulations C.R.C. c.1038*. Canada: Transport Canada, 2017.
- [14] Grin Technologies, “Pedal Assist Systems.” [Online]. Available: <http://www.ebikes.ca/learn/pedal-assist.html>. [Accessed: 26-Apr-2018].

- [15] Grin Technologies, “M3548R Product Description.” [Online]. Available: <http://www.ebikes.ca/m3548r.html>. [Accessed: 31-Oct-2015].
- [16] Grin Technologies, “The Grinfineon Motor Controller - User Manual - Rev 1.0,” 2016. [Online]. Available: [http://www.ebikes.ca/documents/Grinfineon\\_V1.0\\_Web.pdf](http://www.ebikes.ca/documents/Grinfineon_V1.0_Web.pdf). [Accessed: 11-Jun-2018].
- [17] Grin Technologies, “C7225-NC Product Description.” [Online]. Available: <http://www.ebikes.ca/shop/ebike-parts/controllers/c7225-nc.html#>. [Accessed: 31-Oct-2015].
- [18] J. Limre-Elmore, Z. Thompson, M. Vass, and A. Hynek, “Motor Simulator - HS3548.” [Online]. Available: [http://www.ebikes.ca/tools/simulator.html?bopen=false&motor=M3548&batt=cust\\_36\\_0\\_0&cont=C25&frame=cust\\_0\\_0&mass=0&hp=0&wheel=26i&axis=rpm&black=load&throt=100&temp=55](http://www.ebikes.ca/tools/simulator.html?bopen=false&motor=M3548&batt=cust_36_0_0&cont=C25&frame=cust_0_0&mass=0&hp=0&wheel=26i&axis=rpm&black=load&throt=100&temp=55). [Accessed: 23-Apr-2018].
- [19] R. Beeckman, “NEMA Magnet Wire Thermal Class Ratings.” Essex Group.
- [20] McMaster-Carr, “#5972K295 Datasheet (6908 Ball Bearing),” 2017. [Online]. Available: <https://www.mcmaster.com/#5972k295/>. [Accessed: 01-Jan-2017].
- [21] McMaster-Carr, “#6661K104 Datasheet (6203 Ball Bearing),” 2017. [Online]. Available: <https://www.mcmaster.com/#6661k104/>. [Accessed: 01-Jan-2017].

- [22] NTN Corporation, “Ball and Roller Bearings (Cat. No. 2200/E),” no. 2200/E. p. 105, 1997.
- [23] McMaster-Carr, “#1462N47 Datasheet (Silicone Rubber),” 2017. [Online]. Available: <https://www.mcmaster.com/#1462n47/>. [Accessed: 01-Jan-2017].
- [24] JFE, “Electrical Steel Sheets: JFE G-Core, JFE N-Core,” 2015. [Online]. Available: <http://www.jfe-steel.co.jp/en/products/electrical/catalog/f1e-001.pdf>. [Accessed: 23-Apr-2018].
- [25] IEEE Power and Energy Society, *IEEE Standard 43-2013 - Recommended Practice for Testing Insulation Resistance of Electric Machinery*, vol. 2013. 2013.
- [26] E. Wiedenbrug, G. Frey, and J. Wilson, “Impulse Testing and Turn Insulation Deterioration in Electric Motors,” *IEEE*, pp. 50–55, 2003.
- [27] ISO - International Organization for Standardization, “ISO 1940-1 - Mechanical vibration – Balance quality requirements for rotors in a constant (rigid) state – Part 1: Specification and verification of balance tolerances,” *ISO - Int. Organ. Stand.*, vol. 2003, p. 36, 2003.
- [28] MatWeb, “Matweb,” 2018. [Online]. Available: <http://www.matweb.com/>. [Accessed: 12-Feb-2018].
- [29] TriStar Plastics Co., “Quadrant EPP Ketron® 1000 PEEK, Extruded Unfilled Polyetherether Ketone (ASTM Product Data Sheet).” [Online]. Available:

- <http://www.matweb.com/search/DataSheet.aspx?MatGUID=53b9159c018544a599a06726922c9b8e>. [Accessed: 01-Jan-2017].
- [30] McMaster-Carr, “#90145A480 Datasheet (1/8" Dowel Pin),” 2017.  
[Online]. Available: <https://www.mcmaster.com/#90145a480/>. [Accessed: 01-Jan-2017].
- [31] K. O. Kverneland, *Metric Standards for Worldwide Manufacturing*, 8th ed. 2012.
- [32] Advanced Mechanical Engineering Solutions, “Metric Thread Size and Tolerance Calculator (ISO M Thread).” [Online]. Available: <http://www.amesweb.info/Screws/IsoMetricScrewThread.aspx>. [Accessed: 01-Jan-2017].
- [33] McMaster-Carr, “#91292A026 Datasheet (M3 Socket Cap Screw),” 2017.  
[Online]. Available: <https://www.mcmaster.com/#91292a026/>. [Accessed: 01-Jan-2017].
- [34] Tamagawa Seiki Co., “Singlsyn VR Type Resolver Brochure,” 2016.  
[Online]. Available: [https://www.tamagawa-seiki.com/assets/img/downloads/pdf/resolver-synchro/1570N15EJ\\_shusei.pdf](https://www.tamagawa-seiki.com/assets/img/downloads/pdf/resolver-synchro/1570N15EJ_shusei.pdf). [Accessed: 01-Jan-2016].
- [35] McMaster-Carr, “#9714K58 Datasheet (Wave Spring Washer),” 2017.  
[Online]. Available: <https://www.mcmaster.com/#9714k58/>. [Accessed: 01-Jan-2017].

# Appendix

## A. Phase Transformations ( $abc \rightarrow dq$ )

### Phase Transformations

In order to simplify the calculations when accounting for mutual effects between phases, certain transformations are used.

#### Forward Transformation ( $abc \rightarrow \alpha\beta \rightarrow dq$ )

The first transformation, called a ‘Clarke Transformation’, converts a 3-phase  $abc$  system into an equivalent 2-phase  $\alpha\beta$  system:

$$\begin{aligned} \mathbf{z}_{\alpha\beta} &= \begin{bmatrix} z_{\alpha} \\ z_{\beta} \end{bmatrix} \\ &= \frac{2}{3} \begin{bmatrix} 1 & -\frac{1}{2} & -\frac{1}{2} \\ 0 & \frac{\sqrt{3}}{2} & -\frac{\sqrt{3}}{2} \end{bmatrix} \begin{bmatrix} z_a \\ z_b \\ z_c \end{bmatrix} \\ &= \frac{4}{3} \begin{bmatrix} 2z_a - z_b - z_c \\ (\sqrt{3})(z_b - z_c) \end{bmatrix} \end{aligned}$$

After applying the Clarke Transformation, the  $\alpha\beta$  system can be further simplified, by making it a pseudo-stationary  $dq$  system, by use of the ‘Park Transformation’:

$$\begin{aligned} \mathbf{z}_{dq} &= \begin{bmatrix} z_d \\ z_q \end{bmatrix} \\ &= \begin{bmatrix} \cos(\theta_{Elec}) & \sin(\theta_{Elec}) \\ -\sin(\theta_{Elec}) & \cos(\theta_{Elec}) \end{bmatrix} \begin{bmatrix} z_{\alpha} \\ z_{\beta} \end{bmatrix} \end{aligned}$$

$$= \begin{bmatrix} \cos(\theta_{Elec})z_{\alpha} + \sin(\theta_{Elec})z_{\beta} \\ \cos(\theta_{Elec})z_{\beta} - \sin(\theta_{Elec})z_{\alpha} \end{bmatrix}$$

Alternatively, using Euler's identity:

$$e^{j\theta} = \cos(\theta) + j\sin(\theta)$$

$$\mathbf{z}_{dq} = \mathbf{z}_{\alpha\beta} e^{-j\theta_{Elec}}$$

*Reverse Transformation* ( $dq \rightarrow \alpha\beta \rightarrow abc$ )

Typically, the system will be transformed from 3-phase  $abc$  to the  $dq$  reference frame, where any required work is performed. Afterward, it is often desirable to transform back to the  $abc$  frame to present the real values experienced in the motor. An Inverse Park Transformation is first applied to transform from  $dq$  to the  $\alpha\beta$  reference frame:

$$\begin{aligned} \mathbf{z}_{\alpha\beta} &= \begin{bmatrix} z_{\alpha} \\ z_{\beta} \end{bmatrix} \\ &= \begin{bmatrix} \cos(\theta_{Elec}) & -\sin(\theta_{Elec}) \\ \sin(\theta_{Elec}) & \cos(\theta_{Elec}) \end{bmatrix} \begin{bmatrix} z_d \\ z_q \end{bmatrix} \\ &= \begin{bmatrix} \cos(\theta_{Elec})z_d + \sin(\theta_{Elec})z_q \\ \sin(\theta_{Elec})z_d + \cos(\theta_{Elec})z_q \end{bmatrix} \end{aligned}$$

Alternatively, using Euler's identity:

$$\mathbf{z}_{\alpha\beta} = \mathbf{z}_{dq} e^{j\theta_{Elec}}$$

After the Inverse Park Transformation, the Inverse Clarke Transformation is applied to transform from the  $\alpha\beta$  frame to the  $abc$  frame:

$$\mathbf{z}_{abc} = \begin{bmatrix} z_a \\ z_b \\ z_c \end{bmatrix}$$

$$= \begin{bmatrix} 1 & 0 \\ -\frac{1}{2} & \frac{\sqrt{3}}{2} \\ \frac{1}{2} & -\frac{\sqrt{3}}{2} \end{bmatrix} \begin{bmatrix} z_\alpha \\ z_\beta \end{bmatrix}$$
$$= \begin{bmatrix} z_\alpha \\ \left(\frac{\sqrt{3}}{2}\right)z_\beta - \left(\frac{1}{2}\right)z_\alpha \\ -\left(\frac{\sqrt{3}}{2}\right)z_\beta - \left(\frac{1}{2}\right)z_\alpha \end{bmatrix}$$

## B. CSRM Structural Analysis

### Assumptions and Loading Conditions

A static structural analysis assumes that structural loading is applied slowly, so that dynamic effects can be ignored (for example, impact loading, or high frequency loading would require the use of a dynamic analysis). In addition, the materials in this analysis are assumed to deform only elastically under load, without any plastic deformation, strain rate hardening, or fatigue effects.

The fatigue life of each component was analyzed, but assumes the same static case loading is applied cyclically, which differs from true loading conditions, but gives a good estimate. The fatigue life estimation was conducted using the ANSYS Fatigue Tool, constant amplitude, fully reversed loading with a scaling factor of 0.35 for the shaft, and 1 for the other parts.

Other design assumptions were made as shown in TABLE X.1, with the analysis conducted at 35°C using ANSYS Mechanical FEA. The endcaps used 6061-T6 aluminum for the material, where the shaft used 4340-normalized steel



(see TABLE X.2). These materials properties are provided by a mix of ANSYS mechanical pre-set material data and data from the Matweb material database [28], to ensure accurate representation of the real material properties.

<b>Parameter</b>	<b>Description</b>	<b>Value</b>
$m_{Bike}$	lumped mass of rider and bike	70 kg
$\alpha_g$	acceleration due to gravity	$9.81 \text{ m/s}^2$
$d_{Wheel}$	wheel diameter, with tire	0.4064 m (16 inch)
$T_{Ref(1RPM)}$	motor average torque @ 1 RPM	60 Nm
$T_{Ref(400RPM)}$	motor average torque @ 400 RPM	25 Nm

**TABLE X.1** Structural analysis assumptions

Parameter	Aluminum (6061-T6)	Steel (4340-Norm.)	Units
Density	2770	7850	kg/m <sup>3</sup>
Thermal Expansion Coefficient	0.000023	0.000012	/°C
Thermal Expansion – Reference Temperature	22	22	°C
Young’s Modulus	71	205	GPa
Poisson’s Ratio	0.33	0.32	
Yield Strength	280	710	MPa
Ultimate Tensile Strength	310	1110	MPa

**TABLE X.2 Material properties for structural FEA**

Uncertainty due to idealized loading conditions is accounted for with a safety factor in each loading case.

### ***Moment Loading***

Torque loading conditions were based on the simulated output torque characteristics of the finalized SRM design, and applied around the rotation axis of motor. A safety factor of 1.2 is used for this analysis.

$$T_{Motor} = T_{Ref} \cdot SF$$

$$SF = 1.2$$

In the case of the shaft, this loading condition was applied as shown in Fig. X.1. This is the surface that the stator stack interfaces with.

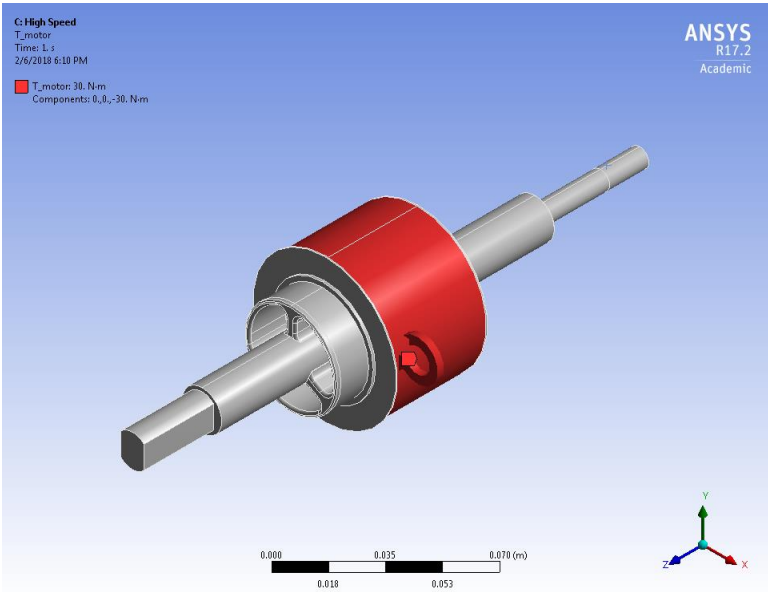


Fig. X.1 Torque condition – shaft surfaces

Both endcaps applied this loading condition to the bolt and dowel pin interface faces, as shown in Fig. X.2. This is justified, as the reaction torque is transmitted through these points by the rotor stack.

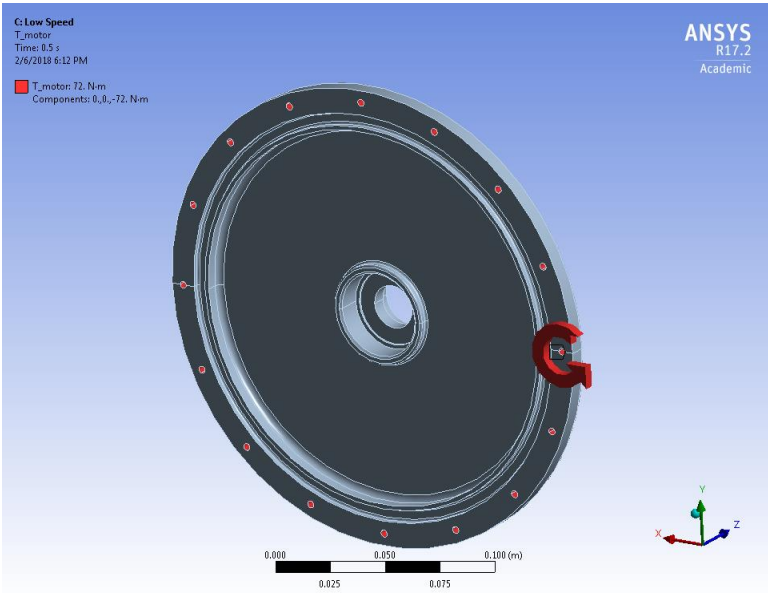


Fig. X.2 Torque condition - front endcap surfaces (rear endcap similar)

### Radial Bump Loading

Radial loading conditions were applied as a distributed bearing force load and the radial loading safety factor depends on the load condition. High speed is expected to be an impact loading case, so the safety factor is set to 5 under static loading (5g loading), where low speed will be a much slower force application, so the safety factor is set to 1 (1g loading).

$$F_{Bump} = m_{Bike} \cdot \alpha_g \cdot SF$$
$$SF = \begin{cases} 1, & \omega_{RPM} = 1 \\ 5, & \omega_{RPM} = 400 \end{cases}$$

The shaft analysis applied the bump loads at the bearing surfaces using a distributed bearing load, as shown in Fig. X.3. This is justified, as the force is transmitted from the rotor, through the endcaps and bearings, and applied to the shaft in this manner.

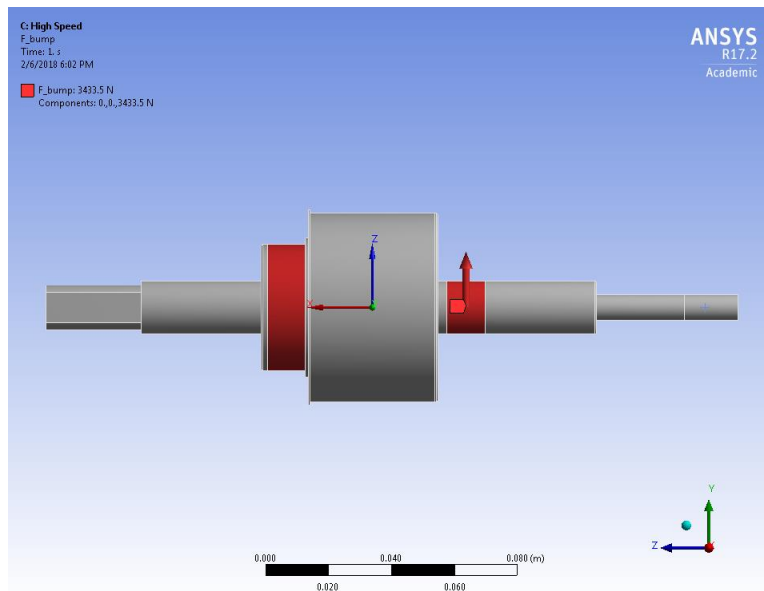


Fig. X.3 Bump loading - shaft surfaces

The endcaps also apply the forces as a distributed bearing load, but the interface surfaces are the same used for the torque condition (see Fig. X.4).

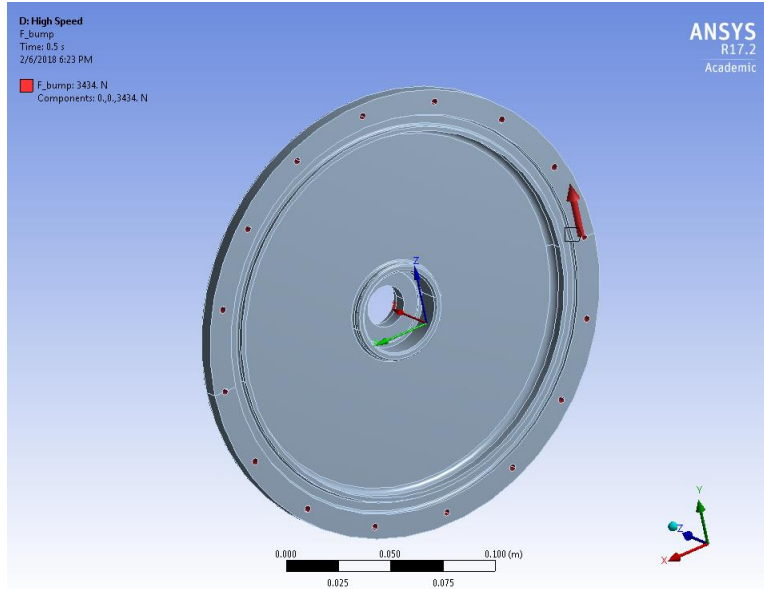


Fig. X.4 Bump loading - front endcap surfaces (rear endcap similar)

### *Axial Corner Loading*

Axial loading conditions were applied as a remote force at the center of the e-bike tire-ground contact patch, assuming a tire diameter of  $d_{wheel}$ . Otherwise, the axial loading conditions are calculated in a similar manner to the radial loading conditions. However, this loading is assumed to be negligible except for the high speed driving case, which uses a safety factor of 1.2.

$$F_{Corner} = m_{Bike} \cdot \alpha_g \cdot SF$$

$$SF = 1.2$$

The shaft is axially loaded through the bearing surfaces, using a remote load as shown in Fig. X.5.

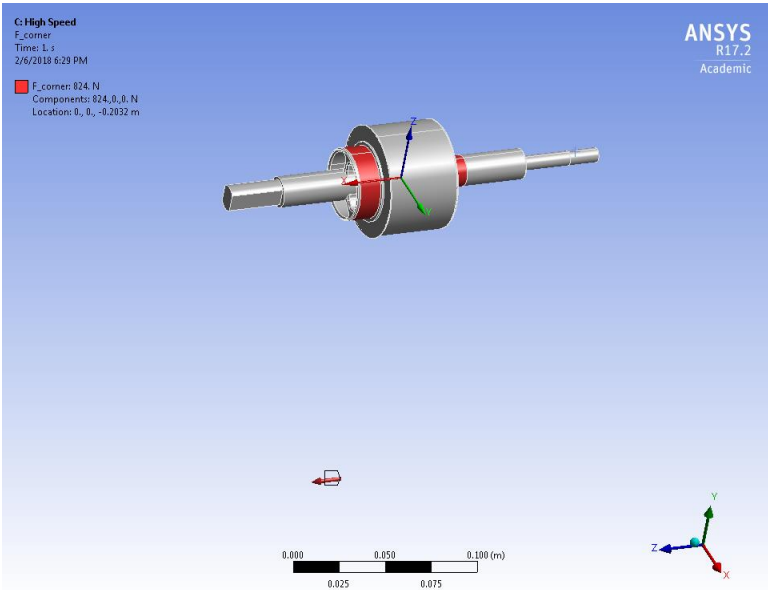


Fig. X.5 Corner loading - shaft surfaces

Both endcaps have the axial loading applied as a remote load to the bottom half of the inner endcap-rotor interface, as it is assumed that the wheel is attached to the rotor stack, meaning the forces are directly transferred in this manner. The axial loading is shown in Fig. X.6.

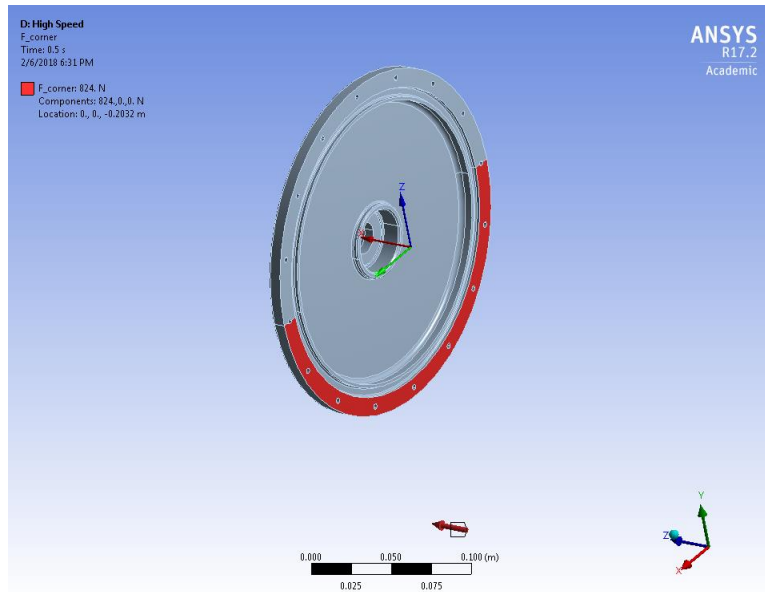


Fig. X.6 Corner loading - front endcap surfaces (rear endcap similar)

### ***Centrifugal Force Loading***

A centrifugal force loading condition was applied for the endcaps depending on the loading case speed ( $\omega_{RPM}$ ).

### ***Mass Loading***

The mass and inertial moment (if applicable) for each component is listed in TABLE X.3. Since each part was analyzed separately instead of using a computationally expensive assembly analysis, gravimetric acceleration and mass loads were applied to model the force exerted by each component. The inertial moments added by auxiliary components, such as the pulley and resolver were also accounted for when relevant in the analysis. The mass and inertia for each component was based on the 3D model mass estimation in Dassault Systèmes Solidworks, using appropriate densities for each material.

Part	Mass [kg]	Moment of Inertia [kg/m <sup>2</sup> ]
<b>Full Rotor Assembly</b> <ul style="list-style-type: none"> <li>• Rotor Stack      • End Caps</li> <li>• Bolts              • Bearings</li> <li>• Dowels</li> </ul>	4.132	$J_x = 0$ $J_y = 0$ $J_z = 0$
<b>Rotor Stack Assembly</b> <ul style="list-style-type: none"> <li>• Rotor Stack</li> <li>• Bolts</li> <li>• Dowels</li> </ul>	2.696	$J_x = 0$ $J_y = 0$ $J_z = 0$
<b>Stator Assembly</b> <ul style="list-style-type: none"> <li>• Stator Stack      • Insulation</li> <li>• Coils              • Thermocouples</li> <li>• End Windings</li> </ul>	7.347	$J_x = 0$ $J_y = 0$ $J_z = 0$
<b>Gearing + Mounting Assembly</b> <ul style="list-style-type: none"> <li>• Gear              • Gearing Adapter</li> <li>• Bolts              • Resolver Rotor</li> <li>• Split Washers      Adapter</li> </ul>	3.052	$J_x = 0.009$ $J_y = 0.012$ $J_z = 0.012$
<b>Resolver Assembly</b> <ul style="list-style-type: none"> <li>• Resolver</li> <li>• Nut</li> <li>• Resolver Stator Bracket</li> </ul>	0.062	$J_x = 0$ $J_y = 0$ $J_z = 0$

**TABLE X.3 Lumped mass and inertia properties of component assemblies**



## Shaft Analysis

There were three separate loading cases applied for the shaft, as shown in

TABLE X.4.

	<b>Case 1 Locked Bearing</b>	<b>Case 2 Low Speed Driving</b>	<b>Case 3 High Speed Driving</b>	<b>Case 4 High Speed Driving</b>	<b>Case 5 Low Speed Dynamo.</b>	<b>Case 6 High Speed Dynamo.</b>
$T_{Motor}$		72	30	30	72	
$F_{Bump}$		686.7	3433.5	3433.5	591.8	
$F_{Corner}$		0	+824	-824	0	
$\omega_{RPM}$						
$Mass +Inertia$		A, B	A, B	A, B	A, B, C, D	
$Fixtures$		A, B	A, B	A, B	A	

TABLE X.4 Loading cases for shaft structural analysis

The mass loading locations referenced by TABLE X.4 are shown in Fig. X.7.

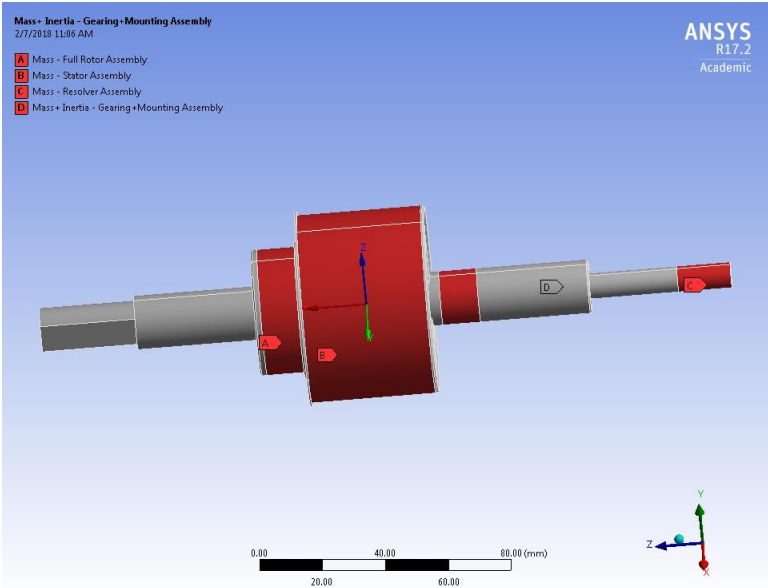


Fig. X.7 Lumped mass + inertia loads - shaft

The fixture locations referenced by TABLE X.4 are shown in Fig. X.8.

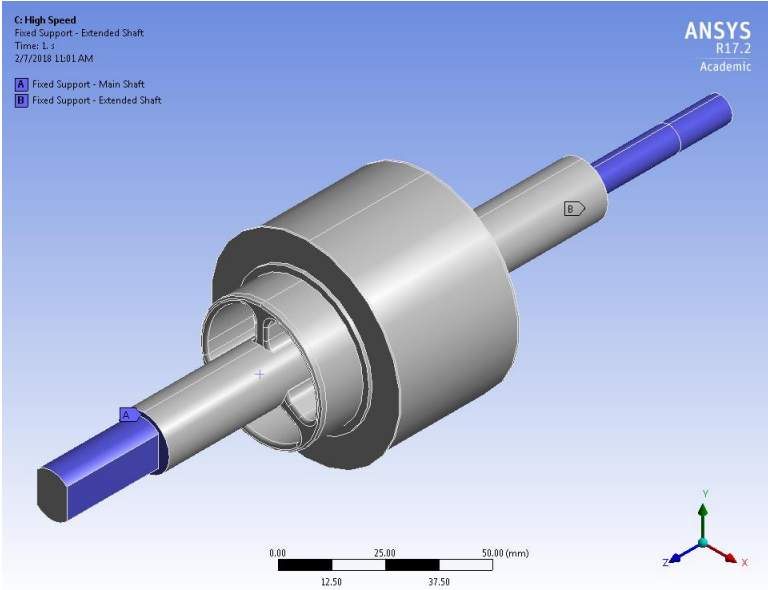


Fig. X.8 Different fixture locations used for shaft analysis

### Von-Mises Stress

The Von-Mises stress for each loading case is shown in Fig. X.9 to Fig. X.12. The maximum stress occurs under loading **case 5** at a peak of **271 MPa**.

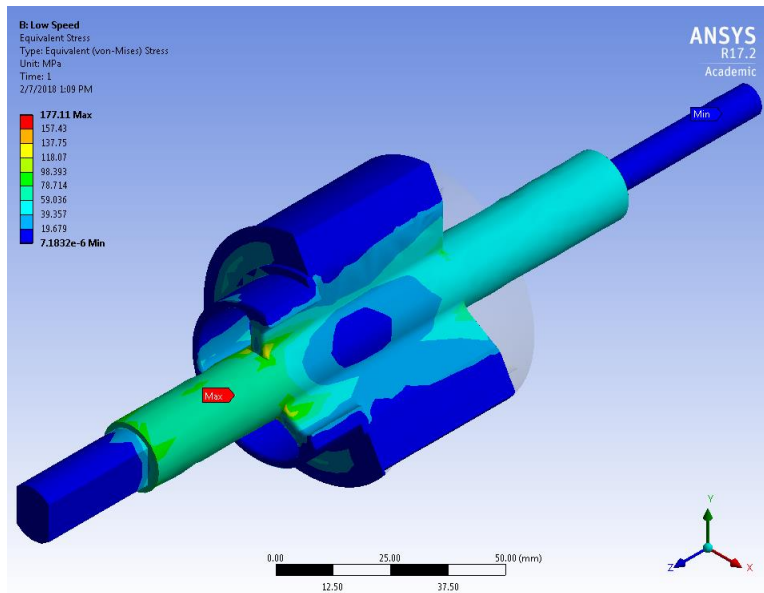


Fig. X.9 Von-Mises stress - shaft (case 2)

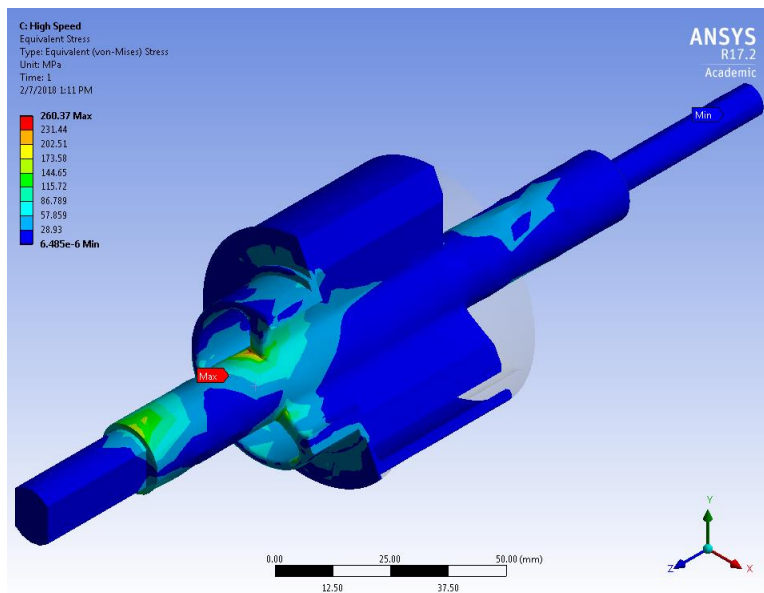


Fig. X.10 Von-Mises stress - shaft (case 3)

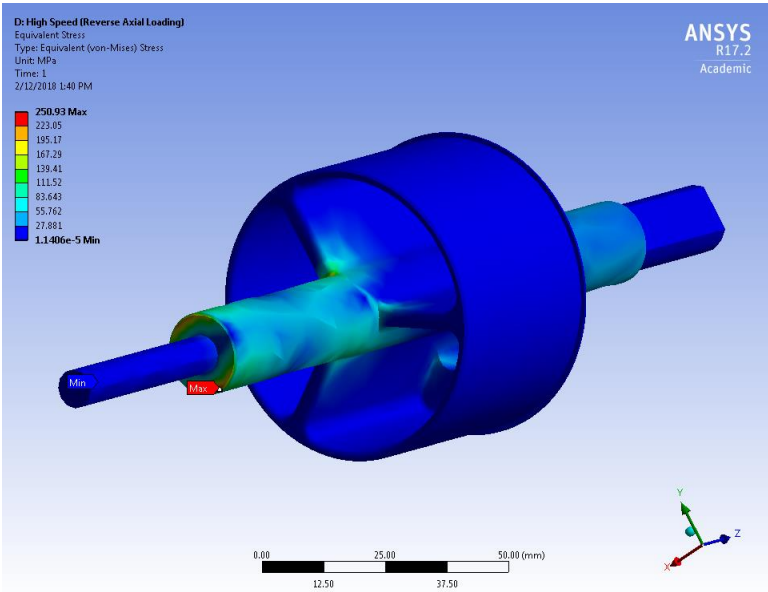


Fig. X.11 Von-Mises stress - shaft (case 4)

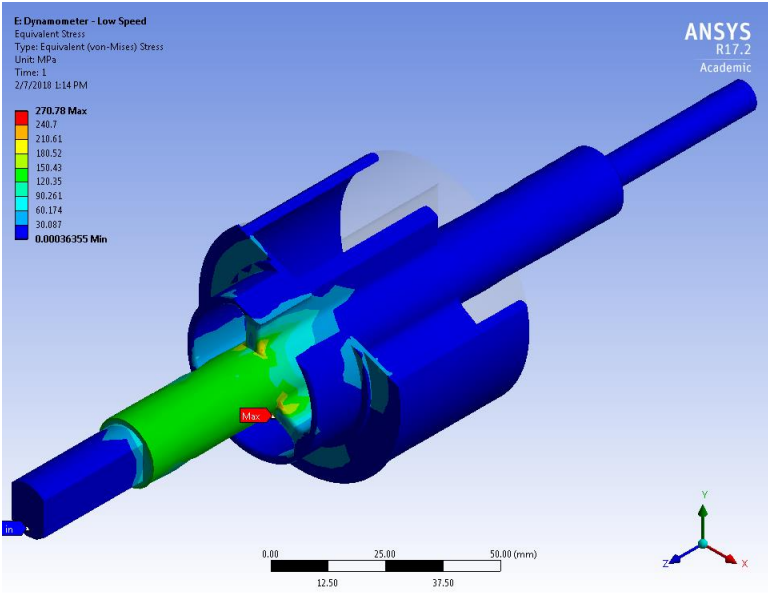


Fig. X.12 Von-Mises stress - shaft (case 5)

**Deflection**

The deflection for each loading case is shown in Fig. X.13 to Fig. X.16. The maximum deflection occurs under loading case 5 at a peak of 0.22 mm.

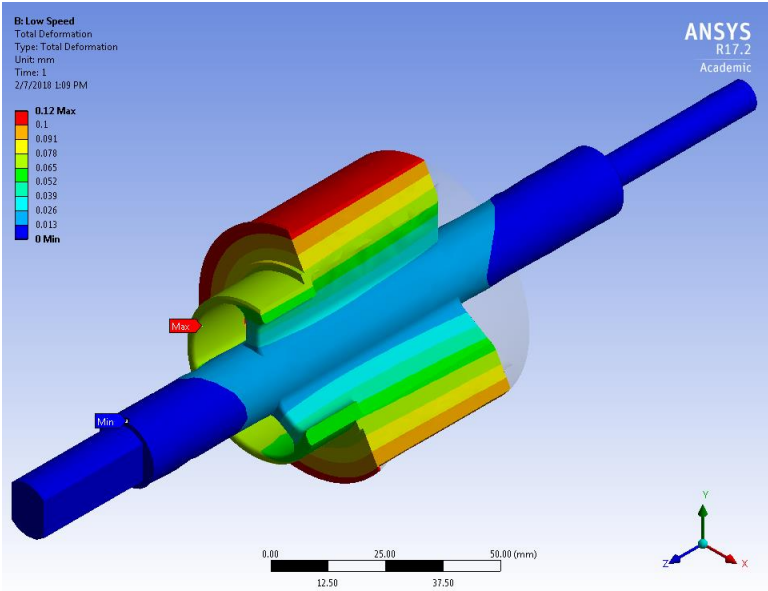


Fig. X.13 Deformation - shaft (case 2)

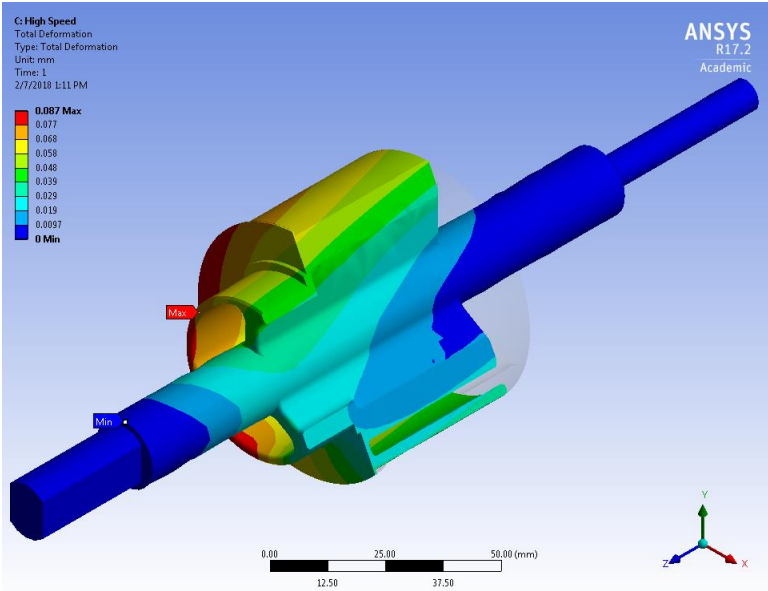


Fig. X.14 Deformation - shaft (case 3)

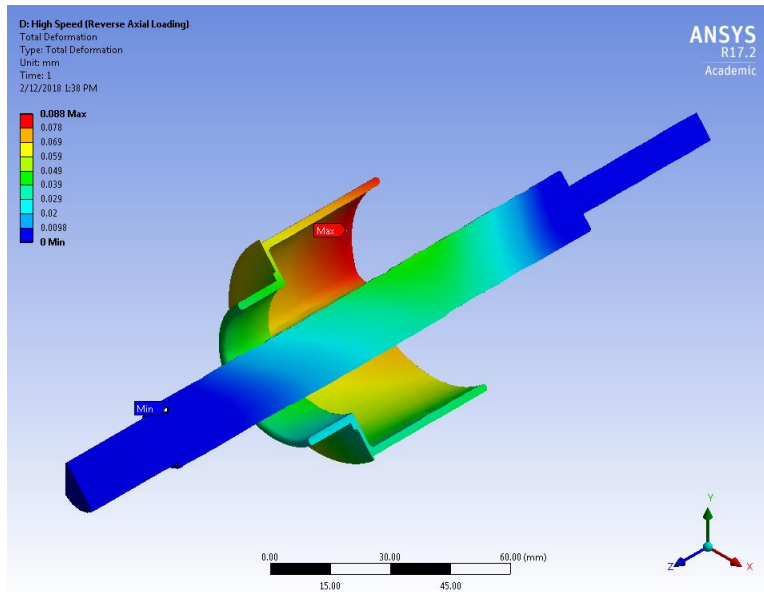


Fig. X.15 Deformation - shaft (case 4)

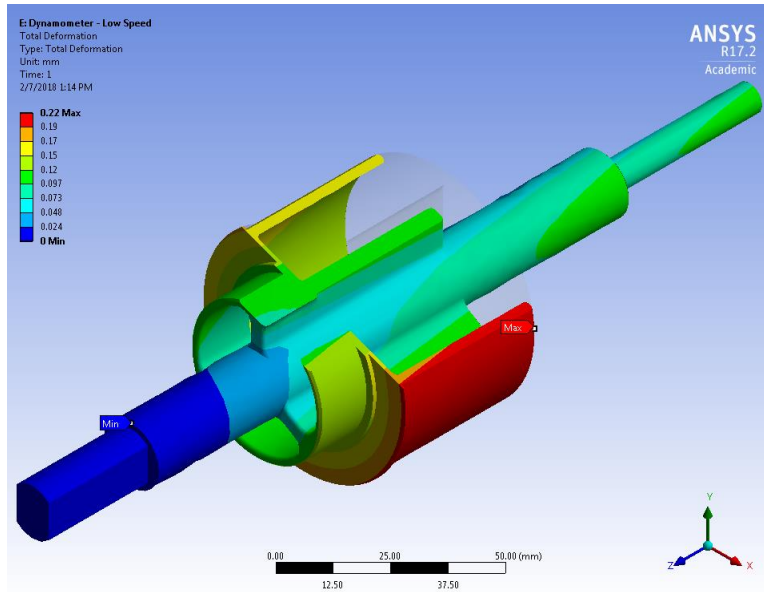


Fig. X.16 Deformation - shaft (case 5)

### *Fatigue Life*

The fatigue life for each loading case is shown in TABLE X.5.

Case	Minimum Cycle Life [cycles x 10 <sup>6</sup> ]
2	1+
3	0.726
4	0.898
5	0.579

TABLE X.5 Minimum fatigue life for each loading case - shaft

The final shaft design experienced a maximum stress of 271 MPa, which translates to a safety factor of:

$$SF = \frac{\sigma_{Yield}}{\sigma_{Max}}$$

$$SF = \frac{710}{271}$$

$$SF = 2.6$$

Considering the safety factor of 2.6 and the additional safety margins added to the loading conditions, the structural design for this part is valid. Under fully reversed loading with 35% load amplitude scaling, the minimum fatigue cycle life is 5.79e5 cycles.

## Front Endcap

There were five separate loading cases applied for the front endcap, as shown in TABLE X.6.

	<b>Case 1 Locked Bearing</b>	<b>Case 2 Low Speed Driving</b>	<b>Case 3 High Speed Driving</b>	<b>Case 4 High Speed Driving</b>	<b>Case 5 Low Speed Dynamo.</b>	<b>Case 6 High Speed Dynamo.</b>
$T_{Motor}$	72	72	30	30	72	30
$F_{Bump}$	0	686.7	3433.5	3433.5	591.8	0
$F_{Corner}$	0	0	+824	-824	0	0
$\omega_{RPM}$	0	1	400	400	1	400
Mass + Inertia	A	A	A	A	A, B	A, B
Fixtures	C	A, D	A, D	A, D	A, B	A, B

**TABLE X.6** Loading cases for front endcap structural analysis

The mass loading locations referenced by TABLE X.6 are shown in Fig. X.17.



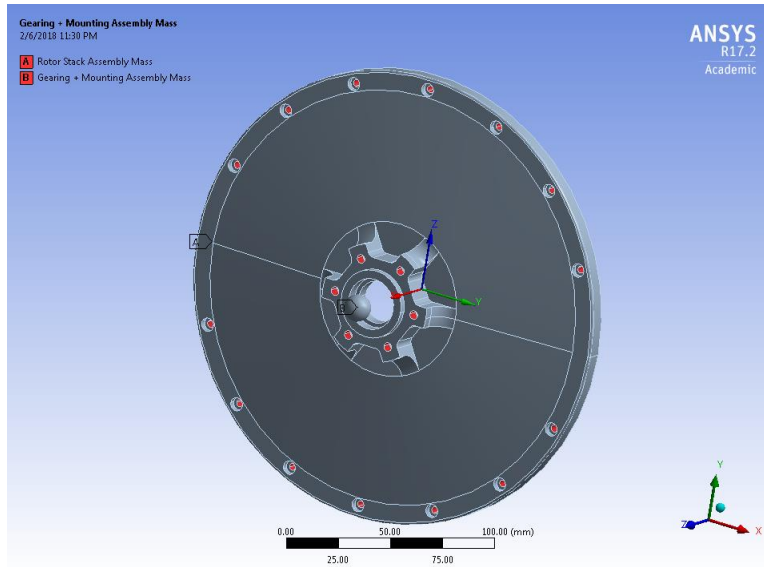


Fig. X.17 Lumped mass + inertia loads - front endcap

The fixture locations referenced by TABLE X.6 are shown in Fig. X.18.

Each fixture has different degrees of freedom, as outlined in TABLE X.7.

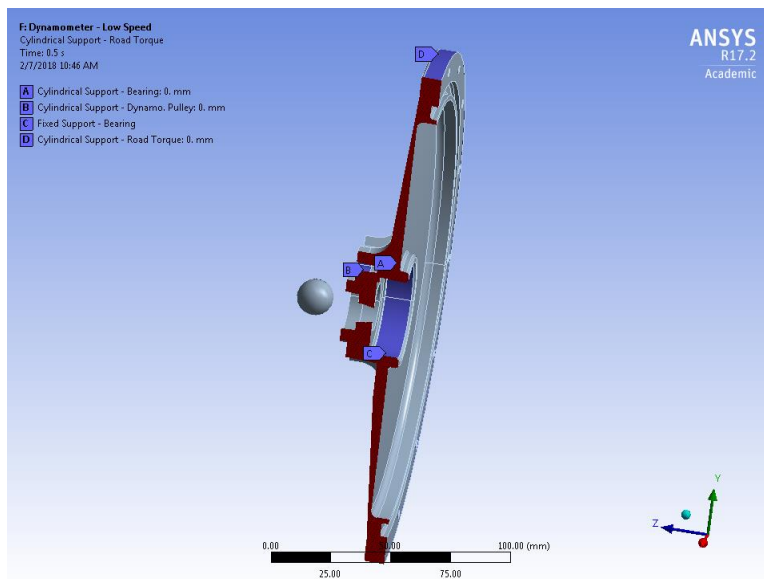


Fig. X.18 Different fixture locations used for front endcap analysis

Fixture Location	Radial Translation	Axial Translation	Tangential Rotation
A	Fixed	Fixed	Free
B	Free	Free	Fixed
C	Fixed	Fixed	Fixed
D	Free	Free	Fixed

TABLE X.7 Fixture degrees of freedom - front endcap

### Von-Mises Stress

The Von-Mises stress for each loading case is shown in Fig. X.19 to Fig. X.24. The maximum stress occurs under loading **case 4** at a peak of **134 MPa**.

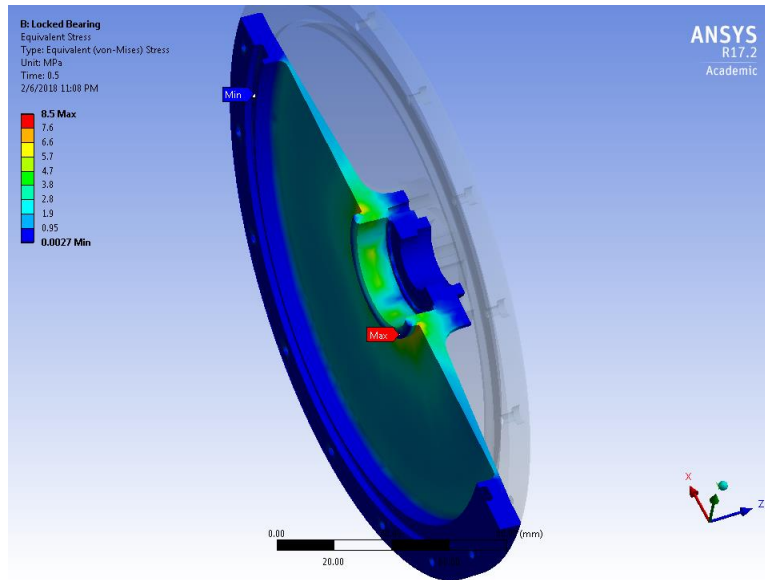


Fig. X.19 Von-Mises stress - front endcap (case 1)

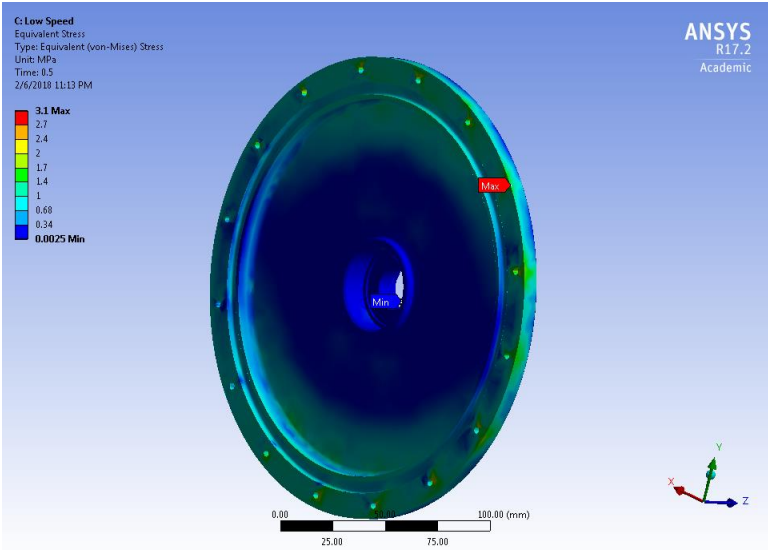


Fig. X.20 Von-Mises stress - front endcap (case 2)

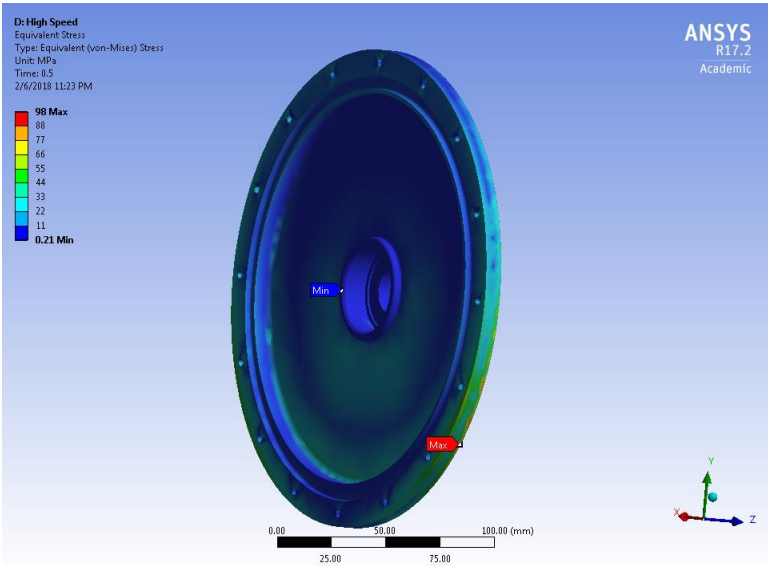


Fig. X.21 Von-Mises stress - front endcap (case 3)

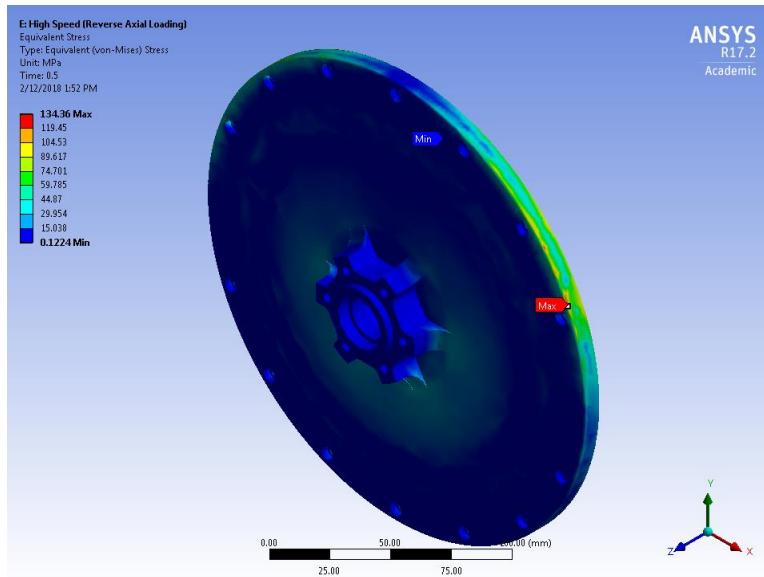


Fig. X.22 Von-Mises stress - front endcap (case 4)

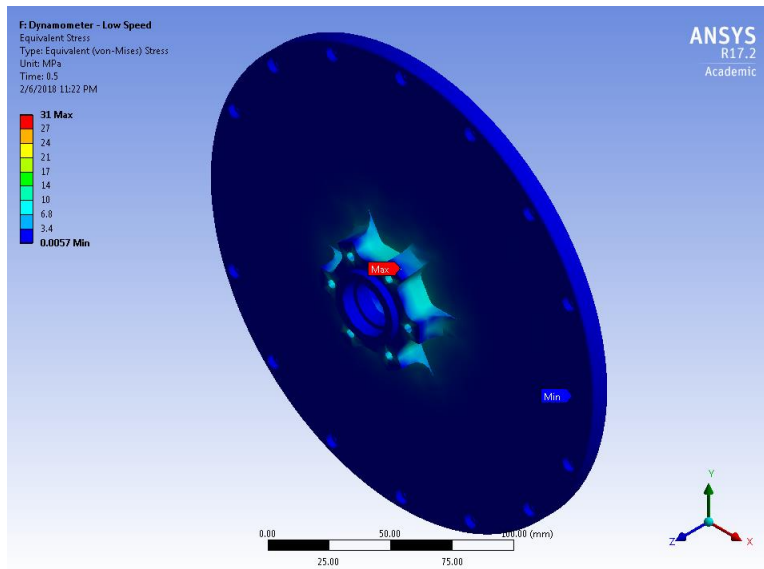


Fig. X.23 Von-Mises stress - front endcap (case 5)

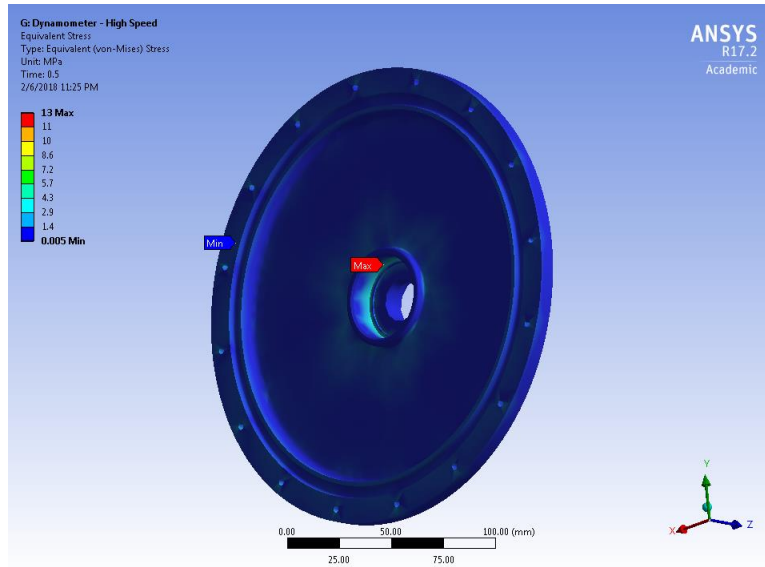


Fig. X.24 Von-Mises stress - front endcap (case 6)

### Deflection

The deflection for each loading case is shown in Fig. X.25 to Fig. X.30. The maximum deflection occurs under loading **case 3** at a peak of **0.28 mm**.

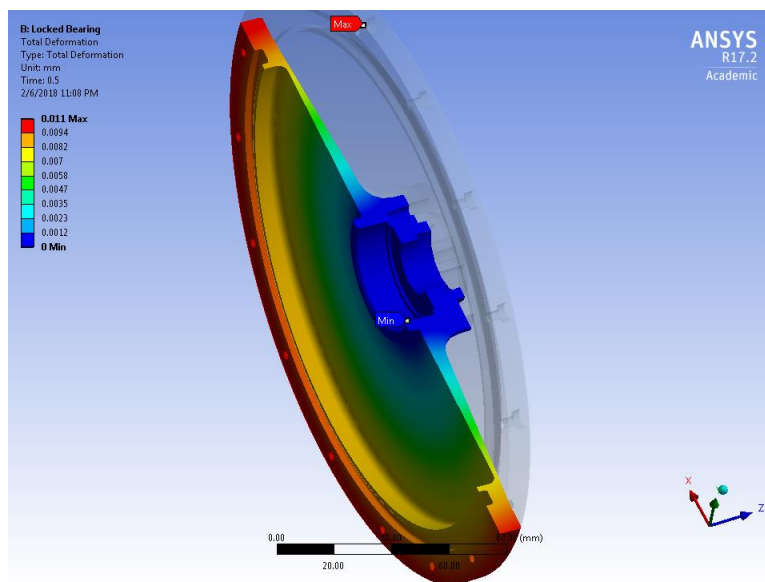


Fig. X.25 Deformation - front endcap (case 1)

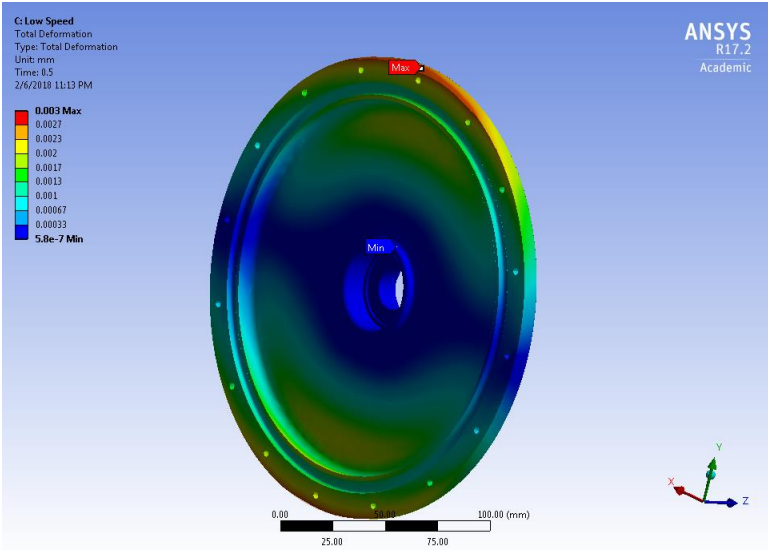


Fig. X.26 Deformation - front endcap (case 2)

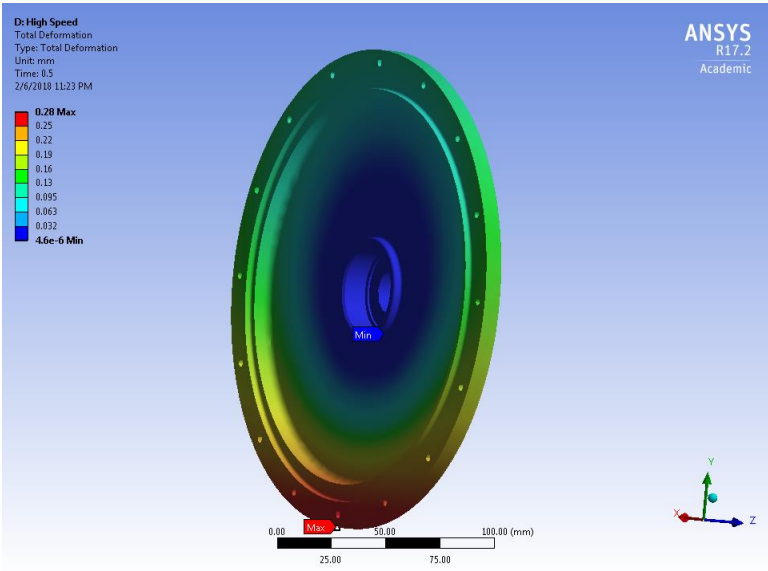


Fig. X.27 Deformation - front endcap (case 3)

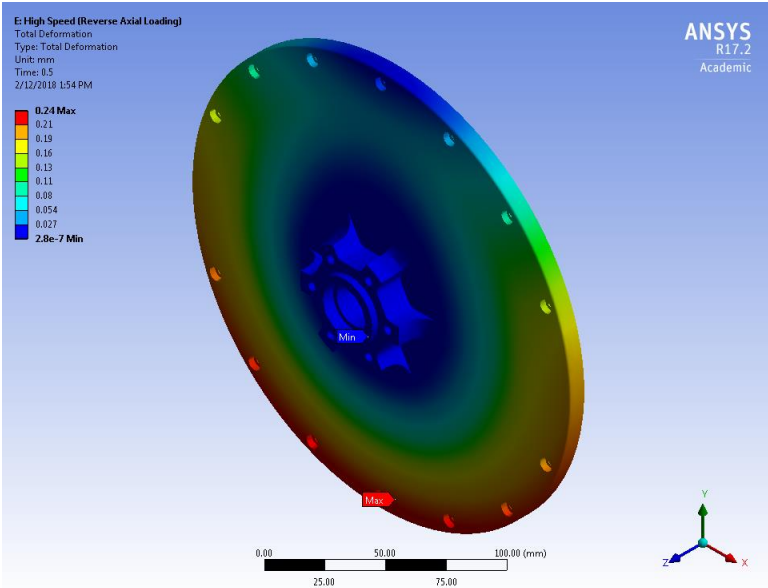


Fig. X.28 Deformation - front endcap (case 4)

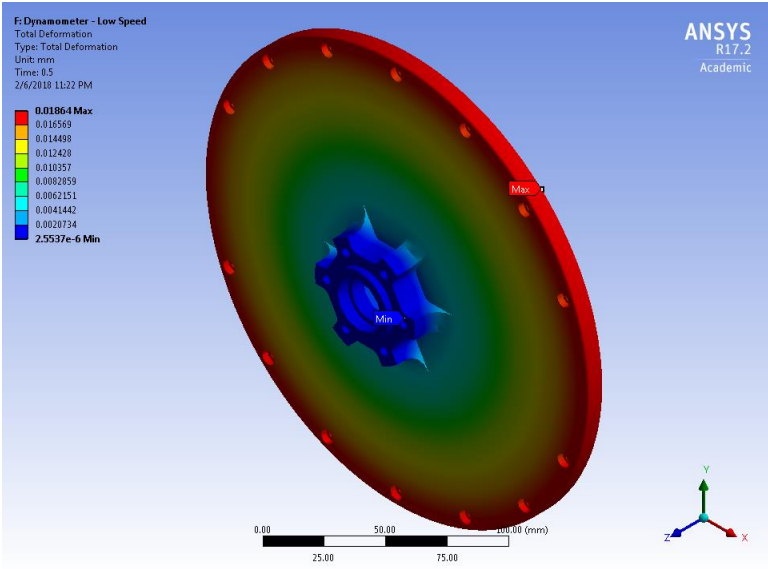


Fig. X.29 Deformation - front endcap (case 5)

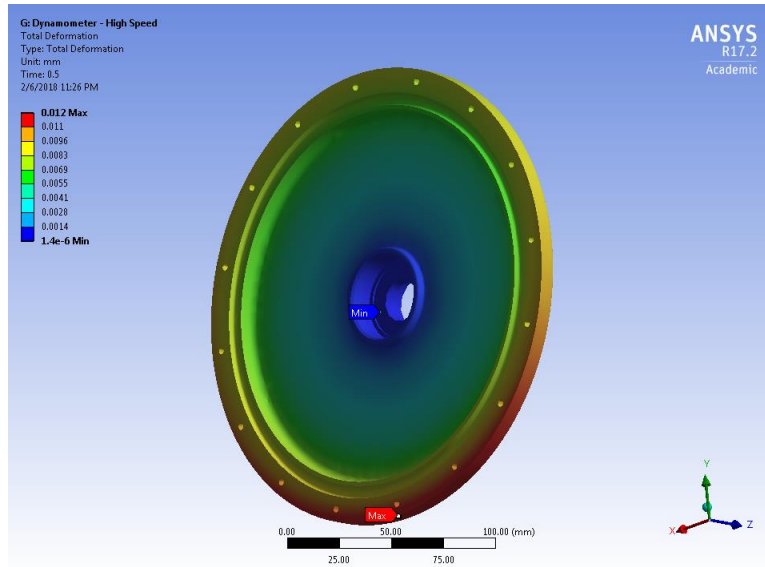


Fig. X.30 Deformation - front endcap (case 6)

**Fatigue Life**

The fatigue life for each loading case is shown in TABLE X.8.

Case	Minimum Cycle Life [cycles x 10 <sup>6</sup> ]
1	100 +
2	100 +
3	20.15
4	0.965
5	100 +
6	100 +

TABLE X.8 Minimum fatigue life for each loading case - front endcap

The final shaft design experienced a maximum stress of 134 MPa, which translates to a safety factor of:

$$SF = \frac{\sigma_{Yield}}{\sigma_{Max}}$$



$$SF = \frac{280}{134}$$

$$SF = 2.1$$

Considering the safety factor of 2.1 and the additional safety margins added to the loading conditions, the structural design for this part is valid. Under fully reversed loading with 100% load amplitude scaling, the minimum fatigue cycle life is 9.65e5 cycles.

## Rear Endcap

There were three separate loading cases applied for the rear endcap, as shown in TABLE X.9.

	<b>Case 1 Locked Bearing</b>	<b>Case 2 Low Speed Driving</b>	<b>Case 3 High Speed Driving</b>	<b>Case 4 High Speed Driving</b>	<b>Case 5 Low Speed Dynamo.</b>	<b>Case 6 High Speed Dynamo.</b>
$T_{Motor}$	72	72	30	30		
$F_{Bump}$	0	686.7	3433.5	3433.5		
$F_{Corner}$	0	0	+824	-824		
$\omega_{RPM}$	0	1	400	400		
<i>Mass + Inertia</i>	A	A	A	A		
<i>Fixtures</i>	A, C	A, B	A, B	A, B		

**TABLE X.9** Loading cases for rear endcap structural analysis

The mass loading locations referenced by TABLE X.9 are shown in Fig. X.31.

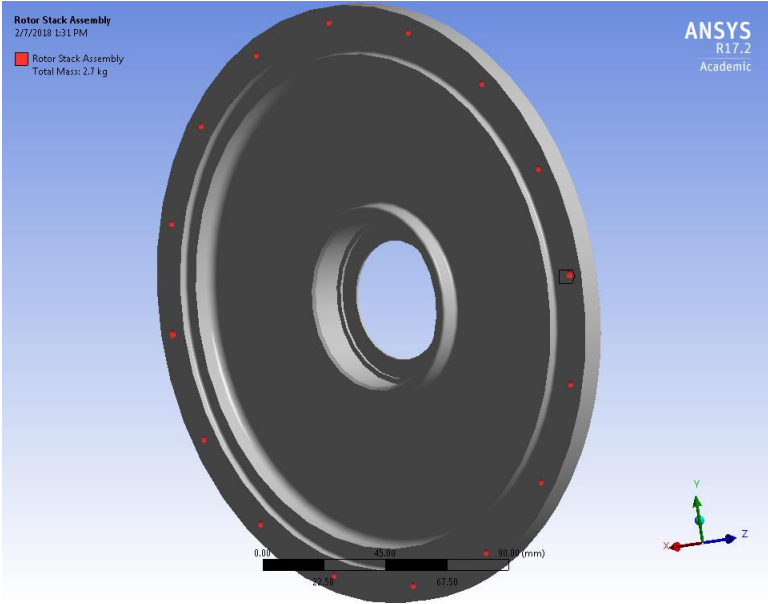


Fig. X.31 Lumped mass + inertia loads - rear endcap

The fixture locations referenced by TABLE X.9 are shown in Fig. X.32.

Each fixture has different degrees of freedom, as outlined in TABLE X.10.

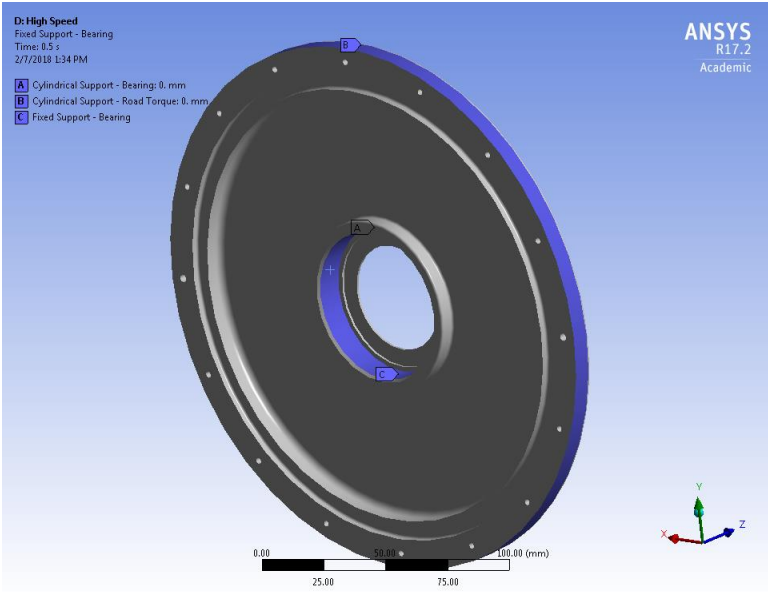


Fig. X.32 Different fixture locations used for rear endcap analysis

Fixture Location	Radial Translation	Axial Translation	Tangential Rotation
A	Fixed	Fixed	Free
B	Free	Free	Fixed
C	Fixed	Fixed	Fixed

TABLE X.10 Fixture degrees of freedom - rear endcap

### Von-Mises Stress

The Von-Mises stress for each loading case is shown in Fig. X.33 to Fig. X.36. The maximum stress occurs under loading **case 4** at a peak of **124 MPa**.

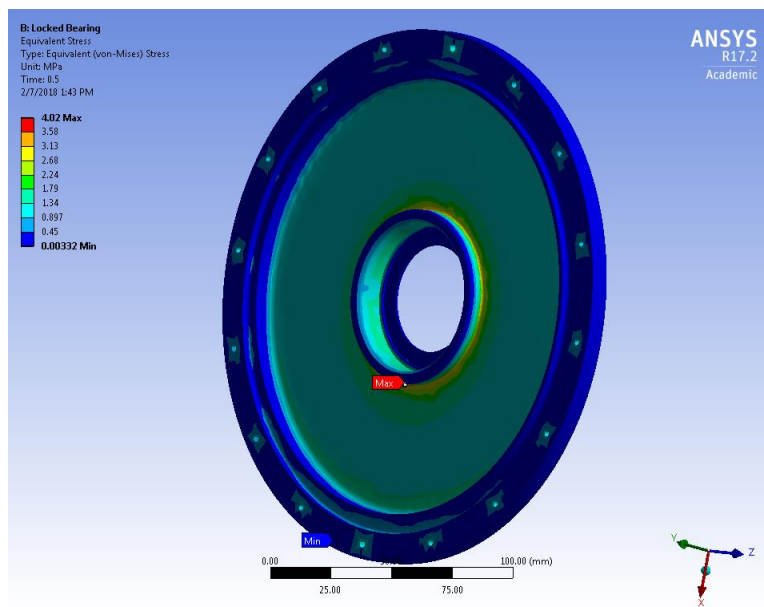


Fig. X.33 Von-Mises stress - rear endcap (case 1)

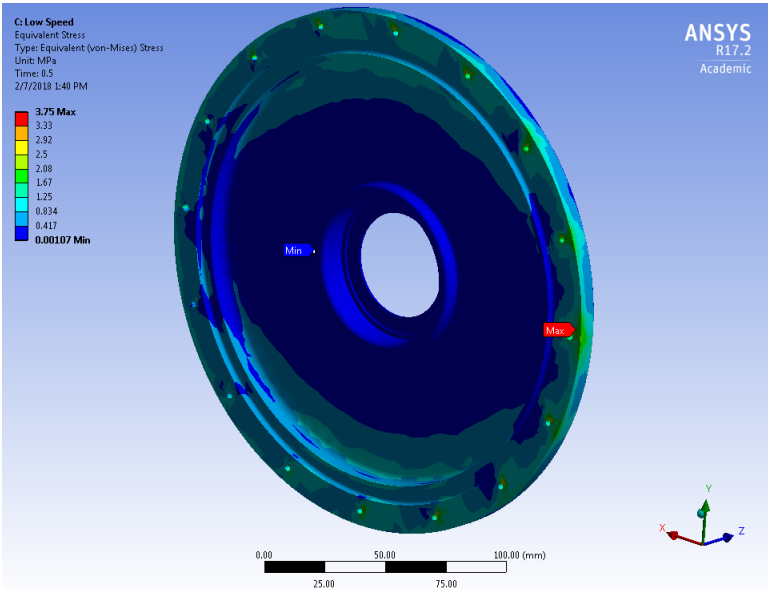


Fig. X.34 Von-Mises stress - rear endcap (case 2)

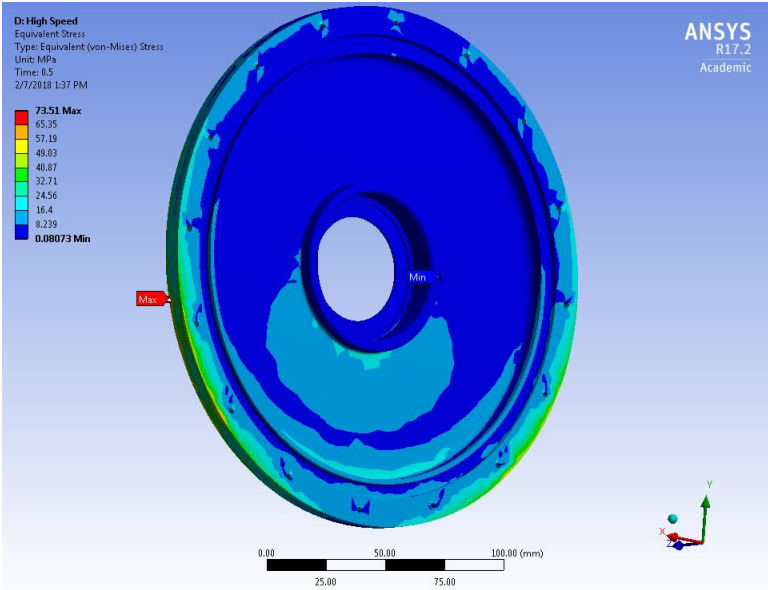


Fig. X.35 Von-Mises stress - rear endcap (case 3)

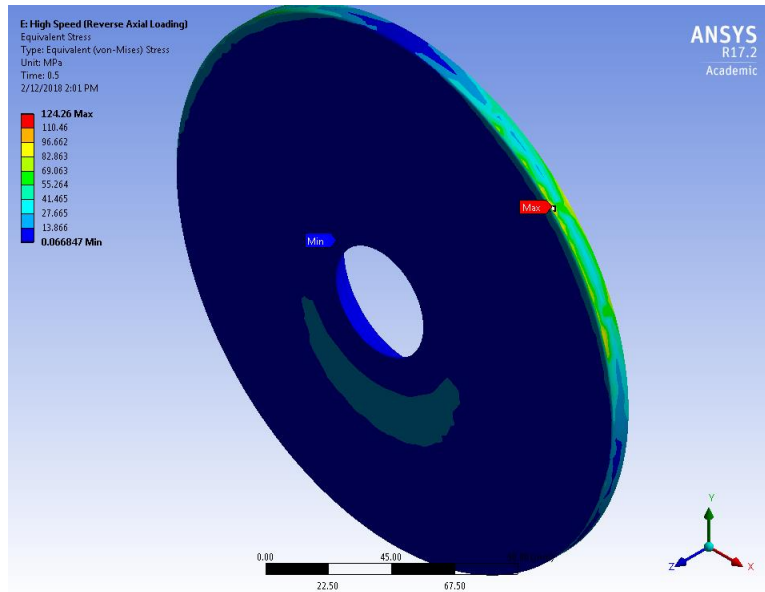


Fig. X.36 Von-Mises stress - rear endcap (case 4)

### Deflection

The deflection for each loading case is shown in Fig. X.37 to Fig. X.40. The maximum deflection occurs under loading **case 3** at a peak of **0.16 mm**.

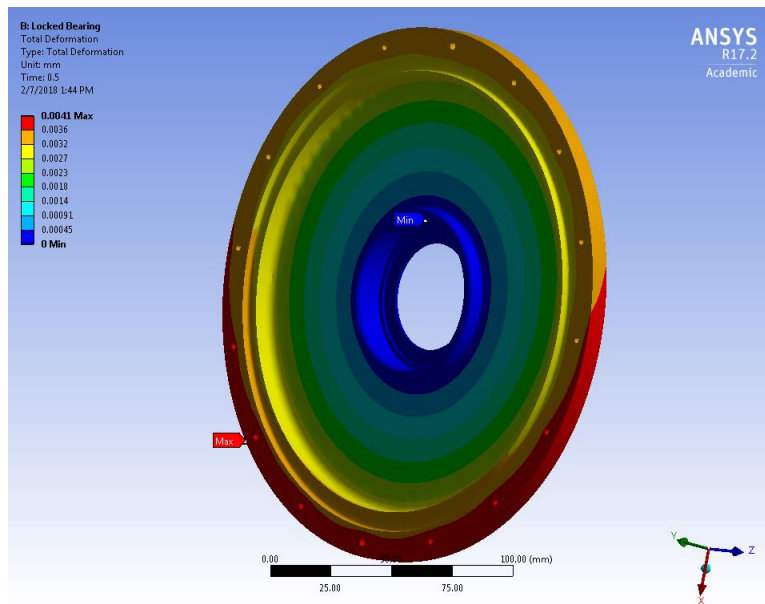


Fig. X.37 Deformation - rear endcap (case 1)

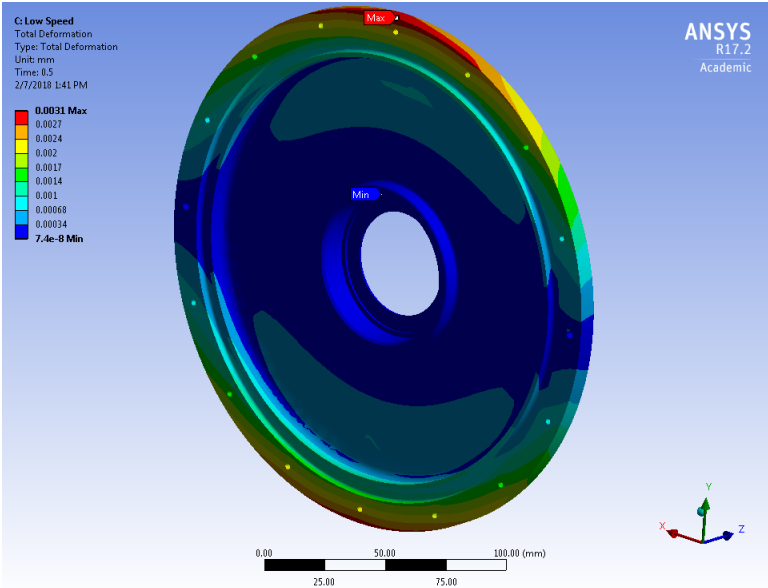


Fig. X.38 Deformation - rear endcap (case 2)

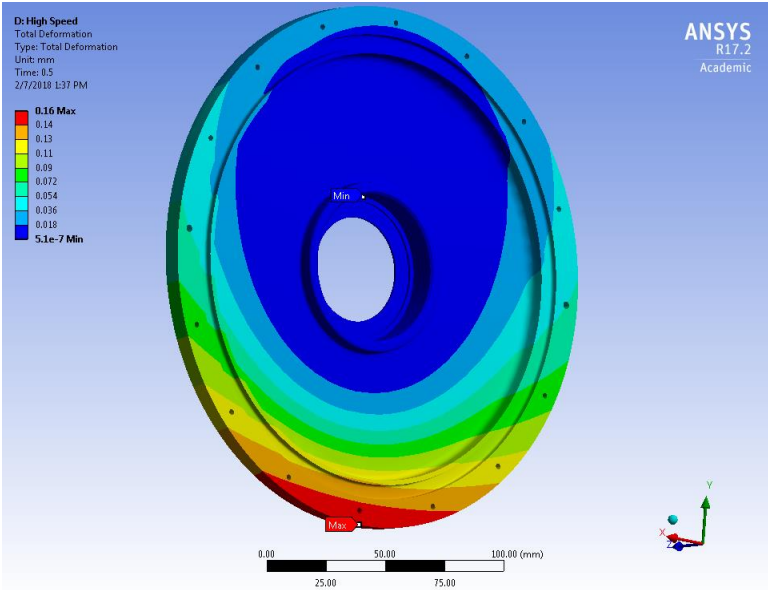


Fig. X.39 Deformation - rear endcap (case 3)

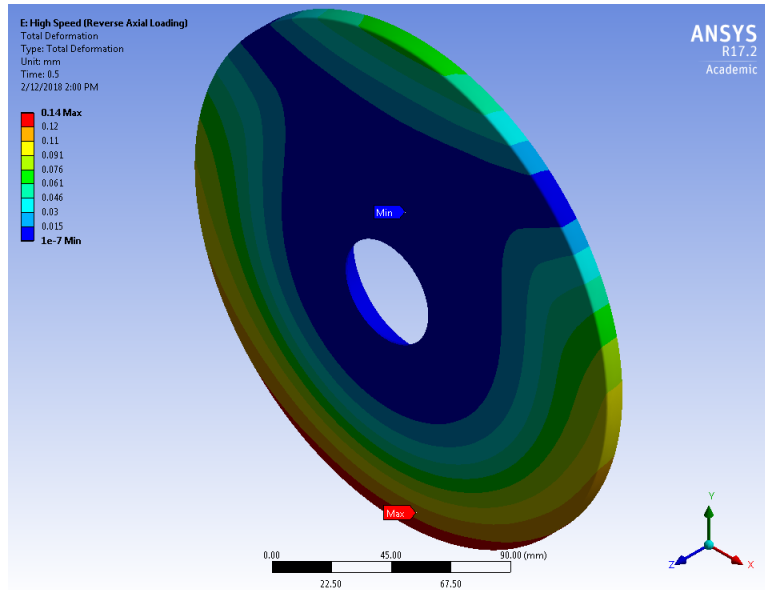


Fig. X.40 Deformation - rear endcap (case 4)

**Fatigue Life**

The fatigue life for each loading case is shown in TABLE X.11.

Case	Minimum Cycle Life [cycles x 10 <sup>6</sup> ]
1	100 +
2	100 +
3	100 +
4	1.65

TABLE X.11 Minimum fatigue life for each loading case - rear endcap

The final shaft design experienced a maximum stress of 124 MPa, which translates to a safety factor of:

$$SF = \frac{\sigma_{Yield}}{\sigma_{Max}}$$

$$SF = \frac{280}{124}$$



$$SF = 2.3$$

Considering the safety factor of 2.3 and the additional safety margins added to the loading conditions, the structural design for this part is valid. Under fully reversed loading with 100% load amplitude scaling, the minimum fatigue cycle life is 1.65e6 cycles.

### **Winding Wedge Engagement**

The windings are retained using slot wedges. Ideally, the thickness and engagement of these wedges is minimized to reduce electromagnetic impacts and to maximize space for the coils. However, it is important to ensure that the engagement and thickness are sufficient to withstand the weight of the coils. In order to verify this, an ANSYS structural FEA simulation has been performed on the finalized slot and wedge geometry.

### ***Loading Conditions***

The analysis accounts for the coil mass load when the wedge and stack are at a constant temperature of 120°C. The analysis parameters are detailed in TABLE X.12, and the material properties are detailed in TABLE X.13. The PEEK material data is provided by [29], while the AISI 1020 steel properties are part of the standard ANSYS Mechanical material library.

Parameter	Value
Coil mass ( $m_{Coil}$ )	0.3227 kg
Wedge thickness	1 mm
Wedge engagement	1.5 mm
Temperature	120 °C
Wedge material	Polyetheretherketone (PEEK)
Iron Material	AISI 1020 steel

TABLE X.12 Slot wedge analysis – simulation parameters

Parameter	PEEK [29]	Steel (AISI 1020 – cold rolled)	Units
Density	1270	7870	kg/m <sup>3</sup>
Thermal Expansion Coefficient	4.68e-4	1.2e-5	/°C
Thermal Expansion – Reference Temperature	20	22	°C
Young’s Modulus	4.14 @ 20°C 3.11 @ 65°C 0.59 @ 150°C	205	GPa
Poisson’s Ratio	0.3	0.29	
Yield Strength	110 (tensile) 138 (compressive)	250	MPa
Ultimate Tensile Strength	N/A	420	MPa

TABLE X.13 Slot wedge analysis - material parameters

The load due to coil mass is calculated as follows, using a loading multiplier (SF) of 2:

$$\begin{aligned} F_{Load} &= SF \cdot m_{Coil} \cdot \alpha_g \\ &= 2(0.3227)(9.81) \\ &= 6.33 \text{ N} \end{aligned}$$

### Results

The maximum deformation experienced by the wedge is approximately 0.15 mm, as shown in Fig. X.41. Considering that the wedge is offset from the airgap by 1 mm, it is clear that the wedge will not intrude on the airgap due to coil loading.

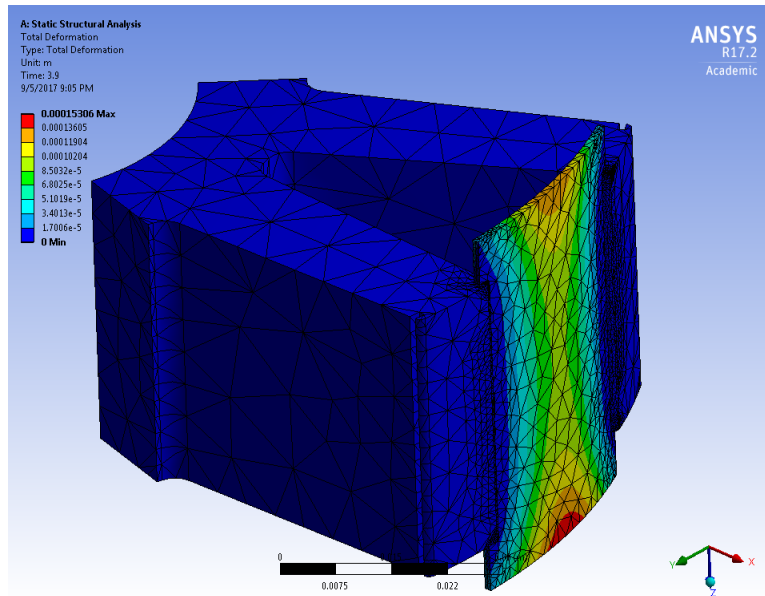


Fig. X.41 Deformation – slot wedge @ 120°C

The maximum stress is 9.26 MPa, as shown in Fig. X.42. The maximum stress is located on the stator pole tips as opposed to the wedge itself, and the loading is marginal when compared to the yield strength of the stack material.

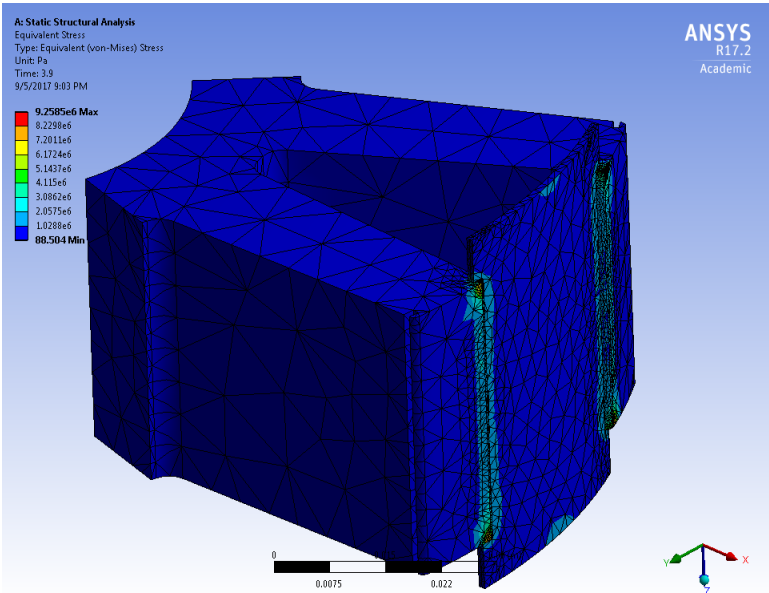


Fig. X.42 Von-Mises stress - slot wedge @ 120°C

## C. MCSRMs Analyses (No Rotor Yoke)

In addition to the cases analyzed in *Chapter 8*, a few of the configurations were also analyzed with effectively no rotor yoke (1 mm thick). Some of the lower rotor pole number MCSRMs designs barely use the rotor yoke during operation. When the rotor yoke is removed, it prevents flux from the one of the phases from linking with the yoke (see Fig. X.43). The result is higher peak torque output, but this increases the torque ripple.

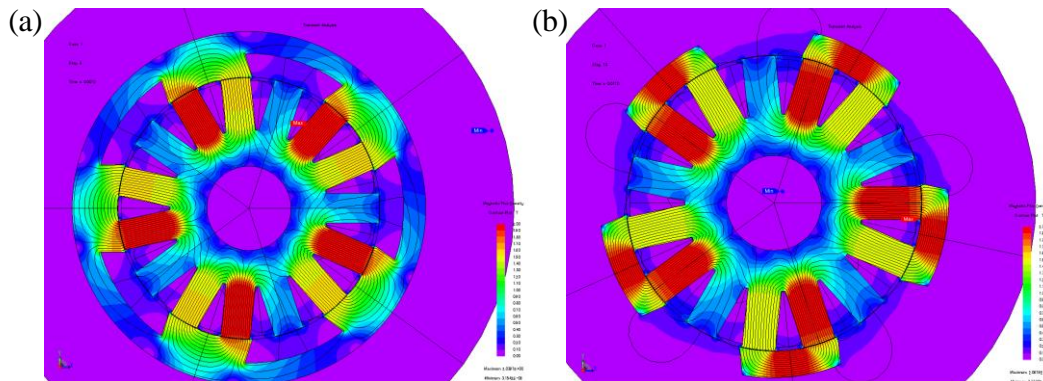


Fig. X.43 15/5 MCSRMs flux path comparison: (a) with yoke; (b) without yoke

The results for the yokeless cases are compared in TABLE X.14, to illustrate the concept, but the torque ripple for these designs was far too high to be considered for the final design.

Pole Configuration	Best $\max(T_{Ave})$			Best $\max\left(\frac{T_{Ave}}{V_{RMS}}\right)$			Best $\max\left(\frac{T_{Ave}}{P_{Cu}}\right)$		
	15/5	21/7	24/8	15/5	21/7	24/8	15/5	21/7	24/8
$T_{Ave}$ [Nm]	61	64	65	49	50	51	49	50	51
$T_{Ripple}$ [%]	241	225	220	233	221	236	233	222	236
$V_{Peak}$ [V]	255	150	150	85	87	94	85	87	94
$V_{RMS}$ [V]	216	111	110	46	52	53	46	52	53
$T_{Ave}/V_{RMS}$	0.28	0.56	0.58	0.81	0.73	0.74	0.81	0.74	0.75
$T_{Ave}/P_{Cu}$	0.11	0.25	0.26	0.41	0.33	0.36	0.38	0.30	0.33

TABLE X.14 Pole configuration performance comparison (no rotor yoke):  
 400 RPM, 3-phase AC @  $I_{Amp} = 75$  A,  $\phi_{dq} = 45^\circ$

## D. CSRМ Expanded Voltage/Torque Equations

In *Chapter 2*, the phase voltage and phase torque equations were outlined for the CSRМ, using a compact matrix format. In order to understand the contributions of each phase to the total phase voltage and total torque, the matrices must be expanded. In this section, **bold** terms represent vector/matrix terms, while **blue** terms represent mutual coupling effects.

### *abc*-Reference Frame

Considering a 3-phase machine [10]:

$$\mathbf{v}_{abc} = \begin{bmatrix} v_a \\ v_b \\ v_c \end{bmatrix} \quad \mathbf{i}_{abc} = \begin{bmatrix} i_a \\ i_b \\ i_c \end{bmatrix} \quad \mathbf{L}_{abc} = \begin{bmatrix} L_a & L_{ab} & L_{ac} \\ L_{ab} & L_b & L_{bc} \\ L_{ac} & L_{bc} & L_c \end{bmatrix} \quad \boldsymbol{\psi}_{abc} = \begin{bmatrix} \psi_a & \psi_{ab} & \psi_{ac} \\ \psi_{ab} & \psi_b & \psi_{bc} \\ \psi_{ac} & \psi_{bc} & \psi_c \end{bmatrix}$$

However, when neglecting mutual coupling effects,  $L_{abc}$  and  $\boldsymbol{\psi}_{abc}$  become:

$$\mathbf{L}_{abc} = \begin{bmatrix} L_a & 0 & 0 \\ 0 & L_b & 0 \\ 0 & 0 & L_c \end{bmatrix} \quad \boldsymbol{\psi}_{abc} = \begin{bmatrix} \psi_a & 0 & 0 \\ 0 & \psi_b & 0 \\ 0 & 0 & \psi_c \end{bmatrix}$$

### *Phase Voltage*

Recall the phase voltage equation (*Equation 2.1*):

$$\begin{aligned} \mathbf{v}_{abc} &= R_{ph} \mathbf{i}_{abc} + \frac{d\mathbf{L}_{abc} \mathbf{i}_{abc}}{dt} \\ &= R_{ph} \mathbf{i}_{abc} + \mathbf{L}_{abc} \frac{d\mathbf{i}_{abc}}{dt} + \frac{d\mathbf{L}_{abc}}{dt} \mathbf{i}_{abc} \end{aligned}$$

When the matrix terms are used, the expanded voltage equation becomes:

$$\begin{bmatrix} v_a \\ v_b \\ v_c \end{bmatrix} = R_{Ph} \begin{bmatrix} i_a \\ i_b \\ i_c \end{bmatrix} + \begin{bmatrix} L_a & 0 & 0 \\ 0 & L_b & 0 \\ 0 & 0 & L_c \end{bmatrix} \begin{bmatrix} \frac{di_a}{dt} \\ \frac{di_b}{dt} \\ \frac{di_c}{dt} \end{bmatrix} + \begin{bmatrix} \frac{dL_a}{dt} & 0 & 0 \\ 0 & \frac{dL_b}{dt} & 0 \\ 0 & 0 & \frac{dL_c}{dt} \end{bmatrix} \begin{bmatrix} i_a \\ i_b \\ i_c \end{bmatrix}$$

$$= \begin{bmatrix} R_{Ph}i_a + L_a \frac{di_a}{dt} + \frac{dL_a}{dt} i_a \\ R_{Ph}i_b + L_b \frac{di_b}{dt} + \frac{dL_b}{dt} i_b \\ R_{Ph}i_c + L_c \frac{di_c}{dt} + \frac{dL_c}{dt} i_c \end{bmatrix}$$

Or, in terms of flux linkage:

$$v_{abc} = R_{Ph}i_{abc} + \frac{d\psi_{abc}}{dt}$$

$$\begin{bmatrix} v_a \\ v_b \\ v_c \end{bmatrix} = R_{Ph} \begin{bmatrix} i_a \\ i_b \\ i_c \end{bmatrix} + \begin{bmatrix} \frac{d\psi_a}{dt} & 0 & 0 \\ 0 & \frac{d\psi_b}{dt} & 0 \\ 0 & 0 & \frac{d\psi_c}{dt} \end{bmatrix} \begin{bmatrix} 1 \\ 1 \\ 1 \end{bmatrix}$$

$$= \begin{bmatrix} R_{Ph}i_a + \frac{d\psi_a}{dt} \\ R_{Ph}i_b + \frac{d\psi_b}{dt} \\ R_{Ph}i_c + \frac{d\psi_c}{dt} \end{bmatrix}$$

### ***Phase Torque***

When expanded, the phase torque equation (**Equation 2.2**) becomes:

$$T_{abc} = L_{abc}i_{abc} \frac{di_{abc}}{d\theta} + i_{abc}^2 \frac{dL_{abc}}{d\theta} - \frac{dW_{Fabc}}{d\theta}$$



$$\begin{aligned}
 &= \begin{bmatrix} L_a & 0 & 0 \\ 0 & L_b & 0 \\ 0 & 0 & L_c \end{bmatrix} \begin{bmatrix} i_a \frac{di_a}{d\theta} \\ i_b \frac{di_b}{d\theta} \\ i_c \frac{di_c}{d\theta} \end{bmatrix} + \begin{bmatrix} \frac{dL_a}{d\theta} & 0 & 0 \\ 0 & \frac{dL_b}{d\theta} & 0 \\ 0 & 0 & \frac{dL_c}{d\theta} \end{bmatrix} \begin{bmatrix} i_a^2 \\ i_b^2 \\ i_c^2 \end{bmatrix} \\
 &\quad - \begin{bmatrix} \frac{W_{F_a}}{d\theta} & 0 & 0 \\ 0 & \frac{W_{F_b}}{d\theta} & 0 \\ 0 & 0 & \frac{W_{F_c}}{d\theta} \end{bmatrix} \begin{bmatrix} 1 \\ 1 \\ 1 \end{bmatrix} \\
 &= \begin{bmatrix} L_a i_a \frac{di_a}{d\theta} + i_a^2 \frac{dL_a}{d\theta} - \frac{W_{F_a}}{d\theta} \\ L_b i_b \frac{di_b}{d\theta} + i_b^2 \frac{dL_b}{d\theta} - \frac{W_{F_b}}{d\theta} \\ L_c i_c \frac{di_c}{d\theta} + i_c^2 \frac{dL_c}{d\theta} - \frac{W_{F_c}}{d\theta} \end{bmatrix}
 \end{aligned}$$

Or, in terms of flux linkage:

$$\begin{aligned}
 \mathbf{T}_{abc} &= \mathbf{i}_{abc} \frac{d\boldsymbol{\psi}_{abc}}{d\theta} - \frac{d\mathbf{W}_{F_{abc}}}{d\theta} \\
 &= \begin{bmatrix} \frac{d\psi_a}{d\theta} & 0 & 0 \\ 0 & \frac{d\psi_b}{d\theta} & 0 \\ 0 & 0 & \frac{d\psi_c}{d\theta} \end{bmatrix} \begin{bmatrix} i_a \\ i_b \\ i_c \end{bmatrix} - \begin{bmatrix} \frac{W_{F_a}}{d\theta} & 0 & 0 \\ 0 & \frac{W_{F_b}}{d\theta} & 0 \\ 0 & 0 & \frac{W_{F_c}}{d\theta} \end{bmatrix} \begin{bmatrix} 1 \\ 1 \\ 1 \end{bmatrix} \\
 &= \begin{bmatrix} i_a \frac{d\psi_a}{d\theta} - \frac{W_{F_a}}{d\theta} \\ i_b \frac{d\psi_b}{d\theta} - \frac{W_{F_b}}{d\theta} \\ i_c \frac{d\psi_c}{d\theta} - \frac{W_{F_c}}{d\theta} \end{bmatrix}
 \end{aligned}$$

### Shaft Torque

The shaft torque is simply the sum of all the phase torques:

$$T_{Shaft} = \sum T_{abc}$$

So, in terms of inductance:

$$T_{Shaft} = L_a i_a \frac{di_a}{d\theta} + L_b i_b \frac{di_b}{d\theta} + L_c i_c \frac{di_c}{d\theta} + i_a^2 \frac{dL_a}{d\theta} + i_b^2 \frac{dL_b}{d\theta} + i_c^2 \frac{dL_c}{d\theta} - \frac{W_{F_a}}{d\theta} - \frac{W_{F_b}}{d\theta} - \frac{W_{F_c}}{d\theta}$$

Or, in terms of flux linkage:

$$T_{Shaft} = i_a \frac{d\psi_a}{d\theta} + i_b \frac{d\psi_b}{d\theta} + i_c \frac{d\psi_c}{d\theta} - \frac{W_{F_a}}{d\theta} - \frac{W_{F_b}}{d\theta} - \frac{W_{F_c}}{d\theta}$$

## E. MCSRМ Expanded Voltage Equation

In *Chapter 2*, the phase voltage equations were outlined for the MCSRМ, using a compact matrix format. The results will be expanded for the  $\alpha\beta$ -reference frame, which would be the format typically used for modelling. In this section, **bold** terms represent vector/matrix terms.

### $\alpha\beta$ -Reference Frame

The  $\alpha\beta$  representations of each matrix are:

$$\mathbf{v}_{\alpha\beta} = \begin{bmatrix} v_{\alpha} \\ v_{\beta} \end{bmatrix} \quad \mathbf{i}_{\alpha\beta} = \begin{bmatrix} i_{\alpha} \\ i_{\beta} \end{bmatrix} \quad \mathbf{L}_{\alpha\beta} = \begin{bmatrix} L_{\alpha} \\ L_{\beta} \end{bmatrix} \quad \boldsymbol{\psi}_{\alpha\beta} = \begin{bmatrix} \psi_{\alpha} \\ \psi_{\beta} \end{bmatrix}$$

### Phase Voltage

Recall the phase voltage equation (*Equation 2.4*):

$$\begin{aligned} \mathbf{v}_{\alpha\beta} &= R_{Ph} \mathbf{i}_{\alpha\beta} + \frac{d\boldsymbol{\psi}_{\alpha\beta}}{dt} \\ \begin{bmatrix} v_{\alpha} \\ v_{\beta} \end{bmatrix} &= R_{Ph} \begin{bmatrix} i_{\alpha} \\ i_{\beta} \end{bmatrix} + \begin{bmatrix} \frac{d\psi_{\alpha}}{dt} \\ \frac{d\psi_{\beta}}{dt} \end{bmatrix} \\ &= \begin{bmatrix} R_{Ph} i_{\alpha} + \frac{d\psi_{\alpha}}{dt} \\ R_{Ph} i_{\beta} + \frac{d\psi_{\beta}}{dt} \end{bmatrix} \end{aligned}$$

If desired, the phase voltage can be then be calculated from the  $\alpha\beta$  voltage by applying the transforms discussed in *Appendix A*:

$$\mathbf{v}_{abc} = \begin{bmatrix} 1 & 0 \\ -\frac{1}{2} & \frac{\sqrt{3}}{2} \\ \frac{1}{2} & -\frac{\sqrt{3}}{2} \end{bmatrix} \mathbf{v}_{\alpha\beta}$$

## F. Tolerance Calculations

### *Dowel Pin Fits*

The dowel OD tolerance (all units in mm) [30] is:

$$d_{Dowel}(actual) = 3.175_{-0.000}^{+0.005}$$

ISO standard shaft-basis H7/h6 locational clearance fit [31] (clearance =  $+\Delta d$ , interference =  $-\Delta d$ ):

$$\Delta d_{Min}(ideal) = +0.000$$

$$\Delta d_{Max}(ideal) = +0.024$$

Ideal hole tolerance for equivalent fit:

$$LB_{Hole}(ideal) = 0.005 + 0.000 = +0.005$$

$$UB_{Hole}(ideal) = 0.000 + 0.024 = +0.024$$

$$d_{Hole}(ideal) = 3.175_{+0.005}^{+0.024}$$

Selected hole diameter tolerance (H7):

$$d_{Hole}(actual) = 3.175_{-0.000}^{+0.012}$$

Calculated clearance (clearance =  $+\Delta d$ , interference =  $-\Delta d$ ):

$$\Delta d_{Min}(actual) = 0.000 + 0.000 = +0.000$$

$$\Delta d_{Max}(actual) = 0.000 + 0.012 = +0.012$$

An ISO “H7” shaft basis fit was selected for the dowel holes, which gives a slightly tighter fit than a standard locational clearance fit, but it was desired to use standard fits to reduce manufacturing cost. Though the fit is close to a transition fit, it is still a clearance fit, and thus this is deemed acceptable.

### ***Bolt Fits***

The bolt OD tolerance (all units in mm) [32] is:

Note: Class 6g6g fit [33].

$$d_{Bolt}(actual) = 3_{-0.126}^{-0.020}$$

ISO standard shaft-basis G7/h6 sliding fit [31] (clearance =  $+\Delta d$ , interference =  $-\Delta d$ ):

$$\Delta d_{Min}(ideal) = +0.005$$

$$\Delta d_{Max}(ideal) = +0.029$$

Ideal hole tolerance for equivalent fit:

$$LB_{Hole}(ideal) = -0.126 + 0.029 = -0.097$$

$$UB_{Hole}(ideal) = -0.020 + 0.005 = -0.015$$

$$d_{Hole}(ideal) = 3_{-0.097}^{-0.015}$$

Selected hole diameter tolerance (G7):

$$d_{Hole}(actual) = 3_{+0.002}^{+0.012}$$

Calculated clearance (clearance =  $+\Delta d$ , interference =  $-\Delta d$ ):

$$\Delta d_{Min}(actual) = 0.002 + 0.020 = +0.022$$

$$\Delta d_{Max}(actual) = 0.012 + 0.126 = +0.138$$

An ISO “G7” shaft basis fit was selected for the bolt holes, which gives a looser fit than a sliding fit, but it was desired to use standard fits to reduce manufacturing cost. The “G7” bolt hole tolerance gives a fit between free running and loose running. However, this is acceptable, as it reduces the positional accuracy required for the bolt holes, reducing manufacturing costs.

## Resolver Press Fit

### *Stator*

The resolver stator OD tolerance (all units in mm) [34] is:

$$d_{ResStator}(actual) = 52_{-0.03}^{+0.00}$$

ISO standard shaft-basis P7/h6 locational interference fit [31] (clearance =  $+\Delta d$ , interference =  $-\Delta d$ ):

$$\Delta d_{Min}(ideal) = -0.002$$

$$\Delta d_{Max}(ideal) = -0.051$$

Ideal hole tolerance for equivalent fit:

$$LB_{Hole}(ideal) = 0.000 - 0.051 = -0.051$$

$$UB_{Hole}(ideal) = -0.030 - 0.002 = -0.032$$

$$d_{Hole}(ideal) = 3.000_{-0.051}^{-0.032}$$

Selected hole diameter tolerance (R6):

$$d_{Hole}(actual) = 52_{-0.054}^{-0.035}$$

Calculated interference (clearance =  $+\Delta d$ , interference =  $-\Delta d$ ):

$$\Delta d_{Min}(actual) = -0.030 - 0.035 = -0.005$$

$$\Delta d_{Max}(actual) = +0.000 - 0.051 = -0.051$$

When checked with calculations, the ISO “R6” hole diameter tolerance is shown to provide a locational interference fit, as desired.

### **Rotor**

The resolver rotor ID tolerance (all units in mm) [34] is:

$$d_{ResRotor}(actual) = 12.7^{+0.03}_{-0.00}$$

ISO standard hole-basis H7/p6 locational interference fit [31] (clearance =  $+\Delta d$ , interference =  $-\Delta d$ ):

$$\Delta d_{Min}(ideal) = 0.000$$

$$\Delta d_{Max}(ideal) = -0.029$$

Ideal shaft tolerance for equivalent fit:

$$LB_{Shaft}(ideal) = 0.000 + 0.030 = +0.030$$

$$UB_{Shaft}(ideal) = 0.030 + 0.000 = +0.030$$

$$d_{Shaft}(ideal) = 12.7^{+0.030}_{+0.030}$$

Selected shaft diameter tolerance (H8):

$$d_{Shaft}(actual) = 12.7^{+0.038}_{+0.033}$$

Calculated interference (clearance =  $+\Delta d$ , interference =  $-\Delta d$ ):

$$\Delta d_{Min}(actual) = 0.030 - 0.033 = -0.003$$

$$\Delta d_{Max}(actual) = 0.000 - 0.038 = -0.038$$

When checked with calculations, the ISO “H8” shaft diameter tolerance is shown to provide a fit that is slightly tighter than locational interference, but this is acceptable.



## Radial Tolerances

### *Airgap*

The airgap tolerance bounds can be calculated as:

$$\begin{aligned}l_{Airgap} &= IR_R - OR_S \\ &= 90_{-0.050}^{+0.050} - 89.6_{-0.050}^{+0.050} \\ &= 0.4_{-0.1}^{+0.1}\end{aligned}$$

where:

$$IR_R = \text{rotor airgap radius [mm]}$$

$$OR_S = \text{stator airgap radius [mm]}$$

$$l_{Airgap} = \text{airgap length [mm]}$$

Thus, if the radial pole deflection due to radial forces is assumed to be negligible, it can be seen that airgap contact will be avoided under all cases.

## Axial Tolerances

### *Stack Alignment (Side “B”)*

The distance to the leading edge of the stator stack is:

$$\begin{aligned}x_{S1} &= x_9 + x_8 \\ &= 12_{-0.12}^{+0} + 1.5_{-0}^{+0.2} \\ &= 13.5_{-0.12}^{+0.2}\end{aligned}$$

The distance to the leading edge of the rotor stack is:

$$\begin{aligned}x_{R1} &= x_0 \\ &= 13.5_{-0}^{+0.1}\end{aligned}$$

Therefore, the leading edge stack misalignment between the rotor and stator is:

$$\begin{aligned}\delta_{Stack1} &= x_{R1} - x_{S1} \\ &= 13.5_{-0}^{+0.1} - 13.5_{-0.12}^{+0.2} \\ &= 0_{-0.1}^{+0.12}\end{aligned}$$

### *Stack Clearance (Side “A”)*

The distance to the trailing edge of the stator stack is:

$$\begin{aligned}x_{S2} &= x_{S1} + x_6 \\ &= 13.5_{-0.12}^{+0.2} + 39.5_{-0}^{+0.5} \\ &= 53_{-0.12}^{+0.7}\end{aligned}$$

The distance to the trailing edge of the rotor stack is:

$$\begin{aligned}x_{R2} &= x_{R1} + x_1 \\ &= 13.5_{-0}^{+0.1} + 39.5_{-0}^{+0.5} \\ &= 53_{-0}^{+0.6}\end{aligned}$$

Therefore, the trailing edge stack misalignment between the rotor and stator is:

$$\begin{aligned}\delta_{Stack2} &= x_{R2} - x_{S2} \\ &= 53_{-0}^{+0.6} - 53_{-0.12}^{+0.7} \\ &= 0_{-0.1}^{+0.12}\end{aligned}$$

### *Coil Clearance (Side “B”)*

The distance to the leading edge of the coil, based on the analytically calculated coil axial length, is:

$$\begin{aligned}x_{C1} &= x_{S1} - x_5 \\&= 13.5^{+0.2}_{-0.12} - 7^{+0}_{-0} \\&= 6.5^{+0.2}_{-0.12}\end{aligned}$$

The distance to the adjacent endcap face is:

$$\begin{aligned}x_{E1} &= x_{R1} - x_3 \\&= 13.5^{+0.1}_{-0} - 8^{+0}_{-0.2} \\&= 5.5^{+0.2}_{+0.1}\end{aligned}$$

Therefore, the leading edge coil clearance between the coil and endcap B is:

$$\begin{aligned}\delta_{Coil1} &= x_{C1} - x_{E1} \\&= 6.5^{+0.2}_{-0.12} - 5.5^{+0.2}_{+0.1} \\&= 1^{+0}_{-0.22}\end{aligned}$$

### *Coil Clearance (Side “A”)*

The distance to the trailing edge of the coil, based on the analytically calculated coil axial length, is:

$$\begin{aligned}x_{C2} &= x_{S2} + x_7 \\&= 53^{+0.7}_{-0.12} + 7^{+0}_{-0} \\&= 60^{+0.7}_{-0.12}\end{aligned}$$

The distance to the adjacent endcap face is:

$$\begin{aligned}x_{E2} &= x_{R2} + x_4 \\ &= 53_{-0}^{+0.6} + 8_{-0.2}^{+0} \\ &= 61_{-0.2}^{+0.6}\end{aligned}$$

Therefore, the trailing edge coil clearance between the coil and endcap A is:

$$\begin{aligned}\delta_{Coil2} &= x_{E2} - x_{C2} \\ &= 61_{-0.2}^{+0.6} - 60_{-0.12}^{+0.7} \\ &= 1_{-0.1}^{-0.08}\end{aligned}$$

### ***Wave-Spring Preload***

The distance to the leading edge of the wave-spring is:

$$\begin{aligned}x_{WS1} &= x_9 + x_{10} + x_{11} \\ &= 12_{-0.12}^{+0} + 42_{-0.15}^{+0.2} + 2.16_{-0.1}^{+0.2} \\ &= 56.16_{-0.37}^{+0.4}\end{aligned}$$

The distance to the trailing edge of the wave-spring is:

$$\begin{aligned}x_{WS2} &= x_{R2} + x_2 - x_{13} \\ &= 53_{-0}^{+0.6} + 16_{-0}^{+0.3} - 12_{-0.12}^{+0} \\ &= 57_{-0.12}^{+0.9}\end{aligned}$$

Therefore, the compressed wave-spring length after installation is:

$$\begin{aligned}\delta_{WS} &= x_{WS2} - x_{WS1} \\ &= 57_{-0.12}^{+0.9} - 56.16_{-0.37}^{+0.4} \\ &= 0.84_{+0.25}^{+0.5}\end{aligned}$$

The preload force range can then be calculated, based on the spring constant for the selected spring. The un-deformed length ( $x_{100\%}$ ) and spring force at 50% deflection ( $F_{50\%}$ ) are specified by the manufacturer in [35]:

$$x_{100\%} = 1.68 \text{ mm}$$

$$F_{50\%} = 33.4 \text{ N}$$

Therefore, the spring constant ( $k$ ) can then be calculated:

$$\begin{aligned} F_{50\%} &= kx_{50\%} \\ k &= \frac{F_{50\%}}{x_{50\%}} \\ &= \frac{2F_{50\%}}{x_{100\%}} \\ &= \frac{2(33.4)}{1.68} \\ &= 39.76 \frac{\text{N}}{\text{mm}} \end{aligned}$$

Once the spring constant is calculated, the preload force ( $F_{Preload}$ ) can be calculated:

$$\begin{aligned} F_{Preload} &= k\delta_{WS} \\ &= (39.76)0.84^{+0.5}_{+0.25} \\ &= 33.4^{+19.9}_{+9.9} \text{ N} \end{aligned}$$

Therefore, the preload is expected to vary between roughly 43 N and 53 N, which is lower than the preload ranges specified in Fig. 7.3. However, as discussed earlier in this chapter, this was intentional.

## G. Torque Equation Validation

The non-coupled CSRSM torque equations (*Equation 2.2* and *Equation 2.3*) have been validated against FEA in Fig. X.44, and the co-energy for each phase has been calculated in Fig. X.45.

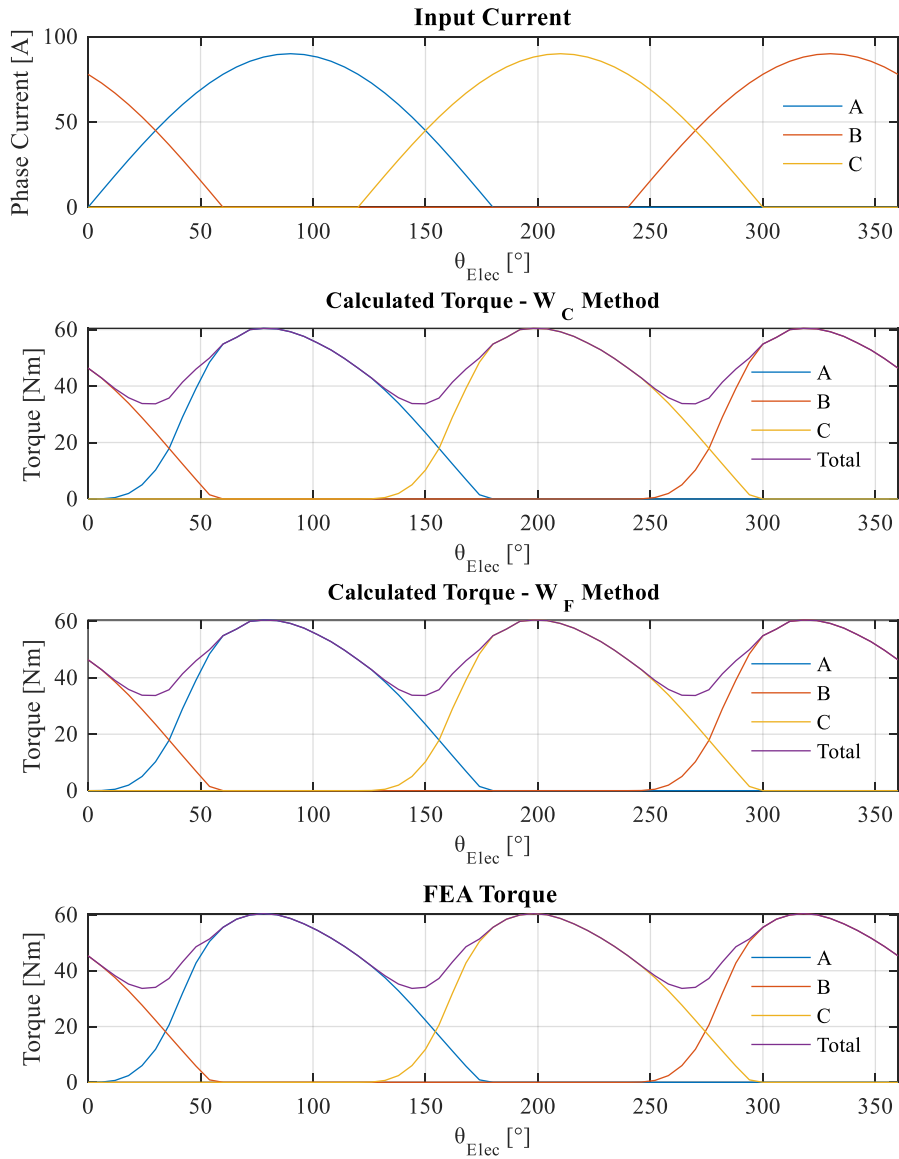


Fig. X.44 Co-energy vs. field-energy torque vs. FEA (12/16 CSRSM)

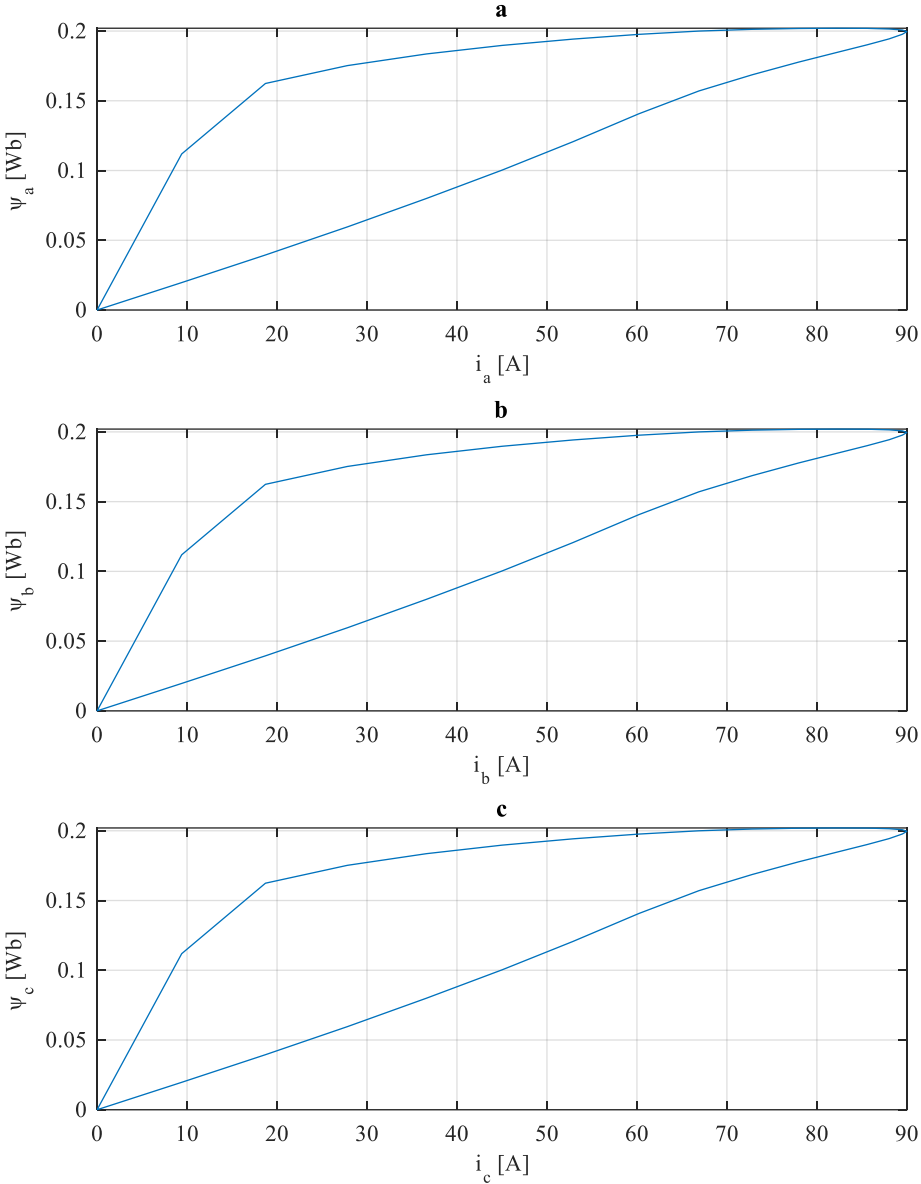


Fig. X.45 Phase  $\psi/i$  plots (12/16 CSRМ)

This page was left intentionally blank